Titre: Title:	Design and Optimization of a Robot for Abrasive Waterjet Polishing of Hydraulic Turbine Blades
Auteur: Author:	Hamed Khakpour
Date:	2014
Type:	Mémoire ou thèse / Dissertation or Thesis
Référence: Citation:	Khakpour, H. (2014). Design and Optimization of a Robot for Abrasive Waterjet Polishing of Hydraulic Turbine Blades [Thèse de doctorat, École Polytechnique de Montréal]. PolyPublie. https://publications.polymtl.ca/1463/

Document en libre accès dans PolyPublie
Open Access document in PolyPublie

URL de PolyPublie: PolyPublie URL:	https://publications.polymtl.ca/1463/
Directeurs de recherche: Advisors:	Lionel Birglen, & Souheil-Antoine Tahan
Programme: Program:	Génie mécanique

UNIVERSITÉ DE MONTRÉAL

DESIGN AND OPTIMIZATION OF A ROBOT FOR ABRASIVE WATERJET POLISHING OF
HYDRAULIC TURBINE BLADES

HAMED KHAKPOUR
DÉPARTEMENT DE GÉNIE MÉCANIQUE
ÉCOLE POLYTECHNIQUE DE MONTRÉAL

THÈSE PRÉSENTÉE EN VUE DE L'OBTENTION
DU DIPLÔME DE PHILOSOPHIÆ DOCTOR
(GÉNIE MÉCANIQUE)
JUIN 2014

UNIVERSITÉ DE MONTRÉAL

ÉCOLE POLYTECHNIQUE DE MONTRÉAL

Cette thèse intitulée :

DESIGN AND OPTIMIZATION OF A ROBOT FOR ABRASIVE WATERJET POLISHING OF
HYDRAULIC TURBINE BLADES

présentée par : KHAKPOUR Hamed
en vue de l'obtention du diplôme de : Philosophiæ Doctor
a été dûment acceptée par le jury d'examen constitué de :

M. BALAZINSKI Marek, Docteur ès sciences, président
M. BIRGLEN Lionel, Ph.D., membre et directeur de recherche
M. TAHAN Souheil-Antoine, Ph.D., membre et codirecteur de recherche
M. ACHICHE Sofiane, Ph.D., membre
M. CARDOU Philippe, Ph.D., membre

DEDICATION

"To my beloved parents, sister,
and brother whose memory is forever in my heart."

ACKNOWLEDGMENTS

RÉSUMÉ

Dans l'industrie de fabrication de turbine hydraulique, toutes les surfaces de turbines qui sont en contact avec de l'eau devraient être polies afin d'obtenir la qualité et l'efficacité maximales. Pour cela, il est nécessaire d'utiliser une méthode de polissage qui peut avoir accès à toutes les surfaces des turbines incluant leurs bords, leurs zones restreintes et leurs courbures serrées. En raison des propriétés particulières qu'offre la technique de polissage par jet d'eau abrasif, celle-ci peut être utilisée pour accomplir cette tâche. Par conséquent, dans cette recherche, les propriétés de cette méthode non-conventionnelle sont examinées dans un premier temps et les principaux paramètres affectant ses performances sont alors déterminés. Ensuite, les conditions nécessaires de manipulations de la buse de pulvérisation vis-à-vis des surfaces courbes sont étudiées et les propriétés d'un bras robotisé pour manipuler celle-ci sont obtenues afin de réaliser cette tâche d'une manière appropriée. Par après, plusieurs mécanismes robotiques tels que des mécanismes sériels, parallèles à membrures, parallèles à câbles, et des robots hybrides sont considérés et leurs capacités à être utilisé dans ce processus sont analysées. Il est alors démontré qu'une l'architecture hybride est le meilleur candidat à retenir pour le design d'un robot de polissage par jet d'eau abrasif.

Ensuite, l'architecture conceptuelle d'un robot hybride à 5 DDL est proposée. La structure du robot est constituée d'un mécanisme parallèle à câbles à 3 DDL et d'un poignet sériel à 2 DDL. Afin d'améliorer les propriétés cinématiques du mécanisme à câbles tout en minimisant le nombre d'actionneurs nécessaires, il est proposé d'utiliser des différentiels pour guider ce robot manipulateur. Aussi, la rigidité et la compacité du mécanisme sont améliorées en utilisant une liaison prismatique.

Par la suite, les systèmes à câbles différentiels sont examinés et les différences entre leurs propriétés cinématiques et celles de systèmes actionnés indépendamment pour chaque câble sont décrites. Il est démontré que la force résultante de tous les câbles d'un différentiel à câbles doit être prise en compte dans son analyse cinématique. En effet, dans un système différentiel planaire, la direction de la force résultante n'est pas fixée vers un point particulier. Mais plutôt, elle se déplace dans le plan de ce système différentiel. Cette propriété peut être bénéfique pour les propriétés cinématiques des robots à câbles. En comparant deux types d'espace de travail de plusieurs robots planaires actionné par des mécanismes différentiels par rapport à leurs équivalents pleinement actionnés, il est alors montré qu'en utilisant ces mécanismes, les espaces de travail des robots planaires à câbles peuvent être améliorés. Cependant, cette même propriété qui augmente la plage de variation de la direction de la force résultante dans un câble différentiel, diminue aussi son amplitude. Ainsi, le design optimal d'un différentiel à câble résulte d'un compromis entre ces deux propriétés.

vi

Ensuite, une méthode de synthèse est présentée afin de déterminer tous les combinaisons possibles de différentiels à câbles pour généraliser l'idée d'utiliser de tels mécanismes dans le design de robots planaires. De plus, l'application de mécanismes différentiels dans des robots spatiaux est aussi envisagée et il est montré qu'ils ont des propriétés similaires aux types planaires.

Le robot manipulateur proposé est commandé par trois systèmes différentiels planaires de telle sorte que trois actionneurs agissent sur six câbles et que le quatrième actionneur agisse sur la liaison prismatique. Pour cela, l'analyse cinématique du robot est développée et à travers la définition de deux indices de performance, à savoir I_{WCW} et I_{WFW}, les espaces de travail "wrench-closure" et "wrench-feasible" du robot sont évalués. En utilisant ces indices, la structure du robot proposée est optimisé. Alors, en comparant les espaces de travail du robot optimisé avec ceux des autres robots pleinement actionnés, il est montré qu'en utilisant des systèmes différentiels, les performances des mécanismes spatiaux à câbles sont améliorées. Ces résultats peuvent aussi être considérés dans le design d'autres robots actionnés par des câbles pour améliorer leurs propriétés cinématiques à faible coût.

Dans la partie suivante de cette étude, un banc d'essai est mis en place pour réaliser des expériences préliminaires sur le procédé de polissage par jet d'eau abrasif et évaluer l'effet des paramètres de polissage sur la qualité de la surface finie. Les résultats de ces tests initiaux sont utilisés pour rendre compte de l'importance relative de ces paramètres. En utilisant ces tests, la forme du profil de retrait de matière est aussi estimée au point de polissage. Pour ce faire, deux indices de performance, à savoir I_{curv} et I_{path}, sont présentés afin d'évaluer l'adaptabilité aussi bien de la surface à polir que de la trajectoire générée au procédé de polissage par jet d'eau abrasif.

Dans la dernière partie de cette thèse, une méthode est développée pour générer des chemins de balayage spécifique à la technique de polissage par jet d'eau abrasif sur des surfaces courbes modélisées par des facettes triangulaires. Dans cette méthode, différentes options sont utilisées pour obtenir une courbe de référence. Cette dernière a un impact significatif sur la forme finale de la trajectoire. Pour trouver les points des courbes décalées, des distances géodésiques sont calculées dans des directions particulières. Une fois que le chemin initial de balayage est généré sur la surface, la possibilité d'existence de discontinuités est vérifiée. Alors, de nouvelles trajectoires continues sont générées en divisant la trajectoire initiale dans ces zones si elles existent. Finalement, en utilisant l'indice I_{path}, la performance du chemin généré obtenu en utilisant chacune des options est évaluée et le meilleur chemin est retenu pour être utilisé dans ce procédé. Cette méthode est développée afin de générer des chemins spécifiques à la méthode de polissage par jet d'eau abrasif. Cependant, elle peut être utilisée pour générer des trajectoires dans d'autres applications où une distance constante de décalage est requise.

ABSTRACT

In hydraulic turbine manufacturing, all surfaces of the turbines which are in contact with the water flow should be polished to obtain the desired quality and maximal efficiency. For this, it is needed to use an effective polishing method which can have access to all surfaces of the turbines including edges, narrow areas and tight bends. Because of the particular properties of the abrasive waterjet polishing technique, it can be used to accomplish this task. Therefore, in this research, the properties of this non-conventional method are first investigated and the main parameters affecting its performance are then determined. Next, the manipulation requirements of the jet nozzle over free-form surfaces are studied and the properties of a robotic arm to appropriately perform this task are obtained. Afterwards, several robotic mechanisms, e.g., serial, linkage-driven parallel, cable-driven parallel, and hybrid robots are considered and their abilities to be used in this process are investigated. It is then shown that a hybrid architecture is the best candidate for the design of an abrasive waterjet polishing robot.

Next, the conceptual design of a 5-DOF hybrid robot is proposed. The structure of this robot is made of a 3-DOF cable-driven parallel mechanism and a 2-DOF serial wrist. To improve the kinematic properties of the cable-driven mechanism while the number of required actuators is kept at a minimum, it is proposed to use cable differentials to drive this manipulator. Also, the rigidity and compactness of the mechanism is improved through the use of a prismatic joint in its structure.

Afterwards, differentially driven cable systems are investigated and the differences between their kinematic properties and these of independently actuated cables are described. It is shown that the resultant force of all cables of a cable differential should be taken into account in its kinematic analysis. Indeed, in a planar differential, the direction of the resultant force is not fixed toward a particular point. Instead, it moves within the plane of that differential. This property can be beneficial in the kinematic properties of differentially driven cable robots. By comparing two types of workspaces of several planar robots actuated by differentials with their fully actuated counterparts, it is then shown that using these mechanisms, these workspaces of planar cable robots can be improved. However, the same property that increases the range of variation of the resultant force direction in a cable differential, decreases its magnitude. Thus, the optimal design of a cable differential is a trade-off between these two properties.

Next, a synthesis method is presented to find all possible arrangements of the cable differentials to generalize the idea of using such mechanisms in the design of planar cable robots. Additionally, the application of differentials in spatial robots is also investigated and it is shown that they have properties similar to the planar types.

The proposed robotic manipulator is driven by three planar differentials so that three actuators

drive six cables and the fourth one drives the prismatic joint. For this, the kinematic analysis of the robot is provided and through the definition of two performance indices, namely I_{WCW} and I_{WFW}, the wrench-closure and wrench-feasible workspaces of the robot are evaluated. Using these indices, the structure of the proposed robot is optimized. Then, by comparing the workspaces of the optimized robot with those of two other fully driven ones, it is shown that, using differentials, the performance of spatial cable mechanisms are improved. These results can also be considered in the design of other cable-driven robots to improve their kinematic properties at low cost.

In the next part of this study, a test rig is built to do preliminary experiments with the abrasive waterjet polishing process and evaluate the effect of the polishing parameters on the quality of the finished surface. The results of these initial tests are used to establish the relative importance of these parameters. Using these tests, the shape of the material removal profile is also estimated at the polishing spot. This profile is then used to define limits to be respected in the polishing path generation. For this, two performance indices, namely I_{curv} and I_{path} are presented to evaluate the adaptability of both the desired free-form surface and the generated trajectory to the abrasive waterjet polishing process.

In the last part of this research, a method is developed to generate scanning paths for the abrasive waterjet polishing technique on the free-form surfaces modeled by triangular faces. In this method, different options are used to obtain a reference curve. This curve has a significant impact on the final shape of the trajectory. To find the points of the offset curves, geodesic distances are calculated in particular directions. When the initial scanning path is generated on a free-form surface, the possibility of existence of discontinuities is checked. Then, new continuous trajectories are generated by dividing the initial trajectory in these areas if they exist. Finally, using the index I_{path}, the performance of the generated path obtained using each option is evaluated and the best path is chosen to be used in the process. This method is particularly developed to generate paths for abrasive waterjet polishing method. However, it can be used to generate trajectories for other applications where a constant offset distance is needed.

TABLE OF CONTENTS

LIST OF TABLES

LIST OF FIGURES

LIST OF ABBREVIATIONS

AAJ	Abrasive air-jet
ANOVA	Analysis of variance
AWJ	Abrasive waterjet
AWJP	Abrasive waterjet polishing
BP	Base platform
CAD	Computer-aided design
CAM	Computer-aided manufacturing
CL	Cutter location
DKP	Direct kinematic problem
DKS	Direct kinematic singularity
DOA	Degrees of actuation
DOF	Degree of freedom
DVP	Direct velocity problem
EE	End-effector
FAWJ	Flash abrasive waterjet
GDI	Global dexterity index
GA	Genetic algorithm
IKP	Inverse kinematic problem
IKS	Inverse kinematic singularity
IVP	Inverse velocity problem
MP	Moving platform
NPSHr	Required Net Positive Suction Head
OAE	Orthogonal array of experiment
PWJ	Pure waterjet
SOD	stand-off-distance
WC	Wrench closure
WCW	wrench-closure workspace
WF	Wrench feasible
WFW	Wrench-feasible workspace

CHAPTER 1

INTRODUCTION

1.1 Hydraulic turbine surface machining

Hydraulic turbines are used to convert the energy of water into kinetic energy to turn an electric generator and produce electricity. Depending on the level of water stored behind a dam and its available flow rate, different types of turbines can be used. Examples of these turbines are Francis, Kaplan, BUlb, and Pelton turbines as shown in Fig. 1.1. Since the efficiencies of these turbines are less than hundred percent, some part of the energy is always lost. Several factors are affecting the efficiency of these turbines. One of them is the friction between the water and the surface of the blades. Thus, it is highly desirable to decrease the amount of the friction loss during the operation of hydraulic turbines.

Friction depends on the quality of the finished surface which is identified as the deviation of the real profile of a machined surface from its nominal designed shape. This variance is measured at macro and microgeometric levels. The first is usually referred to as waviness and caused by machining errors, etc. The latter is the result of the existence of grooves, cracks, crystalline structure/formation on the surface. It is known as the roughness of the surface [1].

Existence of these deviations weakens the integrity of the surface which can result in amplification of the friction force in a turbine runner. Therefore, to increase the efficiency of the turbines, roughness and waviness of the surfaces should be improved. Consequently, in a hydraulic turbine manufacturing industry, after initial machining processes such as sawing, drilling, milling, etc., some supplementary machining procedures are required. Examples of these supplementary steps which can lead to a very fine surface are grinding and polishing. Grinding is defined as removing the remaining material of machining process including swarf and marks of saw from the surface. Polishing is referred to as removing the remains of grinding process at a very low rate to reach a very smooth and uniform surface [2]. The polishing process is the final step of preparation of the surfaces of these turbines.

So far, different methods such as abrasive sanding belts and abrasive sanding discs are used to perform this step. However, polishing narrow areas (e.g., welded fillets located in small spaces between turbine blades) requires a particular technique which can access these hard-to-reach areas and then, appropriately polish them to obtain the desired quality. To do this, in addition to the common methods, a non-conventional technique such as abrasive waterjet polishing method can also be used in the turbine industry. Moreover, a particular manipulation system is needed to
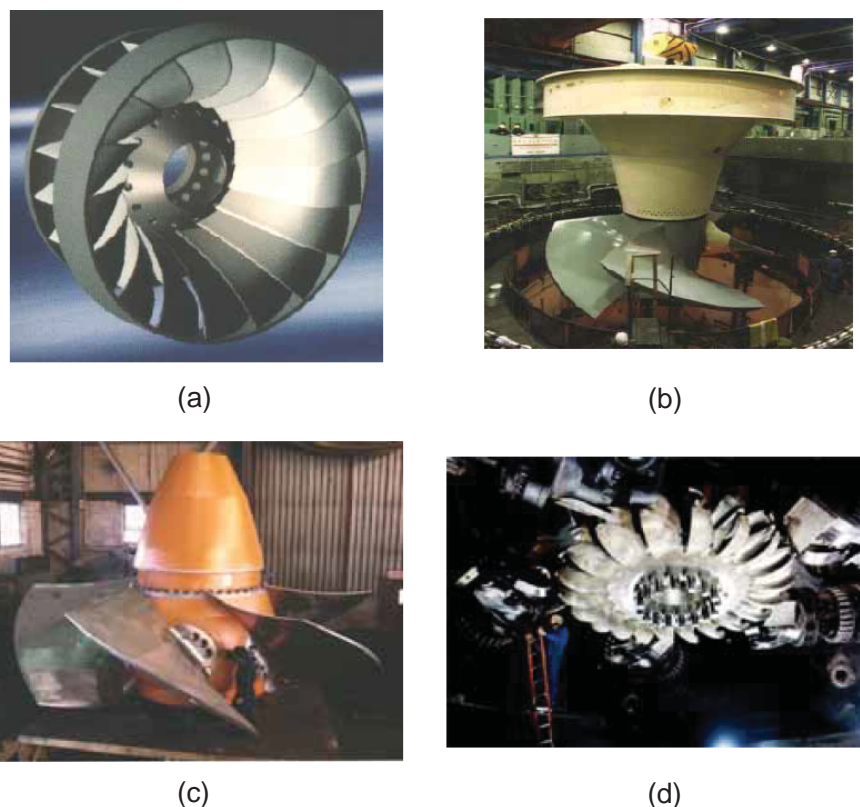
Figure 1.1 Hydraulic turbines: (a) Francis; (b) BUlb; (c) Kaplan (d) Pelton.

deliver the abrasive waterjet to the desired area either on a large surface of a turbine or in a tight and inaccessible location between blades.

Although several studies have been done on abrasive waterjet polishing methods, all aspects of its performance have not been revealed yet. In this study, this technique is investigated and the requirements of a device to implement this process are determined. The main focus of this research is on developing a device able to accomplish abrasive waterjet polishing on all objective areas of the turbines. For this, it is required to design a mechanism able to operate appropriately under the particular environmental characteristics of this technique. The second is dedicated to developing a method to generate polishing paths on the surfaces and edges of turbine blades. In addition, by designing and building a test-rig, an experimental study on the polishing process and the effect of the polishing parameters on the quality of the surface and process duration is done.

This dissertation is based on three papers which have been accepted by or submitted to scientific journals and is written in the following sequences:

- In Chapter 1 an introduction to the requirements of hydraulic turbine manufacturing is provided;
- In Chapter 2 a literature review on the related topics is presented;

– In Chapter 3 the objectives of this research are mentioned;

– In Chapter 4 the organization of the articles is discussed;

– Chapters 5, 6, and 7 are constituted of the three papers showing the main results obtained in this research;

– In Chapter 8 the methodology and results of the experimental research are described;

– In Chapter 9 a general discussion on the results presented in the three articles is mentioned;

– Finally, Chapter 10 conclusions and recommendations for future work are provided.

CHAPTER 2

LITERATURE REVIEW

2.1 Introduction to jet machining

In addition to common machining methods there are other types of non-conventional machining techniques such as electric discharge machining, electrochemical machining, abrasive air-jet machining and abrasive waterjet machining systems. In the abrasive air-jet machining, compressed air is used to produce a high velocity jet while in the latter, the high pressure water is used to produce a waterjet for machining purpose [3, 4].

2.1.1 Air-jet machining systems

Abrasive air-jet (AAJ) machining is an effective and efficient method for machining (e.g., deburring, cutting, drilling, polishing, etc.) of different types of hard and brittle materials such as ceramics, silicon and glasses [5–7]. In this process, compressed air is turned to high speed air-jet by passing through a nozzle, to accelerate abrasive grains and produce a high velocity abrasive jet performing the material removal via erosive action [6–8]. Compared to common machining methods, using this system for machining of hard and brittle materials has several advantages such as no thermal effect on the workpiece, no contact with the object, low cutting force, high machining versatility, and machining of hard-to-reach areas [3, 5, 7, 9].

In AAJ machining, the material removal takes place in two ways, i.e., brittle and ductile erosions [10]. The brittle erosion results from the propagation of the lateral and radial cracks caused by the collision of abrasives with the surface [3, 8]. In the brittle erosion, the material removal rate mainly depends on the vertical component of the velocity of the abrasive particles with respect to the surface and their sizes. It mostly happens where velocity vectors of the particles are perpendicular to the surface. On the contrary, ductile erosion happens due to the plastic deformation caused by cutting and plowing actions and mostly depends on the tangential component of the particle velocity [8, 10]. Consequently, as illustrated in Fig. 2.1, the material removal from the surface of a ductile workpiece increases when the angle of the nozzle is decreased from $90°$ to $30°$ [6, 9, 10].

The material removal rate of this system is limited and depends on the size and velocity of abrasive particles, impact angle and stand-off-distance (SOD) [6, 9]. The velocity of abrasive particles is in the range of $60 - 240$ m/s [10, 13, 14] and the required air pressure is around $2 - 10$ bar [5–10, 12–14]. The diameter of nozzles used in this technique are usually in the range of $0.36 - 4$ mm [5–10, 12]. Increasing this diameter leads to higher material removal rate [6]. SOD
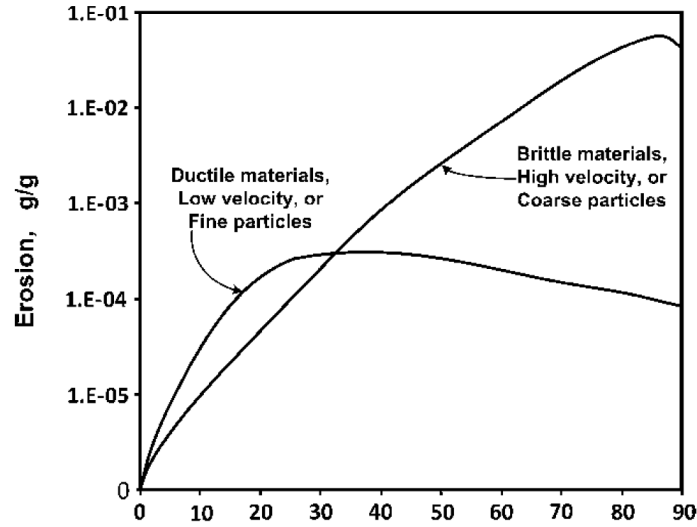
Figure 2.1 Effect of impact angle on the erosion of brittle and ductile materials [11].
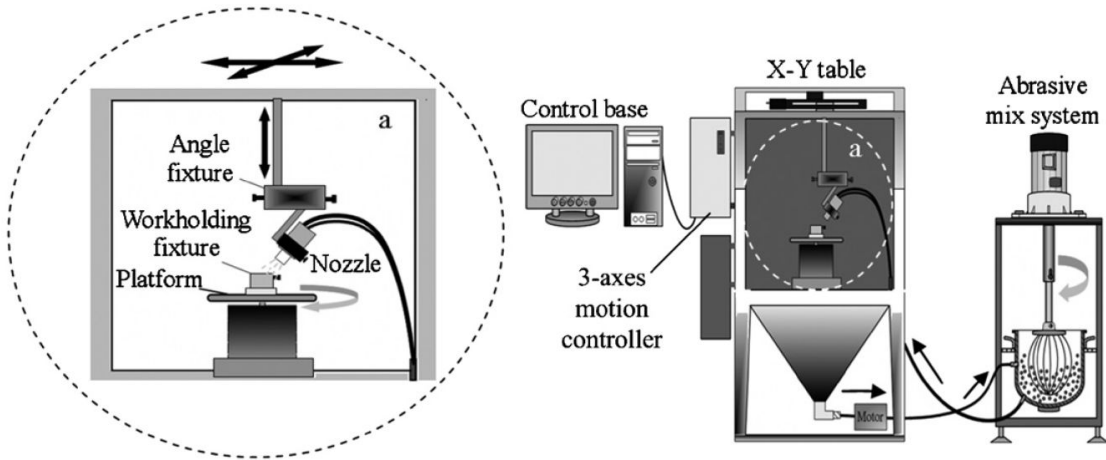
Figure 2.2 Schematic of an abrasive air-jet polishing setup [12].

is the distance between the nozzle tip and the surface of the workpiece and is around $1-25$ mm [5–10, 12]. In AAJ system, different types of grains such as aluminum oxide (Al_2O_3), silicon carbide (SiC), and silicon dioxide (SiO_2) are used as abrasive materials [6–9, 12]. Depending on the required quality of the surface, the size of abrasive particles is around $10-150$ μm in diameter [6–8, 13].

In AAJ, collision among high speed abrasive particles and the workpiece can lead to an undesirably high rate of material removal. Therefore, in polishing process where a lower removal rate is needed, water is added to the compressed air to adjust the system for abrasive jet polishing [12]. The schematic of such system is shown in Fig. 2.2. In this system, to improve the sliding motion

of the abrasive materials on the surface, a water-solvent oil is added as a lubricant.

2.1.2 Waterjet machining systems

Abrasive waterjet (AWJ) system has a great potential to be used in the industry. Indeed, almost all types of materials including metals, nonmetals, composites and nanomaterials can be machined using this technology [16]. The modern waterjet technology was developed by Franz in 1968 [17]. Later, a waterjet system was used as a cutting machine instead of a saw to cut pieces of wooden puzzles in 1975 for the first time [18]. In 1980, abrasives were added to pure waterjet systems and the resultant slurry was used to cut harder materials such as steel and glass [4]. Next, robotic waterjet systems emerged to produce three dimensional (3-D) parts in the automotive industry [18, 19].

By definition, the waterjet technique is a method which produces a high pressure stream of water using a high pressure water pump and turns it to a high velocity stream using a narrow nozzle for machining (i.e., cutting, drilling, polishing, etc.) [4, 20]. To the best of the author's knowledge, so far, three types of waterjet systems have been developed: plain waterjet or pure waterjet (PWJ), abrasive waterjet (AWJ) and flash abrasive waterjet (FAWJ) [16, 20, 21].

In the PWJ system, the high-pressure pure water is used to cut soft materials such as candy bars, papers, plastics, etc [20, 21]. In the AWJ system, abrasive grains are added to the waterjet to increase its penetration power. In this system, due to the transmission of the momentum from water to abrasives, with the same system (e.g., pump, nozzle, etc), the velocity of the discharging jet is lower than that of PWJ [19]. The FAWJ can be considered as the enhanced version of AWJ where in the discharge side of the nozzle, the superheated waterjet is turned to steam [16]. This can result in higher quality of workpiece surface in cutting process particularly with delicate materials.

Among these techniques, the AWJ system has more applications in the industry. So far, this system has been mostly applied as a cutting machine. This machine can perform the machining of difficult-to-cut materials like titanium aluminide (TiAl) and different types of ceramics [16, 21]. An example of such systems is shown in Fig. 2.3.

For cutting purposes, the pressure of the water before the orifice is usually in the range of $130 - 400$ MPa [16, 18, 20–22] and thus, the jet of water smashes the workpiece with a supersonic speed (around $1 - 3$ Mach) [18, 20]. The orifice is made of a very hard material such as sapphire and diamond. Also, the diameter the orifice is around $0.1 - 0.5$ mm. The maximum SOD is less than 50 mm [18]. Moreover, different grains such as garnet and aluminum oxide (Al_2O_3) can be used as abrasives in AWJ cutting machines [19, 21, 22].

Figure 2.3 A 5-Axis AWJ cutting head [15].

2.1.3 Abrasive waterjet polishing systems

Modifying an AWJ system to perform a more delicate process such as polishing is a novel technique and the current information around this particular application of AWJ is limited. This technique is also known as abrasive waterjet polishing (AWJP) and was developed at Delft University of Technology in 1998. In this method, a medium pressure pump delivers water to a nozzle where it is mixed with abrasive particles to produce the abrasive jet [23].

In AWJP, the material can be removed from the surface of the workpiece through collision and shearing actions between abrasive particles and the surface [23]. In other words, similarly to AAJ systems, two types of material removal occur: either brittle or ductile removal. In the former, the kinetic energy of abrasives produces the permanent imprint on the surface and leads to material removal while the latter happens by shearing action between abrasives and the surface [4, 23]. In AWJP, the kinetic energy of abrasives is low and thus usually ductile erosion occurs. In general, several factors affect the performance of this machining system [23]:

– abrasive material type and size;
– velocity (related to the water pressure) of slurry water and abrasives;
– abrasive feeding rate;
– stand-off-distance (SOD);
– angle between the nozzle axis and the tangential plane at the polishing spot.

Compared to traditional polishing methods, using AWJP provides several advantages [16, 19, 21, 23]:

– polished surface is not affected by the distortion of the polishing tool;
– there is no contact between the polishing tool and the workpiece;
– physical and mechanical properties of the surface are not changed;
– there is no thermal effect on the surface;
– hard-to-reach areas of the workpiece can be polished;
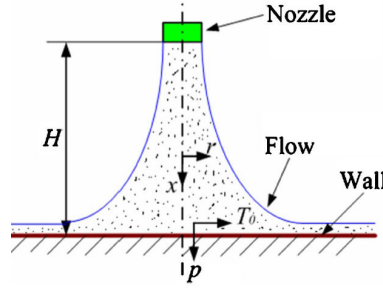
Figure 2.4 The schematic of the cross section of waterjet flow in polishing process [23].

– high machining versatility.

In AWJP, the slurry goes across the nozzle with a pressure of 1 to 10 bar [23, 24]. Taking into account the hardness of the workpiece, the waterjet pressure can exceed this range. For instance, Zhu et al, [4] used waterjet with a pressure of 20-150 bar to polish hard materials such as silicate glass, alumina ceramic and silicon nitride ceramic. Also, for polishing very hard stones like granites, the same pressure of AWJ cutting system (i.e., around 2000-4000 bar) is used [25]. In this technique, the velocity of the jet is considerably lower than that of waterjet cutting machines [23, 24]. The speed of waterjet is theoretically calculated based on the Bernoulli Equation. However, due to pressure loss before the orifice and inside the nozzle, and also energy loss caused by smashing the waterjet and abrasive particles inside the mixing chamber (if the water is mixed with the abrasives after the orifice), the real velocity of the jet is less than its theoretical value.

Depending to the properties of the workpiece and timing of the process, in AWJP, the inner diameter of the nozzle varies from 0.3 to 4 mm [4, 23]. To polish most types of materials like metals, this diameter is around $1 - 2$ mm and smaller sizes are used for polishing very hard materials such as granites and marbles. In this process, the SOD is in the range of $10 - 100$ mm [23, 25]. The jet impact zone is the area on the surface where the material removal takes place and its efficient ratio is stated in [23] to be around $r/H \leq 0.22$, where r is the jet radial distance and H is the SOD as shown in Fig. 2.4.

In addition, different types of abrasive grains like cerium oxide (CeO_2), silicon carbide (SiC), aluminum oxide (Al_2O_3) and boron carbide (B_4C) are used in this process [23, 24, 26, 27]. The size of these abrasive grains is selected based on the material of the workpiece and the required quality for the surface. However, larger abrasive grains increase the material removal rate while using smaller ones results in a very smooth surface but increases the polishing time [26].

In AWJP, the nozzle axis can be located in vertical and oblique directions with respect to the surface. In the first situation, the profile of pressure distribution on the surface is annular and the material removal occurs symmetrically while in the second situation the pressure profile turns to an
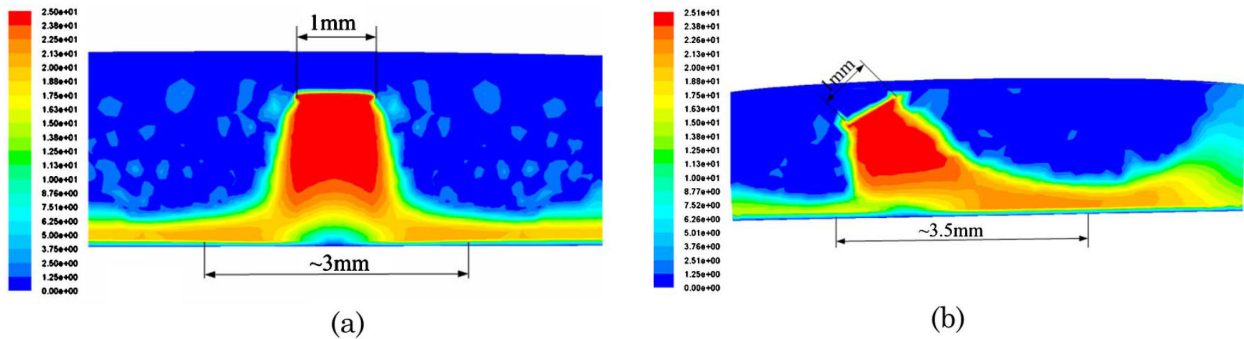
Figure 2.5 Simulation of velocity distribution in AWJP process for nozzle with: (a) normal angle; (b) oblique angle of 45° [23].
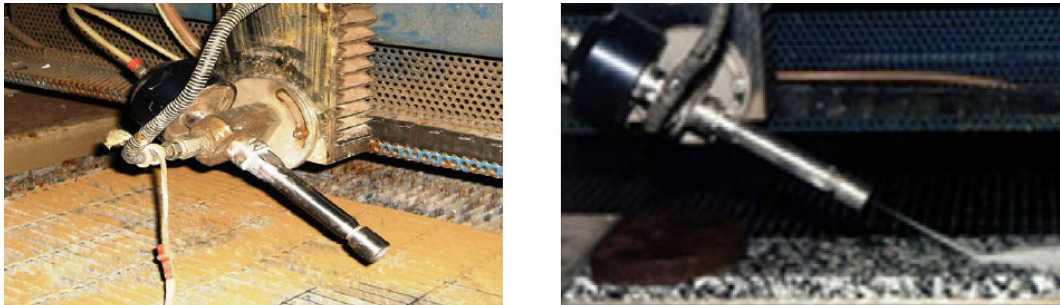
Figure 2.6 AWJP nozzle heads [25].

elliptical shape and the material removal pattern has an irregular shape [23].

To investigate the effect of nozzle angle on the AWJP process, Li et al. [23] simulated the material removal process for two different nozzle inclination angles. In their investigation, the nozzle diameter was 1 mm and the waterjet speed was 25 m/s. As it is illustrated in Figs. 2.5-a and b, the width of the polishing zone increases from 3 to 3.5 mm when the nozzle angle is changed from 90° to 45°. As shown in Fig. 2.5-a, when the nozzle angle is 90°, because of collisions among abrasive components and the ones reflected by the surface in the center of polishing zone, the velocity of waterjet on the surface is almost zero. This phenomenon results in a relatively small polishing area (in this simulation around $1-3$ mm). With an oblique angle this effect is reduced. Consequently, in AWJP, the nozzle is usually tilted [23, 25, 27]. Examples of AWJP nozzle heads are shown in Fig. 2.6.

Considering all parameters affecting the performance of the AWJP process, some researchers have presented general analyses on the nature of this system and tried to obtain the best set of parameters for a particular application. For example Chen and Wang [28] investigated the effect

of the AWJP on the roughness of the surfaces of two different materials. They used the Taguchi method to design their experiments. As a result of these tests, they found the importance of the effect of each parameter on the quality of the surface and optimized these parameters. In their experiments, they used Al_2O_3, CeO_2 and SiC grains as abrasive and also 40CrMnMo7 steel and BK7 glass as materials for the workpiece. Their results revealed that the nozzle diameter has the most and the SOD has the least important impact on the roughness (R_a) of the surface. Luc et al. [29] performed a similar study on the AWJP of Zr-based balk metallic glass and tried to optimize the polishing parameters using Taguchi method. They also developed another test-rig to do a similar investigation on the air-driven waterjet polishing of N-BK7 workpiece [30]. In this study, they used compressed air as a driving fluid to accelerate the mixture of water and abrasives to produce abrasive jet. Finally, using Taguchi method they found the best polishing parameters for this particular application.

2.2 Automatic and robotic polishing

Manual grinding and polishing by skilled workers is a traditional method used in the industry to finalize the machining process but it is time consuming, lead to uneven and imprecise surface and can threaten the health of workers [31]. Therefore, to properly conduct this process, replacing unreliable manual machining with a more precise automated method seems to be necessary. Consequently, in many industries, these processes are accomplished via NC and CNC machines (or robotic systems for more advance machining) programmed by computer-aided design/computer-aided manufacturing (CAD/CAM) techniques [32].

In polishing process, the amount of force exerted to the tool is smaller than the one of other machining processes and great accuracy in positioning is not required. Therefore, although NC and CNC machines have high accuracy and payload, using dexterous and swift robots is preferred for polishing free-form surfaces [33, 34]. Moreover, polishing these types of surfaces is a time consuming and exhausting task, and utilizing robots can improve the efficiency of the process. Also, comparing to NC and CNC machines, robots do not need to contain the workpiece within their structure, instead, they can be mounted on or inside the object aimed to be polished. Therefore, robots have more compatibility to machine larger objects at lower cost. Furthermore, polishing and grinding of free-form surfaces need more than three degrees of freedom (DOF) so robots with four to six DOFs are more suitable for these tasks while most of the NC and CNC machines have only 3-DOF, and others with more DOFs are usually expensive.

Due to these advantages of robots over other machines for soft machining processes, several types of manipulators were used for these tasks. To do this, many attempts have been done. For instance, Lee et al. [32] presented an automatic polishing method where a 5-DOF robotic system
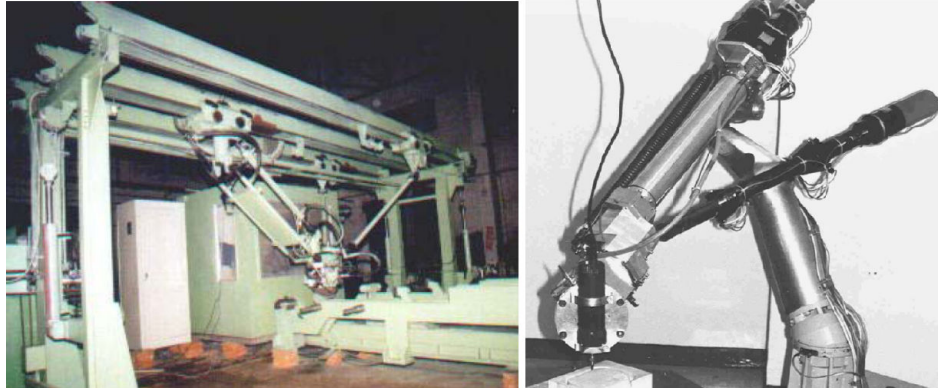
Figure 2.7 A 3-DOF 3-legged parallel robot designed by Baofu et al. (left) [35]; the RNT hybrid robot (right) [36].

was employed to maintain the direction of the polishing tool normal to the surface of the workpiece. This device included a three-axis table and a two axis robot. Huang et al. [37] utilized a robotic belt grinding and polishing system for a turbine vane overhaul. They developed an adaptive trajectory generation method and a passive force control strategy to automatically polish surfaces of the turbines. Also, Hazel et al. [38] performed experiments on robotic polishing of hydraulic turbine blades. In the latter, by decreasing the roughness on the surface of turbines from 15 μm to 0.1 μm, they improved the efficiency of turbine around $0.2 - 0.5\%$. For this, they used the Scompy robot [39] which was manipulated on several rails to be able to reach the entire surface of a huge turbine blade.

Most of the researchers used serial robots in their studies. However, others considered parallel and hybrid or even mobile robots to perform the polishing process. Initial investigations on using parallel robots for machining have been done in the beginning of 1980s [36]. Luo et al. [40] introduced two 5-DOF parallel manipulators with bridge-type trusses which were suitable for grinding and polishing tasks. Due to the shape of their trusses, the dimensions of the workpieces they could machine were quite small and they were not suitable for machining hard-to-reach areas. Next, Baofu et al. [35] presented another parallel robot with three translational degrees of freedom (Fig. 2.7-left). Their experiments revealed that this robot was capable to perform grinding tasks.

Beside studies on parallel robots, Zielinski et al. [36] introduced a hybrid (serial-parallel) robot called RNT which was suitable for several machining tasks including polishing. This robot is shown in Fig. 2.7-right. Robin et al. [43] tried to optimize the trajectory of a hybrid robot to polish objects with large dimensions. This robot consisted of a serial part acting as a wrist and a parallel part which was the Tricept IRB940 ABB robot which was itself mounted on a 1-DOF translational base.

Others tried to employ mobile robots for polishing free-form surfaces. Gui et al. [41] devel-
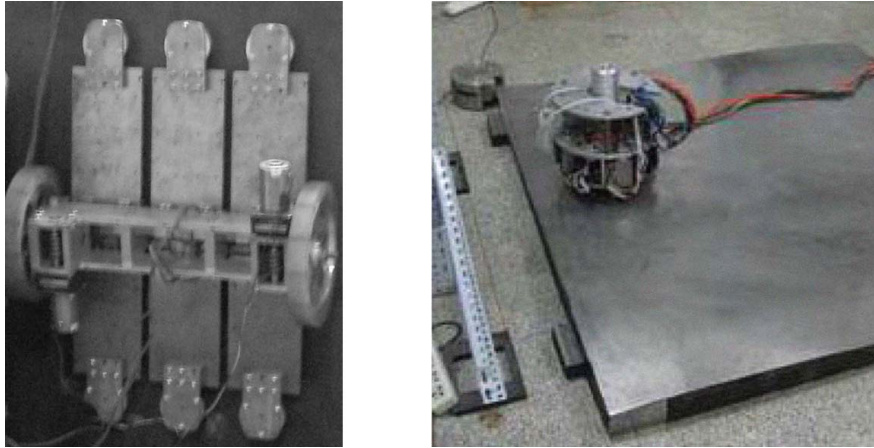
Figure 2.8 Mobile platform developed by Gui et al. (left) [41]; Mobile robot used in the investigation of Li et al. (right) [42].

oped a mobile robot (depicted in Fig. 2.8-left) which could climb the walls made of ferromagnetic material. This robot was used to repair a hydraulic turbine blade and thanks to its self-adapting 3-DOF structure it was able to move on the curved surfaces. This robot was very agile and could move on the surface without using any rail. In addition, Li et al. [42] investigated the capability of another mobile robot (presented in Fig. 2.8-right) to polish large free-form surfaces. They also proposed a strategy called direction paralleled algorithm to generate a particular trajectory to move this robot on the surface.

However, these platforms only could polish areas located inside a large surface and due to their manipulation limits they were not able to polish edges, narrow areas and locations close to the boundaries of the surface. Besides, during the process, their path planning algorithm could not find the exact normal vector of the tangential plane attached to the polishing point. Consequently, they cannot be used to position a polishing tool which should be kept at a fixed direction with respect to a surface.

2.3   Requirements of robots for automatic AWJ machining

The requirements of a AWJ system in cutting and polishing tasks are not the same. Thus, the properties of the robots used in these two tasks are different. Robots utilized in AWJ polishing should have the following properties [18, 24, 44]:

1. due to the distribution of water and steam, the robot should be able to work in a highly humid environment;
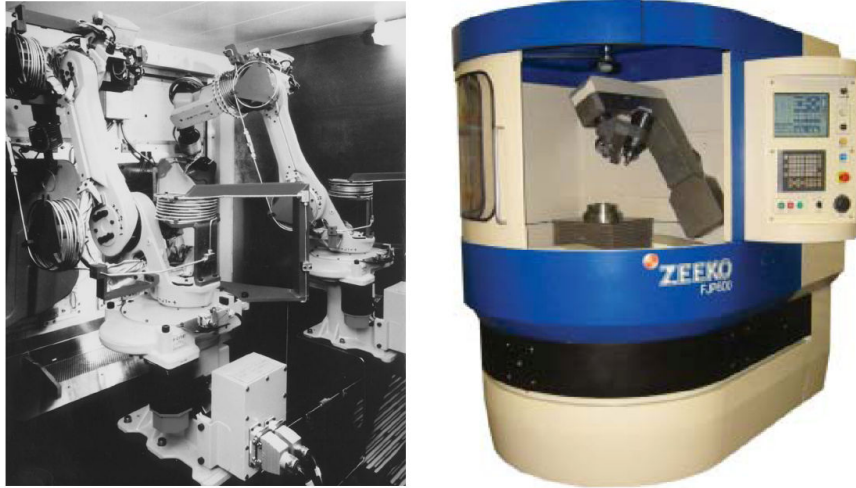
Figure 2.9 Two Fanuc M-6 serial robots (left) [45]; the Zeeko machine bed equiped with a serial robotic arm (right) [24].

2. all the mechanical parts of a robot (e.g., joints, actuators, gears, etc.) should be protected from being contaminated by abrasive particles;

3. it is preferable to suspend the robot from the top of the working area to protect it from being affected by the AWJP process (i.e., water and abrasive grains);

4. to increase safety, the actuators and other electrical components should be located far from the waterjet nozzle and humid area;

5. its workspace should be large enough to cover the entire surface to be polished;

6. it should be rigid enough to resist the shocks produced by reaction force exerted from the slurry jet to the end-effector (EE);

7. the material used in the body of the robot should be resistant against humidity and erosion.

So far, several robots have been used to manipulate an AWJ nozzle. Most of the robots which were used in the AWJ process were serial robots, e.g., ABB's IRB 2400 robot and Fanuc M-6 Robot (Fig. 2.9-left) were employed in the AWJ cutting process and Zeeko robotic unit (Fig. 2.9-right) which was equipped with a serial manipulator, was used for high quality abrasive jet polishing of high precision lenses [18, 24, 45]. Also Hou et al. [46] designed a 5-DOF serial robotic system specialized for abrasive waterjet machining. This robot has a simple and agile structure and can perform the machining process in a 3-D space.

Other researchers investigated the possibility of using parallel robots in waterjet polishing process. For example, in 2004, Abu Ibrahim [47] designed, analyzed and manufactured a prototype of a 2-DOF parallel robot to manipulate a 2D waterjet cutting process. In this study, the possibility of

using different types of joints (e.g., prismatic and revolute) and architectures were investigated. The prototype had a short working area of 310×310 mm and was suitable for cutting small workpieces.

As it was noted in this work, serial robots are not the only option to be used in AWJ machining. Considering the requirements of AWJP systems, parallel robots, hybrid robots, and cable robots can be potentially used in this process. Consequently, the possibility of using other robotic systems in AWJP and finding the best architecture adapted to this task and designing a robot to properly execute this is what is sought in the first part of this dissertation. For this matter, all these mechanisms are first studied and then the preferred one is chosen as the basis of a design of a robot to do the AWJP process.

2.4 Investigating the properties of different robotic systems

Based on the function of the robots, they are categorized as: manipulators (robotic arms), motion simulators, locomotors (mobile robots), swimming robots and flying robots [48]. For this research, the first type is considered to implement the desired task. Taking into account the structure of the robotic arms, they are classified as either serial or parallel manipulators [48, 49]. Subsequently, there are three types of these mechanisms:

– Serial robots,
– Parallel robots (including linkage-based and cable-driven robots),
– Hybrid robots (combination of two first types).

2.4.1 Serial robots

Serial robots are the most common robots employed in the industry and many researches have been carried out on these robots. A serial manipulator is an open kinematic chain mechanism which is made of series of kinematic pairs (i.e., binary links) connected to each other via mechanical constraints (i.e., different types of joints) [48, 50].

If these robots have the same degrees of freedom/actuator as the dimension of their task space (i.e., 6-DOF or less), they are called fully-actuated serial manipulators. Most of the initial studies in robotic field were accomplished on these units and different aspects of their performances were unearthed as presented in details [48, 49, 51].

Besides, there is another type of serial manipulators known as redundant serial robots for which the number of DOF is greater than the dimension of the task space [52]. As specified in [53], three types of redundancy are defined for robotic manipulators:

1. **Intrinsic redundancy:** when the dimension of the joint space is greater than the dimension of the operational space;
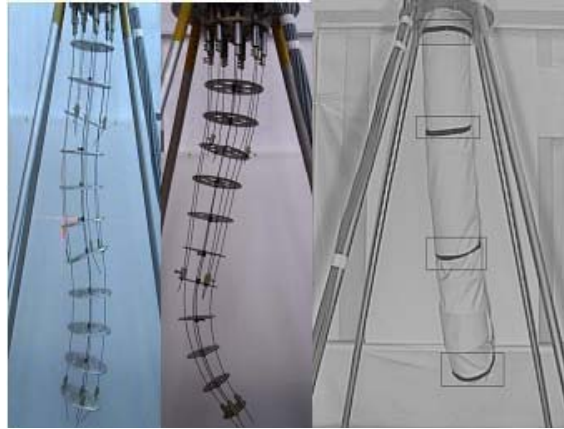
Figure 2.10 Hyper-redundant serial arms [54].

2. **Functional redundancy:** when the dimension of the operational space is greater than the dimension of the task space (i.e., subspace of operational space);

3. **Kinematic redundancy:** when the dimension of the joint space is greater than the dimension of the task space. This happens when each or both of the above redundancies exist.

In addition, there is a special class of redundant robots with large or even infinite number of degrees of redundancy. It is called hyper-redundant manipulator [52, 55]. These robots are known as continuum or tentacular robots and considering their body movement, they are classified as either continuous or discrete types [54, 56]. Some examples of these types are shown in Fig. 2.10.

As mentioned earlier, in many cases, using these robots for manipulation tasks is preferred to NC and CNC machines. On the other hand, comparing to parallel robots with closed kinematic chain, the open kinematic chain of serial robots leads to some disadvantages as [40, 57]:

– lower stiffness, payload and precision,
– errors are accumulated and amplified from link to link,
– large mass and inertia of the actuators installed on the links.

So far, many researchers worked on serial robots and revealed many aspects of their performances. As a result of these studies, many of these robots have been commercialized for decades. In the last two decades, researchers focused on redundant and hyper-redundant robots. Chirikjian and Burdick [55] for instance presented an approach to solve the direct kinematic problem (DKP), inverse kinematic problem (IKP), and path planning of a hyper-redundant manipulator. Zanganeh and Angeles [56] presented a spline-based solution strategy where the geometry of the manipulator is modeled by cubic and quintic splines. Pin and Tulloch [58] proposed a method for path planning and control of redundant robots while constraints such as joint limits and obstacles were considered.
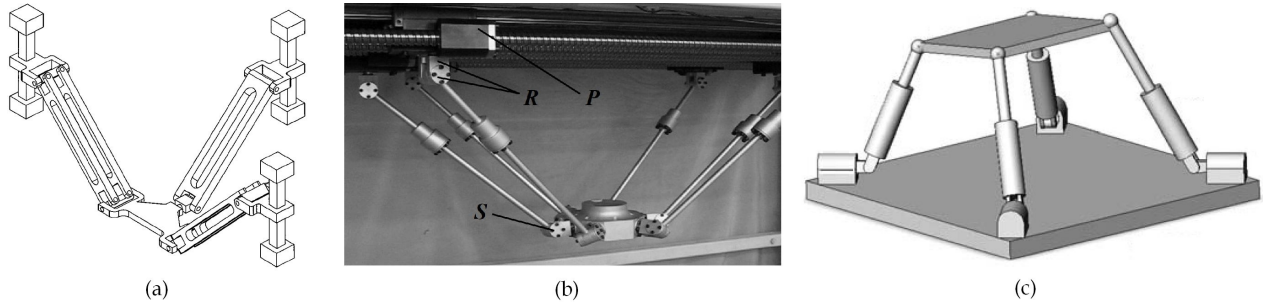
Figure 2.11 (a) Schematic of the HANA parallel mechanism [57]; (b) prototype of a 6-DOF PRRS parallel robot [59]; (c) schematic of a 4-legged redundant parallel robot [60].

2.4.2 Parallel robots

Parallel robots are a type of mechanisms with closed kinematic chains composed of two rigid bodies, one is fixed to the ground and referred to as the base platform (BP) and the other is the moving platform (MP) which is connected to the fixed one through at least two kinematic chains [48, 57]. Most of the parallel robots like the Stewart-type mechanism have 6-DOF and are equipped with six actuators. Some may be redundantly actuated, i.e., their degrees of actuation (DOA) are greater than their DOF. This property can increase their stiffness, acceleration, payload and uniformity in load distribution [60, 61]. Regardless of DOA, all of these six degrees of freedom are not required for all tasks while this fact makes the kinematic analysis of these mechanisms more complicated. As a result, many researchers worked on other parallel robots with less than 6-DOF and tried to analyze different aspects of their performances, i.e., workspace, DKP, IKP, singularity, dexterity, etc. Some examples of these robots are shown in Fig. 2.11. In parallel robots, the relationship between the twist $\dot{\mathbf{x}}$ of the MP and the joint rates $\dot{\mathbf{q}}$ is obtained as [62]:

$$\mathbf{J}_x\dot{\mathbf{x}} = \mathbf{J}_q\dot{\mathbf{q}} \tag{2.1}$$

where $\mathbf{J}_x$ and $\mathbf{J}_q$ are respectively the direct Jacobian matrix and the inverse Jacobian matrix of the robot. If the mechanism is far from singular configurations, $\mathbf{J}_x$ and $\mathbf{J}_q$ are invertible and then, Eq. (2.1) can be used for the analysis of the inverse and direct velocity kinematics of the robot. Considering these two Jacobians, the four possible singularities in the manipulation of parallel robots are [62, 63]:

1. **Inverse kinematic singularity (IKS):** takes place when $\mathbf{J}_q$ is not invertible, i.e., $\mathbf{det}(\mathbf{J}_q) = 0$. In this case, the actuators cannot move the MP or in other words, the mechanism is locked.

2. **Direct kinematic singularity (DKS):** occurs when $\mathbf{J}_x$ is not invertible. Since it may not be a square matrix, if it is not a full rank matrix then it is singular. In this case, the MP can have an infinitesimal motion while actuators are locked.

3. **Combined singularity:** happens when the MP is able to move while all of the actuators are locked and vice-versa. This singularity arises when both Jacobians are singular.

4. **Constraint singularity:** takes place when the manipulator has 5-DOF or less and locally obtains more DOFs. In this case, it is not able to fully constrain the MP.

In the recent years, many studies have been done on the architecture of parallel mechanisms and their kinematic analyses. Liu et al. [64] proposed the 3-DOF HANA parallel mechanism (illustrated in Fig. 2.11-a) with high rotational capability. They found closed-form solutions of its both DKP and IKP. They also studied its direct, inverse and combined singular configurations. Afterwards, in [57], they performed a comprehensive study on the new types of parallel robots. In this approach, they used planar parallelograms to create new parallel manipulators with two to six degrees of freedom (where at least one of their legs was made of a parallelogram). This mechanism brings new properties to these robots such as higher stiffness of the legs and better rotational capability of the robot.

Next, Li [59] proposed a 6-DOF PRRS parallel robot with a large workspace. He solved the inverse dynamic problem of the robot using Lagrange method and the virtual work principle. The prototype of this robot is shown in Fig. 2.11-b. Furthermore, Abedinnaasab and Vossoughi [60] introduced a 6-DOF 8-DOA 4-legged redundant parallel robot. The schematic of this robot is illustrated in Fig. 2.11-c. They used the principle of virtual work to analysis the inverse dynamic of this manipulator. In this approach, they applied the minimum norm method to find a unique solution for the inverse dynamic problem of the robot.

Then, Li and Xu [62] presented a 3-PRS parallel manipulator with prismatic actuators mounted on adjustable layouts (shown in Fig. 2.12-left). They investigated the mobility of the robot using screw theory and found a closed-form solution for its IKP. Afterwards, they used Newton iterative method to solve the DKP. For singularity analysis, they derived direct, inverse, combined and constraint singular configurations. Among them, the three firsts were obtained from direct and inverse Jacobians while the latter was found by screw theory. Tahmasebi [66] presented a closed-form solution for DKP and IKP of a parallel robot with similar structure where prismatic actuators were coplanar and mounted on the base. This robot had a very small workspace and was suitable for the cases where just tip and tilt rotations in a very small area were required. Also, Cammarata et al. [65] studied the kinetostatic and inertial conditioning of the McGill Schönflies-Motion Generator shown in Fig. 2.12-right. These two indices were respectively related to the condition number of the Jacobian matrix and the generalized inertia matrix of this parallel manipulator.
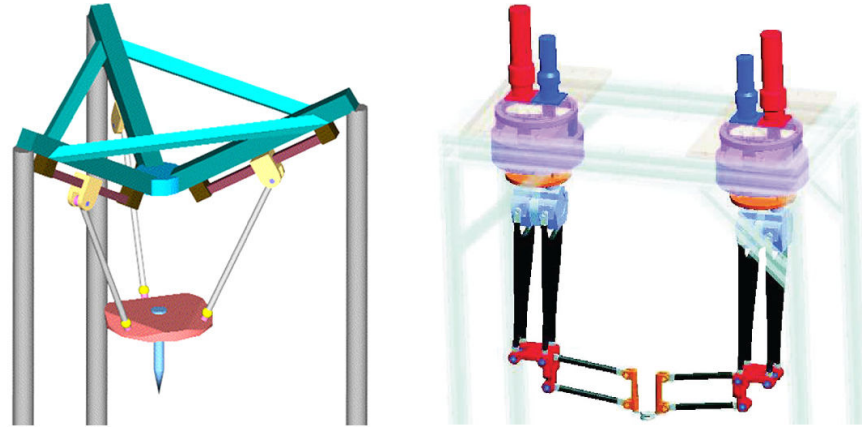
Figure 2.12 3-PRS parallel robot with adjustable layout of actuators (left) [62]; McGill Schönflies-Motion Generator (right) [65].

As mentioned in Section 2.4.1, parallel robots have several advantages over their serial counterparts. However, these mechanisms have some disadvantages which are mostly due to their closed kinematic chains and limits in the range of their joints (e.g., spherical joints) [35, 62, 67], namely:

– small workspace,
– many singular configurations inside their workspace,
– coupled motion (due to closed kinematic chain of the mechanism, the actuators should operate together),
– complex kinematics (particularly the forward kinematics),
– limited rotational capability.

2.4.3 Cable robots

Cable robots are a special type of parallel robots where solid legs are replaced by flexible cables [68]. In other words, cables are used to manipulate the MP. This characteristic provides particular properties for these mechanisms. Due to the unilateral property of cables (i.e., they can only produce tension forces), to completely constrain the MP in a n-DOF workspace, at least $n+1$ cables are required [69]. Also, works from the literature proved that using more cables will result in even larger workspace and better performance of the robot [70, 71]. However, the performance of cable robots, and the number of their DOF depend on the number and geometrical arrangement of their cables.

The aforementioned characteristics of cables lead to some differences between the criteria considered in the analysis of cable-driven and linkage-driven parallel robots. The main difference is the calculation of the workspace of these robots. Contrary to linkage-base parallel robots where the

existence of the IKP was the criterion of finding the workspace, in cable-driven ones, it is obtained as a set of configurations where all of the cables are in tension or in other words, the force-closure condition is satisfied [70–73].

If in a cable robot the force-closure condition is true, then other analyses can be performed. The relationship between cable tensions and the wrench applied to the MP in a n-DOF cable robot with m cables, is calculated as [72]:

$$\mathbf{Wt} = \mathbf{f} \tag{2.2}$$

where $\mathbf{W}$ is the associated $n \times m$ cable-tension matrix, $\mathbf{t}$ is a $m \times 1$ vector of tensions and $\mathbf{f}$ is a $n \times 1$ vector of external wrench. Also, for these robots, the Jacobian matrix, $\mathbf{J}$, is defined as [71]:

$$\mathbf{J} = \mathbf{W}^T \tag{2.3}$$

Due to the straightness of cables, the IKP of cable robots is straightforward. On the contrary, the DKP is more complicated and can be found in the same way as other parallel robots. In the analysis of these robots, Eq. (2.2) is used to investigate other aspects of their performance including: external wrench, cable tensions, workspace, dexterity, singularity, etc.

Generally, cable robots have two types of structure: incompletely or fully restrained. In the former which is also called cable suspended robot, the MP is suspended from the ceiling by cables. This category has fewer problems with the volume of the space occupied by cables. It is mostly employed on construction sites, shipyards and airplane hangars [71, 74]. On the other hand, the latter can perform tasks in any direction regardless of the direction of wrench exerted to its MP [72].

Cable mechanisms inherit not only advantages from the parallel robots, but also gain a few other properties. Examples of these properties are [69, 70, 72, 75]:

– large workspace and high dexterity,
– simple, light and low inertia of moving parts,
– no need for spherical joints.

However, as a result of the unilateral nature of the cables, they have the following drawbacks [72, 75]:

– limits in the tension of the cables (both minimum and maximum),
– collision of cables with each other or with the workpiece inside their workspace,
– redundancy in fully constrained types,
– weak compactness,
– vibrations.

Many researchers studied and analyzed different aspects of cable robots. During these attempts,
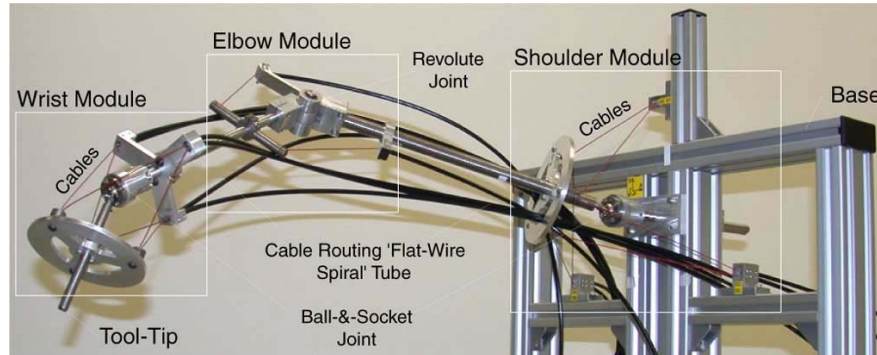
Figure 2.13 Prototype of a 7-DOF cable-driven robotic arm [76].

they tried to obtain the characteristics of these mechanisms and optimize their performances according to the requirements of the task. For instance, Kawamura et al. [77] developed an ultra-high speed cable robot called as FALCON. This cable-driven mechanism has high speed and acceleration. They used internal force control to reduce the vibration of cables caused by its fast action. Zhou et al. [78] designed a planar cable robot in which by reconfiguration of the cable attachment points on the BP the cable distribution could be properly controlled and consequently the wrench-feasible workspace of the robot was improved.

Yang et al. [70] presented a 7-DOF humanoid robotic arm which was composed of 3 modules including shoulder, elbow, and wrist. They found a closed-form solution for the DKP of the mechanism and since, due to kinematic redundancy, there were infinite sets of solutions for the IKP, they proposed an optimization method to solve this problem. Afterwards, they manufactured a prototype of this mechanism (illustrated in Fig. 2.13) and presented a self-calibration method to increase its accuracy [76].

In several investigations the analysis of the workspace of cable robots was targeted. Pusey et al. [73] presented a design of an incompletely restrained cable suspended robot and analyzed its workspace. Considering the global dexterity index (GDI) of the mechanism, they optimized its workspace. In addition, Yang et al. [72] studied on the workspace of a fully restrained cable robot. They considered the tension of the cables of this robot as a factor to optimize its workspace. This factor measures the relative tension distribution among the cables to estimate the force-closure quality of the mechanism. Lau et al. [79] optimized the cable arrangement of a spatial 3-DOF cable robot. In this optimization, the minimum cable tensions (while following a particular trajectory) and the maximum wrench-closure workspace were targeted.

Others worked on the design of cable robots for special applications. Tadokoro et al. [75, 80] proposed a 6-DOF cable-driven robot as a motion base which could be employed as motion simulator. For this, they optimized the arrangement of the cables to maximize the workspace of the
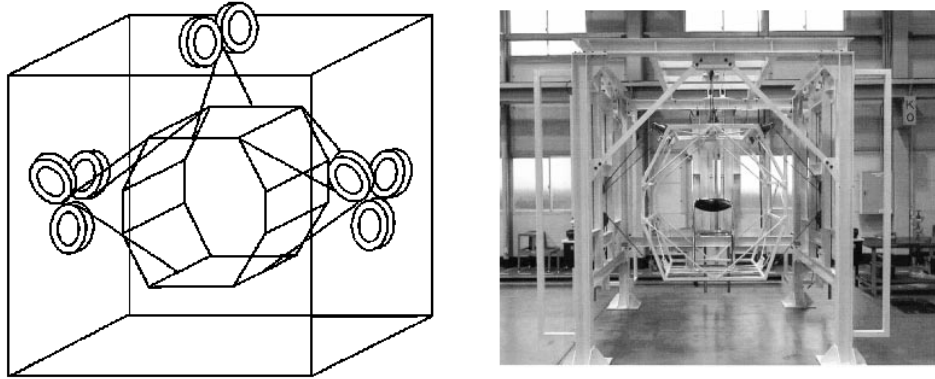
Figure 2.14 Schematic of a motion base cable-driven robot (left); prototype of this motion base (right) [75].
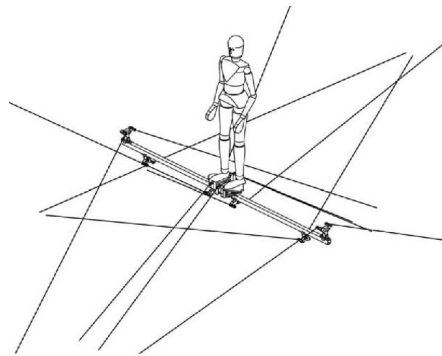
Figure 2.15 CAD model of a cable-driven locomotion interface [69].

robot. The schematic and prototype of this robot are shown in Fig. 2.14.

Also, Perreault and Gosselin [69] used two 6-DOF cable robots to develop a mechanical base as a locomotion interface. The model of this interface is shown in Fig. 2.15. To design the geometry of the robots, two criteria were considered, i.e., wrench-closure workspace and mechanical interference. The former is related to the area where any wrench can be exerted to the MP of the mechanism and the latter evaluates the interference among all components located inside the workspace, i.e., cables and moving bodies.

2.4.4 Hybrid robots

In addition to robotic architectures which possess a specific structure to manipulate their EE, there is another type in which the structure is the combination of the architecture of other individual mechanisms, i.e., serial, parallel and cable-driven manipulators. It is called a hybrid robot. These

robots can be designed in such a way that the advantages of each individual manipulator is obtained while its drawbacks are compensated [81]. The main advantages of these robots are [67, 81]:

- – large workspace,
- – high speed, dexterity, stiffness and accuracy,
- – considerable payload capacity,
- – decoupled structure.

Although these mechanisms inherit the advantages of the individual architectures used in their body, they can also have their weaknesses, e.g., complexity of parallel systems, limits in cable tension (if cables are used in their body), placement of actuators in serial parts and so on. Most of the common hybrid robots which are known as serial-parallel manipulators, have tripod structures [67]. This architecture is not mandatory and there are other types such as cable-driven hybrid robots which have tensegrity structure and are made of linkage-based kinematic chains which are either manipulated by cables or constrained by them [84]. In these types, the stiffness of the robot strongly depends on the tension forces in the cables.

In tripod type hybrid mechanisms, the kinematic analysis can be followed by analyzing each individual mechanism independently. However, regarding the diversity of the design of hybrid systems, there is not a specific procedure to express their kinematics. However, in some cases, researchers tried to evaluate the performance of the entire mechanism simultaneously. In this case, the main issue is developing the total Jacobian matrix that directly relates the twist and the actuated joint rates [85]. Then, this matrix is used in the analysis of velocity, singularity, dexterity, relations between wrench and the actuation forces/torques, etc. In this approach, the main idea is to see the whole mechanism as an individual mechanism (mostly like a serial robot).

To solve the aforementioned problems of robotic mechanisms, researchers tried to design hybrid systems with different properties. Then to improve their performance, they developed new hybrid structures, analyzed all of their kinematic aspects and executed different optimizations.

For instance, Hyung et al. [86] introduced dynamic analysis of a 5-DOF hybrid (serial-parallel) robot which was designed for machining applications. The body of this robot is a parallel mechanism and is used to position the MP in the desired location. A 2-DOF wrist with serial structure is mounted on its MP to control the orientation of the EE. Also, Liu et al. [82] proposed a conceptual design of a 5-DOF hybrid robot. As illustrated in Fig. 2.16-a, this robot is made of a parallel mechanism connected to a prismatic limb to form a 3-DOF hybrid architecture and a 2-DOF wrist is mounted on its head. The 3-DOF parallel structure of this robot is composed of two degrees of rotation and one degree of translation.

Moreover, Brau and Gosselin [83] designed a prototype of hybrid haptic interface called ICARE 3D which has a cable-driven architecture. As shown in Fig. 2.16-b, this interface is composed of a jack with a parallelogram architecture and three cables connecting its handle to the base. Using

(a)   (b)   (c)
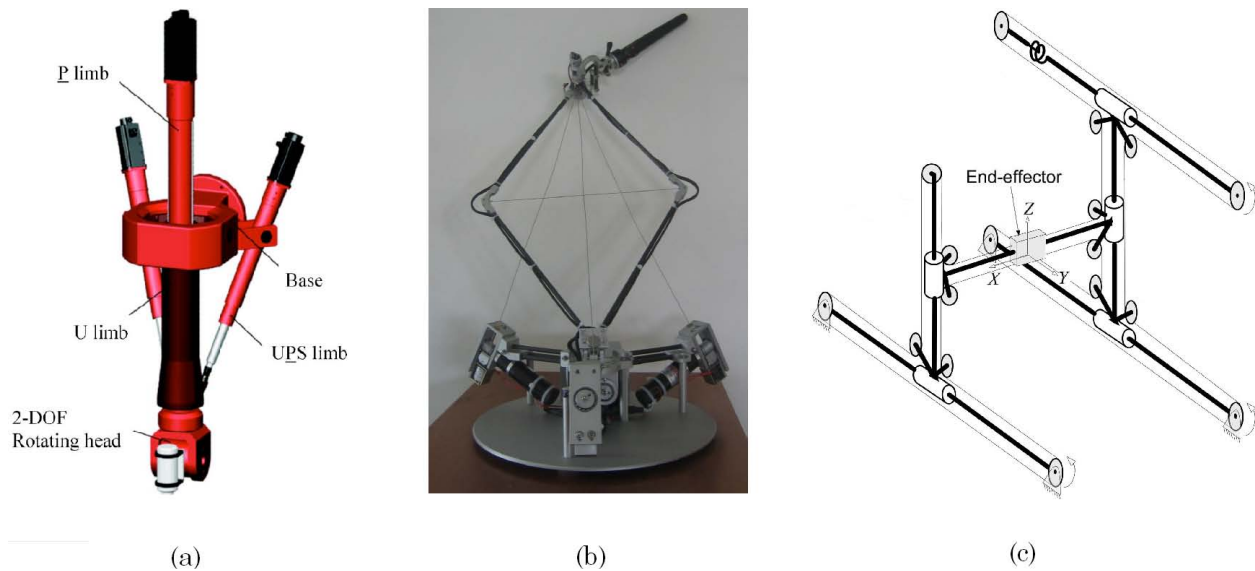
Figure 2.16 Hybrid mechanisms: (a) 5-DOF hybrid (serial-parallel) robot [82]; (b) prototype of the ICARE 3D (hybrid haptic interface) [83]; (c) schematic of a cable-driven hybrid robot [84].

this jack, the weakness of cable mechanisms in their compactness was solved. In this work, they analytically solved the DKP and IKP of the mechanism and obtained the relation between the cable forces and the resultant force on the handle by finding its Jacobian matrix.

Then, Behzadpour [84] introduced a cartesian hybrid cable-driven mechanism (c.f. Fig. 2.16-c). This manipulator was made of a cartesian linkage mechanism actuated by a pre-stressed cable-driven system. Using this architecture, the number of the required actuators is kept at minimum and the problem of actuation redundancy is solved. It was also proved that robot's DKP and IKP are independent of its configuration. Also Duan et al. [87] analyzed the kinematics of a new hybrid cable-driven structure. This system was made of a cable suspended mechanism and a steward parallel manipulator and was developed to be used in a large spherical radio telescope. Pisla et al. [88] developed a new parallel hybrid robot for surgery application. The robot is composed of two mechanisms, i.e., the robotic arm and the surgical mechanism. They also studied the kinematic and dynamic of this robot and investigated its workspace.

2.5 Literature review on generation of polishing paths on free-form surfaces

One of the important aspects in automatic polishing process is to develop a proper trajectory for the polishing tool to pass over the surface of a workpiece. The shape of this path has a significant impact on the quality, smoothness and uniformity of the surface. In the case of polishing free-form
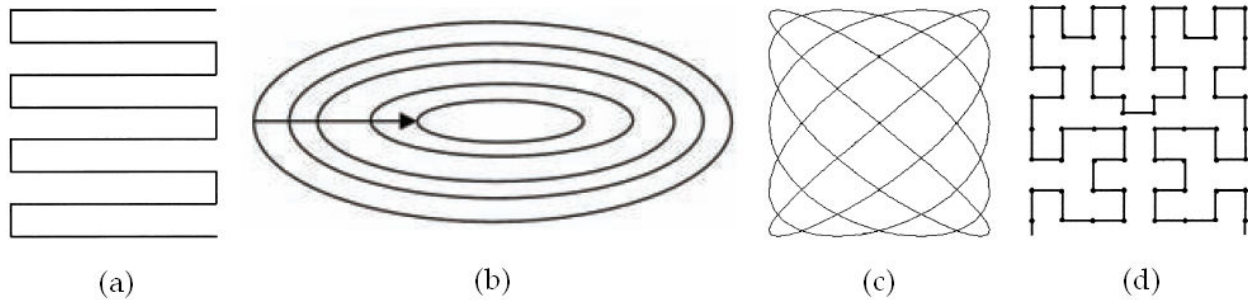
Figure 2.17 (a) scanning path [34]; (b) Spiral path [89]; (c) Lissajous path [34]; (d) Peano path [34].

surfaces this issue becomes critical.

So far, several methods for polishing path generation have been presented. In most of them, the CAD data of the workpiece was used to obtain the actual shape of its surfaces. Then, using this data, they produced the cutter location (CL) data which presents the appropriate location and orientation of the polishing tool with respect to the workpiece surface [33, 89]. Subsequently, different types of paths were developed and compared to increase the smoothness and decrease the roughness of the surface. Among them, the most common path which is considered in many applications is the zigzag path (also known as scanning path) which is shown in Fig. 2.17-a.

In general, all paths can be categorized as continuous, offset, and discontinuous [90]. In the first type, the tool follows the entire trajectory without any need to disrupt the polishing process. Zigzag, staircase, and sweep paths are examples of continuous paths. The offset path is made of several closed loops surround each other and the polishing tool can pass them from the inner loop toward the outer one or vice-versa so that after passing each loop the process is stopped and the tool is placed on the adjacent path. This type is also known as spiral path which is illustrated in Fig. 2.17-b. In the last type, the path is neither continuous nor spiral and after finishing each path, the tool moves from its end-point to the starting-point of the next path. As mentioned in [90], among these three categories, employing the continuous path results in the fastest polishing process and encounters less computational complexity.

In addition to common continuous polishing paths, there are some other trajectories with particular properties. Examples of these paths are lissajous and peano paths which are illustrated in Fig. 2.17-c and d. For polishing a planar surface, using lissajous path can result in higher quality in comparison with scanning path. However, generation of the lissajous path on a free-form surface is more complicated and the quality of the surface polished using this path, is not studied yet [34].

This path can be generated using the following equations [91, 92]:

$$x = A\sin(at + \delta) \quad , \quad y = B\sin(bt) \tag{2.4}$$

The peano path is a type of fractal curves with dimension of 2. Different shapes of this path can be used for polishing aims. The density of this path depends on the order of the fractal used to generate it. This means that the pitch distance (also known as step-over distance) between the adjacent paths approaches toward zero when this order goes to infinity. Increasing the density of this path results in longer polishing time.

Regardless of the type of the surface-covering trajectories (i.e., continuous, offset, etc.), based on the way of coverage of a free-form surface, they are classified in two main groups. In the first group, the uniformity in the coverage of the entire surface is not considered. This means that the pitch distances between adjacent paths of a trajectory are not necessarily constant. In these types, the pitch distance is usually variable and depends on the curvature/boundary of the surface and also the technique used to generate the path. To produce this group of trajectories several methods were developed. In many of them, the parametric surfaces are used [93–95]. For this, the original free-form surface is mapped onto a 2-D plane which has a simpler boundary (e.g., rectangular, circular, etc.) in which the entire surface is well-defined by a coordinate system. Each point on this planar surface represents a point on the original surface. Then, the trajectory is produced on this plan. Next, the locations of the points of the initial trajectory are mapped back onto the desired free-form surface.

This method is used in several tool path generation approaches such as iso-plane, iso-parametric, iso-cusp, etc [94]. For example, Yang et al. [93] presented a boundary-conformed iso-parametric tool path generation method for free-form surfaces. In this approach, simpler boundaries are first considered for a complex surface. Next, this surface is trimmed into an area with defined spatial boundaries. These boundaries are then used to map this area onto a 2-D plane where iso-parametric paths are created. In this method, the configuration of the paths can be adapted to the shape of the defined boundary. Yuwen et al. [94] introduced a similar iso-parametric method to generate boundary-conformed paths on the free-form surface modeled by triangular faces. In this method, using harmonic map, the triangular faces are parameterized. This includes mapping the boundary point and the interior points on the 3-D surface onto the parametric plane. Next, considering the machining tolerance, the CL data and the path intervals are generated and finally the resultant trajectory is obtained. Two example of paths produced via this method are shown in Fig. 2.18.

Also, Tam et al. [34] developed a pitch adaption method to generate tool paths. In this method, the pitch distance is determined based on the surface profile, surface curvature, and the size of the polishing tool. Also, the maximum distance between the two adjacent paths is less than a maximum
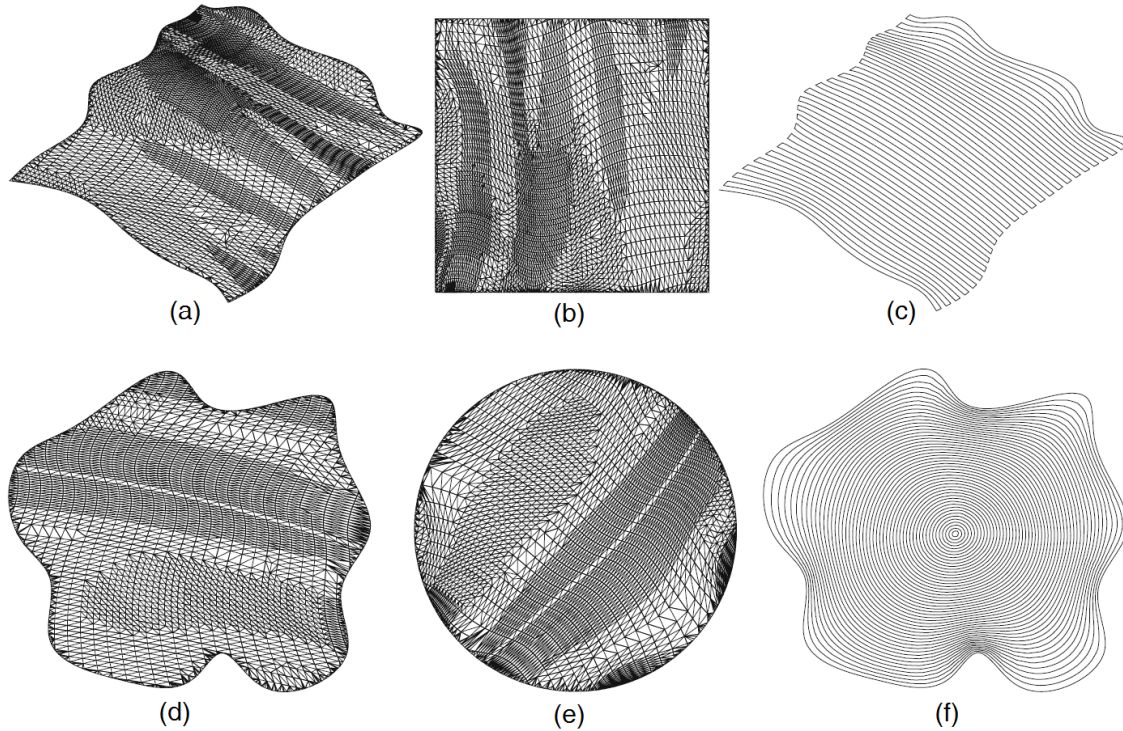
Figure 2.18 Generation of a scanning path: (a) original free-form surface; (b) harmonic map of the faces of this surface onto a rectangular zone; (c) resultant scanning path generated using iso-parametric approach. Generation of a spiral path using similar approach: (d) original free-form surface; (e) resultant circular zone; (f) the generated spiral path [94].

pre-defined value. However, the pitch distance is still variable and can be controlled only in one direction on the parametric plane. Thus, by turning the direction of the scanning path they produce a bi-direction path in which the paths cross each other to have pitch adaptation in both directions. Examples of these paths are shown in Fig. 2.19.

Sheng et al. [95] presented another trajectory planning method to generate paths on compound surfaces and optimize the motion of the tool on such surfaces. The path generation is performed in two steps. In the first step, considering the configuration of a complex surface, it is partitioned into simpler areas and then each area is mapped onto a flat plane. In the second step, the optimal direction of the tool path and subsequently the pattern of the scanning path on each area is determined. Example of generation of paths on the surface of the inner hood of a car using this method is presented in Fig. 2.20. Kim and Choi [97] proposed a guide surface based method to generate tool paths for 3-axis machining. This process was performed in five steps. First, the area to be machined was determined. Then, by considering the configuration of this area, a guide surface was constructed. Afterwards, considering the pre-defined path topology the guide path planes were
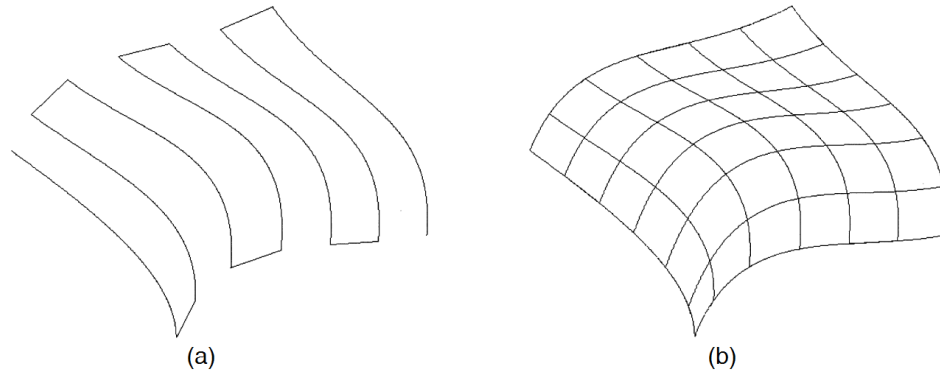
Figure 2.19 Schematic of (a) unidirectional and (b) bi-directional scanning paths generated using pitch adaptation method [34].
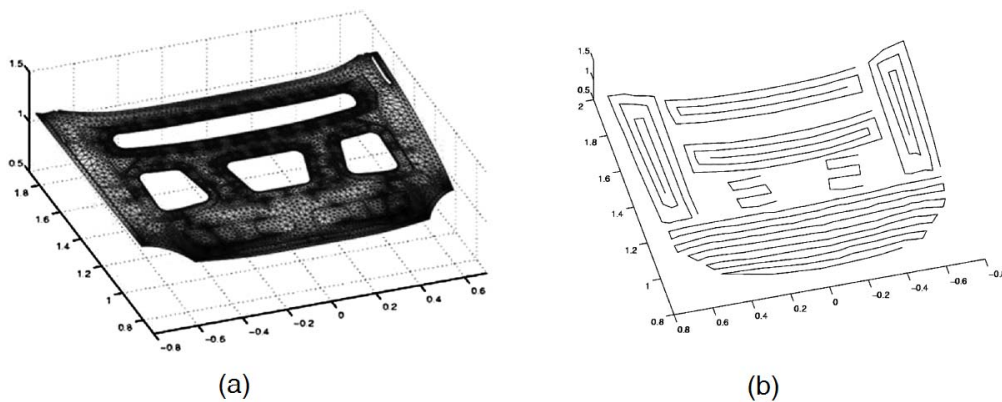
Figure 2.20 (a) Inner hood of a car; (B) set of scanning path generated on this surface by Sheng et al. [95].

defined on the guide surface. Next, these guide paths were projected onto the region which was determined in the first step to create the cutter contact paths. Finally, the CL data (cutter location path) was computed using the cutter contact paths. In this method, the guide paths were generated as a set of iso-parametric curves defined according to the configuration of the guide surface.

Zou and Zhao [96] proposed another iso-parametric strategy to generate tool paths using a cloud of points which is defining a free-form surface. In this approach, a conformal map was used to parameterize the points of the surface and then, the tool path parameters were computed. The tool paths were generated in several ways such as direction parallel and contour parallel. Consequently, this method can also be used to generate boundary-conformed trajectories. Examples of the paths generated using this method are presented in Fig. 2.21. In some other methods, the trajectories are directly produced by intersecting a set of parallel planes with a free-form surface. Usually, the
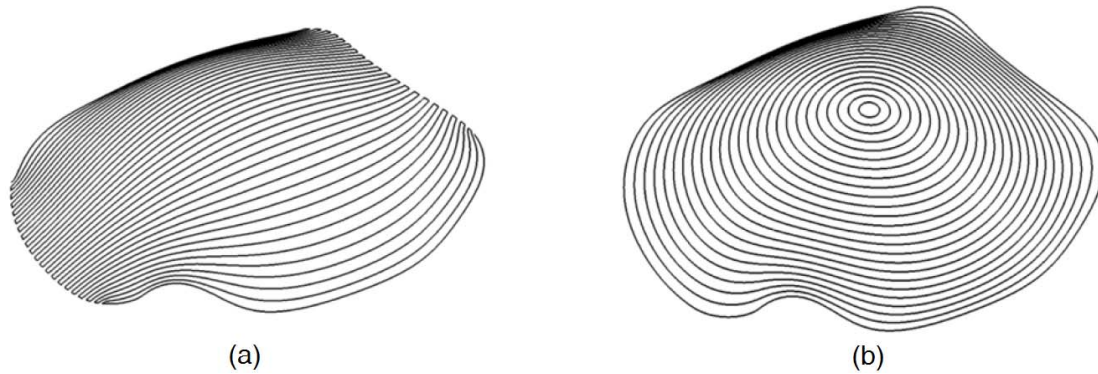
Figure 2.21 Tool paths generated with (a) direction parallel curves; (b) contour parallel curves, by Zou and Zhao [96].

configuration of the trajectory developed through this strategy is not uniform and depends on the curvature of the surface. Therefore, this method is not suitable for surfaces with high curvature [98].

In the second group of surface-covering trajectories, it is critical to uniformly cover the entire surface so that regardless of the configuration of the surface the density of trajectory on the surface is constant. This group of trajectories is mainly used in applications such as waterjet polishing where the processing tool targets a particular area at a time and no area should be repeatedly passed or ignored. In these types of applications, the pitch distance between paths is determined according to the width of the aforementioned working area of the tool.

To produce this type of trajectory, a reference is often used as a starter to obtain the adjacent path which is located at a constant offset distance from it. Then, the other paths are found as a set of curves (either closed or open) with the same distance from the previously generated one. Depending on the type of the application, this reference can be a point [98, 100], a seed curve [98, 101–103], or a boundary of the surface [98, 101, 104, 105]. To find the offset curves of this reference on the free-form surface, the concept of geodesic distance fields is applied by many researchers [98, 100–102, 106]. This method was initially presented by Surazhsky et al. [100]. They developed this strategy based on the interval propagation idea proposed by Mitchell et al. [107]. Afterwards, Bommes et al. [101] generalized the original algorithm to precisely and efficiently compute the geodesic distance field. Conversely to the earlier work in which only a point was used as a reference, their method was able to compute the geodesic distance fields for both open and closed polygons on free-form surfaces modeled by triangular faces. In this method, they regenerated the triangular faces in critical areas where there were sharp turns in the direction of the paths to produce precise and smooth curves. In addition, Sethian et al. [108] approximated the distance field via solving the discrete Eikonal differential equations to generate paths on the triangular mesh model of free-form
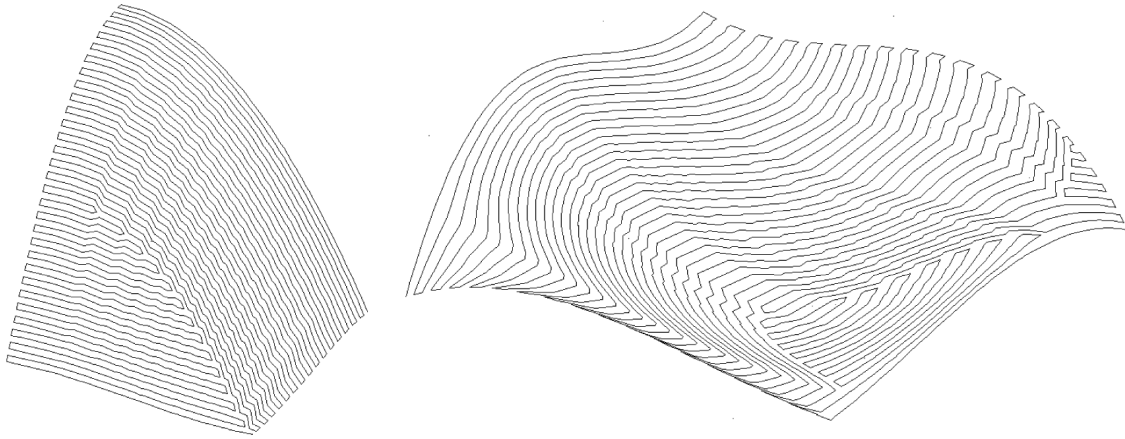
Figure 2.22 Two examples of generation of the extended scanning paths on two different parametric free-form surfaces using a method developed by Tam [99].

surface.

Besides using geodesic distance field, other researchers used the parametric surface approach to generate uniform surface-covering paths on 3-D surfaces while a constant pitch distance was preserved. For example, Tam [99] introduced the extended scanning curves in the generation of uniform surface-covering scanning path. In this method, the full scanning and sub scanning coverage of the surface were used to generate the path on all areas of the surface. For this, considering the pitch distance and curvature of the surface, as shown in Fig. 2.22, additional scanning paths were generated within the paths of the main scanning trajectory.

In the generation of trajectories for AWJP purpose, if the pitch distance between two adjacent paths is larger than the diameter of the effective polishing area, then, some unpolished areas may remain. If it is smaller, then more passes are required to accomplish the task. These can lead to decreasing the efficiency of the polishing process [90]. Thus, to obtain a uniformly polished area on a free-form surface, this distance should be kept constant. Besides, the amount of overlaps among the paths of a trajectory should be minimized or even avoided because it results in over polishing of these locations. Also, in the case of multi-stage polishing (i.e. polishing the same area in several steps) the path of the trajectories should pass over each other in several directions to increase the uniformity of the surface [109]. All in all, the surface-covering trajectory should provide the following properties for a robotic system to be able to properly perform the machining task [110]:

1. robot should be able to move on the entire surface;

2. paths should not overlap;

3. paths should be followed continuously without repeating any of them;

4. obstacle must be avoided;

5. paths should provide the simplest movement for the robot to ease its control.

With AWJP, there is no contact between the object and the polishing tool. Thus, the path planning problem is reduced to a position and orientation problem and there is no need to force control. However, SOD and the nozzle angle are two new parameters to be considered. If these parameters are kept constant during the process, the other issues which can affect the polishing process is the traverse speed of the nozzle. This speed is tangent to the polishing path and should have a constant magnitude to maximize the integrity in the smoothness of the surface along the path.

When the CL data of the polishing path is known, a smooth path can be generated by interpolation among the pre-defined positions and orientations obtained from this data. The CL data of the ith point on the free-form surface can be expressed in vector form as [33, 89]:

$$\mathbf{cl}(i) = \left[\mathbf{cl}_P^T(i) \quad \mathbf{cl}_R^T(i) \right]^T \tag{2.5}$$

where $\mathbf{cl}_P(i)$ and $\mathbf{cl}_R(i)$ are respectively the position vector of the polishing tool and the unit vector of rotational axis in the ith CL. Several methods were presented in the literature to interpolate the CL of polishing tool between two CLs. In [33, 89], a method was proposed to interpolate the configuration of the polishing tool between two consecutive points where $\mathbf{r}(j) = [\mathbf{r}_P^T(j) \ \mathbf{r}_R^T(j)]^T \in [\mathbf{cl}(i), \mathbf{cl}(i+1)]$ and $\mathbf{v}(j) = [v_x(j), v_y(j), v_z(j), 0, 0, 0]^T$ were defined as the configuration vector and the velocity vector of the tip point of the tool at jth point (angular velocity is not defined for a point). The magnitude of the velocity, $\|\mathbf{v}(j)\|$, was assumed to be constant. Consequently, the velocity vector in the jth point was calculated as [33, 89]:

$$\mathbf{v}(j) = \|\mathbf{v}(j)\| \frac{\mathbf{cl}_P(i+1) - \mathbf{cl}_P(i)}{\|\mathbf{cl}_P(i+1) - \mathbf{cl}_P(i)\|} \tag{2.6}$$

The position vector of the tool, $\mathbf{r}_P(j)$, is then calculated as [33]:

$$\mathbf{r}_P(j) = \mathbf{cl}_P(i) + \mathbf{v}(j)(j-1)\Delta t \quad , \quad j = 1..n \tag{2.7}$$

It can be easily noticed that $\mathbf{r}_P(1) = \mathbf{cl}_P(i)$ and $\mathbf{r}_P(n) = \mathbf{cl}_P(i+1)$. It should be noted that Δt is the sampling time between j and $j+1$. The position of the jth point between two consecutive CL points is illustrated in Fig. 2.23.

To interpolate the orientation on the polishing tool, Nagata et al. [89] considered the angles of the axis $\mathbf{r}_R(j)$ with the coordinate axes z and y, namely, $\theta_1(j)$ and $\theta_2(j)$. These angles were interpolated between $\mathbf{cl}_R(i)$ and $\mathbf{cl}_R(i+1)$ as [89]:
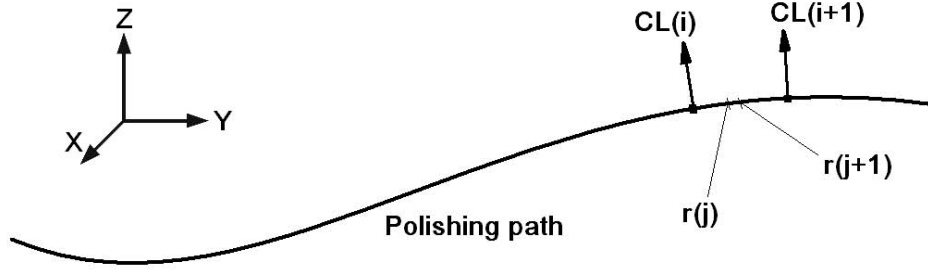
Figure 2.23 Position of the points along the polishing path obtained via interpolation of the CL data [33].

$$\theta_k(j) = \theta_k(i) + (\theta_k(i+1) - \theta_k(i)) \frac{\| \mathbf{r}_P(j) - \mathbf{cl}_P(i) \|}{\| \mathbf{cl}_P(i+1) - \mathbf{cl}_P(i) \|} \quad , \quad k = 1, 2 \qquad (2.8)$$

In addition, Feng and Tian [33] used quaternions for the tool axis to interpolate the orientation of the tool between two CLs. They have shown that, using quaternions changes the direction of the tool in highly curved areas is done more smoothly. The quaternion is defined as $\mathbf{q} = (v_0, \mathbf{v})$, where $v_0 = \cos(\alpha/2)$ and $\mathbf{v} = \mathbf{e}_v \sin(\alpha/2)$. α and $\mathbf{e}_v$ are respectively the rotational angle and the unit vector of rotational axis. To change the direction of tool from $\mathbf{cl}_R(i)$ to $\mathbf{cl}_R(i+1)$, first quaternions $\mathbf{q}_1$ and $\mathbf{q}_n$ which respectively represent the orientation of tool axis in the points i and $i+1$ are taken into account. Then, the interpolation is performed as:

$$\mathbf{q}(j) = \frac{\sin\left((1 - \frac{j-1}{n-1}) \theta \right)}{\sin \theta} \mathbf{q}_1 + \frac{\sin(\frac{j-1}{n-1} \theta)}{\sin \theta} \mathbf{q}_n \quad , \quad j = 1..n , \qquad (2.9)$$

where $\theta = \cos^{-1}(\mathbf{q}_1 \cdot \mathbf{q}_n)$ and $\mathbf{q}(j)$ is the tool axis obtained via interpolation. Using this interpolation method, a smooth transfer from one CL to another one can be obtained [33, 89]. In other methods, polynomials and splines were used to interpolate among the known points of the path [48]. These interpolations were aimed to produce continuous and smooth curves. For example, using a 3-4-5 polynomial (which has variables with the order of 3 to 5), the resultant path can satisfy the continuity in position, velocity and acceleration of the tool in starting and ending points while using a 4-5-6-7 polynomial (which has variables with the order of 4 to 7), even the jerk can be continuous. However, these interpolating polynomials are mainly suitable for pick and place trajectories. To smoothly pass through a set of via points in 3-D space, parametric cubic splines are employed. Finally, in the method used to interpolate all points of the trajectory, particular requirements of the AWJP (i.e., fixed direction of the tool with respect to the surface) should be satisfied.

CHAPTER 3

RESEARCH PROBLEMS AND OBJECTIVES

Taking into account the specificities of the hydraulic turbine manufacturing industry to polish all surfaces and edges of the turbine blades, it is desired to use a dedicated method of polishing which can have access to all parts of turbines including hard-to-reach areas. This can be done using waterjet polishing which can reach the edges, narrow areas and tight bends of turbines. Therefore, the performance of this process for the polishing of free-form surfaces should be first investigated. For this, it is needed to develop a robotic system adapted to abrasive waterjet polishing which can appropriately manipulate the nozzle over the surface of a turbine. This robot should be able to safely perform the task in humid and contaminated areas because humidity and abrasive materials can damage its actuators, as well as its mechanical and electrical parts.

Additionally, since most of the surfaces of the turbines are modeled by triangular faces in computer aided design (CAD), it is required to develop a method to generate particular trajectories in which the requirements of AWJP of free-form surfaces (e.g., constant offset distance, cross section of waterjet, etc.) are considered. Consequently, the generated path is able to uniformly deliver the abrasive jet to all areas of the desired surface. In summary, in this research, it is aimed to find solutions for two issues: finding the best manipulation system which can appropriately polish free-from surfaces of turbine blades using AWJP technique and second, obtaining the best strategy to move the polishing nozzle over these surfaces. Thus, the main objective of this project is:

Developing a robotic system adapted to the abrasive waterjet polishing of large turbines and developing a polishing path generation algorithm to obtain the desired surface quality.

To meet this objective, a comprehensive investigation on properties of abrasive waterjet polishing system is first done and then, the properties of a robotic system to perform this process are determined. Also, the structure of different types of robotic systems, their properties, advantages and disadvantages are discussed. Next, based on the requirements of AWJP of hydraulic turbine surfaces of, a robotic system with a proper architecture is selected.

Considering the architecture of this robot, the idea of using differentially driven cable mechanism in its structure is then proposed. The performances of several planar mechanisms using this technique are then analyzed and compared to fully driven mechanisms. Next, a synthesis method to obtain all possible valid designs for differentially driven cable systems is presented. Then, different aspects of the proposed differentially actuated robotic system including direct and inverse kinematics, direct and inverse velocity problem, wrench-closure and wrench-feasible workspaces are

analyzed. Finally, by defining two indices measuring the workspace of this robot, its performance is optimized.

In the second part of this thesis, by designing and manufacturing a test rig, experiments are done with the AWJP process. The results of these tests are then used to investigate the shape and roughness of the polished surface and determine the particular requirements of this process to be considered in the generation of polishing path. Next, a modular method is proposed to generate trajectories adapted to the requirements of AWJP process on the triangular mesh model of free-form surfaces of hydraulic turbines. This method is able to produce trajectories with a constant offset distance between adjacent paths on 3-D surfaces with holes and complex boundaries. Afterwards, using two indices the capability of the generated path for AWJP is evaluated. Consequently, the proper trajectory to be used by the proposed robotic arm in the AWJP process is obtained.

CHAPTER 4

ORGANIZATION OF THE ARTICLES

As it was mentioned in Chapter 3, the objectives of this study are divided in two phases. The first phase involves developing a robotic system for abrasive waterjet polishing process. To do this, based on the investigation of the architecture of robotic manipulators and the requirements of AWJP, a hybrid cable-driven structure is first chosen. The reasons of this selection are discussed in details in Chapter 9. Next, a theoretical investigation on this mechanism is done and the idea if using differential mechanisms in the architecture of cable-driven robots is presented in the first two articles presented in Chapters 5 and 6. The second step focuses on generating polishing paths on free-form surfaces to perform AWJP process. The method developed to generate this type of trajectories is addressed in the article provided in Chapter 7.

Chapter 5 presents the first article entitled "Synthesis of differentially driven planar cable parallel manipulators". In this work, the idea of using differentials in the structure of cable-driven parallel robots is introduced. Using differentials, the number of required actuators can be kept at minimum (namely, $n + 1$ actuators for a n-DOF cable robots) while the performance of the robot and particularly its workspace is improved. As the initial part of this study, the scope of this work is limited to planar cases. In this article, cable differentials and their specific characteristics are first described and then, the required properties (e.g., kinematic constraints) to use such systems in cable robots are expressed. Next, via comparing several differentially driven planar cable robots with fully actuated ones, the advantages of using such systems in the architecture of cable-driven robots are discussed. Afterwards, a synthesis method is presented to find all possible arrangements of cables in a single differential system and select the best ones. The results of this article are used as a basis to design and analyse a robotic manipulator able to work in 3-D space which is investigated in the second article.

Chapter 6 presents the second article entitled "Analysis and optimization of a new differentially-driven cable parallel robot". In this work, a new differentially actuated cable-driven mechanism with hybrid structure is proposed. This robot is a 3-DOF mechanism and is actuated with a prismatic actuator and three differentials, each composed of two cables actuated by a single actuator. Next, different aspects of their kinematics are analyzed and the difference between the properties of these systems and other common fully-driven cable robots are provided. Then, by defining two indices the performance of the proposed spatial mechanism is optimized. Afterwards, its performance (i.e., its workspaces) is compared with two other fully-actuated spatial robots with similar architectures. Through this comparison, it is shown that using differentials and with a proper de-

sign one can expect better performances and larger workspaces for cable robots. The results of this article can then be used as a basis to design and manufacture a cable-driven robotic system with optimized performance which can satisfactorily meet the requirements of abrasive waterjet polishing process.

Chapter 7 presents the third article entitled "Uniform scanning path generation for abrasive waterjet polishing of free-form surfaces modeled by triangulated meshes". In this study, a modular method is presented to generate scanning paths of free-form surfaces to polish them using AWJP technology. The surfaces considered in this methodology are modeled by triangular faces. This method is able to produce trajectories on 3-D surfaces while a constant offset distance is preserved between all adjacent curves. These paths can be generated on surfaces with arbitrary boundaries and inner holes without reconfiguration of the triangular mesh of the surface. To do this, the particular requirements of this polishing technique in the path generation are investigated. Next, via simulation of the material removal, the limits to be respected in the polishing path are estimated. Then, through several options, the reference curve was obtained. By computing the geodesic distances in specific directions with respect to the points of each path, the adjacent offsets are found. After generation of the entire trajectory, its continuity is checked. If discontinuous areas are detected along the original trajectory then, it is divided into several sub-trajectories by reconfiguring the connections between the offset paths in these areas. Finally, by defining two indices, the effect of the shape of the surface and the configuration of the generated path on the uniformity of the distribution of waterjet is evaluated. Through several examples, it is shown that the presented method can properly generate scanning paths on free-form surfaces adapted to the requirements of the AWJP technique.

CHAPTER 5

ARTICLE 1: SYNTHESIS OF DIFFERENTIALLY DRIVEN PLANAR CABLE PARALLEL MANIPULATORS

Hamed Khakpour [a], Lionel Birglen [a], Souheil-Antoine Tahan [b]

[a] *Mechanical Engineering Department, Ecole Polytechnique de Montreal, Montreal, QC, CANADA, H3T 1J4*

[b] *Mechanical Engineering Department, Ecole de technologie superieure, Montreal, QC, CANADA, H3C 1K3*

5.1 Abstract

In this paper, the idea of using cable differentials in the architecture of planar cable-driven parallel robots is introduced. Cable differentials are a type of mechanisms with several outputs driven by a single input. Using them in cable parallel manipulators can decrease their cost and control complexity. However, due to their kinematic constrains, cable differentials cannot be arbitrarily used in the design of these manipulators. Thus, a synthesis method is proposed to tackle this issue. First, the general requirements and characteristics of differentially driven planar cable mechanisms are reviewed. Then, the advantages of using these differentials instead of typically actuated cables are shown through a comparison between differentially actuated planar cable robots and fully actuated ones. The results reveal that with the same number of actuators, using differentials may lead to larger workspaces and improved kinetostatic properties. Subsequently, the systematic synthesis of differentially driven planar cable mechanisms is presented. For this, a method to find the different arrangements of q cables in a differential is proposed. Then, valid arrangements with 2, 3, and 4 cables are investigated. Finally, several differential actuation schemes are considered and all possible differentials with q = 2, 3, and 4 cables are found.

Keywords: *Differential mechanisms, kinematic synthesis, workspace, cable robot, parallel robot.*

5.2 Introduction

Cable manipulators are a special type of parallel robots where rigid legs are replaced by cables [1]. In other words, cables are used to manipulate the moving platform (MP). This characteristic yields particular properties to these mechanisms, for instance, they inherit not only some advantages of linkage-driven parallel robots, but also gain a few additional characteristics which allow them to be the preferred solution in certain application. Examples of these beneficial properties are: a simple structure, lightness and low inertia of the moving parts, a high dexterity, typically low friction, large workspace (compared to linkage-driven parallel mechanisms), etc. [2–6].

On the other hand, they also suffer from some drawbacks amongst which the more common are limits in the cable tensions, poor compactness, possible interferences between cables, and vibrations [3, 4]. Also, as a result of the unilateral nature of the cables which can only produce tension forces, redundancy in the actuation is necessary. This means that to completely constrain the MP of an n-DOF cable robot, $m > n$ cables are required [2, 7, 8]. Several research initiatives have proved that using more cables results in larger workspace and generally better overall performance of the robot [6, 9].

Broadly speaking, cable robots are categorized as either incompletely or fully restrained [4, 10].

In the former, either $m \leq n$ cables are in tension or the MP is suspended from the ceiling by cables and motion relies on gravity (which is also often referred to as cable-suspended robot [4, 11]). In the case of $m \leq n$ cables, the control of the system becomes more complex [8]. Yet, in cable-suspended robots (where $m > n$) there are usually fewer problems with the controllability and also the volume occupied by the cables. A few robots based on this design are now commercialized and typically used for cargo transport (e.g., the NIST Robocrane [12]) or camera manipulation (e.g., Skycam [13] and Cablecam [14]). Fully restrained cable robot on the other hand can operate in any direction regardless of the direction of the wrench exerted to its MP [4].

In recent years, several aspects of cable robots such as kinematics, workspace, force distribution and cable arrangement were studied and analyzed. For instance, Shiang et al. [15] designed an incompletely restrained 3-DOF robot, derived its motion equations while the flexibility of the cables was considered, and optimized the force distribution among cables. Tadokoro et al. [16] investigated the optimal distribution of eight independently actuated cables of a cable mechanism. Jiang and Kumar [17–19] investigated the kinematics of cable-suspended mechanisms driven by a set of aerial robots for cargo transportation usage. They solved the direct and inverse kinematics of suspended cable systems with $m = 2, \ldots, 6$ cables and developed a method to analyze the stability of the mechanism in all its static equilibrium poses. Carricato et al [20–22] proposed an elimination method to find a complete solution for the direct and inverse geometrico-static problem of unconstrained cable robots with three and more cables. Yang et al. [6] presented a 7-DOF modular cable-driven humanoid robotic arm and mainly focused on the workspace of the 3-DOF modules constituting this arm. The same authors proposed in [4] the Tension Factor (TF) index to evaluate the tension of cables and assess force-closure in a cable-driven robot in order to obtain its workspace. Rosati et al. [23] proposed a systemic methodology to optimally design a new class of cable-driven mechanisms. In this approach, they used posture dependent local performance indices instead of a global index to maximize the performance of the mechanism.

Gouttefarde and Gosselin [24] presented many theorems to characterize the wrench-closure workspace (WCW) of planar cable-driven robots. Then, these theorems were used to find the WCW of the robot within its reachable workspace. Next, Gouttefarde et al. [25] presented an interval analysis based method to investigate the wrench-feasible workspace (WFW) of a n-DOF cable robot. This method evaluates whether a given Q-dimensional box is located inside the WFW or not. Additionally, Bouchard and Gosselin [1] proposed a geometrical method to analyze the capability of a cable-driven robot with two to six-DOFs to generate a set of wrenches on its MP.

In all cases, the number of necessary actuators is always strictly greater than the number of DOF which increases the cost and complexity of the control equipment. This issue is even more critical since generally, the more cables are used in the structure of the robot, the better the performance in terms of the size of the WCW and WFW [6, 9]. Therefore, keeping the number of actuators

at minimum while increasing the number of cables (and thus the performance of the mechanism) appears to be a dilemma.

In this paper, it is proposed to solve this conundrum by using differentials to actuate several cables of a planar cable-driven mechanism by a single actuator. To this aim, these mechanisms are first introduced and their properties are presented. Then, some examples showing the performance of planar mechanisms actuated with differentials are compared with fully actuated cable-driven architectures. Finally, in the second part of this paper, the general methodology for the synthesis of differential cable mechanisms is presented and illustrated with examples for $q = 2$, 3, and 4 cables in each differential.

5.3   Differential Cable-driven Manipulator

Using differentials in machines and mechanisms is a popular method to distribute an actuation source to several degrees of freedom [27]. A differential is a 2-DOF mechanism producing two outputs from a single input or vice-versa [26]. To drive an even greater number of outputs from a single input, these mechanisms can be connected either in serial or parallel combinations [27]. Examples of commonly found differentials are seesaw mechanisms, automotive bevel gear boxes, planetary gear differentials, and mobile pulley-cable arrangements [28].

The idea of using differentials in cable robot is to replace an actuated cable with two, three, or more cables, each connected by a mechanism but driven by the same actuator. The distribution of a driving force/torque to several degrees of freedom in a robotic system has previously been studied extensively including by the authors [27, 29–34] where several types of either tendon or linkage-based differentials have been used to drive phalanges of robotic fingers. In these works, the shape adaptation property of these fingers was obtained mechanically using differentials such as cables and pulleys, bevel gears, etc. and it was shown in [34] that using differentials and the spatial distribution of the generated forces were a key element in their design. In this paper, it is shown that the same principles apply when designing planar cable robots and that using differentials is again beneficial.

To use differential systems in a cable robot instead of a robotic finger, two questions should be answered: 1- which conditions should be satisfied to fully constrain the MP in this new design; 2- how can a single actuated cable be usefully replaced by a differential cable-driven mechanism.

The first question is all about the arrangement of the cables around the MP. These cables should be able to lock the pose of the MP or equivalently be able to provide full translational and rotational motions. For this, the cables should surround the MP in all directions of the task space to be able to produce any arbitrary force or torque. In other words, they should be able to satisfy the static equilibrium condition of the MP regardless of the direction of any external wrench, i.e.:
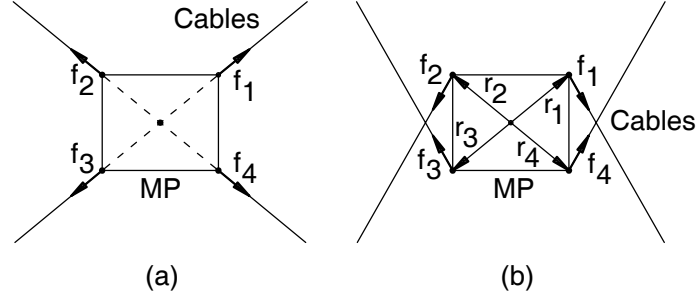
Figure 5.1 MP with (a) only translational motion; (b) both rotational and translational motion.

$$\sum \mathbf{f}_i + \mathbf{f}_{ext} = 0 \quad \text{for} \quad i = 1, \ldots, m \tag{5.1}$$

$$\sum \mathbf{r}_i \times \mathbf{f}_i + \tau_{ext} = 0 \quad \text{for} \quad i = 1, \ldots, m \tag{5.2}$$

where $\mathbf{f}_i$ and $\mathbf{r}_i$ are respectively the tension force vector applied on the MP by the ith cable and the position vector of the point of application of this force with respect to an arbitrary point on the MP. Additionally, $\mathbf{f}_{ext}$ and τ_{ext} are respectively the external force and torque exerted to the MP. From these equations, it appears that certain geometric configuration should be avoided, for instance, if the directions of all cables intersect in one point they obviously cannot produce any torque and thus, they cannot constrain the rotational motion of the MP. Mathematically, this is because Eq. (5.2) is not satisfied in that case unless $\tau_{ext} = \mathbf{0}$. This situation is shown for a planar cable robot with 4 cables in Fig. 5.1(a). On the other hand, in Fig. 5.1(b), the cable directions do not intersect and consequently, the cables can theoretically exert any torque on the MP.

The second question raised before is all about how to use a differential instead of a single actuated cable while preserving the force-closure condition. As mentioned before, m independent cables can constrain up to $(m-1)$-DOF. If some of these cables are connected to the same actuator through a mechanism they cannot change their lengths independently and thus, self-motion may happen, i.e., cables (and consequently the MP) might have non-zero velocities while the associated actuator is locked.

To account for this problem, instead of considering the force in each individual cable driven by a differential, the resultant force of all cables connected by the latter should be taken into account. For example, let us consider the two mechanisms shown in Fig. 5.2. In case (a) each cable is connected to a separate actuator generating an independent force and two independent forces in two different directions can completely constrain the single-point MP [a spring is assumed to pull the MP away from the base platform (BP)]. In case (b) these two cables are replaced by a cable and pulley mechanism actuated by a single actuator. In this case, since there is just one actuator,
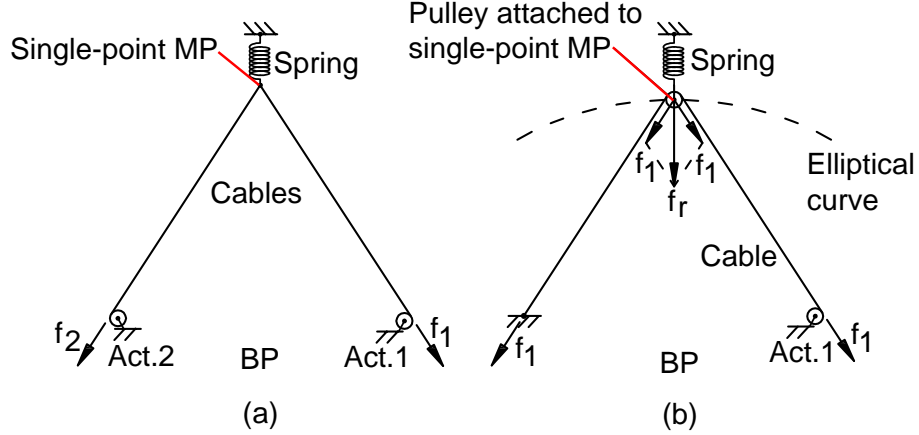
Figure 5.2 Single-point MP actuated with (a) two independent cables; (b) a cable and pulley differential.

the attachment point of the cables (i.e., the axis of the pulley if its radius is negligible) can move along an elliptical trajectory while the actuator is locked. This happens because the resultant force of the two branches of cables always lies on their bisector (in ideal frictionless condition) and the pulley can move in the direction perpendicular to the direction of this force. Thus, considering the resultant forces of the differentials, the MP is fully constrained if and only if the twist vector reciprocal to the space of all constraint wrench vectors is zero-dimensional.

5.4 Comparison between Differential and Fully Actuated Cable-driven Mechanisms

The main question in using differentials is about evaluating their advantages in comparison with the fully actuated architectures. As mentioned before, using this novel solution, the number of actuators can be kept at minimum ($n + 1$ for a n-DOF robot) while the number of cables connecting the MP to the BP is increased. Hence, a single thick cable can be replaced by several lighter cables which is beneficial with high payload cable-driven architectures where the masses of the cables are not negligible [11]. Additionally, without adding other actuators, for a given size of cables the payload of the robot can be increased. This also leads to a better distribution of the mass of the MP on the BP.

The uniqueness of using differentials on the kinematic of the mechanism yields from the direction of the resultant force of all its cables. To illustrate this, the free movement of the pulley of the mechanism introduced in Fig. 5.2(b) while its actuator is locked, is shown again in Fig. 5.3. As is apparent in this figure, for a fixed cable length, when the pulley is on the line of equidistant points from the attachment points A and A' (i.e. in point B), the bisector of the two cable directions passes through point C. In this case, the differential system is instantaneously equivalent to a single cable
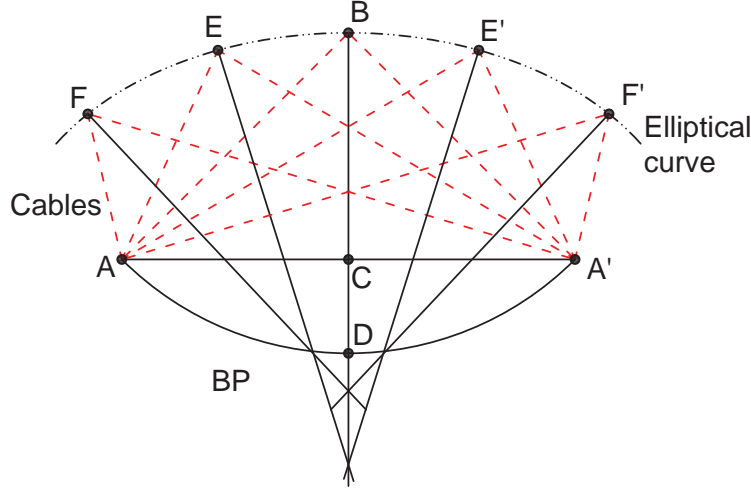
Figure 5.3 Direction of the bisector of a cable differential when actuator is locked and the attachment point on MP (e.g. the pulley) moves on resultant elliptical curve.

connecting the MP to the BP at point C. However, when the pulley moves away from point B, the intersection point between the bisector and the line AA' travels along this latter line segment. This means that the illustrated differential behaves as a single actuated cable in which the attachment point on the BP is variable. This property can be beneficial for the WCW and WFW of a cable-driven mechanism as will be shown. For this, first, the methods used to find these workspaces are briefly recalled.

The WCW of a cable-driven robot is the set of poses where the forces of the cables as well as their resultant torques (if they exist) can surround the center of the MP in all directions in the considered Q-dimensional space (the force-closure condition [4]). To find the WCW, a method similar to the one introduced in [6] is used in this paper. Namely, the unit vectors of the forces $\mathbf{e}_i$ which are in the direction of the cables in fully actuated cable mechanisms or in the direction of the resultant forces of the differentials, are used to define the positions of a set of points constituting a convex polyhedron. Next, if the origin of these vectors is located inside this polyhedron then the mechanism can produce forces in all directions. Similarly, this situation can be investigated for the torques exerted by the MP. However, since a single-point MP is used here as an example, this second step does not apply.

To obtain the WFW, a geometrical approach similar to the one proposed in [1] is used. For this, it is assumed that the tensions in all the cables should be between t_{min} and t_{max}. Then, the tension vectors $\Delta\mathbf{t}_i = (t_{max} - t_{min})\mathbf{e}_i$ can be evaluated. Next, these vectors are used as a basis to construct a zonotope (a particular class of convex polytopes) which in turn is used to calculate the WFW of the robot. For this, the vectors $\Delta\mathbf{t}_i$ are taken as a set of line segments and by calculating the Minkowski
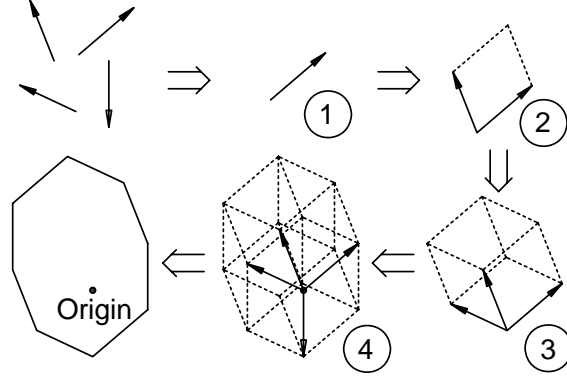
Figure 5.4 Four step generation of a 2D zonotope from four coplanar vectors.

sum [1] of these lines, the initial zonotope is obtained. Afterwards, the resultant force of all the vectors with minimum values (i.e., t_{min}), is added to the Minkowski sum to modify the positions of the vertices of the zonotope and obtain its final shape. The volume of this polytope, Z, is defined as [1]:

$$Z = \alpha_1 \Delta \mathbf{t}_1 \oplus \alpha_2 \Delta \mathbf{t}_2 \oplus \cdots \oplus \alpha_m \Delta \mathbf{t}_m + \sum_{i=1}^{m} \mathbf{t}_{i^{min}} \tag{5.3}$$

where m is total number of the independent force vectors, $\alpha_i \in [0,1]$, and the symbol $\oplus$ represents the Minkowski sum of the line segments. Finally, the radius of the largest circle that can be completely located inside the resultant zone with its origin attached to the origin of the 2-D polytope is the magnitude of the maximum permissible force. If this force is larger than the specified minimum allowable force then that pose belongs to the WFW of the robot. In the case of the cable robots driven by differentials, instead of the tension vectors $\Delta \mathbf{t}_i$ of the cables of each differential, their resultant vector $\Delta \mathbf{t}'_j$ should be used in Eq. (5.3). In general, this property should be valid for both force and torque vectors which are investigated, separately. In Fig. 5.4, an example of the generation of a 2-D zonotope from four coplanar vectors is illustrated.

Considering the above definitions, the WCWs of four planar cable mechanisms are compared for illustration purposes as illustrated in Fig. 5.5. All these mechanisms have a single-point MP (for the sake of simplicity) and three actuators. The attachment points of their cables on their BP are on the same circle (with identical center and radius). In all cases, the MP has the same coordinate with respect to the inertial frame attached to the center of the BP circle. The attachment points on the BP of the fully actuated mechanism in Fig. 5.5(a) lies on an equilateral triangle while those of the differentially actuated mechanisms in Fig. 5.5(b) define a hexagonal shape, and in the cases shown in Figs. 5.5(c) and (d) they are symmetrically located on three sections of the circumcircle.

In Fig. 5.5(b), it is assumed that the MP is connected to three differentials on the BP respectively

Figure 5.5 Schematic of planar cable mechanisms driven by (a) three actuated cables; (b) three differentials with $q = 2$ cables; (c) three differentials with $q = 3$ cables; (d) three differentials with $q = 4$ cables.

at points $B_1 - B_2$, $B_3 - B_4$, and $B_5 - B_6$. In the particular location of the MP shown in this figure, the bisectors of the cables attached to the differentials defined by $B_1 - B_2$ and $B_5 - B_6$ (i.e. the direction of the resultant forces of these cables) intersect the base circle at two points further away from point S_2 than points S_1 and S_3.

As a result, in Fig. 5.5(b), the triangle made by the unit vectors along these bisectors includes the MP while the triangle created by unit vectors along cables in Fig. 5.5(a) does not. Consequently, in Fig. 5.5(b) the location of the MP is inside the WCW and in Fig. 5.5(a) it is outside the WCW. Thus, as shown in this introductory example, with a proper design and even in the same limited area for the BP, one can expect a larger WCW with the cable mechanisms using differentials.

In Figs. 5.5(c) and (d) differentials with respectively $q = 3$ and 4 cables are used in the architecture of this planar mechanism. Following the same rule and in ideal conditions (friction and the diameters of the pulleys are ignored) for the illustrated location of the MP, the directions of the resultant forces of the differentials are obtained. As it can be seen in these figures, in both cases the MP is again inside the aforementioned triangle but compared to case (b) the MPs are closer to

one edge of the triangle (and so closer to the boundary of the WCW). Compared to the differential $B_1 - B_2$ in Fig. 5.5(b), in Fig. 5.5(c), the middle cable of the differential $B_1 - S_1 - B_2$ connected to point S_1, brings the direction of the resultant force a little closer to this point and so decreases the advantage of using differentials. Similar results are obtained for the direction of the resultant forces of differential $B_1 - D_1 - D_2 - B_2$ in Fig. 5.5(d).

Consequently, both the arrangement and the number of cables of differentials affect their performance. When the distance between attachment points of the cables on the BP [e.g. the distance between points B_1 and B_2 in Figs. 5.5(b)-(d)] becomes larger, the particular effect of the differentials (illustrated in Fig. 5.3) increases. On the other hand, the magnitude of the resultant force of those cables decreases. If more cables are used in the structure of the differential, the maximum magnitude of the resultant force can be improved but its direction may also be influenced (and thus, the performance of the differential can be either weakened or improved). Therefore, in Fig. 5.5(d), if the points D_1 and D_2 coincide respectively with points B_1 and B_2, then the WCW of cases (b) and (d) are identical. Also, if points D_1 and D_2 are located on the circumcircle beyond the boundary between B_1 and B_2, then the volume of the WCW even expands.

To illustrate the advantages and limitations of using differentials in the design of a cable robot in more details, the three planar differentially actuated mechanisms depicted in Figs. 5.5(b)-(d) (each with three differentials driving respectively six, nine, and twelve apparent cables) are compared to two typical fully actuated planar mechanisms with similar geometries. The differentially driven cable robots shown in Figs. 5.5(b)-(d) are here respectively referred to as 6-3, 9-3, and 12-3 differential mechanisms. The differentials in each of these mechanisms have $q = 2$, 3, and 4 cables. The first fully actuated mechanism is shown in Fig. 5.5(a) and has three actuated cables and is called henceforth the 3-3 full mechanism. The second fully actuated cable mechanism has six actuated cables and is similarly called the 6-6 full mechanism. It has the same geometric architecture as the 6-3 differential mechanism [c.f. Fig. 5.5(b)]. In this paper, the performance metrics used to analyze the planar cable robots, are the sizes of the WCW and WFW.

5.5   Implementation and results

An algorithm is then used to numerically calculate the WCW and WFW of the aforementioned five planar cable architectures. For this, numerical values are chosen, e.g. it is assumed that the radius of the BP circle is 70 cm. Moreover, in the 12-3 mechanism, the points D_i are located on the circle at the middle of points B_i and S_j [c.f. Fig. 5.5(d)]. Also, the maximum and minimum tension in the cables are arbitrarily chosen to be $t_{min} = 10$ N and $t_{max} = 100$ N respectively. The minimum force to be exerted to the MP of the robots in any direction is chosen at 50 N.

The results of the workspace calculations for these mechanisms are presented in Figs. 5.6-6.5
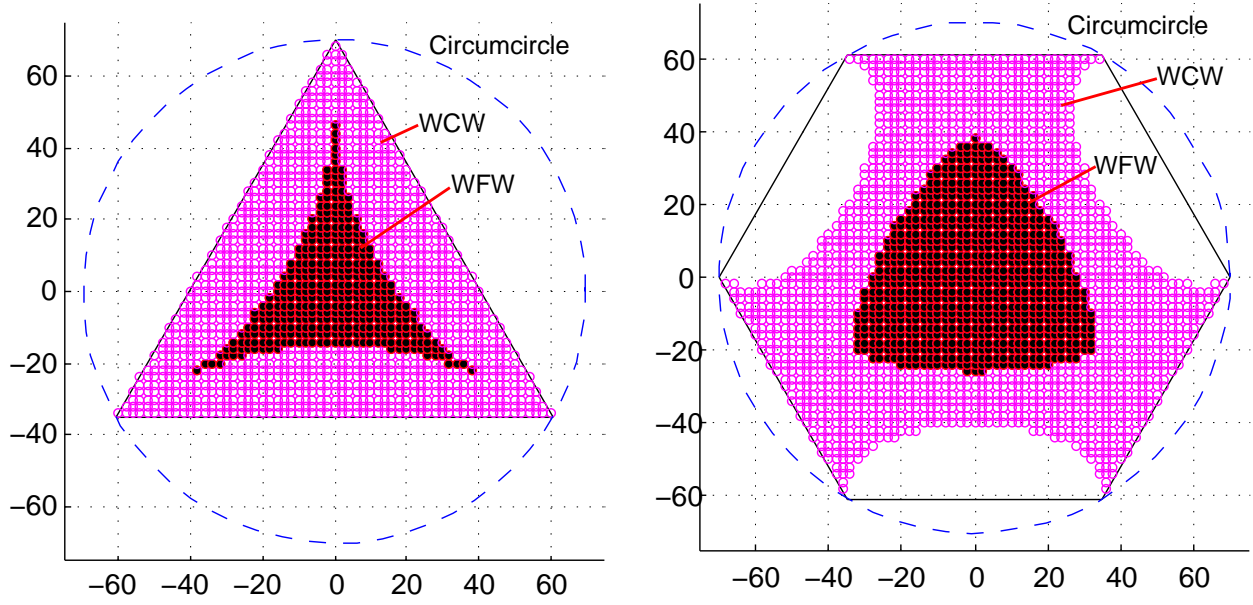
Figure 5.6 WCW and WFW of (left) the 3-3 full mechanism; (right) the 6-3 differential mechanism ($q = 2$).

Table 5.1 The ratios of the areas of the WCW and WFW to the base circle area of the mechanisms.

Type of workspace	3-3 full	6-3 diff.	9-3 diff.	12-3 diff.	6-6 full
WCW	0.4132	0.6019	0.4859	0.5248	0.8287
WFW	0.0937	0.1887	0.2704	0.3076	0.4965

and Table 5.1. Note that, WCW is a type of WFW where there is no boundary for the cable tensions and the amount of the required wrench set, thus, the WFW is a subset of the WCW [24]. The ratios of the areas of the WCW and WFW to the base circle area of the mechanisms are listed in Table 5.1. As expected, the results reveal that both the WCW and WFW of the 6-3 differential mechanism are larger than these of the 3-3 full mechanism but smaller than those with the 6-6 full mechanism. The same results are obtained for workspaces of the 9-3 and 12-3 differential mechanisms. But when the three differential robots are compared together an interesting conclusion can be drawn. Unlike what is generally expected with the fully actuated cable robots (i.e., using more cables one can have a better performance), with differential cable robots, using more cables in each differential the WCW may expand or shrink. As presented in Table 5.1, although the WFW is grown by increasing the number of cables of each differential, the 9-3 architecture has a smaller WCW than the two others. Consequently, with more independent cables or differentials, larger workspaces
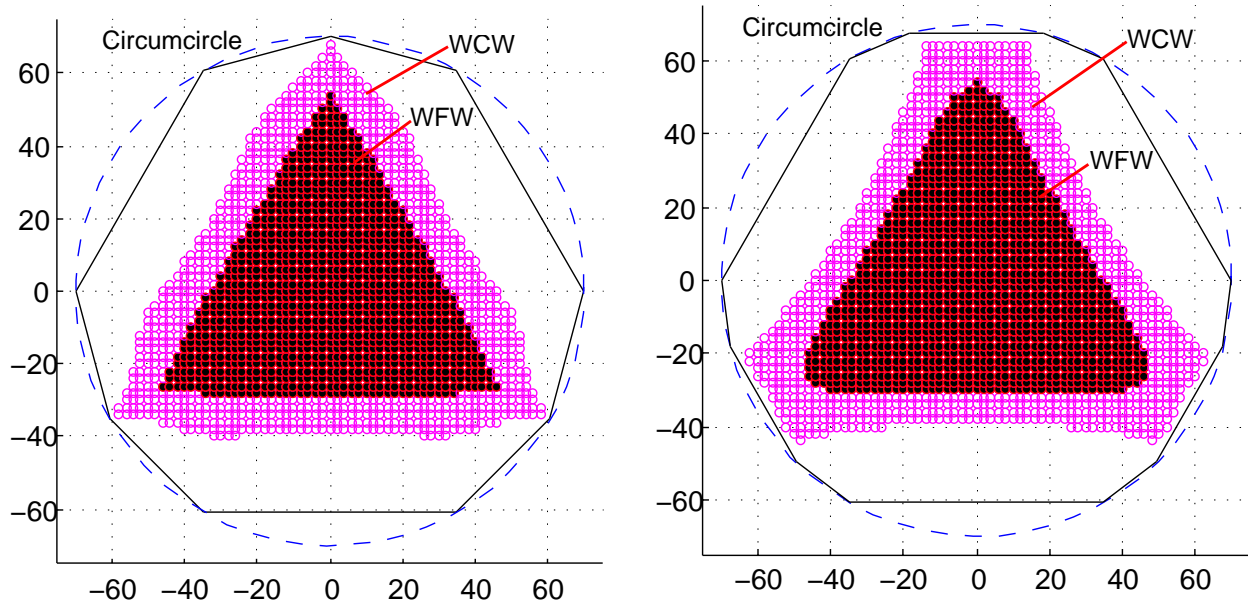
Figure 5.7 WCW and WFW of (left) the 9-3 differential mechanism ($q = 3$); (right) the 12-3 differential mechanism ($q = 4$).
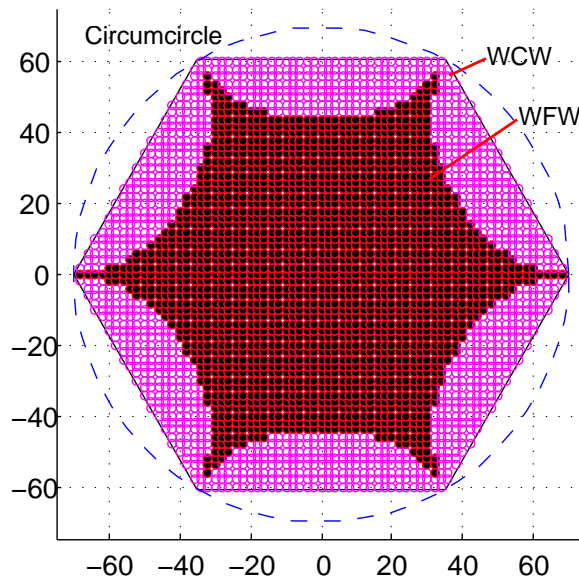
Figure 5.8 WCW and WFW of the 6-6 full mechanism.

can be expected, but the number of cables in each differential is not necessarily included in this hypothesis. Furthermore, the WCW of a cable robot generally depends on the cable configuration and the location of the attachment points of the cable on the BP and the MP [24].
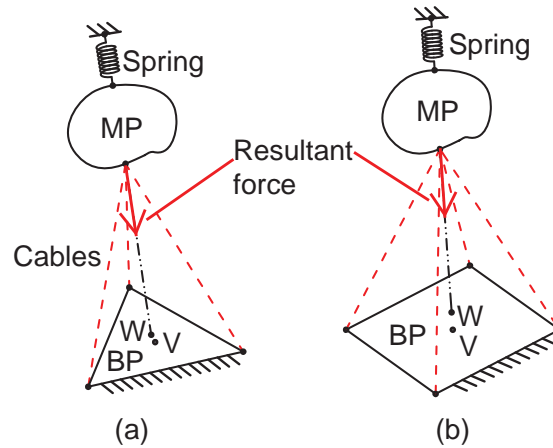
Figure 5.9 Schematic of a spatial differential with (a) $q = 3$ cables; (b) $q = 4$ cables.

In the proposed architecture, the WCW is analyzed by the direction of the resultant forces of the differentials. Therefore, if using more cables shortens the range of variations in their directions, then, the benefit of using differentials is decreased. Because, the differential then acts similar to a usual cable system. However, with a proper design of a cable mechanism and using differentials one can improve both the WCW and WFW of a cable robot without requiring more actuators. Of course, due to the dependency of the forces in the cables of a differential, these mechanisms cannot have the same performance as the ones in which all the cables are independently actuated. However, they offer a relatively simple and inexpensive way to improve the WCW and WFW of these robots.

This paper is dedicated to the investigation of the application of differentials in planar cable robots. However, this option can also be used in spatial cable robots and similar results can be expected for them. This issue is briefly addressed here and will be investigated and analyzed in detail in another paper. Regardless of the dimension of the space in which the mechanism operates (e.g., either 2-D or 3-D), the proposed differential systems work with the same principle. This means that again the resultant force of all cables of a differential arranged in 3-D space would have to be considered in the kinematic analysis. Also, the advantage of using a differential in spatial robots depends on the range of variation it allows in the direction of the resultant force. Similarly to the 2-D case, with spatial mechanism, it is critical to arrange the cables of a differential in such a way that this range is increased. If it happens, then one can expect larger WCW and WFW for spatial differentially driven cable robots. However, with spatial robots, there are more options to be considered with differentials in the structure of the robot. Namely, in addition to the planar differentials, spatial types can also be used. Examples of spatial differentials with $q = 3$ and 4 cables are illustrated in Fig. 5.9 where points V and W are respectively representing the center of

the attachment points of cables on the BP and the intersection point of the direction of the resultant force and the plane of the BP. In these examples, by moving the MP, point W moves around point V. In a spatial cable robot, when the actuator is locked, the attachment points of the cables of a differential on the MP are free to move on a free-form surface (e.g. an ellipsoid surface if $q = 2$).

Using differentials in the structure of a cable robot can also bring some difficulties. In the practical design, since there is friction among the cables and pulleys, the magnitude of the tension force of the cables may not be exactly the same. This can affect the force distribution and leads to some uncertainties in the direction of the resultant force. Also, the radii of the pulleys make the calculation of the direction of the cable force more complicated. These issues increase the difficulty of the kinematic analysis of this robot. Hence, it is preferred to minimize the use of pulleys especially if attached to the MP. However, since the total length of the cables of a differential, its rate, and its acceleration are considered in the kinematic analysis, a minimal number of sensors and actuators are then used to control this mechanism. Thus, these drawbacks can be partly compensated.

5.6 Synthesis of Planar Differential Cable-driven Mechanisms

In this section, a method to efficiently replace a single actuated cable with a differential driving two or more cables is presented. The synthesis of differential cable-driven mechanism is divided in two parts, namely the valid arrangement of the cables and how to drive all cables of a differential using a single actuator.

5.6.1 Synthesis of cable arrangements driven by one actuator

The main challenge to synthesize differential cable-driven mechanisms is to find how to connect the MP to the BP via these cables (i.e., their arrangement). This issue has been investigated for a certain number of independently actuated cables in [16]. To solve this problem for cables of a differential, each cable is first modeled as a line segment with two nodes at its ends (one attached to the MP and the other to the BP). Also, as illustrated in Fig. 5.10, it is assumed that the attachment points of the cables on each body (either the MP or the BP) which are called here locations, are defined along an arbitrary planar open path. Therefore, the order of these points is important. Then, the problem is to find all possible connections between these points, referred here to as nodes, on each body. In addition, several cables can be attached at the same location on a body. In summary, the problem of finding all possible configurations of an architecture with q cables can be divided in two steps:

1. Finding all possible solutions for the placement of nodes along the defined paths on each body (MP or BP).
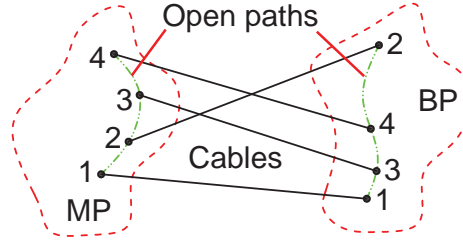
Figure 5.10 Schematic of the distribution of nodes with four cables on four different coplanar locations.

2. Finding all possible solutions for connecting these nodes from the MP to the BP for each set of locations found in step 1.

The first step deals with finding all possible arrangements of nodes, namely the number of distinct locations, the number of nodes in each location, and the combination of all these possibilities without repetition. To do this, an algorithm is developed to find how q nodes can be located in a set of l locations where $1 \leq l \leq q$. For each l, the number of solutions can be calculated as:

$$\binom{l}{i}\binom{l-i}{j}\cdots\binom{l-i-j\cdots-k=h}{h} = \frac{l!}{i!\,j!\cdots h!} \tag{5.4}$$

where $i, j, \cdots, h$ are respectively the number of locations with $a, b, \cdots, c$ nodes while $l = i + j + \cdots + h$ and $q = a + b + \cdots + c$.

As an example, the total number of arrangements of 5 nodes is presented in Table 5.2. As shown in this table, there are 7 different possible solutions to locate 5 nodes and considering their combinations, a total of 16 arrangements are found. To better illustrate this, the equivalent problem of placing five balls in one to five different boxes is shown in Fig. 5.11. All possible arrangements are then clearly apparent.

For the second step, an algorithmic solution is proposed in this paper based on using a matrix referred to as the slider. The aim is to find all possible solutions for connecting the nodes from the MP to the BP. For this, at each step of the calculation, two node solutions (one for each body) are chosen, e.g. arrangements no. 2 for the MP and no. 6 for the BP as described in Fig. 5.11. The node arrangement of the MP is represented by a vector called "master" and the one of the BP in another vector called "slave" defined as:

$$master = \begin{bmatrix} a_1 & a_2 & \cdots & a_{l_1} \end{bmatrix} \text{ and } slave = \begin{bmatrix} b_1 & b_2 & \cdots & b_{l_2} \end{bmatrix} \tag{5.5}$$

Table 5.2 Total number of possible arrangements for 5 nodes.

No.	Locations & number of nodes	Solutions of each set (C_{mas} or C_{slv})
1	1,1,1,1,1	$\frac{5!}{5!} = 1$
2	2,1,1,1	$\frac{4!}{1!3!} = 4$
3	2,2,1	$\frac{3!}{2!1!} = 3$
4	3,2	$\frac{2!}{1!1!} = 2$
5	3,1,1	$\frac{3!}{1!2!} = 3$
6	4,1	$\frac{2!}{1!1!} = 2$
7	5	$\frac{1!}{1!} = 1$
Total		16
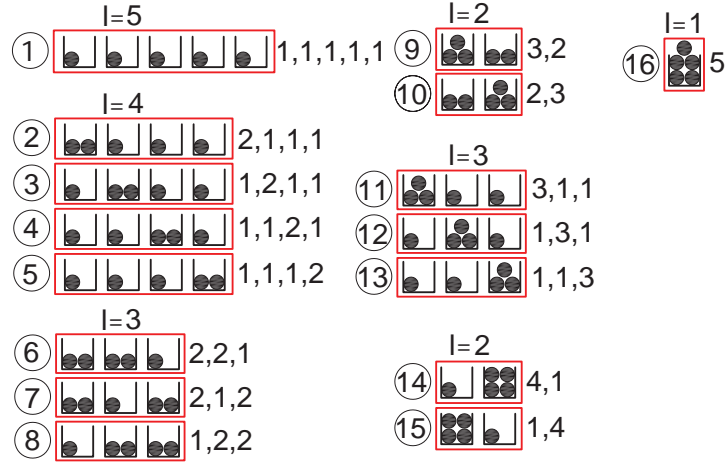
Figure 5.11 All solutions for placing five balls (representing the nodes) in one to five bins ($q = 5$ and $l = 1, \ldots, 5$).

where a_i and b_i are respectively the number of nodes in the ith location on the MP and BP; l_1 and l_2 are respectively the number of these locations on the MP and BP where $a_1 + a_2 + \cdots + a_{l_1} = b_1 + b_2 + \cdots + b_{l_2} = q$. In the previous example with the arrangements no. 2 and 6, one has $master = \begin{bmatrix} 2 & 1 & 1 & 1 \end{bmatrix}$ and $slave = \begin{bmatrix} 2 & 2 & 1 \end{bmatrix}$. Next, the slider matrix is used to iteratively find all possible solutions for connecting the nodes associated with each set of master and slave vectors. In each iteration, the slider matrix has a $a_i \times l_2$ structure. In each row of this matrix, there is a non-zero component and its value is one. During the process, the column numbers of these non-zero components are changed to search for the valid solutions.

Table 5.3 Number of solutions for $q=2, \ldots, 10$ cables.

q	Solutions	q	Solutions
2	5	7	546193
3	33	8	9132865
4	281	9	171634161
5	2961	10	3581539973
6	37277		

Using Eq. (5.4), the algorithm calculates all possible combinations for each of these node arrangements (e.g., third column of Table 5.2 for $q = 5$) and considers them as coefficients C_{mas} and C_{slv} respectively for the master and slave vectors. For s different possibilities of locating q nodes, there are $\binom{s+1}{2}$ possible sets of two node arrangements (as presented in Table 5.2, for five nodes one has $s = 7$) and for each set, all possible connection patterns between q nodes on two bodies are calculated iteratively as:

$$Sum_j = Sum_{j-1} + \begin{cases} C_{mas}C_{slv} & \text{if } master = slave \\ 2C_{mas}C_{slv} & \text{if } master \neq slave \end{cases} \tag{5.6}$$

Using this algorithm, the number of all possible non-repetitive arrangements of q cables is calculated. In Table 5.3, these values for $q = 2, \ldots, 10$ cables are presented.

As it can be seen in this table, the number of solutions rapidly increases with the number of cables as would have been expected. In this paper, only the arrangement of differentials with 2, 3, and 4 cables are numerically investigated to limit the number of cases to consider to a reasonable number. The methodology is however general and can be extended to any number of cables.

The next step in the synthesis process is to seek out the valid arrangements amongst the myriads previously found. To this aim, manipulation requirements and physical restrictions are used as criteria to find the appropriate architectures:

1. the cables should not interfere;

2. all cables of each differential should be driven by only one actuator which due to the design considerations should be located on the BP (to have the lightest possible MP);

3. amongst all arrangements with similar properties, only the simplest is considered.

In Fig. 5.12, all arrangements previously found for two cables are illustrated. As shown in this figure, in case 1, the two cables can have either the same direction as in case 5 or an angle similar to case 4, while these two cases are more compact and have fewer attachment points on the MP. Also, the cables in case 2 intersect each other and in case 3 there are more attachment points on the
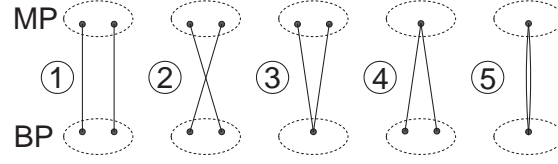
Figure 5.12 All arrangements of $q = 2$ cables connecting BP to MP.
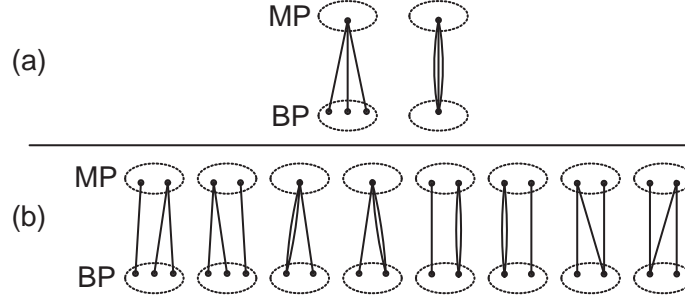
Figure 5.13 Valid $q = 3$ cables with (a) symmetric, (b) non-symmetric solutions.

MP than on the BP. Thus, based on the previously listed criteria, only cases 4 and 5 are considered valid.

Using the same technique, amongst all 33 arrangements found for three cables many cases can actually be discarded. Then, as shown in Fig. 5.13, the remaining solutions are categorized as either symmetric or non-symmetric. Since these differentials are assumed to be used instead of a single actuated cable, in this paper, the symmetry means that the number of nodes in each location and the number of the locations on each body (i.e., either the BP or the MP) on two sides of this imaginary single actuated cable, are the same. This symmetry is not based on physical dimensions. Using non-symmetric arrangements usually results in asymmetrical force directions. Thus, the shape of the workspace of the robot and also its control become more complex. Therefore, although they are technically valid, they are not considered in this paper.

Finally, the proper arrangements of $q = 4$ cables are also found and the final valid symmetric architectures for 2, 3, and 4 cable systems are illustrated in Fig. 5.14. It should be again noted that this procedure can be followed to find the valid arrangements for five and more cables, but the number of architectures found grows exponentially.

5.6.2 Actuation Synthesis

In the next step, the main issue is to equally distribute the actuation force amongst all the cables. Indeed, because of practical limits in their tensions, when the actuation force is equally distributed
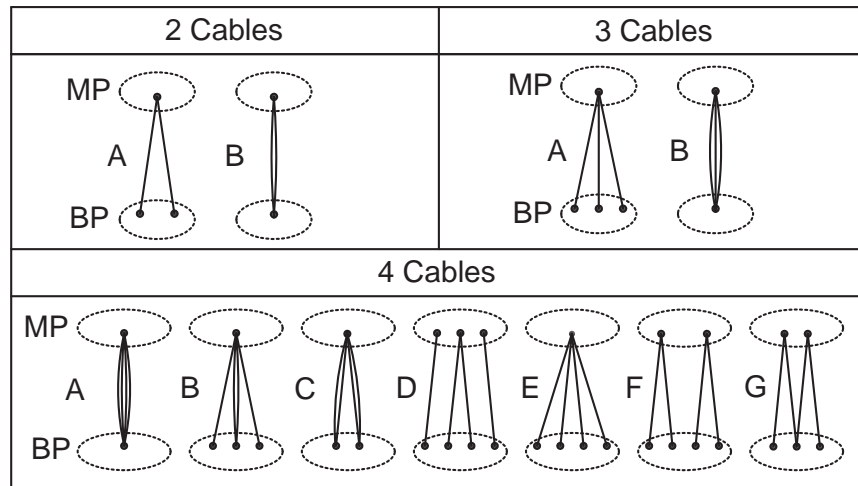
Figure 5.14 All valid symmetric arrangements with $q = 2$, 3, and 4 cables.

amongst all the cables of a differential, then, that mechanism can produce a larger force for the same posture. To drive the cables, three solutions are considered here:

1. The cables are branches of a single tendon connecting the MP to the BP via several pulleys, and one or both of its ends are connected to a actuated winch system. An example of this was presented in Fig. 5.2(b).

2. The cables are connected to the actuator using a differential (e.g., a bevel gear differential).

3. A combination of the two previous cases.

Since in the mechanical design of the systems different types of mechanisms are able to do the same task, it is difficult to determine exactly the number of systems that could be used in a particular application. This paper focuses on the types which are already used in other systems [28]. However, they may not be the only options. To drive a cable arrangement, four types of differential systems are therefore considered here, either individually or combined. They are the cable and pulley system [Fig. 5.2(b)], the single winch double cable system (i.e., the two ends of a cable are connected to the same winch), the double winch bevel gear system (i.e. two winches connected to the two outputs of a bevel gear system to drive two separated cables), and the triple winch planetary & bevel gear system (i.e., a combination of a bevel gear and planetary differential systems connected to three winches to drive three separate cables while the actuation force/torque is equally distributed amongst them) [28, 35, 36]. These four differentials will be respectively referenced by symbols Cp, Sw, Bg, and Tw in the figures. The schematics of the last three systems are shown in Fig. 5.15.
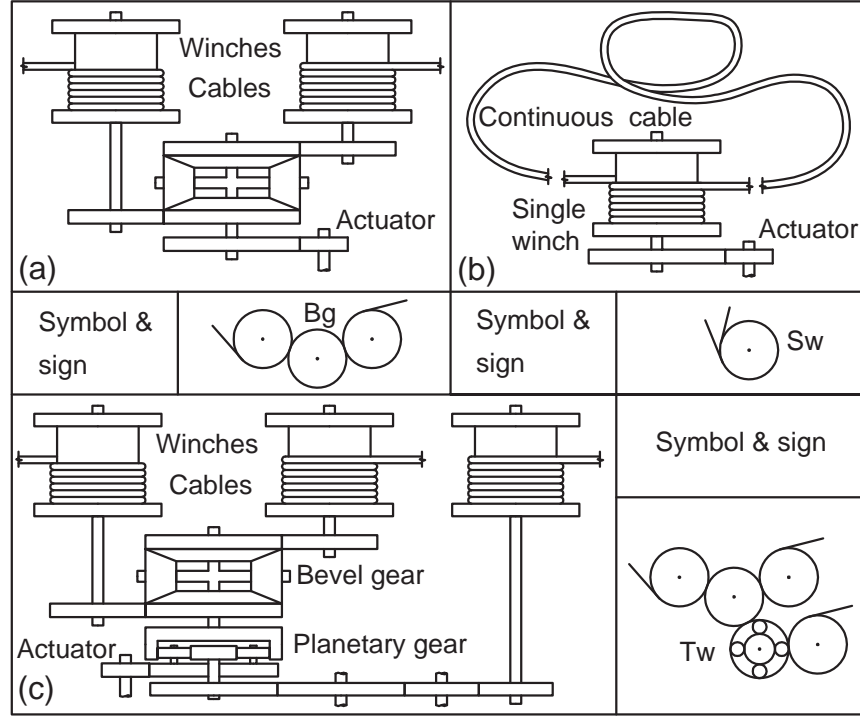
Figure 5.15 Schematics of (a) the double winch bevel gear system; (b) the single winch double-cable system; and (c) the triple winch planetary & bevel gear system.

Taking these four differentials into account, the relationships between inputs and outputs (i.e., respectively actuation torque/speed and winch torque/speed) can be easily obtained. To do this, it is assumed that the pulleys and gears are massless. The magnitudes of the ith velocity and force outputs in cables are respectively v_i and f_i. Also, ω_a and τ_a are respectively the angular velocity and torque of the actuator. In Cp and Sw differentials, these relationships are obtained as:

$$\omega_a = (v_1 + v_2)/r_w \text{ and } \tau_a = f_1 r_w \text{ in } Cp \tag{5.7a}$$

$$\omega_a = (v_1 + v_2)/(2r_w) \text{ and } \tau_a = (f_1 + f_2)r_w \text{ in } Sw \tag{5.7b}$$

where r_w is the radius of the winch. For the two latter differentials, first the radii of the gears, input torque/angular velocity (i.e., τ_a/ω_a) and output torques/angular velocities (i.e., $\tau_1, \tau_2, \tau_s/\omega_1, \omega_2, \omega_s$) are defined as illustrated in Fig. 5.16. Then, the relationships for the Bg and the Tw differentials are obtained as:

$$\omega_a = (\omega_1 + \omega_2)/2 \text{ and } \tau_a = 2\tau_1 \text{ in } Bg \tag{5.8a}$$
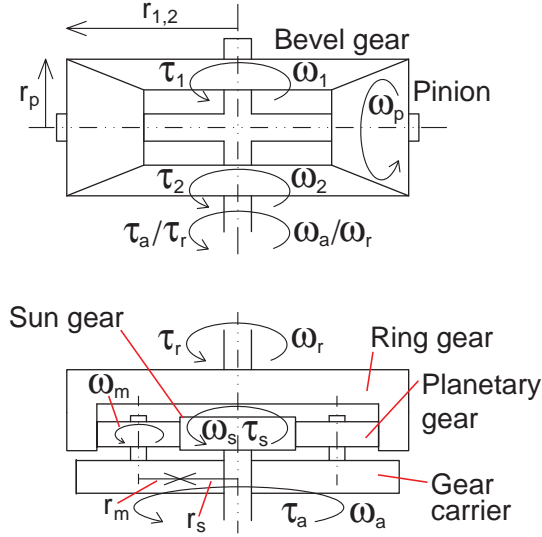
Figure 5.16 Definition of the radii of the gears, input and output torques/angular velocities.

$$\begin{cases} \omega_a = \frac{(\omega_1+\omega_2)(r_s+2r_m)/2+\omega_s r_s}{2(r_s+r_m)} & \text{in } Tw \\ \tau_a = \tau_1 \frac{4(r_s+r_m)}{r_s+2r_m} \end{cases} \qquad (5.8b)$$

With Tw differentials, the output of the planetary gear system is connected to the input shaft of the bevel gear system. It is assumed that the differentials can equally divide the input torque between the outputs. Since, the torques τ_s and $\tau_1=\tau_2$ are dependent, there should be a particular constraint in the gear ratios, namely $r_s = r_{1,2} = 2r_m$. Consequently, one has $\omega_a = \frac{\omega_1+\omega_2+\omega_s}{3}$ and $\tau_a = 3\tau_1$. Depending on how the differentials are connected to the cables (i.e., either directly via winches or by connecting their outputs to the inputs of other differentials), Eqs. (5.7a)-(b) and (5.8a)-(b) can be combined together.

The main issue which affects the selection of the type of differential is the number of required cables. With a q cable differential mechanism, q is not necessarily the number of individual cables. It is the number of connections between the MP and the BP. For example, in a $q = 4$ system, there are four connections between the MP and the BP. Assuming that two of the connections are made by the two individual cables and two remaining are created by two branches of a single cable, then, there are three individual cables constituting this arrangement. Considering this peculiarity, from 1 to t distinct cables can be used to produce the required connections (where $1 \leq t \leq q$).

The synthesis of the actuation of such systems can be done by finding all combinations of afore-mentioned four differential systems able to pull t cables. For this, the followings are considered:

1. If a single cable makes x connections between the MP and BP, then, at least $x - 1$ pulleys are required;

Table 5.4 Total number of solutions for the actuation of a cable differential with $q = 2, 3$.

q	2		3		
Valid types	2-A,B		2-A,B		
t	1	2	1	2	3
No. of passes with t cables	(2)	(1,1)	(3)	(1,2)	(1,1,1)
Cp_{tj}	1,1	0,0	3,1	0,0	0,0
Sw_{tj}	1,1	0,0	0,0	0,0	0,0
Bg_{tj}	0,0	1,1	0,0	0,0	0,0
Tw_{tj}	0,0	0,0	0,0	0,0	1,1
Co_{tj}	0,0	0,0	0,0	4,2	1,1
Total	(2,2)	(1,1)	(3,1)	(4,2)	(2,2)
	6		14		

2. A single winch double-cable system needs at least one pulley on the MP side because it should be connected to the two ends of the same cable;

3. To drive two independent cables, one bevel gear system is used. For any additional cable, one more bevel gear system should be added. These systems can be combined in parallel or serial configurations [27, 28];

4. If one bevel gear system is used to drive three or four cables, depending on the case, one or both of its winch(es) should be replaced by a single winch double-cable system;

5. To actuate t cables where $t = 2k + 1$ and $k \geq 1$, triple winch planetary & bevel gear differentials are used, either individually or in combination with the other types;

6. A bevel gear system should not be connected to both ends of the same cable.

Considering these rules, the possible solutions for actuating $q = 2$, 3, and 4 differential cable-driven systems are obtained. For this, all combinations of t separate cables needed to produce the arrangements of Fig. 5.14 are found while similar architectures are again discarded. Then, for each remaining architecture, an adequate actuation system is selected.

In Table 5.4, the different solutions to drive differential systems with $q = 2$ and 3 are listed. In this table, all combinations of t cables to connect the MP to the BP within q connections are presented and then the valid actuation option is selected and the total number of possibilities for each valid type of arrangement is found as:

$$T = \sum_{t=1}^{q} \sum_{j=1}^{g} (Cp_{tj} + Sw_{tj} + Bg_{tj} + Tw_{tj} + Co_{tj}) \tag{5.9}$$
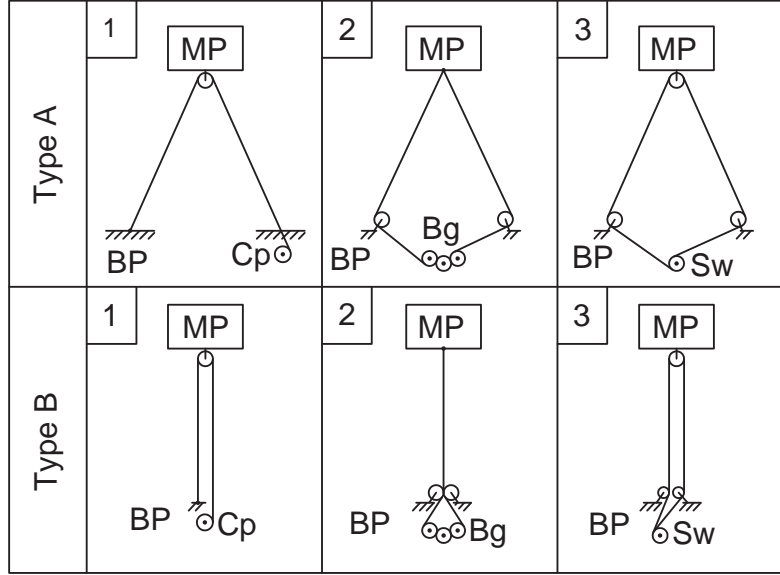
Figure 5.17 Schematics of the options to drive a $q = 2$ cable system.

where g is the total number of valid arrangements for q connections (row 2 of Table 5.4); Cp_{tj}, Sw_{tj}, Bg_{tj}, and Tw_{tj} are respectively the number of architectures, in which one can use Cp, Sw, Bg and Tw differentials for the jth valid arrangement. Finally, Co_{tj} is the number of different combinations of these systems that can be used for j^{th} valid arrangement.

In Fig. 5.17, all possible actuation of a $q = 2$ system are presented. Amongst all of these, some are redundant or have technical problems. To select the proper architectures, a new set of criteria is again used, namely:

1. If two cables have the same attachment points on both bodies they can be replaced by one thicker cable and a differential is not required except when the actuator only generates a part of the required total tension force.

2. Considering the friction, in similar differential systems the one with a simpler structure and fewer pulleys or gears is preferred.

3. Symmetric force distribution in the cables is preferred.

These criteria are used to select the kinematically practical architectures but neither for comparing them together nor for investigating their efficiency and performance (which remains as future work). Considering them, amongst the architectures of Fig. 5.17, in types A, the force distribution can be affected by friction. However, in type $A1$, since just one side of the cable is pulled by the actuator, although it suffers from less friction than $A2$ and $A3$, the force distribution may be asymmetrical. In type $B1$, the cables are parallel, thus, the force distribution is not affected by friction.
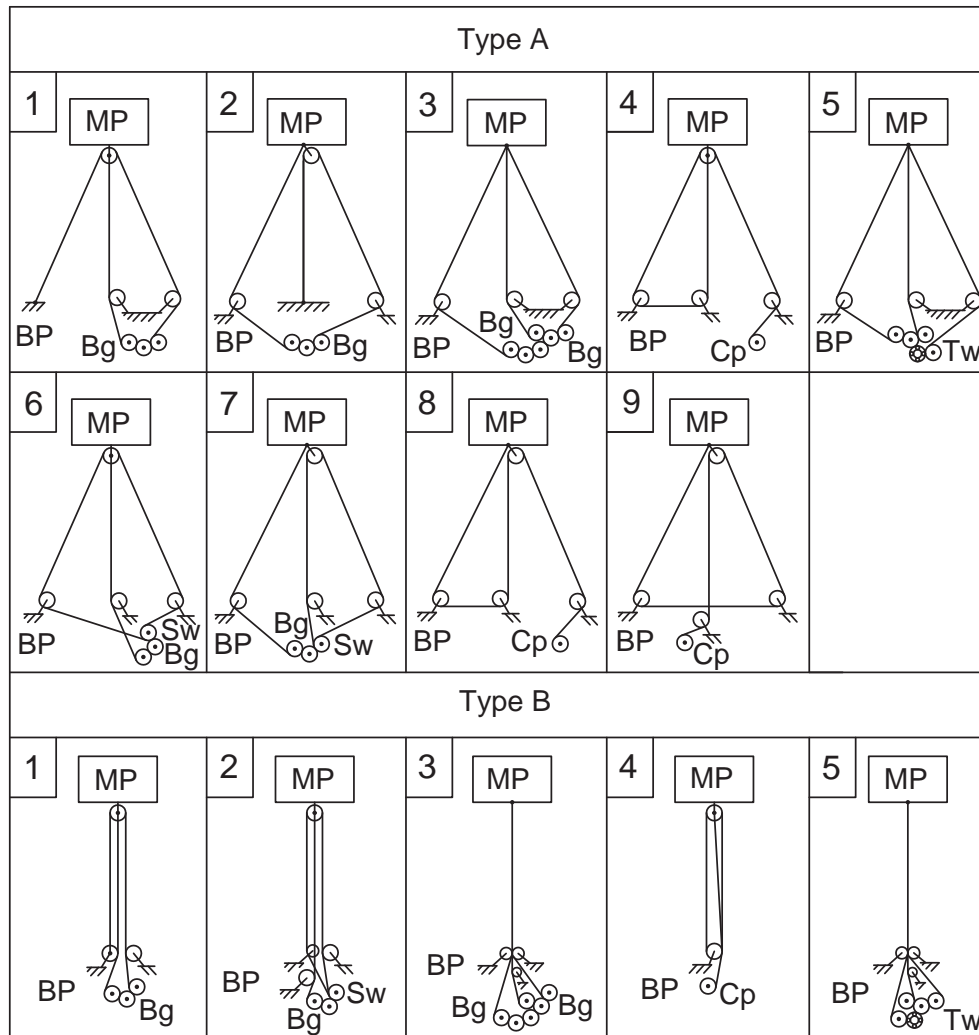
Figure 5.18 Schematics of the options to drive a $q = 3$ cable system.

Types $B2$ and $B3$ can be replaced with a single thicker cable. Consequently, for $q = 2$, types A, and $B1$ are kinematically preferred.

Actuation configurations of cable differentials with $q = 3$ are shown in Fig. 5.18. Again due to friction, the force distributions in types A may not be symmetrical. Amongst them, from a kinematic point of view, types $A1$, $A2$, $A4$, and $A6$ have simpler structure, less gears/pulleys and suffer less from asymmetrical force distribution. Thus, they are preferred to the other types. The force distributions in types $B1$ and $B4$ is not affected by friction and the actuator generates part of the total tension force while in the other types B, the differential system is useless.

A similar procedure is followed to find the architectures for a $q = 4$ cable system. As presented in Table 5.5 (row 4), there are five different solutions for using t independent cables to connect the

Table 5.5 Total number of solutions to drive a cable differential with $q = 4$.

q	4				
Valid types	7-A,B,C,D,E,F,G				
t	1	2		3	4
No. of passes with t cables	(4)	(1,3)	(2,2)	(1,1,2)	(1,1,1,1)
Cp_{tj}	1,6,3, 14,14, 14,14	0,0,0,0, 0,0,0	0,0,0,0, 0,0,0	0,0,0,0, 0,0,0	0,0,0,0, 0,0,0
Sw_{tj}	0,0,0,0, 0,0,0	0,0,0,0, 0,0,0	0,0,0,0, 0,0,0	0,0,0,0, 0,0,0	0,0,0,0, 0,0,0
Bg_{tj}	0,0,0,0, 0,0,0	0,0,0,0, 0,0,0	0,0,0,0, 0,0,0	0,0,0,0, 0,0,0	3,10,5,10 ,10,10,10
Tw_{tj}	0,0,0,0, 0,0,0	0,0,0,0, 0,0,0	0,0,0,0, 0,0,0	2,6,4,8, 8,8,8	0,0,0,0, 0,0,0
Co_{tj}	1,4,3,8, 8,8,8	1,6,3, 12,12, 12,12	3,10,7, 17,17, 17,17	4,14,8, 24,24, 24,24	0,0,0,0, 0,0,0
Total	2,10,6, 20,20, 20,20	1,6,3, 12,12, 12,12	3,10,7, 17,17, 17,17	6,20,12, 32,32, 32,32	3,10,5,10 ,10,10,10
	98	52	88	166	58
	462				

MP to the BP. The number of architectures for each of the actuation systems as well as the total number of the architectures are presented in the other rows of Table 5.5. In total, for a $q = 4$ system, 462 architectures exist. Finally, amongst these, using the same method, 18 options are determined as the kinematically preferred architectures (c.f. Fig. 5.19).

5.7 Conclusions

In this paper, the idea of using cable differentials in the architecture of cable-driven robots was proposed for the first time to the best of the authors' knowledge and the required properties to use such mechanisms in cable parallel robots were investigated. Next, the advantages of using differentials in the structure of these robots were discussed. Comparing three planar differential cable robots with two fully actuated ones showed that, while the number of actuators is kept at minimum (i.e., $n + 1$ actuators for a n-DOF cable robots), using differentials one can expect larger WCW and WFW for a mechanism with the same MP and constrains on the BP. Then, the synthesis of differential cable-driven mechanisms was presented. To do this, a method was developed to find
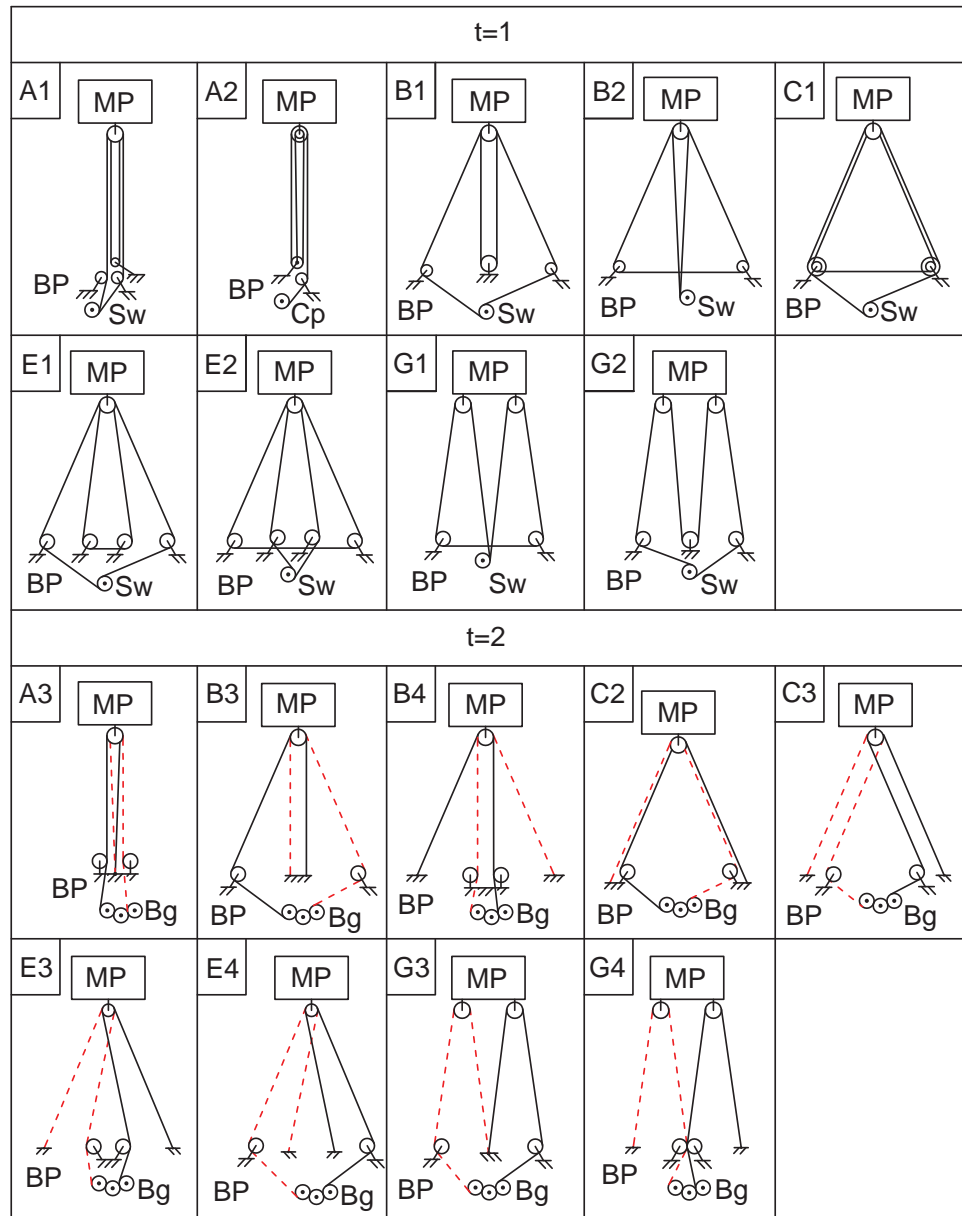
Figure 5.19 Schematics of the kinematically preferred options to drive a $q = 4$ cable system.

different arrangements of q cables in a differential and then, the valid arrangements with 2, 3, and 4 cables were found. Afterwards, four differential actuation systems were selected to drive the systems and finally, the valid possible mechanical architectures with $q = 2$, 3, and 4 cables were presented.

References

[1] S. Bouchard, C.M. Gosselin, and B. Moore, "On the ability of a cable-driven robot to generate a prescribed set of wrenches", *ASME Journal of Mechanisms and Robotics*, vol. 2, no. 1, pp. 011010 (1-10), Feb. 2010.

[2] S. Perreault and C.M. Gosselin, "Cable-driven parallel mechanisms-application to a locomotion interface", *J. Mech. Des. (USA)*, vol. 130, no. 10, pp. 1023011-1023018, Oct. 2008.

[3] S. Tadokoro, Y. Murao, M. Hiller, R. Murata, H. Kohkawa, and T. Matsushima, "A motion base with 6-DOF by parallel cable drive architecture", *IEEE ASME Trans Mechatron*, vol. 7, no. 2, pp. 115-123, June 2002.

[4] G. Yang, C.B. Pham, and S.H. Yeo, "Workspace performance optimization of fully restrained cable-driven parallel manipulators", *IEEE Int Conf Intell Rob Syst*, Beijing, China, pp. 85-90, Oct. 2006.

[5] F. Ferlay and F. Gosselin, "A new cable-actuated Haptic interface design", *Lect. Notes Comput. Sci.*, pp. 474-483, June 2008.

[6] G. Yang, W. Lin, M.S. Kurbanhusen, C.B. Pham, and S.H. Yeo, "Kinematic Design of a 7-DOF Cable-Driven Humanoid Arm: A Solution-in-nature Approach", *IEEE ASME Int Conf Adv Intellig Mechatron AIM*, Monterey, California, USA, pp. 444-449, July 2005.

[7] S. Kawamura, W. Choe, S. Tanaka, and S.R. Pandian, "Development of an ultrahigh speed robot FALCON using wire drive system", *Proc IEEE Int Conf Rob Autom*, vol. 1, Nagoya, Japan, pp. 215-220, May 1995.

[8] M. Carricato and J.P. Merlet, "Stability analysis of underconstrained cable-driven parallel robots", *IEEE Trans. Robot.*, vol. 29, no. 1, pp. 288-296, Feb. 2013.

[9] A. Fattah and S.K. Agrawal, "On the design of cable-suspended planar parallel robots", *Trans. ASME, J. Mech. Des. (USA)*, vol. 127, no. 5, pp. 1021-1028, Sept. 2005.

[10] A.T. Riechel, P. Bosscher, H. Lipkin, and I. Ebert-Uphoff, " Concept paper: Cable-driven robots for use in hazardous environments", *Conf. Robot. Remote. Syst. Proc.*, vol. 10, Gainesville, FL, pp. 310-316, Mar. 2004.

[11] M. Gouttefarde, J. Collard, N. Riehl, and C. Baradat, "Simplified static analysis of large-dimension parallel cable-driven robots", *Proc IEEE Int Conf Rob Autom*, Saint Paul, Minnesota, pp. 2299-2305, May 2012.

[12] J. Albus, R. Bostelman, and N. Dagalakis, "The NIST ROBOCRANE", *J Rob Syst*, vol. 10, no. 5, pp. 709-724, July 1993.

[13] R.R. Thompson and M.S. Blackstone, "Three-dimensional moving camera assembly with informational cover housing", US Patent 6,873,355, Mar. 2005.

[14] J. Rodnunsky, "Cabling system and method for facilitating fluid three-dimensional movement of a suspended camera", US Patent 7,088,071, Aug. 2006.

[15] W.J. Shiang, D. Cannon, and J. Gorman, "Optimal force distribution applied to a robotic crane with flexible cables", *Proc IEEE Int Conf Rob Autom*, San Francisco, CA, pp. 1948-1954, Apr. 2000.

[16] S. Tadokoro, S. Nishioka, T. Kimura, M. Hattori, T. Takamori, and K. Maeda, "On fundamental design of wire configurations of wire-driven parallel manipulators with redundancy", *Proceedings of the Japan-USA Symposium on Flexible Automation*, vol. 1, Boston, MA, USA, pp. 151-158, Jul. 1996.

[17] Q. Jiang and V. Kumar, "The Kinematics of 3-D Cable-Towing Systems", *Chapter 6 of the book: 21st Century Kinematics*, Springer, 2012.

[18] Q. Jiang and V. Kumar, "The Inverse Kinematics of Cooperative Transport With Multiple Aerial Robots", *IEEE Trans. Robot.*, vol. 29, no. 1, pp. 136-145, Feb. 2013.

[19] Q. Jiang and V. Kumar, "Determination and Stability Analysis of Equilibrium Configurations of Objects Suspended From Multiple Aerial Robots", *J. Mech. Robot.*, vol. 4, no. 2, pp. 021005-1-21, May 2012.

[20] M. Carricato, "Direct geometrico-static problem of underconstrained cable-driven parallel robots with three cables", *J. Mech. Robot.*, vol. 5, no. 3, pp. 031008-1-10, Aug. 2013.

[21] M. Carricato, "Inverse geometrico-static problem of underconstrained cabled-riven parallel robots with three cables", *J. Mech. Robot.*, vol. 5, no. 3, pp. 031002-1-11, Aug. 2013.

[22] M. Carricato and G. Abbasnejad "Direct Geometrico-Static Analysis of Under-Constrained Cable-Driven Parallel Robots with 4 Cables", Mechanisms and Machine Science, *Cable-Driven Parallel Robots*, Springer-Verlag,vol. 12, pp. 269-285, 2013.

[23] G. Rosati, D. Zanotto, and S.K. Agrawal, "On the design of adaptive cable-driven systems", *J. Mech. Robot.*, vol. 3, no. 2, pp. 021004-1-13, May 2011.

[24] M. Gouttefarde and C.M. Gosselin, "Analysis of the wrench-closure workspace of planar parallel cable-driven mechanisms", *IEEE Trans. Robot. (USA)*, vol. 22, no. 3, pp. 434-445, June 2006.

[25] M. Gouttefarde, J.P. Merlet, and D. Daney, "Wrench-feasible workspace of parallel cable-driven mechanisms", *Proc IEEE Int Conf Rob Autom*, Rome, Italy, pp. 1492-1497, Apr. 2007.

[26] IFToMM Commission A, "Terminology for the Theory of Machines and Mechanisms", *Mech Mach Theory*, vol. 26, no. 5, pp. 435-539, 1991.

[27] S. Hirose, "Connected differential mechanism and its applications", *Proceedings of International Conference on Advanced Robotics*, Tokyo, Japan, pp. 319-325, Sept. 1985.

[28] L. Birglen, T. Laliberte, and C. Gosselin, *Underactuated Robotic Hands*, New York, Springer-Verlag, vol. 40, 2008.

[29] L. Birglen and C.M. Gosselin, "Kinetostatic analysis of underactuated fingers", *IEEE Trans. Robot. Autom. (USA)*, vol. 20, no. 2, pp. 211-221, Apr. 2004.

[30] L. Birglen and C.M. Gosselin, "On the force capability of underactuated fingers", *Proc IEEE Int Conf Rob Autom*, Taipei, Taiwan, pp. 1139-1145, Sept. 2003.

[31] L. Birglen and C.M. Gosselin, "Force analysis of connected differential mechanisms: Application to grasping", *Int J Rob Res*, vol. 25, no. 10, pp. 1033-1046, Oct. 2006.

[32] R. Ozawa, K. Hashirii, and H. Kobayashi, "Design and Control of Underactuated Tendon-Driven Mechanisms", *Proc IEEE Int Conf Rob Autom*, Kobe, Japan, pp. 287-292, May 2009.

[33] S. Krut, V. Begoc, E. Dombre, and F. Pierrot, "Extension of the form-closure property to underactuated hands", *IEEE Trans. Rob.*, vol. 26, no. 5, pp. 853-866, Oct. 2010.

[34] S. Krut, "A Force-Isotropic Underactuated Finger", *Proc IEEE Int Conf Rob Autom*, Barcelona, Spain, pp. 2314- 2319, Apr. 2005.

[35] J. Penaud, D. Alazard, and A. Amiez, "Kinematic analysis of spatial geared mechanisms", *J Mech Des, Trans ASME*, vol. 134, no. 2, pp. 021009(1-6), Feb. 2012.

[36] C. Xiao An and C. Hong, "Analytical geometry method of planetary gear trains", *Sci. China Ser. E, Technol. Sci. (Netherlands)*, vol. 55, no. 4, pp. 1007-1021, Apr. 2012.

[37] D. Gross, W. Hauger, J. Schröder, W.A. Wall, and N. Rajapakse, *Engineering Mechanics 1: Statics*, New York, Springer, 2009.

CHAPTER 6

ARTICLE 2: ANALYSIS AND OPTIMIZATION OF A NEW DIFFERENTIALLY-DRIVEN CABLE PARALLEL ROBOT

Hamed Khakpour [a], Lionel Birglen [a], Souheil-Antoine Tahan [b]

[a] *Mechanical Engineering Department, Ecole Polytechnique de Montreal, Montreal, QC, CANADA, H3T 1J4*

[b] *Mechanical Engineering Department, Ecole de technologie superieure, Montreal, QC, CANADA, H3C 1K3*

6.1 Abstract

In this paper, a new 3-DOF differentially-actuated cable parallel robot is proposed. This mechanism has a hybrid architecture and is driven by a prismatic actuator and three cable differentials. Through this design, the idea of using differentials in the structure of a spatial cable robot is investigated and their differences with architectures using individually-actuated cables are specified. Considering their particular properties, the kinematic analysis of the robot and the relationship between the actuation forces and the external wrench are presented. Then, two indices are defined to evaluate the wrench closure and wrench feasible workspaces of the robot. Using these indices, the robot is subsequently optimized. Finally, the performance of the optimized differentially-driven robot is compared with fully-actuated mechanisms. The results show that through a proper design methodology, the robot can have a larger workspace and better performance using differentials than fully-driven cable robots using the same number of actuators.

Keywords: *cable robot, differential mechanism, kinematic analysis, workspace, optimization.*

6.2 Introduction

Due to the higher dexterity, larger payload and greater precision of parallel robots over common serial architectures, an abundant range of literature can be found dedicated to this class of robotic manipulators and many industrial applications are now common. These mechanisms are mainly categorized as either cable-driven or linkage-driven parallel robots [1]. Cable-driven manipulators are a particular class of parallel mechanisms where the moving platform (MP) is connected to the base platform (BP) through a set of cables [2].

Compared to linkage-driven designs, cable robots are usually less expensive, simpler, lighter, have low friction/inertia, and larger workspace [3–8]. Because of these properties, they can be used in areas where a dexterous machine with a very large reachable workspace is demanded [9]. Several cable robots are now commercialized and used in many fields (e.g., the ultrahigh speed robot Falcon [10], Skycam [11], NIST Robocrane [12], and Cablecam [13]). On the other hand, they suffer from the unilateral and limited force in the cables, are prone to vibrations, and the possibility of interferences among cables. These issues can weaken their capability to be used in some applications [4, 5, 9].

Since cables are flexible, they can only sustain tension but not compression [9]. Thus, n-DOF cable-driven robots should have at least $n+1$ cables to fully constrain and manipulate the MP [3, 10, 14]. It should be noted that, using more cables, one can expect better performance and larger workspace for these mechanisms as reported in the literature [7, 9]. The unilateral nature of cables also leads to some major differences between the criteria considered in the analysis of cable-

driven and linkage-driven robots. One of them is the method of calculation of their workspaces [1, 5, 7, 9].

Previously, different properties of cable-driven mechanisms such as wrench closure and wrench feasible workspaces (WCW & WFW), arrangement and interference of cables were at the center of attention of many research initiatives. For instance, Pusey et al. [1] presented an incompletely restrained 6-6 cable-suspended robot and considered the global dexterity as an index (GDI) to optimize its workspace. Later, Fattah and Agrawal [9] proposed a similar analysis for the optimal design of a cable-suspended planar robot, in which the GDI and the area of the workspace were used as indices to optimize the number of cables, size and geometry of the MP. Shiang et al. [15] analyzed the kinematic properties of a 3-DOF cable-suspended crane. In this study, the flexibility of cables was considered to obtain the equations of motion. Gouttefarde and Gosselin [8] developed an algorithm to find the wrench-closure and reachable workspaces of a planar cable robot. For this, several theorems were presented to define the WCW of this type of robot.

Also, Bouchard and Gosselin [2] introduced a geometrical approach to investigate the wrench-feasible (WF) property of cable robots with two to six DOFs. Mao and Agrawal [16] designed and manufactured a new 5-DOF cable-driven rehabilitation mechanism with adjustable cable connection points which has a light and compact structure. The workspace of this device was improved by optimizing the locations of the attachment points of all cables.

With all these robots, an actuation redundancy is necessary which significantly increases the cost and makes it harder to control the robots. In general, since the performances of these mechanisms are improved by employing more cables, these drawbacks become a painful burden. To overcome this issue, in this paper, a new 3-DOF cable-driven mechanism is proposed in which the MP is manipulated by three differentials instead of a set of independently actuated cables. The idea of using cable differentials in the structure of a planar cable robot was presented and investigated by the authors in [17]. In this paper, their impact on the performance of a spatial architecture is analyzed. The differentials considered in this paper are composed of two cables simultaneously driven by a single actuator through a differential mechanism. As described in [17] for planar cases, this technique can be generalized by using diverse numbers of cables with different arrangements while few actuators are considered. Through the comparison of this differentially-driven mechanism with fully actuated solutions the authors reveal that by using differentials in the structure of this robot, its performances are improved.

6.3 A New Differentially-driven Cable Robot

Differentials are widely used in many mechanical devices to resolve an actuation source into two outputs or combine two inputs into a single output. By definition, they have two degrees of
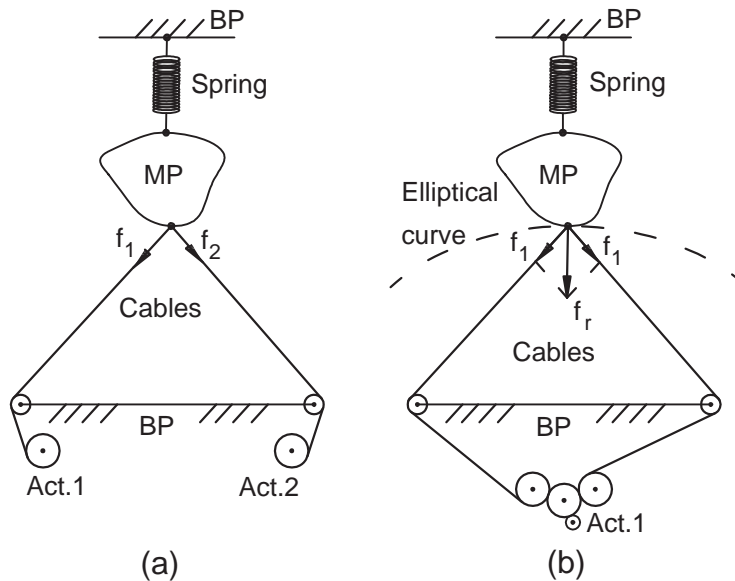
Figure 6.1 Planar cable mechanisms actuated by (a) two independent cables; (b) two cables driven by a differential

freedom [18, 19]. Thus, to produce more outputs, they have to be connected together for instance in serial or parallel patterns [19]. Commonly used examples of these mechanisms are bevel gear differentials, planetary gear differential, seesaw mechanisms, and tendon-pulley arrangements [20].

To illustrate the difference between differentially actuated cables and independently driven ones, two planar cable mechanisms shown in Fig. 6.1 can be compared. In Fig. 6.1 (a), a pair of cables connecting the MP to the BP are controlled by two distinct actuators (the spring is only used to maintain the tension force in the cables). In this example, the cables and spring constrain the position of the MP. On the other hand, the cables of the differential system depicted in Fig. 6.1 (b) have dependent forces (with ideally equal magnitude). Thus, their resultant force lies on a particular line (ideally again, on the bisector of the two cables) and they can constrain the MP only in one direction. Consequently, the MP can move on a direction normal to this force. Therefore, if the actuator is locked, the attachment point of the cables on the MP will define an elliptical curve.

This property can be beneficial because, as illustrated in Fig. 6.2, the direction of the resultant force is always normal to the curve of an imaginary ellipse. When the attachments point of the cables on the MP lies on point A (equidistant of points S_1 and S_2), the direction of this force passes though the midpoint of line S_1S_2. Then, this system acts as a single cable connected at points A and D. On the other hand, if this attachment point moves away from point A (e.g., towards points B or C), the bisector of the two cables crosses the line S_1S_2 at points different than the midpoint D (e.g., points E or F). This gives a unique property to differentials when they are used in the structure of
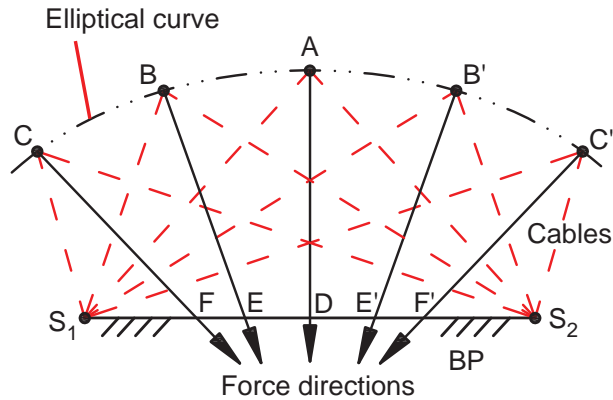
Figure 6.2 Direction of resultant force of the two cables of a differential when its actuator is locked
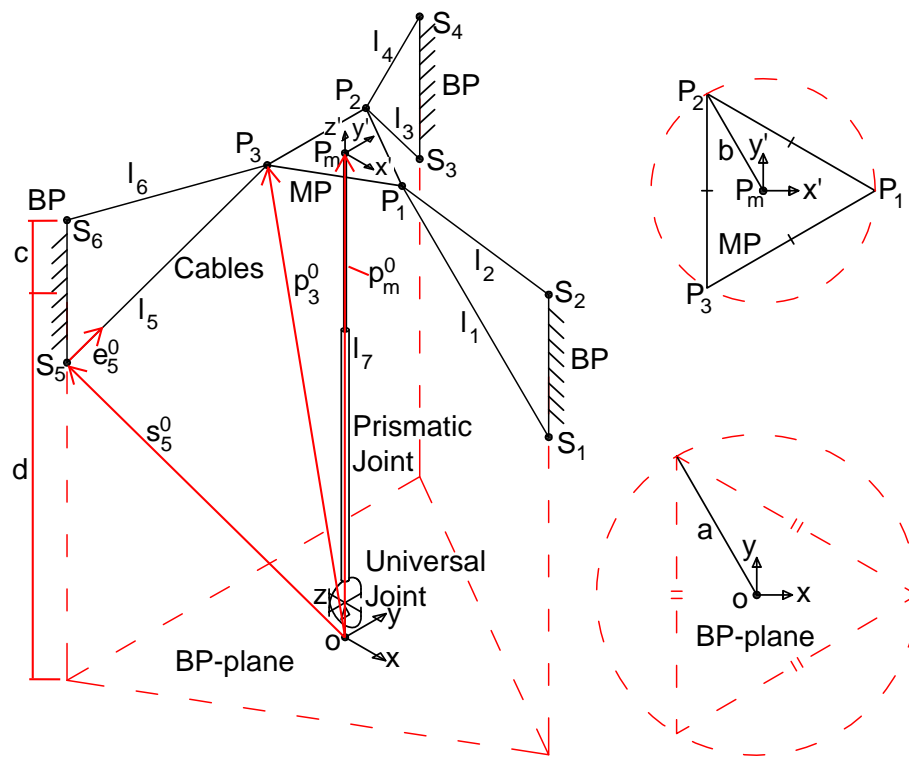
Figure 6.3 Schematic of the proposed 3-DOF differential cable-driven robot

a cable driven robot, namely to have variable virtual attachment points on the BP.

The objective in designing a differentially-driven cable robot is to use differentially-driven cables in its architecture to fully constrain its MP while the number of the actuators is kept at minimum and more cables are used. In the presented mechanism, an actuated prismatic joint similar
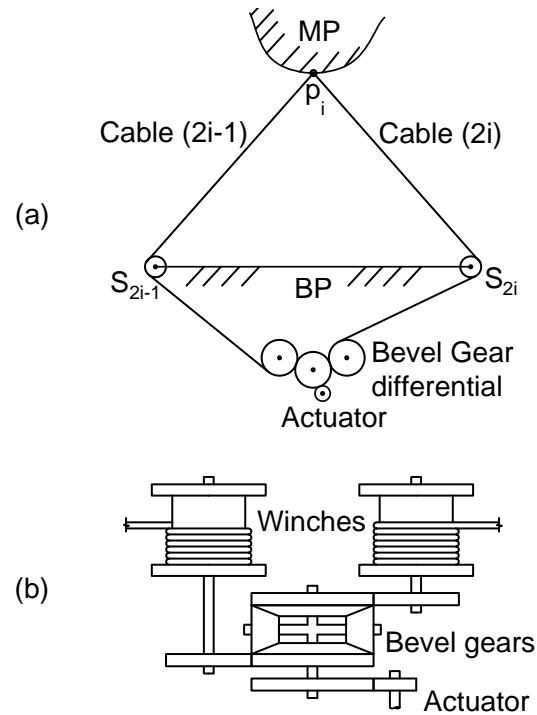
Figure 6.4 Schematic of: (a) a differentially actuated cable system; (b) a typical bevel gear actuated differential

to the one presented in [21] is used to increase the stiffness of the robot and maintain the cable tensions. As illustrated in Fig. 6.3, this robot is cylindrically symmetric and the prismatic joint is connected to the BP through a passive universal joint. It is then rigidly connected to the MP in order for this robot to have 3-DOF. The cables of the three differentials are connecting the three vertices of the triangular MP to the virtual cylindrical surface on the BP along three lines parallel to the axis of this cylinder. Consequently, the robot has four actuators (three in the differentials and one in the prismatic joint) and is overconstrained.

In this robot, there are seven connections between the MP and the BP, namely a prismatic joint and six cables. These cables are driven by three differentials embedded in the BP at points $S_1 - S_2$, $S_3 - S_4$, and $S_5 - S_6$, so that point P_i is connected to points S_{2i-1} and S_{2i} via the cables $2i - 1$ and $2i$. Note that the reason to select these pairs of cables to be differentially driven is to maximize certain characteristics (which will be specified later) related to the performance of this robot. Nevertheless, other pair of cables can also be chosen but the resulting performance would be actually weakened. The schematics of one of these three identical single differentials and its bevel gear mechanism are illustrated in Fig. 6.4. As can be seen in this figure, each differential has a single actuator installed in the BP and drives the two cables through a bevel gear differential mechanism while the other sides of the cables are attached to the MP. These three mechanisms are here referred to as
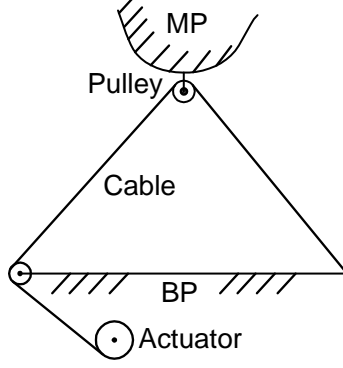
Figure 6.5 Typical differential made of a cable and pulley system

$S_1 - P_1 - S_2$, $S_3 - P_2 - S_4$, and $S_5 - P_3 - S_6$.

It should be noted that, the introduced differential can also be replaced by other types of differentials. For example, a cable and pulley system can be used instead of the bevel gear differential in order for the cable to be attached to the BP at one end, passed through a pulley (which is attached to the MP), and then, connected to an actuator in the BP at its other end as illustrated in Fig. 6.5. In this case, the actuator just produces the tension of one side of the cable. But, due to the friction in the pulley, the tension of the cable is not equal in its two branches and therefore, the resultant force may not lay on the bisector of the two cables. Thus, from a kinematic point of view, this design yields uncertain practical performances and consequently, is not considered in this paper.

6.4 Kinematic Analysis of the robot

6.4.1 Direct and inverse kinematic problems

The first step in the analysis of the robot is to solve its direct and inverse kinematic problems (DKP & IKP). For this, the position vectors of the attachment points of the cables on the BP with respect to the inertial frame (centered in O, cf. Fig. 6.3), $\mathbf{s}_j^0$ for $j = 1, \cdots, 6$, and on the MP with respect to the local frame (centered in P_m, cf. Fig. 6.3), $\mathbf{p}_i^m$ for $i = 1, 2, 3$, are considered. Then, the positions of points P_i^0 with respect to the inertial frame are found as:

$$\mathbf{p}_i^0 = \mathbf{R}_m^0 \mathbf{p}_i^m + \mathbf{p}_m^0 \quad \text{for } i = 1, 2, 3, \tag{6.1}$$

where $\mathbf{p}_m^0 = [x, y, z]$ is the position vector of the center of the MP and $\mathbf{R}_m^0$ is the rotation matrix of the later expressed as $\mathbf{R}_m^0 = \mathbf{R}_x(\theta_1)\mathbf{R}_y(\theta_2)$, where $\mathbf{R}_x(\theta_1)$ and $\mathbf{R}_y(\theta_2)$ are respectively the rotation matrix around the x-axis of the inertial frame with an angle θ_1, and then, around the y-axis, with an angle θ_2, of the resulting frame attached to the universal joint.

By considering $\mathbf{e}_j$ for $j=1,\cdots,6$ as unit vectors along the cables from S_j to P_i defined in the inertial frame, and also knowing the position vector $\mathbf{p}_m^0$, the IKP is solved as:

$$\theta_1 = -atan2(z,y) \quad \text{where} \quad \theta_1 \in [-\pi, \pi], \tag{6.2a}$$

$$\theta_2 = \arcsin(\frac{x}{l_7}) \quad \text{where} \quad \theta_2 \in [-\frac{\pi}{2}, \frac{\pi}{2}], \tag{6.2b}$$

$$l_j = \left\| \mathbf{s}_j^0 - \mathbf{p}_i^0 \right\| \text{ for } \begin{cases} j=1, 2 \text{ if } i=1 \\ j=3, 4 \text{ if } i=2 \text{ and } l_7 = \left\| \mathbf{p}_m^0 \right\|, \\ j=5, 6 \text{ if } i=3 \end{cases} \tag{6.2c}$$

$$l_{a1} = l_1 + l_2, \quad l_{a2} = l_3 + l_4, \quad l_{a3} = l_5 + l_6, \tag{6.2d}$$

where l_7 is the length of the prismatic joint, l_j for $j=1,\cdots,6$ is the length of the jth cable and l_{ai} for $i=1, 2, 3$ is the total length of the cables driven by the ith differential.

In the DKP, the total length of the cables of the differentials, l_{ai}, and the prismatic joint, l_7 are known and the position and orientation of the MP should be found. Since the robot is overconstrained, the DKP is defined by an over-determined system of equations. To solve this problem a numerical method such as a gradient descend method can be used.

6.4.2 Direct and inverse velocity problems

To obtain the relationships between the twist of the MP and the actuated joint rates, the Jacobian matrix of the robot must be defined. This matrix can be readily obtained by taking the derivatives of the position vectors $\mathbf{p}_i^0$. Knowing the twist of the MP at the point P_m, the inverse velocity problem (IVP) of this mechanism is solved as:

$$\begin{bmatrix} \dot{l}_1 \\ \dot{l}_2 \\ \dot{l}_3 \\ \dot{l}_4 \\ \dot{l}_5 \\ \dot{l}_6 \\ \dot{l}_7 \end{bmatrix} = \begin{bmatrix} \mathbf{e}_1^T & (\mathbf{p}_1^0 \times \mathbf{e}_1)^T \\ \mathbf{e}_2^T & (\mathbf{p}_1^0 \times \mathbf{e}_2)^T \\ \mathbf{e}_3^T & (\mathbf{p}_2^0 \times \mathbf{e}_3)^T \\ \mathbf{e}_4^T & (\mathbf{p}_2^0 \times \mathbf{e}_4)^T \\ \mathbf{e}_5^T & (\mathbf{p}_3^0 \times \mathbf{e}_5)^T \\ \mathbf{e}_6^T & (\mathbf{p}_3^0 \times \mathbf{e}_6)^T \\ \mathbf{e}_7^T & \mathbf{0}_{1 \times 3} \end{bmatrix} \begin{bmatrix} \mathbf{v}^{\|} \\ \omega \end{bmatrix} \leftrightarrow \dot{\mathbf{l}} = \mathbf{J}\mathbf{t}, \tag{6.3}$$

where $\dot{l}_j$ for $j=1,\cdots,7$ are the length change rates of the six cables and the prismatic joint; $\dot{\mathbf{l}}$ and $\mathbf{t}$ are respectively the vectors of the joint rates and the twist; $\mathbf{v}$ and ω are respectively the linear and angular velocity vectors of the MP at the point P_m and $\mathbf{v}^{\|} = \mathbf{e}_7 \mathbf{e}_7^T \mathbf{v}$. Since the robot only has 3 DOF, the vectors $\mathbf{v}$ and ω are related. To find this, by projecting the vector $\mathbf{v}$ onto a plane with

normal of $\mathbf{e}_7$ and calculating the derivative of position vector $\mathbf{p}_m = l_7\mathbf{e}_7$, the passive joint rates (in the universal joint) are obtained as:

$$\dot{\theta}_1 = \frac{\frac{-v_y^{\perp}}{l_7} + \dot{\theta}_2 s_{\theta_1} s_{\theta_2}}{c_{\theta_1} c_{\theta_2}} \quad \text{and} \quad \dot{\theta}_2 = \frac{v_x^{\perp}}{l_7 c_{\theta_2}}, \tag{6.4}$$

where $v_x^{\perp}$ and $v_y^{\perp}$ respectively denote x and y components of the vector $\mathbf{v}^{\perp} = (\mathbf{I}_{3\times3} - \mathbf{e}_7\mathbf{e}_7^T)\mathbf{v}$. Next, the angular velocity is found as:

$$\omega = \begin{bmatrix} \dot{\theta}_1 \\ \dot{\theta}_2 c_{\theta_1} \\ \dot{\theta}_2 s_{\theta_1} \end{bmatrix}. \tag{6.5}$$

The linear velocities of the actuators of the differentials (i.e., the displacement rates of the two cables of each differential) are then found as $\dot{\mathbf{l}}_a = \mathbf{T}\dot{\mathbf{l}}$ where $\dot{\mathbf{l}}_a = [\dot{l}_{a1} \ \dot{l}_{a2} \ \dot{l}_{a3} \ \dot{l}_7]^T$ is the vector of actuation rates and matrix $\mathbf{T}$ is found from Eq. (6.2d) as:

$$\mathbf{T} = \begin{bmatrix} 1 & 1 & 0 & 0 & 0 & 0 & 0 \\ 0 & 0 & 1 & 1 & 0 & 0 & 0 \\ 0 & 0 & 0 & 0 & 1 & 1 & 0 \\ 0 & 0 & 0 & 0 & 0 & 0 & 1 \end{bmatrix}. \tag{6.6}$$

Finally, the IVP can be solved as:

$$\begin{bmatrix} \dot{l}_{a1} \\ \dot{l}_{a2} \\ \dot{l}_{a3} \\ \dot{l}_7 \end{bmatrix} = \begin{bmatrix} \mathbf{e}_1^T + \mathbf{e}_2^T & (\mathbf{p}_1^0 \times (\mathbf{e}_1 + \mathbf{e}_2))^T \\ \mathbf{e}_3^T + \mathbf{e}_4^T & (\mathbf{p}_2^0 \times (\mathbf{e}_3 + \mathbf{e}_4))^T \\ \mathbf{e}_5^T + \mathbf{e}_6^T & (\mathbf{p}_3^0 \times (\mathbf{e}_5 + \mathbf{e}_6))^T \\ \mathbf{e}_7^T & \mathbf{0}_{1\times3} \end{bmatrix} \begin{bmatrix} \mathbf{v}^{\parallel} \\ \omega \end{bmatrix}. \tag{6.7}$$

The first matrix in the right hand side of Eq. (6.7) is referred to as a modified Jacobian, $\mathbf{J}_m$, particular to the proposed differential cable-driven robot.

The direct velocity problem (DVP) aims at finding the twist of the MP when the joint rates are known. Considering Eqs. (6.4), (6.5) and (6.7) and knowing the configuration of the robot, there are four equations and three unknowns (i.e., the components of $\mathbf{v}$). Therefore, if one of these equations is dependent to the others then there is a solution, otherwise, that vector of joint rates $\dot{\mathbf{l}}$ is deemed not feasible.

6.4.3 Actuation forces and output wrench relationships

The tension matrix of a cable robot is defined as $\mathbf{A} = \mathbf{J}^T$ [9]. Using the principle of virtual work the relationship between the forces in the cables and the prismatic joint of the robot and the corresponding wrench at its MP is:

$$\mathbf{A}\mathbf{f} = \mathbf{w}, \tag{6.8}$$

where $\mathbf{f}$ and $\mathbf{w}$ are respectively the vectors describing the tension forces and the wrench. They are defined as:

$$\mathbf{f} = \begin{bmatrix} t_1 & t_2 & t_3 & t_4 & t_5 & t_6 & t_7 \end{bmatrix}^T \text{ and } \mathbf{w} = \begin{bmatrix} \mathbf{f}_w^T & \mathbf{n}_w^T \end{bmatrix}^T, \tag{6.9}$$

where t_j for $j = 1, \cdots, 6$ is the magnitude of the force in the jth cable and t_7 is the magnitude of the force in the prismatic joint. Also, $\mathbf{f}_w$ and $\mathbf{n}_w$ are respectively the vectors of force and torque exerted to the MP at the point P_m. In a frictionless ideal case, the bevel gear system can produce equal tensions on both cables in each differential, i.e., $t_1 = t_2$, $t_3 = t_4$ and $t_5 = t_6$. Consequently, vector $\mathbf{f}$ can be changed to $\mathbf{f} = \begin{bmatrix} t_1 & t_1 & t_3 & t_3 & t_5 & t_5 & t_7 \end{bmatrix}^T$.

The total torque to be generated by the actuators of the differentials are $\tau_{a1} = 2r_g t_1$, $\tau_{a2} = 2r_g t_3$, and $\tau_{a3} = 2r_g t_5$ where r_g is the gear ratio. Additionally, with this robot, the resultant force of the cables of each differential is considered to characterize its performance. Therefore, similar to the velocity problem and using the modified Jacobian, Eq. (6.8) is changed to:

$$\mathbf{A}_m \mathbf{f}_m = \mathbf{w}, \tag{6.10}$$

where $\mathbf{A}_m = \mathbf{J}_m^T$ and $\mathbf{f}_m = [t_1 \ t_3 \ t_5 \ t_7]^T$. This robot is a 3-DOF mechanism (with two rotations and one translation) and works in a three dimensional space. On the other hand, an external wrench imposed to this robot as well as the resultant force and torque generated by the three differentials and the prismatic joint can have arbitrary directions. Indeed, considering the constraint exerted by the universal joint to the MP, the wrench that should be resisted by the actuators is limited to a force in the direction of $\mathbf{e}_7$ and a torque on a plane created by two cross axes of the universal joint with a normal defined as $\mathbf{e}_U = \begin{bmatrix} 0 & -s\theta_1 & c\theta_1 \end{bmatrix}^T$ [22]. Therefore, to eliminate the components of the force and torque vectors which are passively resisted by the universal joint not the actuators, they are projected to the relevant directions using the matrix $\mathbf{C}$ defined as:

$$\mathbf{C} = \begin{bmatrix} \mathbf{e}_7 \mathbf{e}_7^T & \mathbf{0}_{3 \times 3} \\ \mathbf{0}_{3 \times 3} & \mathbf{I}_{3 \times 3} - \mathbf{e}_U \mathbf{e}_U^T \end{bmatrix}_{6 \times 6}. \tag{6.11}$$

Then, if the vector $\mathbf{f}_m$ is known, by using the matrix $\mathbf{C}$, the left hand side of Eq. (6.10) is projected onto the specific directions so that the vector $\mathbf{w}$ which is not compensated by the passive

reaction of the universal joint is found as:

$$\mathbf{CA}_m\mathbf{f}_m = \mathbf{w}. \tag{6.12}$$

On the other hand, if an arbitrary external wrench vector, $\mathbf{w}_a$, is exerted to the MP and the vector $\mathbf{f}_m$ is to be found, this wrench should be first mapped into the directions controlled by the actuators, namely:

$$\mathbf{A}_m\mathbf{f}_m = \mathbf{Cw}_a. \tag{6.13}$$

In Eqs. (6.12) and (6.13), the projection matrix $\mathbf{C}$ is used to take into account the components of the vectors of these equations in the actuated directions. Thus, one cannot compute any of these equations from the other. Any vector which has the same component in these directions would be a possible solution for these equations (either the generated wrench on the MP on the right hand side of Eq. (6.12) or the cable tensions in the left hand side of Eq. (6.13)). The other components of these vectors are resisted by the passive support of the robot.

Finding the resultant wrench using Eq. (6.12) is straightforward while in Eq. (6.13), there appears to be six equations and four variables. However, due to the constraints of the robot, there are only three independent equations. Therefore, this is an underdetermined system of equations. To solve this problem the WF condition is used. In this approach, it is assumed that one of the variables is known. Then, the three other variables are parametrically calculated. Next, the minimal and maximal allowed tensions in the cables are considered so that the minimum value is set for a cable which has the lowest tension while the tensions of the others should not exceed the maximum value. If such a force vector $\mathbf{f}_m$ is found, then, that wrench can be resisted by this robot.

The support of the robot (constituted by the universal joint) must be able to resist all the forces and torques applied by the actuators as well as an external wrench. To calculate this, it is assumed that an arbitrary wrench $\mathbf{w}_a$ is exerted to the MP and the actuation force vector $\mathbf{f}_m$ is found from Eq. (6.13). Then, the wrench imposed to the support is found as:

$$\mathbf{w}_s = \mathbf{C}'(\mathbf{w}_a - \mathbf{A}_m\mathbf{f}_m) + \begin{bmatrix} t_7\mathbf{e}_7 \\ \mathbf{0}_{3\times 1} \end{bmatrix}. \tag{6.14}$$

The support wrench vector $\mathbf{w}_s$ and the projection matrix $\mathbf{C}'$ are defined as:

$$\mathbf{w}_s = \begin{bmatrix} \mathbf{f}_s^T & \mathbf{n}_s^T \end{bmatrix}^T, \tag{6.15}$$

$$\mathbf{C}' = \begin{bmatrix} \mathbf{I}_{3\times 3} & \mathbf{0}_{3\times 3} \\ \mathbf{0}_{3\times 3} & \mathbf{e}_U\mathbf{e}_U^T \end{bmatrix}_{6\times 6}, \tag{6.16}$$

where $\mathbf{f}_s$ and $\mathbf{n}_s$ are respectively the vectors of resultant force and torque exerted to the support of the robot.

6.4.4   Workspace of the robot

Usually in the literature, two types of workspaces are defined for a cable-driven robot i.e., the WCW and WFW [5]. The WCW is a volume where the MP of the robot can be located and regardless of the exerted wrench, all its cables are in tension. The WFW is a subset of WCW where all cable tensions are within a specified range.

To find the WCW of the proposed robot, the distribution of the forces and torques produced by the actuators onto its MP must be investigated. These force/torque vectors should be able to span all directions in the considered n-D force/torque workspace to be able to produce any arbitrary wrench. To evaluate this for the forces, the unit vectors along the resultant force vector created by each differential at the MP and the prismatic joint (which can be either under compression or tension) are used to define a convex polyhedron. The starting points of these vectors are attached to the origin of the force workspace and their end points define the vertices of this polyhedron. Then, all these vertices are mapped onto a line which passes through the origin of this space and is parallel to $\mathbf{e}_7$ (i.e. $\mathfrak{R}^3 \to \mathfrak{R}^1$). If the origin is located between the two projected vertices most far apart, then, the robot can generate any arbitrary force along $\mathbf{e}_7$ in that specific configuration. The four unit vectors are:

$$\mathbf{u}_i = -\frac{\mathbf{e}_{2i-1}+\mathbf{e}_{2i}}{\|\mathbf{e}_{2i-1}+\mathbf{e}_{2i}\|} \text{ for } i=1,\, 2,\, 3 \text{ and } \mathbf{u}_4 = \beta\mathbf{e}_7, \tag{6.17}$$

where $\beta = -1$ or 1 depending on the direction of the force in the prismatic joint for each configuration of the robot. In the same way, by considering the unit vectors along the resultant torque vectors of the differentials (the prismatic joint cannot exert any torque on the MP) and projecting them onto a plane with normal $\mathbf{e}_U$, the wrench closure (WC) condition can be investigated for the torques. The unit vectors are defined by:

$$\mathbf{v}_i = \frac{\mathbf{p}_i^0 \times \mathbf{e}_{2i-1}+\mathbf{p}_i^0 \times \mathbf{e}_{2i}}{\|\mathbf{p}_i^0 \times \mathbf{e}_{2i-1}+\mathbf{p}_i^0 \times \mathbf{e}_{2i}\|} \quad \text{for } i=1,\, 2,\, 3. \tag{6.18}$$

To check the WC condition for the forces in each pose of the robot, first the vectors $\mathbf{u}_i' = \mathbf{e}_7\mathbf{e}_7^T\mathbf{u}_i$ for $i=1,\cdots,4$ are obtained. Then, the dot products $h_i = \mathbf{e}_7^T\mathbf{u}_i'$ for $i=1,\cdots,4$ are calculated. Next, if there is at least one change in the sign of h_i then, the force-closure condition is satisfied. For the torques, first, the mapped vectors $\mathbf{v}_i' = (\mathbf{I}_{3\times3} - \mathbf{e}_U\mathbf{e}_U^T)\mathbf{v}_i$ are computed. Afterwards, a procedure similar to the one introduced in [5] is used. Namely, the cross product of the unit vectors $\mathbf{v}_i'$ are obtained as $\mathbf{m}_{ij} = \mathbf{v}_i' \times \mathbf{v}_j'$ for $i,j = 1,\, 2,\, 3$ and $i \neq j$. Then, $k_{ij} = \mathbf{e}_U^T\mathbf{m}_{ij}$ is calculated. Finally, if

for each $\mathbf{m}_{ij}$ there is at least one change in the sign of k_{ij}, then, this condition is satisfied and if this happens simultaneously for both the force and torque vectors, that configuration belongs to the WCW of this robot.

To obtain the WFW, a geometrical method similar to the one proposed in [2] is used. This procedure is again implemented separately for the force and the torque vectors. For the force analysis, the tensions of all cables are desired to be between t_{min} and t_{max}. Then, vectors $\Delta \mathbf{t}_i = -(t_{max} - t_{min})(\mathbf{e}_{2i-1} + \mathbf{e}_{2i})$ for $i = 1, 2, 3$ and $\Delta \mathbf{t}_4 = \beta(t'_{max} - t'_{min})\mathbf{e}_7$ are considered respectively for the three differentials and the prismatic joint. Afterwards, similarly to the vectors $\mathbf{u}_i$, the vectors $\Delta \mathbf{t}_i$ are projected onto the direction of the vector $\mathbf{e}_7$ as $\Delta \mathbf{t}'_i = \mathbf{e}_7 \mathbf{e}_7^T \Delta \mathbf{t}_i$ for $i = 1, \cdots, 4$. Next, these vectors are used to generate a zonotope (a convex polytope with parallel edges [2]) which here is turned to a line segment and is used to calculate the WFW of the robot.

To produce this zone, first, the vectors $\Delta \mathbf{t}'_i$ for $i = 1, \cdots, 4$ are considered as a set of line segments. Next, their Minkowski sum [2] is calculated. Then, the vectors $\mathbf{t}_{imin} = -t_{min}(\mathbf{e}_{2i-1} + \mathbf{e}_{2i})$ for $i = 1, 2, 3$ and $\mathbf{t}_{4min} = \beta t'_{min} \mathbf{e}_7$ are used to modify the zonotope and obtain its final shape. The zone inside this polytope is found as [2]:

$$Z_f = \alpha_1 \Delta \mathbf{t}'_1 \oplus \alpha_2 \Delta \mathbf{t}'_2 \oplus \cdots \oplus \alpha_4 \Delta \mathbf{t}'_4 + \sum_{i=1}^{4} \mathbf{e}_7 \mathbf{e}_7^T \mathbf{t}_{imin}, \tag{6.19}$$

where $\alpha_i \in [0, 1]$ for $i = 1, \cdots, 4$, and the symbol $\oplus$ represents the Minkowski sum of line segments. Finally, the magnitude of the largest force vector that can be located in any direction inside this one-dimensional zone while its origin coincides with the origin of the zone, is the magnitude of the maximal allowable force.

A similar procedure is followed to obtain the maximal permissible torque. For this, vectors $\Delta \tau_i = (t_{max} - t_{min})\mathbf{p}_i^0 \times (\mathbf{e}_{2i-1} + \mathbf{e}_{2i})$ for $i = 1, 2, 3$ are calculated and similar to the vectors $\mathbf{v}_i$, they are projected onto a plane with normal $\mathbf{e}_U$ as $\Delta \tau'_i = (\mathbf{I}_{3\times3} - \mathbf{e}_U \mathbf{e}_U^T)\Delta \tau_i$ to create a two dimensional zonotope. At the end, the final location of this geometry is obtained by using the vectors of minimal torques as $\tau_{imin} = t_{min} \mathbf{p}_i^0 \times (\mathbf{e}_{2i-1} + \mathbf{e}_{2i})$ for $i = 1, 2, 3$. This two-dimensional zone is defined by:

$$Z_\tau = \gamma_1 \Delta \tau'_1 \oplus \gamma_2 \Delta \tau'_2 \oplus \gamma_3 \Delta \tau'_3 + \sum_{i=1}^{3} (\mathbf{I}_{3\times3} - \mathbf{e}_U \mathbf{e}_U^T)\tau_{imin}, \tag{6.20}$$

where $\gamma_i \in [0, 1]$ for $i = 1, 2, 3$. Finally, the radius of the largest circle which can be located inside the resultant two dimensional polytope with its center fixed to the origin of the geometry, is the magnitude of the maximum torque that can be resisted by the mechanism. If the maximum magnitude of both force and torque are larger than their specified minimally allowable values, then, that pose belongs to the WFW of the robot. In Fig. 6.6, an example of a three-dimensional zonotope
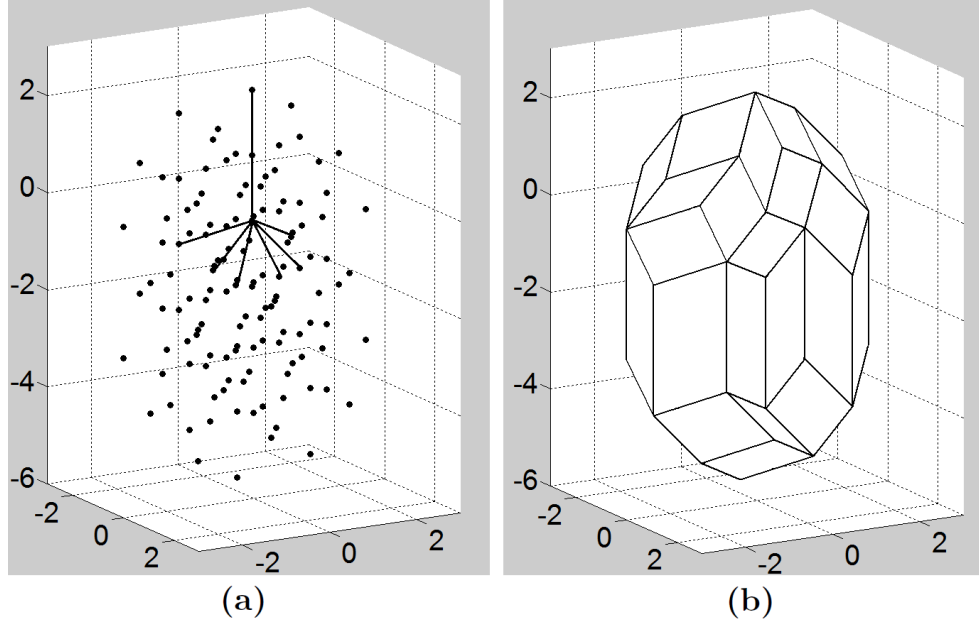
Figure 6.6 (a) Seven line segments representing the base vectors of the zonotope and all nodes created by Minkowski sum of these lines; (b) Zonotope made of the nodes creating the boundary of the zone

created by seven vectors is presented.

6.5   Defining the characteristic indices

The proposed robot is assumed to work in a cylindrical workspace with a radius r_c and a height h_c. As shown in Fig. 6.7, the base of this cylinder is parallel to the BP plane and is located at a distance d_c from it. To optimize the performance of this robot, different aspects of its performance should be measured. In this paper, two measures are taken into account, namely, the size of the WCW and WFW. The investigation of these properties is performed via defining two dimensionless indices.

WCW: evaluated by an index I_{WCW}. This index is defined as the ratio between the volume of the conceptual cylinder and the sum of the volumes of this cylinder and the WCW of the robot, namely:

$$I_{WCW} = \frac{c}{c+q},$$
(6.21)

where c and q are the volume of respectively the cylinder and the WCW.
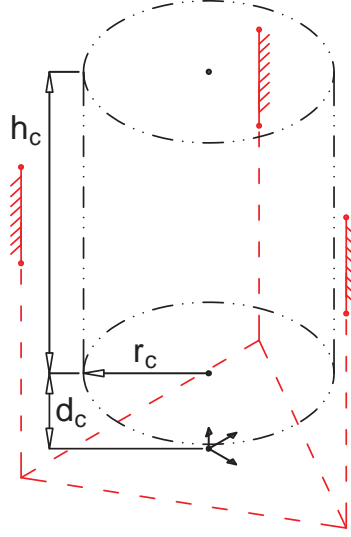
Figure 6.7 Conceptual cylinder representing the volume in which the robot works

WFW: measured by the index I_{WFW} which is defined as:

$$I_{WFW} = \frac{c}{c+m}\left(\frac{f_{min}}{f_{min}+\frac{1}{m}\int_m f_i dv} + \frac{n_{min}}{n_{min}+\frac{1}{m}\int_m n_i dv}\right), \tag{6.22}$$

where m is the volume of the WFW; f_i and n_i are respectively the maximum feasible force and torque for each position of the MP in the WFW; also, f_{min} and n_{min} are respectively the specified minimal amount of force and torque the robot should be able to resist inside its WFW. The terms inside the parentheses in Eq. (6.22) show the normalized ratios between f_{min}/n_{min} and the average values of the maximum feasible force/torque inside the WFW. This index considers both the volume of the WFW and the magnitude of the maximal permissible force and torque for all points in this workspace.

6.6 Optimization and the results

The main objective in the optimization of the robot is to improve the performance of its three differentials to have a larger workspace. For this, the two indices and the conceptual cylinder are used to obtain the best set of design parameters. With this robot, the dimensions of the BP, i.e., a and d are assumed to be fixed while the dimension of the MP and the distance between two points of each differential (i.e. S_{2i-1} and S_{2i} for $i = 1, 2, 3$), respectively b and c are to be found (c.f. Fig. 6.3). Considering the design limits of the robot, two boundaries are considered for these two

Table 6.1 Values of all parameters used in the optimization process

Parameters	Values	Parameters	Values
a	60 cm	t_{min}	10 N
d	90 cm	t_{max}	100 N
r_c	40 cm	t'_{min}	0 N
h_c	120 cm	t'_{max}	600 N
d_c	30 cm	f_{min}	400 N
		n_{min}	90 N.m
a_1	3	Range for b	[5,30] cm
a_2	1	Range for c	[0,60] cm

Table 6.2 Resultants of the optimization process

Variables	Values	Dimensions
c	16.51	cm
b	5.00	cm

goal parameters. In this process, the objective function to be minimized is defined as:

$$F_{GA} = a_1 I_{WCW} + a_2 I_{WFW} \ , \tag{6.23}$$

where a_1 and a_2 are weight coefficients. The input parameters of the optimization procedure re the dimensions of the conceptual cylinder and the BP, the boundaries of the cables tensions and the force in the prismatic joint, and finally the minimum amount of force and torque the robot should resist inside its WFW.

To optimize this robot, a genetic algorithm (GA) which is embedded in a commercial numerical software is used. The chosen values of all input parameters and the boundaries are presented in Table 6.1.

Since the WFW is a subset of the WCW and its volume depends on the minimum permissible force f_{min} and torque n_{min} (which are user defined parameters), with larger WCW the robot has the potential of having bigger WFW. Therefore, in this paper, a larger weight coefficient is considered for the WCW in the objective function.

Considering all these values, a GA with 120 individuals and 100 generations is run. The results of the optimization are presented in Table 6.2 and the schematic of the optimized robot in an arbitrary position inside its workspace is illustrated in Fig. 6.8.

As can be seen in Table 6.2, the GA found the best value for b exactly at the lower boundary.
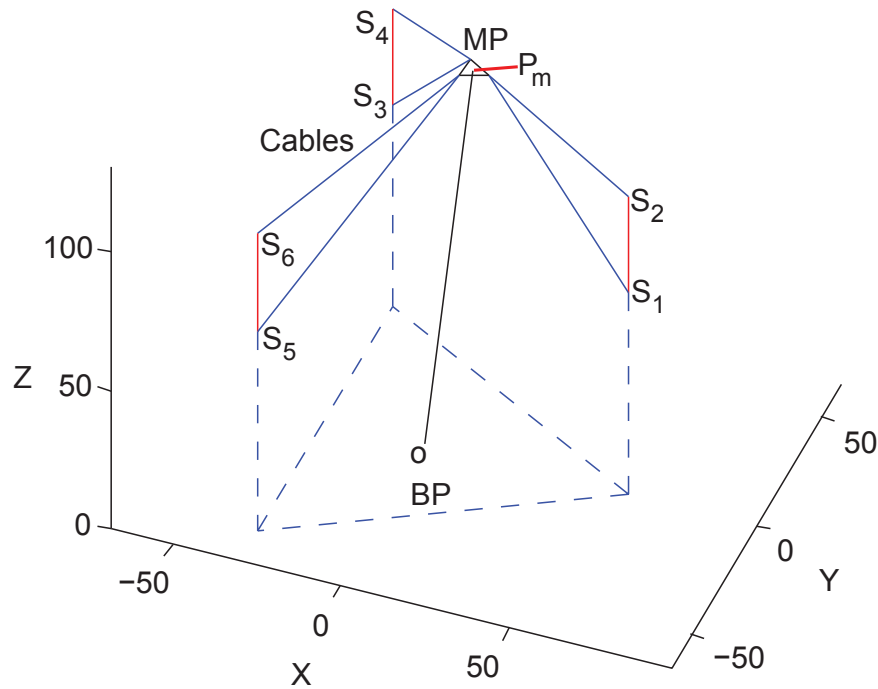
Figure 6.8 Schematic of the optimized robot in an arbitrary location inside its workspace

The same optimization with no boundary for b shows that this value is close to zero which is physically impractical. The reason for this is that in the areas of the cylinder close to each of the differentials, with smaller value of b, there is a smaller angle between the cables of that differential and so these cables can produce larger resultant force. Thus, to get rid of this problem, a lower bound is considered.

Finally, this optimization reveals that the effects of using differential in a cable robot is a trade off between the expansion of the range of changes in the direction of resultant force vector of each differential (which improves both the WCW and the WFW) and the increase of the angle between their cables (which weakens the maximum value of the resultant force and so decreases the WFW).

6.7   Comparing the proposed differential cable robot with two fully actuated ones

In this section, to investigate the effect of using differentials in the structure of a cable robot, the optimized differentially actuated robot, referred to as 6-3-differential (with 6 cables and 3 actuators), is first compared with two fully actuated designs. The first mechanism has an architecture similar to the proposed robot but it is driven by three single cables instead of three differentials. The schematic of this robot which is here referred to as 3-3-full is illustrated in Fig. 6.9. The second fully actuated robot, called 6-6-full, has the same structure as the differential cable robot shown in
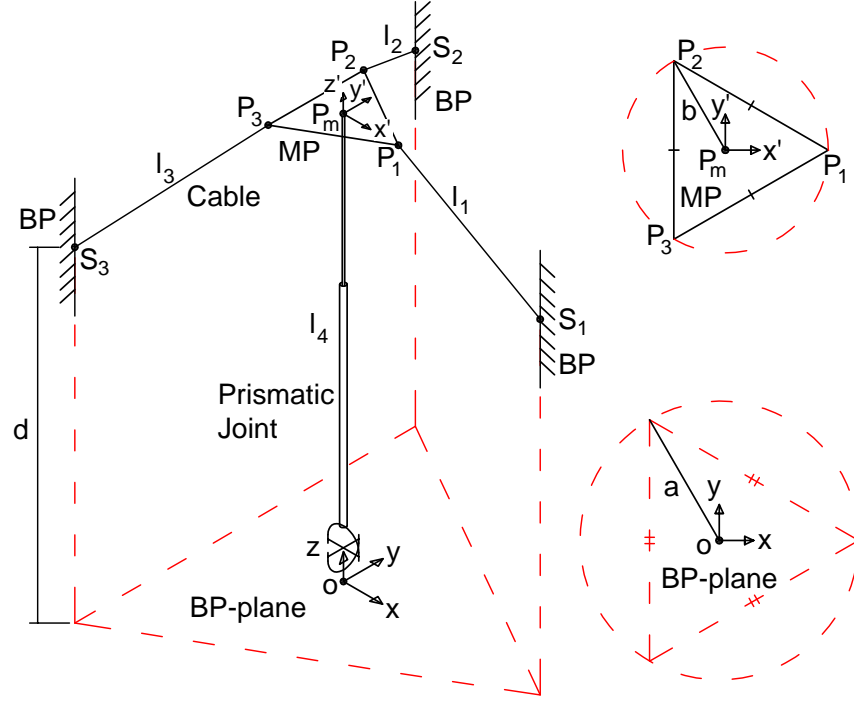
Figure 6.9 Schematic of the 3-3-full cable robot with three independently actuated cables

Fig. 6.3, but all its cables are independently actuated.

This comparison is implemented for the two workspaces (WCW and WFW) of these robots. To do this, by taking the parameters of Tables 6.1 and 6.2 , the indices I_{WCW} and I_{WFW} as well as the ratios between the volumes of these workspaces (i.e. respectively v_{WCW} and v_{WFW}) and the volume of the cylinder v_c are measured and the results are presented in Table 6.3.

As can be seen in this table, with the same values for the design parameters, the two indices of the 6-3-differential cable robot are smaller (i.e. better) than the ones of the 3-3-full mechanism. This means that using differentials, while the number of actuators are kept at minimum (three in this case) one can expect a larger wrench closure and wrench feasible workspaces (which can also be seen as the ratios $\frac{v_{WCW}}{v_c}$ and $\frac{v_{WFW}}{v_c}$ in Table 6.3). This improvement is obtained as a result of two phenomena, i.e.:

1. The capability of using more cables with the same actuator via differentials;

2. The change in the direction of the resultant force of the cables of each differential (c.f. Fig. 6.2).

On the other hand, as one expected, these indices are even smaller with the 6-6-full robot than with the differentially actuated one. This shows that although the same number of cables is used in both architectures, due to the limits in the direction of the resultant force of the differentials, the

Table 6.3 Comparing the performance of differential cable-driven robot with other mechanisms

Robot type	WCW		WFW	
	I_{WCW}	$\frac{v_{WCW}}{v_c}$	I_{WFW}	$\frac{v_{WFW}}{v_c}$
3-3-full cable robot	0.6194	0.6146	2	0
6-3-double cable robot	0.6194	0.6146	0.8473	0.0710
6-3-differential cable robot	0.6157	0.6241	0.8499	0.0705
6-6-full cable robot	0.5855	0.7081	0.8463	0.0731

6-3-differential robot cannot have workspaces as large as the fully actuated one.

Next, a similar comparison is done between the optimized robot and another fully actuated mechanism which is here referred to as 6-3-double cable robot with the same architecture of 3-3-full but with two parallel cables attached to each other (to account for a thicker cable), i.e. $c = 0$. The results of this comparison are shown in Table 6.3. It seems that the optimized robot has a larger WCW but smaller WFW. Because in the 6-3-double mechanism, the angle between two cables is always zero and the magnitude of the resultant force is the scalar sum of the forces of the two cables. Nevertheless, as previously discussed, having greater WCW is more important than having larger WFW. Besides, the concept of using differential can also be valid for 3-3-double cable robot so that by using the cable and pulley differential presented in Fig. 6.5 one can increase the load capacity of the robot while the kinematic properties of the mechanism is the same as the 3-3-full manipulator.

6.8   Conclusions

This paper proposed a new 3-DOF cable parallel robot which is actuated by differentials instead of independent cables. This robot has a hybrid structure in which the MP is driven by four actuators, one is a prismatic joint and three others are connected to three differentials to drive six cables. For this, first the effects of using differentials on the forces exerted by the six cables on the MP were investigated. It was shown that, instead of the force and torque vectors produced by each single cable, the resultant force and torque vectors of the cables of each differential should be used. Next, the kinematic analysis of the robot was presented. Afterwards, to evaluate the two workspaces of the robot, the indices I_{WCW} and I_{WFW} were defined. By implementing the Genetic algorithm method and considering these indices, the performance of the robot was optimized. Then, the workspaces of the optimized differentially-driven robot were compared with the ones of fully

actuated mechanisms. The results showed that through a proper design and using differentials, the robot can have larger WCW and WFW with respect to the mechanism with the same number of actuators driving independent cables.

References

[1] Pusey, J., Fattah, A., Agrawal, S., Messina, E., and Jacoff, A., 2003, "Design and Workspace Analysis of a 6-6 Cable-Suspended Parallel Robot", IEEE Int Conf Intell Rob Syst, Las Vegas, USA, Oct. 27-31, pp. 2090–2095.

[2] Bouchard, S., Gosselin, C.M., and Moore, B., 2010, "On the ability of a cable-driven robot to generate a prescribed set of wrenches", J. Mech. Rob., **2**(1), pp. 011010 (1-10).

[3] Perreault, S. and Gosselin, C.M., 2008, "Cable-driven parallel mechanisms-application to a locomotion interface", J Mech Des, Trans ASME, **130**(10), pp. 1023011–1023018.

[4] Tadokoro, S., Murao, Y., Hiller, M., Murata, R., Kohkawa, H., and Matsushima, T., 2002, "A motion base with 6-DOF by parallel cable drive architecture", IEEE ASME Trans Mechatron, **7**(2), pp. 115–123.

[5] Yang, G., Pham, C.B., and Yeo, S.H., 2006, "Workspace performance optimization of fully restrained cable-driven parallel manipulators", IEEE Int Conf Intell Rob Syst, Beijing, China, Oct. 9-15, pp. 85–90, .

[6] Ferlay, F. and Gosselin, F., 2008, "A new cable-actuated Haptic interface design", Devices and Scenarios - 6th International Conference EuroHaptics, Madrid, Spain, Jun. 10-13, pp. 474–483.

[7] Yang, G., Lin, W., Kurbanhusen, M.S., Pham, C.B., and Yeo, S.H., 2005, "Kinematic Design of a 7-DOF Cable-Driven Humanoid Arm: A Solution-in-nature Approach", IEEE ASME Int Conf Adv Intellig Mechatron AIM, California, USA, Jul. 24-28, pp. 444–449.

[8] Gouttefarde, M. and Gosselin, C.M., 2006, "Analysis of the wrench-closure workspace of planar parallel cable-driven mechanisms", IEEE Trans. Robot., **22**(3), pp. 434–445.

[9] Fattah, A. and Agrawal, S.K., 2005, "On the design of cable-suspended planar parallel robots", J Mech Des, Trans ASME, **127**(5), pp. 1021–1028.

[10] Kawamura, S., Choe, W., Tanaka, S., and Pandian, S.R., 1995, "Development of an ultrahigh speed robot FALCON using wire drive system", Proc IEEE Int Conf Rob Autom, Nagoya, Japan, May 21-27, pp. 215–220.

[11] Brown, G.W., 1984, "Improved suspension system for supporting and conveying equipment, such as a camera", US Patent No. 4 710 819.

[12] Albus, J., Bostelman, R., and Dagalakis, N., 1993, "The NIST ROBOCRANE", J. Robot. Syst., **10**(5), pp. 709–724.

[13] Rodnunsky, J., 2006, "Cabling system and method for facilitating fluid three-dimensional movement of a suspended camera", US Patent No. 7 088 071.

[14] Carricato, M. and Merlet, J.P., 2013, "Stability analysis of underconstrained cable-driven parallel robots", IEEE Trans. Robot., **29**(1), pp. 288–296.

[15] Shiang, W.J., Cannon, D., and Gorman, J., 2000, "Optimal force distribution applied to a robotic crane with flexible cables", Proc IEEE Int Conf Rob Autom, San Francisco, USA, Apr. 24-28, pp. 1948–1954.

[16] Mao, Y. and Agrawal, S.K., 2011, "A cable driven upper arm exoskeleton for upper extremity rehabilitation", Proc IEEE Int Conf Rob Autom, Shanghai, China, May 9-13, pp. 4163–4168.

[17] Khakpour, H., Birglen, L., and Tahan, S. A., 2014, "Synthesis of differentially driven planar cable parallel manipulators", IEEE Trans. Robot. [article in press]

[18] IFToMM Commission A, 1991, "Terminology for the Theory of Machines and Mechanisms", Mech. Mach. Theory, **26**(5), pp. 435–539, .

[19] Hirose, S., 1985, "Connected differential mechanism and its applications: robotic manipulator", Proceedings of International Conference on Advanced Robotics, Tokyo, Japan, Sep. 9-10, pp. 319–326.

[20] Birglen, L., Laliberte, T., and Gosselin, C., 2008, *Underactuated Robotic Hands*, Springer-Verlag, New York, vol. 40.

[21] Landsberger, S. and Sheridan, T. 1987, "Parallel link manipulators", US Patent No. 4 666 362

[22] Carricato, M and Gosselin, C., 2009, "On the Modeling of Leg Constraints in the Dynamic Analysis of Gough/Stewart-Type Platforms", J. Comput. Nonlinear Dyn., **4**(1), pp. 1–8.

CHAPTER 7

ARTICLE 3: UNIFORM SCANNING PATH GENERATION FOR ABRASIVE WATERJET POLISHING OF FREE-FORM SURFACES MODELED BY TRIANGULATED MESHES

Hamed Khakpour [a], Lionel Birglen [a], Souheil-Antoine Tahan [b]

[a] *Mechanical Engineering Department, Ecole Polytechnique de Montreal, Montreal, QC, CANADA, H3T 1J4*

[b] *Mechanical Engineering Department, Ecole de technologie superieure, Montreal, QC, CANADA, H3C 1K3*

7.1 Abstract

In this paper, a method is proposed to generate scanning paths to be used in automated abrasive waterjet polishing of free-form surfaces. This method is able to produce trajectories with constant offset distance between curves on surfaces with holes and complex boundaries without reconfiguration of their triangular mesh model. For this, the particular requirements of this polishing technique to be kept along the path are investigated. Next, a reference curve is obtained and using geodesic distances in specific directions, the adjacent offset curves are found. Finally, if needed, the main trajectory is divided into a set of continuous sub-trajectories. By defining two indices, the effect of the shape of the surface and the configuration of the generated path on the uniformity of the distribution of the waterjet is evaluated. Through several examples, it is shown that the method can effectively generate scanning paths adapted to the requirements of this technique.

Keywords: *Abrasive waterjet polishing, trajectory planning, triangular mesh, free-form surface.*

7.2 Introduction

In high-tech manufacturing, to produce objects with free-form surfaces, different steps of machining including milling, grinding, and polishing may be performed. Amongst them, the polishing process is one of the most delicate procedures in which the method of sweeping the tool on the surface has a significant impact on its final quality.

So far, several techniques (e.g., sanding disc, electric discharge, ultrasonic, and abrasive waterjet polishing (AWJP) [1, 2]) have been developed to polish surfaces with different shapes and properties. Amongst these, AWJP is a novel non-conventional method in which the material removal from the surface takes place due to the collision of the abrasives with the surface [3]. In this method, there is no direct contact with the surface and the area affected by the jet is usually short (usually a few millimeters). Thus, it is critical to keep the material removal rate of the process constant and uniformly deliver the slurry jet to all areas of the desired surface. For this, it is required to keep the AWJP parameters at their optimal levels during the process and generate a polishing path in which the particular properties of this technique are considered. This paper is dedicated to the study of the requirements of a trajectory generated for this particular application and then, the development of a method to produce this type of paths.

Trajectory planning is a well-known field in computer-aided design (CAD) and many works have been done in this area. Depending on the application, different methods of surface-covering path generation were developed [4–15]. These trajectories are mainly generated in two ways. In the first, the main objective is to only pass the tool over the entire surface, and thus, a constant

offset distance between adjacent paths is not important. One of the common strategies used for this type of trajectories is to use parametric surfaces [10–12]. In these approaches, the trajectory is first generated on a planar surface and then, it is mapped onto the desired free-form surface. The pitch adaption method developed by Tam et al. [14], and boundary-conformed iso-parametric tool path generation methods presented by Yang et al. [11] and also Yuwen et al. [12] are examples of this strategy.

In the second approach, it is critical to uniformly cover the entire surface with the trajectory. For this, the trajectory is often obtained by considering a reference point/line/path as a starter to generate the adjacent offset curves while the constant offset distance is preserved. Depending on the requirements of the application, this reference can be a point [16, 17], a seed curve [4, 17–19], or a boundary of the surface [6, 8, 17, 18]. In this approach, the concept of geodesic distance fields is typically used to find the offset curve of a reference on the free-form surface [16–20]. This method was investigated and formulated by Patrikalakis et al. [21, 22] for free-form surfaces. For the case of surfaces modeled by triangulated faces, it was initially used by Surazhsky et al. [16] and was based on the interval propagation presented by Mitchell et al. [23]. Subsequently, Bommes et al. [18] improved the original algorithm by reconfiguring the triangular mesh of the surface to obtain a fine and smooth curve.

In this paper, the shape of the material removal profile in the area polished by the AWJP method is first investigated. Then, considering its properties, the limits for the curvature of the surface, pitch distance, and the configuration of the trajectory are determined. Afterwards, by modeling the material removal from the surface (in the planar case), it will be shown that the shape of the trajectory affects the uniformity of the material removed from a surface. Finally, a modular method is proposed to generate the surface-covering scanning path on a triangular mesh model defining the free-form surfaces to be polished. This method is developed to generate uniformly distributed trajectories on single surface with arbitrary shape (within the particular limits for the AWJP process), including holes and a complex outer boundary. In the proposed algorithm, instead of using windows (intervals) to find geodesic distances from a point or a line [16, 18, 23], the geodesic distances are calculated in specific directions. Thus, this method is simpler than the geodesic distance approach but still effective and can generate smooth trajectories on a surface for AWJP process while reconfiguration of the triangular mesh is not necessary. Lastly, by defining indices, the performance of the generated trajectories for AWJP process is investigated.

7.3   Estimation of material removal in AWJP

7.3.1   Shape of the material removal profile

In AWJP, the material removal occurs due to the collision of abrasive particles and the surface. The shape of the material removal profile depends on several polishing parameters including the nozzle diameter/angle, stand-off-distance, abrasive type/size, and speed of the jet [3]. The authors have done an experimental study on the effect of AWJP parameters on the quality on the polished surface (which is out of the scope of this paper). In these experiments, the nozzle traversed along straight lines over flat surfaces. As a part of this study, the profile of the material removal in the direction perpendicular to the nozzle movement direction was determined (assumed to be symmetrical). Although the dimension of the profile depends on the aforementioned parameters, its general shape was similar in all the tests. An example of the profile obtained by combining the results of several experiments is shown in Fig. 7.1(a). In this figure, the polished line is along x axis and the dimension in the direction of z axis (depth of penetration) is normalized to keep the generality of the model.

However, the exact shape of this profile is not always the same and depending on the polishing parameters it may vary a little. Thus, the presented profile is used to only give an idea about how to find the desired pitch distance. Also, the scanning path is considered as the polishing trajectory to find the distribution of waterjet. This model is only used to estimate the distribution of waterjet over the surface but not the real shape of the polished area. The hypothesis is valid only if the ratio of the depth of penetration to the width of the polished area, D/W, is negligible. Otherwise, the interaction between abrasives and the surface may be affected and thus, this model cannot estimate the consequences. Taking into account these considerations, the estimation of material removal from the surface using three parallel lines are presented in Figs. 7.1(b)-(e).

As it can be seen in Figs. 7.1(b) and (c), when the pitch distance p between two adjacent lines is properly adjusted, the material removal happens evenly. On the other hand, when p is longer or shorter, some hills or valleys may respectively remain between the paths (c.f. Figs. 7.1(d) and (e)). In the particular case shown in Fig. 7.1 where $W = 10$ *mm*, the total variation in the depth of the polished area in case (c) with $p = 4$ *mm* is 1.6% of D, while in cases (d) and (e) it is respectively 37.4% for $p = 5$ *mm* and 13.9% for $p = 3$ *mm*. Since the exact curve of the profile may slightly change with different polishing parameters, these values give an order of magnitude but can vary in practice. However, knowing the shape of the profile, the optimal pitch distance can be properly estimated by trial and error.

With free-form surfaces, the initial profile of the surface can be wavy and assuming the nozzle axis perpendicular to the surface, the interaction between profiles can be different. This difference highly depends on the ratio between the depth of the penetration and the radius of curvature of
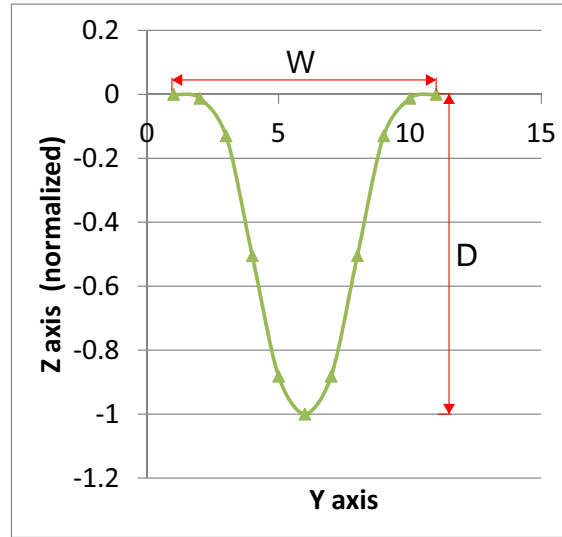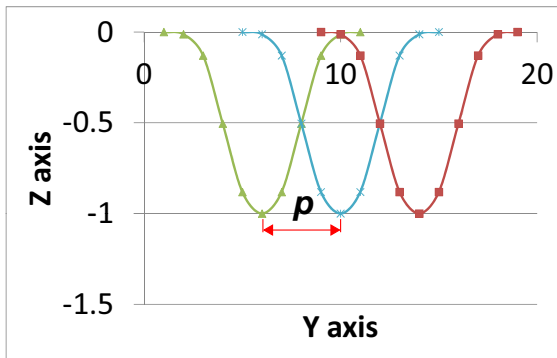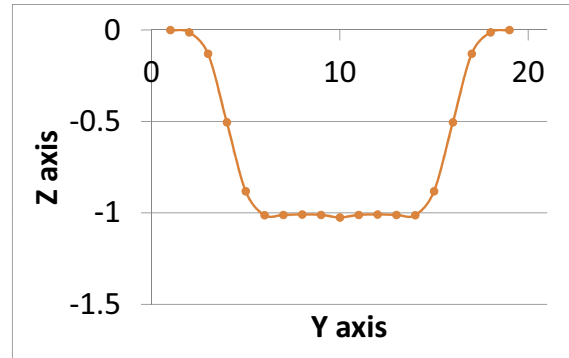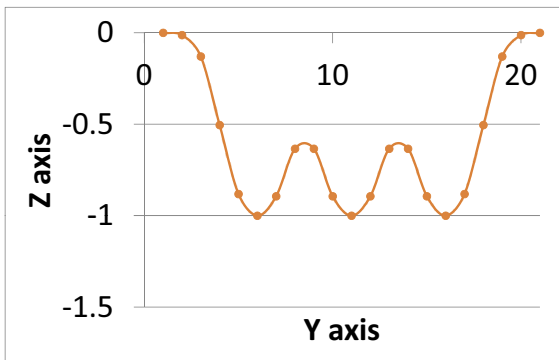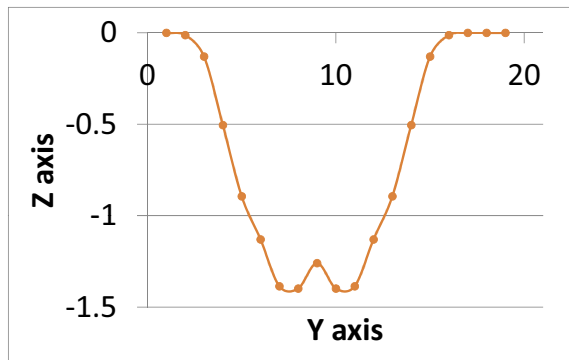
Figure 7.1 (a) Profile of the material removal obtained from experiments (with normalized depth); (b) profiles of three consecutive polishing lines; (c) estimated profile of material removal using three polishing lines with $p=4mm$; (d) $p=5mm$; and (e) $p=3mm$.
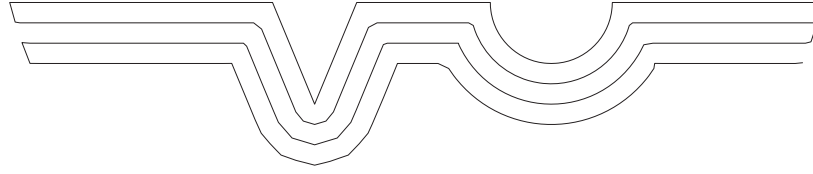
Figure 7.2 Planar trajectory with sharp turns along the paths ($p=4mm$).

the surface around the polished area, i.e. D/r_k. If this ratio is large (e.g. $D/r_k = 0.25$) then, in concave or convex parts of the surface the deepest parts of the profiles respectively diverge from each other or converge together and consequently the overall shape of the machined surface changes. However, since in polishing process D is very small (usually less than 20 μm), this effect is often negligible. On the other hand, the angle between the nozzle axis and the surface has a significant impact on the shape of the profile. Thus, it is necessary to minimize the effect of the radius of curvature of the surface, r_k, on this angle. Consequently, to have a constant pitch distance on the entire trajectory and maintain the uniformity of the shape of profile, the condition $r_{k.min}/W \geq 6$ is introduced to be respected for the minimal radius of curvature on the entire surface in order to keep the maximum difference in the angle between the normal of the surface and the jet nozzle axis less than 5 degrees. Thus, to polish a surface with smaller $r_{k.min}$, it is recommended to use a nozzle with smaller diameter.

7.3.2   Effect of configuration of the trajectory on the uniformity of polishing process

Considering the geometry of a surface, preserving the desired pitch distance does not guarantee the uniformity of the polishing process. The other parameter which can affect its uniformity is the configuration of the trajectory. Indeed, the distribution of waterjet on the areas with almost straight offset curves is not the same as that of curves with sharp turns. Therefore, an algorithm is developed to investigate the capability of the generated path in the uniform distribution of abrasive waterjet on a flat surface. As an example, the 2-D scanning path illustrated in Fig. 7.2 is considered. It is assumed that the nozzle axis is normal to the surface and thus, as presented in Fig. 7.3(a), the resultant profile of the material removal is symmetric (this can actually be done with any other profile). Then, considering a constant traversing speed along the path, the final shape of the surface is predicted and shown in Figs. 7.3(b) and (c).

This simulation reveals that if there is a sharp turn along the path then the variation in the depth of penetration increases. Consequently, the uniformity of waterjet distribution is lost around that area. With the example shown in Fig. 7.3, the maximum variation in the areas with sharp turn (indicated by ellipses) is 39.8%. To decrease this, a limit should be taken into account for the
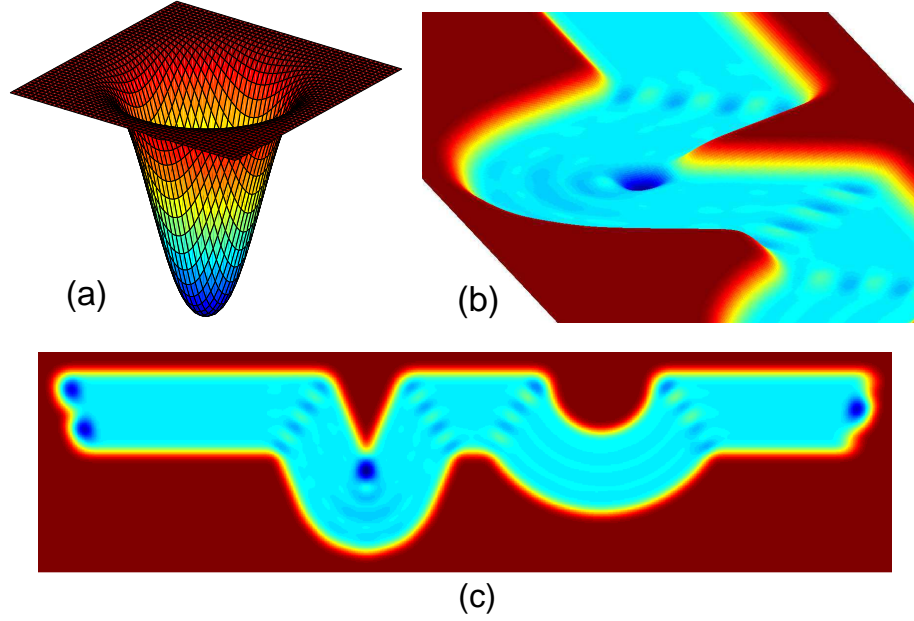
Figure 7.3 (a) Profile of material removal in polishing spot by a nozzle with normal angle ($W =$ 10mm); (b) 3-D view of the simulation of the shape of a surface polished through a planar trajectory ($p = 4mm$); (c) top view of this surface.

Table 7.1 Effect of the curve of the trajectory on the variation of depth of the polished area in a flat surface.

	length of r_{path}, ($W=10$ & $p=4$) all in mm				
	4	8	12	16	20
Variation %	11.5	7.1	5.4	2.52	2.44

radius of curvature along the path, r_{path}. Using this algorithm, the ratios between the variations of the depths of the polished areas in curved parts of the trajectory and D are calculated and presented in Table 7.1. As expected, by increasing the r_{path}, this variation decreases. Thus, considering the particular profile of material removal illustrated in Fig. 7.3(a), with $r_{path}/W \geq 1.5$, a less than 5% of variation can be expected. Additionally, as computed, if a piecewise path is used to create this curvature, to keep the variation smaller than this value, the maximal angle between two consecutive line segments of the path, θ_{path}, should be smaller than $\pi/6$.

7.4 Scanning path generating algorithm

In the proposed method, a reference curve is first created through several options. Afterwards, for each point on this path, the tangential vector is computed as a bisector of the two consecutive

line segments sharing this point, to define the normal of a plane. This plane is used to find the particular direction(s) in which the points of the adjacent offset curve located at the same geodesic distance from the point is searched. Afterwards, the procedure continues to obtain the next curve until no new one can be found. This procedure is then finished by connecting the ends of the curves to have a single scanning path. In the cases where it is not possible to generate continuous path, several methods were presented in the literature to divide an original surface into regions in which single continuous trajectories can be produced [24]. However, since in the proposed method the entire trajectory is first generated, an algorithm is developed to detect the discontinuous areas on the original trajectory and divide it into several continuous sub-trajectories.

7.4.1 Generation of the reference path

The algorithm starts the path generation process by collecting the data of the triangular faces of the surface. Next, it searches for the boundaries of the surface. There can be both outer and inner boundaries (i.e. the edges of either holes or obstacles inside the surface, if they exist), designated by OB and IB respectively. Next, the starting and final points (respectively P_s and P_f) of the reference curve are determined. The positions of these points on the surface have a critical impact on the general shape and pattern of the entire trajectory which significantly affects the uniformity of the distribution of the waterjet on the surface . To find them, three options are considered in this algorithm:

1. Selecting the two furthest vertices on the outer boundary of the surface;

2. If the outer boundary can be recognized as a set of edges connected together through sharp ends (e.g., boundary of a rectangular surface), then the two end points of the longest edge can be chosen, otherwise either the previous or the next option may be used (e.g., in the case of a surface with a rounded outer boundary);

3. If a particular direction or pattern is needed, two user-defined points can be used.

With the first two options, the OB is used. With option 1, the centroid of all the vertices of the OB is first found, and then, the furthest vertex from this point is selected as the starting point. The final point is the furthest vertex of the OB from the latter. With option 2, the angle θ_b, between each pair of two consecutive edges of the boundary and the average of all these angles, $\bar{\theta}$, are calculated. Then, the vertices for which this angle exceeds a predefined maximum limit are considered as sharp ends.

In one strategy, the reference curve can be obtained as an intersection of the surface and a plane passing through these two points. To find the coordinates of this plane, first, the average normal of the whole surface is obtained as $\bar{\mathbf{e}} = \frac{\sum_{g=1}^{n} \mathbf{e}_g}{\left\| \sum_{g=1}^{n} \mathbf{e}_g \right\|}$, where $\mathbf{e}_g$ is the normal vector of the gth face.

(a)

(b)

(c)
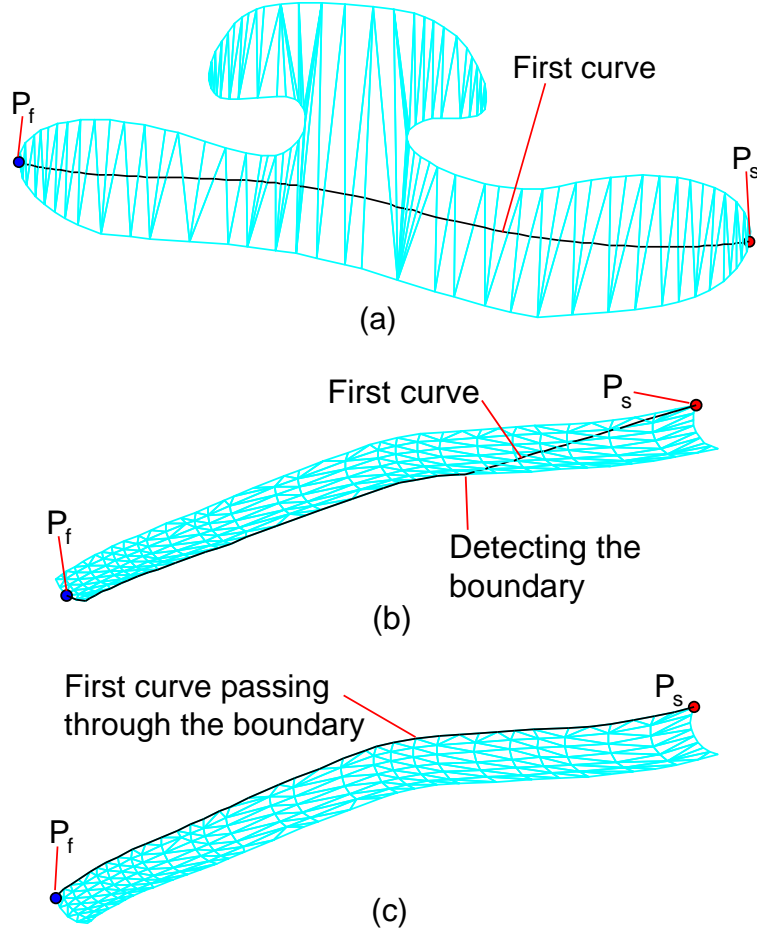
Figure 7.4 Creating the reference curves using (a) the two furthest points while it completely passes though the surface; (b) the two furthest points while it partially coincides with the boundary; (c) two points on two sharp ends of the boundary.

Then, the normal of this plane is calculated as $\mathbf{e}_p = \frac{\mathbf{v}_{if} \times \bar{\mathbf{e}}}{\|\mathbf{v}_{if} \times \bar{\mathbf{e}}\|}$ where $\mathbf{v}_{if} = \mathbf{p}_f - \mathbf{p}_i$, $\mathbf{p}_i$ and $\mathbf{p}_f$ are respectively the position vectors of the current point (initially $P_i = P_s$) and point P_f.

Next, the intersection of this plane with the surface (which is a set of points creating the reference curve) can be found. This intersection curve may not be continuous and in some cases the plane may go beyond the boundaries of the surface. To avoid this problem, the algorithm starts searching for intersection points from the point P_s and step by step proceeds toward point P_f. In each step, one point is found and is considered as point P_i to obtain the next intersection.

If the point P_i is on a inner boundary (a hole) of the surface and no face exists in the way toward the point P_f, the next intersection of this boundary with the plane in the proceeding direction is considered as a new point. If it is on the outer boundary and again no face exists in the desired direction, the algorithm follows the corresponding boundary in the proper direction until it reaches the point P_f. In Figs. 7.4(a) and (b), examples of creating the reference path using the two furthest

points method are illustrated. As the latter figure shows, when the current point reaches the surface outer boundary, it follows the latter until point P_f.

With the second option, the previously discussed plane is not used and as shown in Fig. 7.4(c), the corresponding sub-boundary between points P_s and P_f is considered as the reference curve. If the third option (user defined points) is used, the strategy described for the first option is used again. Using different options to find the reference path gives the algorithm the capability to generate scanning paths with different properties and then select the one with the best performance (based on the indices which are presented in Section 4).

With this method, the number of points found when constructing the reference curve depends on the number of faces/edges located along its way. Therefore, the distances between pairs of these points are variable. This can affect the precision of the offset curves and weakens the uniformity of the entire trajectory. Thus, this distance should be kept shorter than an appropriate limit which is defined as:

$$UL = min\left\{ \frac{p}{s} , Ed_m + \left(\frac{Ed_M - Ed_m}{s'} \right) \right\} \tag{7.1}$$

where Ed_M and Ed_m are respectively the lengths of the longest and shortest edges of the surface; s and s' are respectively constant values used to adjust the effect of the pitch and the shape of the faces on this limit. By trial and error it is suggested to use $s \geq 2$ and $s' \geq 20$ to obtain smooth and accurate offsets. If the distances between each pair of two consecutive points are larger than UL then, by interpolation, new point(s) are generated between them. Then, without reconfiguring the surface and increasing its total number of faces, the precision of the path can be controlled.

7.4.2 Generation of the offset curves

The ideal offsets for a pair of line segments of a piecewise curve in the planar case are shown in Fig. 7.5. As depicted in this figure, in the acute angle side of these lines, the offsets intersect each other. While in the obtuse angle side, a part of the offset has a circular shape. Since, the path has a piecewise structure, this circular parts are modeled by a set of lines. For this, as illustrated in Fig. 7.6, some cases are defined to obtain the number of points which are representing the circular area and keep the error in the exact values of the pitch distance lower than its maximal accepted value. To calculate the angle θ between one of these two consecutive lines and the vector $\mathbf{e}_{dir.b}$ (which is along the intersection of their bisector plane with the three-dimensional (3-D) surface), they are first mapped onto the tangential plane attached to point P_i. Through this mapping, the effect of the curvature of the surface on this angle is cancelled.

As shown in Fig. 7.6, in case (1), $\theta < 105°$ and only the vector $\mathbf{e}_{dir.b}$ is used. In case (2), $105° \leq \theta < 120°$ and the vectors $\mathbf{e}_{dir.n1}$ and $\mathbf{e}_{dir.n2}$ are also obtained. They are the intersections between the surface and the planes defined by point P_i and normals along the two consecutive lines.
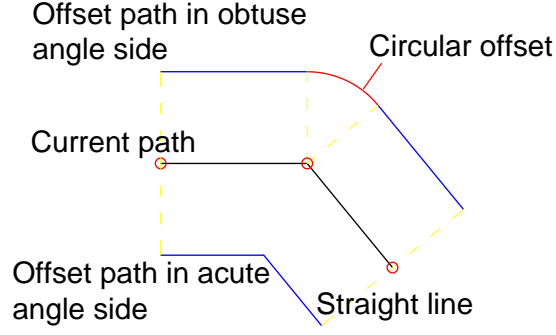
Figure 7.5 Ideal offsets for a pair of line segments in a planar surface.
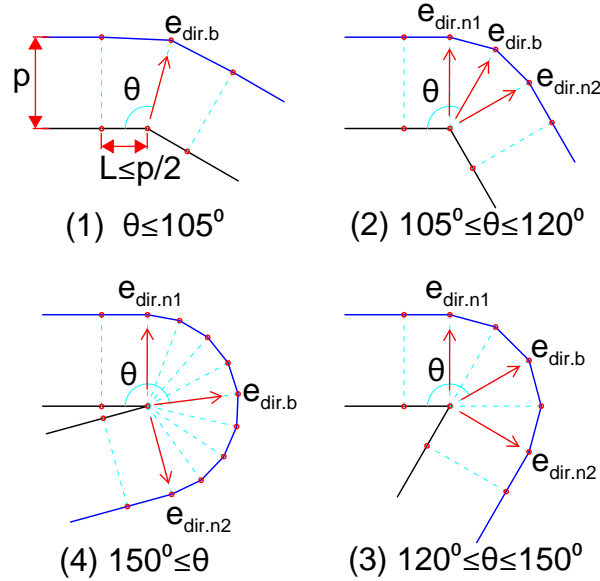
Figure 7.6 Directions considered to find the points of the next offset based on the angle between the line segments and their bisector in obtuse side of the path.

In case (3), $120° \le \theta < 150°$ and the two bisector planes between these three consecutive vectors are computed and then, their intersections with the surface around point P_i are considered as the two additional directions. Finally, in case (4), $\theta \ge 150°$ and similarly, four other vectors amongst the abovementioned five consecutive vectors are obtained. Then, the maximum error would be less than 3.7% on a planar surface.

When the initial direction is known, the search for next point on the offset curve, P_{off}, is started. For this, conversely to the conventional method of propagation of intervals through triangular faces, in this paper, the geodesic distance is calculated for particular initial directions. With the limits
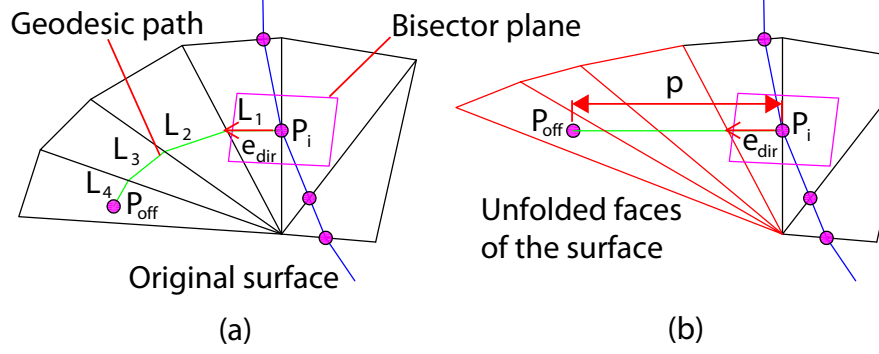
Figure 7.7 (a) Geodesic distance between points P_i and P_{off} on a part of the 3-D surface modeled by triangular faces; (b) the geodesic distance coincides with the Euclidean distance when the corresponding faces are unfolded.

considered for the curvature of the surface with respect to the pitch distance (as a ratio of W) in the AWJP process, this method is efficient and precise while kept simple. In the proposed method, the point P_{off} is found by unfolding the triangles which are located in the direction started from P_i and defined by the assigned direction vector $\mathbf{e}_{dir.j}$ (subscript $dir.j$ indicates the jth direction vector found for P_i). Then, the 3-D surface made of triangular faces is changed to a planar surface and the geodesic distance coincides with its Euclidean counterpart. Example of this process is depicted in Fig. 7.7.

This procedure is started by finding the face/edge on which the geodesic curve should be followed toward the new point P_{off}. When the first reference face/edge is obtained, the algorithm obtains the location of the first temporary point $P_{temp.1}$ which is located in the proceeding direction toward point P_{off}. If this reference is a face, the algorithm finds the edge located in the side of positive direction of the vector $\mathbf{e}_{dir.j}$ with respect to point P_i and then calculates the intersection of this edge and jth plane associated with vector $\mathbf{e}_{dir.j}$ (i.e., the point $P_{temp.1}$). If the reference object in an edge, the vertex which is in the positive direction of the vector $\mathbf{e}_{dir.j}$ is considered as point $P_{temp.1}$.

If point P_i is on a boundary of the surface, then that boundary is used to search for the new offset point. For this, the algorithm recalls the vertices of that boundary and finds the edge/vertex on which point P_i is located. Then, the proper direction along an edge of that boundary is obtained either using the vector $\mathbf{e}_{dir.j}$ or the location of the previous offsets on the same boundary. Then, the first vertex of boundary located in the proper direction is considered as $P_{temp.1}$. But, if the adjacent points of P_i on the current path (which is initially the reference curve) are also located on the same boundary and the vector $\mathbf{e}_{dir.j}$ is pointed toward outside of the surface, then this calculation for point P_i is stopped.

If point $P_{temp.1}$ is found, the length of the line segment $P_iP_{temp.1}$ (i.e., L_1 in Fig. 7.7) is calculated. If $L_1 > p$, the position vector of the offset point is obtained as:

$$\mathbf{p}_{off} = p\frac{\mathbf{p}_{temp.1} - \mathbf{p}_i}{\left\|\mathbf{p}_{temp.1} - \mathbf{p}_i\right\|} + \mathbf{p}_i, \qquad (7.2)$$

If $L_1 = p$, then $\mathbf{p}_{off} = \mathbf{p}_{temp.1}$. In both situations, the search for a new point finishes. On the other hand, if $L_1 < p$, the position of the point $P_{temp.1}$ is considered as the new current point, the offset distance is changed to $p_{tm} = p - L_1$. Also, the vector $\mathbf{e}_{dir.j}$ is rotated around the intersection of the planes of the current face and the next face which is located in the proper direction (this intersection includes their shared edge/vertex) to be placed on the plane of the next face (this is equivalent to unfolding the next face with respect to the current one) as:

$$\mathbf{e}'_{dir.j} = \mathbf{R}_{\mathbf{u},\gamma}\mathbf{e}_{dir.j} \qquad (7.3)$$

where $\mathbf{R}_{\mathbf{u},\gamma}$ is the rotation matrix around vector $\mathbf{u}$ with the angle of γ. It is defined as:

$$\mathbf{R}_{\mathbf{u},\gamma} = \mathbf{1}\cos\gamma + sin\gamma\left[\mathbf{u}\right]_\times + (1 - \cos\gamma)\mathbf{u}\mathbf{u}^T \qquad (7.4)$$

where $\mathbf{u} = \frac{\mathbf{n}_1 \times \mathbf{n}_2}{\|\mathbf{n}_1 \times \mathbf{n}_2\|}$ and $\gamma = \arccos\left(\mathbf{n}_1^T\mathbf{n}_2\right)$. Vectors $\mathbf{n}_1$ and $\mathbf{n}_2$ are respectively normals of the current face and the next face on which the vector $\mathbf{e}_{dir.j}$ should be placed. Also, $\left[\mathbf{u}\right]_\times$ is the cross product matrix of the vector $\mathbf{u}$. Next, the same process is continued with new temporary point and direction vector until the fth step where $L_f < p$ and consequently the point P_{off} is found (e.g., $f = 4$ in Fig. 7.7(a)).

If the new point $P_{temp.d}$ is on a vertex or an edge of a boundary, then similarly to point P_i, instead of following the geodesic path that boundary is followed until the point P_{off} is found. Thus, if the boundary in the proceeding direction toward the point P_{off}, then this point is always found on that boundary. Consequently, the continuity of the offset path is not disrupted by that boundary and no area on the surface is lost.

In Fig. 7.8, an example of generating offset points for a curve on free-form surface is presented. In the parts of the reference curve where there is no sharp turn, the resultant set of new points can constitute a smooth offset curve. But, in areas with sharp turns in the current curve, as expected, the offset points may collide with each other in the acute angle side. Therefore, after obtaining the offset points for the current curve, another subroutine is needed to modify these points in the following steps:

1. Replacing the points of the offset curve which are closer together than the threshold (e.g., $p/50$) with a point located in their middle;

2. Deleting the offset points which are closer than a specified minimal distance to the current
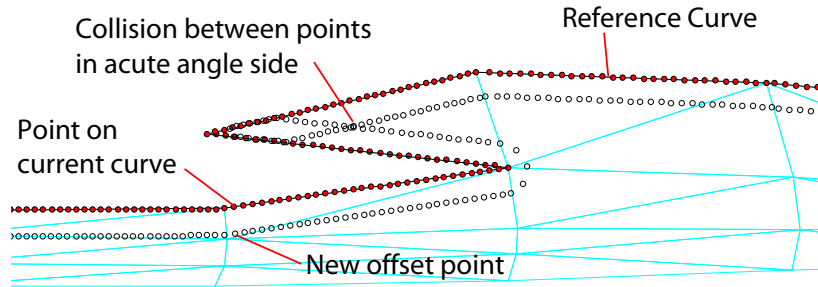
Figure 7.8 Finding the offset points of a curve with two sharp turns on a free-form surface
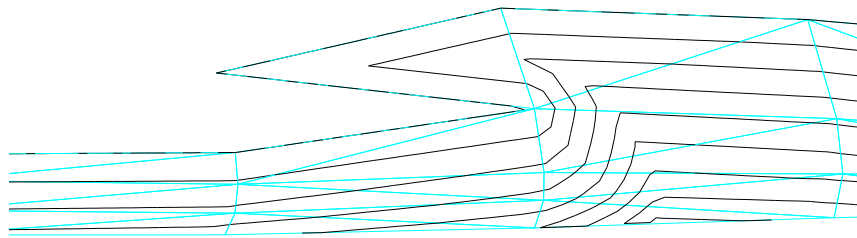
Figure 7.9 Post-processed offset curves when the reference curve has sharp turns on a free-form surface

curve. This usually happens in the acute angle side of the current curve (c.f. Fig. 7.8) or when the points are located on the boundary;

3. Checking the angle between each pair of two consecutive points on the new path and detecting sharp zigzags, turns, and loops caused by the tolerances considered in this numerical approach. Then, either modify or delete these points;

4. Comparing the distance between each pair of new points with the upper limit presented in Eq. (7.1). Then, if needed, new points are added to this curve similarly to the reference curve.

After all these modifications, the final shape of the new path is obtained. Then, it is connected to the previously generated paths to create the total trajectory. Following this step, the algorithm uses the new path as a current curve to repeat the same process and obtain the next curve. This procedure is continued until no offset curve can be found for the current path. As an example, the offset paths generated considering the reference curve with sharp turns shown in Fig. 7.8 are illustrated in Fig. 7.9. Next, the algorithm returns to the reference curve and with the same procedure obtains all offset curves on the other side of the reference path.

The final single trajectory generated on the free-form surfaces of a turbine blade, a channel, and a fillet (previously illustrated in Fig. 7.4c) are presented in Figs. 7.10a-c. As it can be seen in
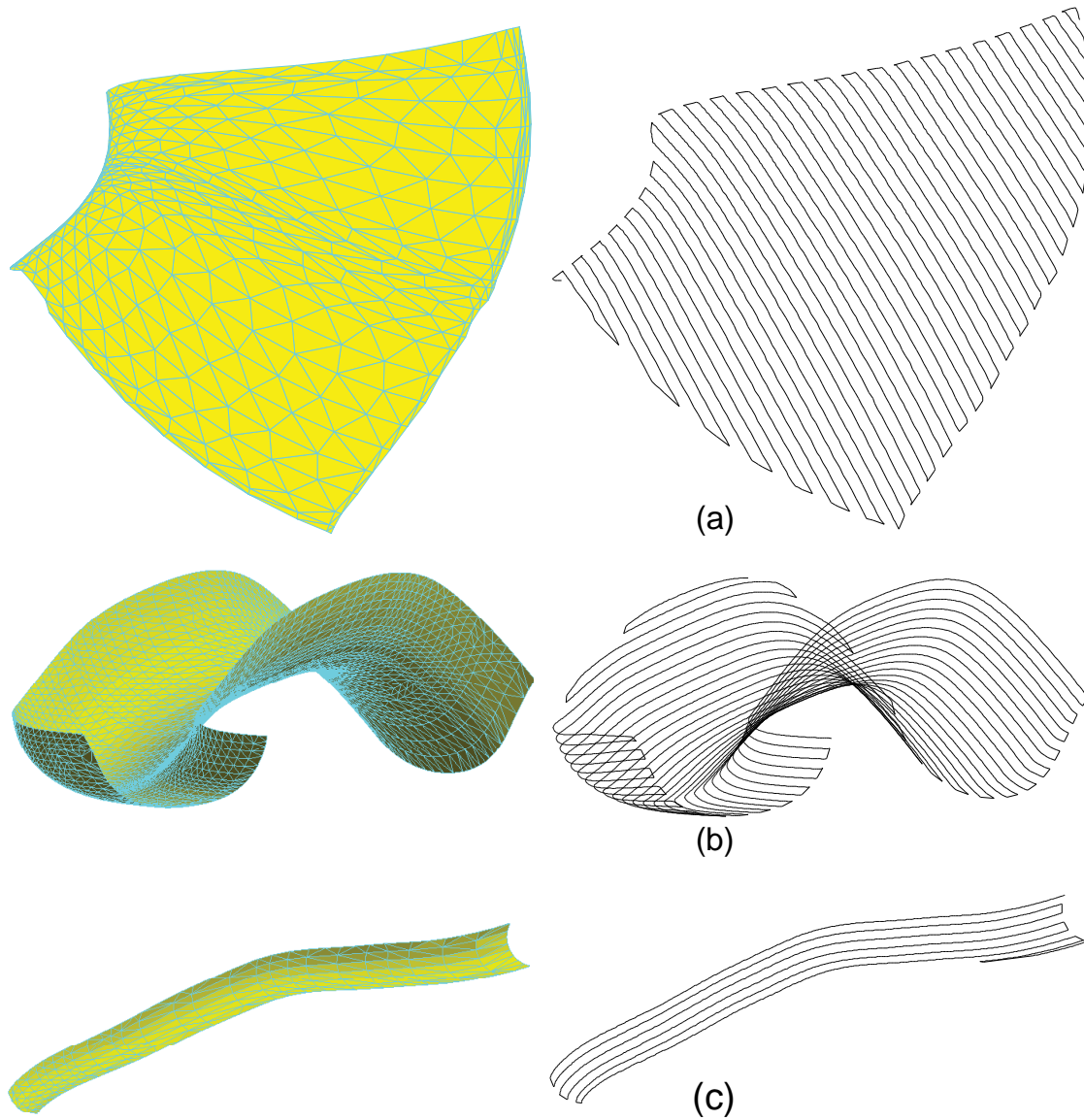
Figure 7.10 Single scanning path generated on the free-form surface (a) of a turbine blade; (b) inside a channel with irregular shape; (c) inside a fillet.

these figures, the offset distance is kept constant between all the offset curves, except for the two distal ones on each side of the trajectory. The algorithm does this alteration intentionally to adapt the configuration of these two end paths to the shape of the boundary.

7.4.3   Dividing the original trajectory

In the path generation process, if the surface has either concave parts in the outer boundary or internal holes, the generated curves may not be continuous on the surface and thus, they have to be
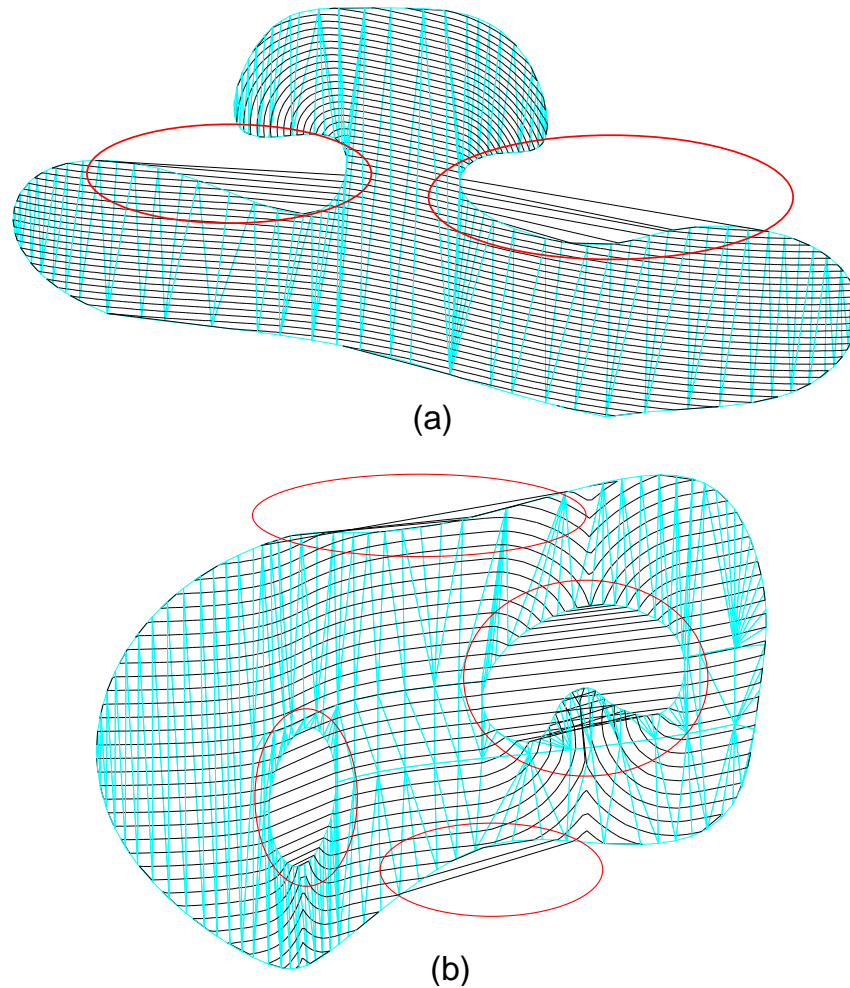
Figure 7.11 Discontinuous scanning paths (highlighted by red ellipses) generated on a surface with (a) a concave boundary; (b) a concave boundary and two holes.

divided into several pieces. Examples of these situations are shown in Fig. 7.11. These examples reveal that it is not always possible to have a single continuous scanning path on any arbitrary surface while a constant offset distance is maintained.

Thus, another supplementary module is used to detect these areas and divide the main trajectory into a set of sub-trajectories which are properly adapted to the surface. This module is made of two subroutines. The first one checks for the discontinuous areas of the trajectory. The second reconfigures the trajectory in these areas to produce a new set of the trajectories.

The first subroutine takes the first point of the trajectory and follows the path toward its other end and searches for lines which are not located on the surface. To find whether a line is on the surface or not, it evaluates the length of that line and the location of its midpoint. If this length is larger than a limit defined based on the maximum distance of two consecutive points on the

generated path, the current line is eliminated from the trajectory. Otherwise, the algorithm checks the location of its midpoint. If this point is on the surface or if it is not on the surface but its distance with the boundary of the surface is less than a specified limit, then the current line remains valid and the corresponding point is considered in the current sub-trajectory. The subroutine then proceeds with the next line segment. If it is not accepted, the second subroutine is used to search for the new connecting line. It takes this last point and searches for the remaining points of the main trajectory which are located within a specified distance. When these points are found, they are sorted as either located on the boundaries or inside the surface.

If the last point of the current sub-trajectory is located inside the surface, then both of these groups of points are considered. But if it is on a boundary, then only the first group of points is taken into account. Next, the subroutine does the same test on the new line segments created by this last point and all those points (i.e., checking their length and midpoint position). Amongst valid line segments, the one with the shortest distance is considered. When a new point is accepted, the subroutine checks the main trajectory from this point to its other end. Finding no connection point means the end of the current sub-trajectory. Thus, again the same subroutines are used to obtain other sub-trajectories from the remaining points of the trajectory.

This modification is done for the surfaces previously shown in Fig. 7.11 and the resultant sub-trajectories are presented in Fig. 7.12. However, as it can be seen in these figures, some sub-trajectories are quite short. The reason for this is that the subroutine tries to use all the generated points and does not discard them until no more points remained around. Depending on the application, these short sub-trajectories may be manually ignored by the user.

7.5 Performance of the generated path in AWJP

The discused method is developed to generate trajectories for AWJP process. As mentioned in Section 2, for the AWJP of a free-form surface, some particular requirements are to be preserved. Since the shape of the reference curve has a critical impact on the configuration of the final trajectory, several options are considered to obtain this first curve. Also, in this algorithm two indices are defined to evaluate the properties of the surface and the generated path for the AWJP process. They are the curvature index, I_{curv}, and the path index I_{path}. The first one evaluates the curvature of the surface and is defined as:

$$I_{curv} = \frac{a_m}{a_t} \left(\frac{BL1}{\frac{1}{m} \sum_{j=1}^{m} r_{k.min.BL1}(j)} \right) \tag{7.5}$$

where a_t is the total area of the surface; a_m is approximation of the area around the vertices on which the minimum radius of curvature is less than its limit $BL1$ (e.g., $BL1 = 6W$); $r_{k.min.BL1}(j) \in$
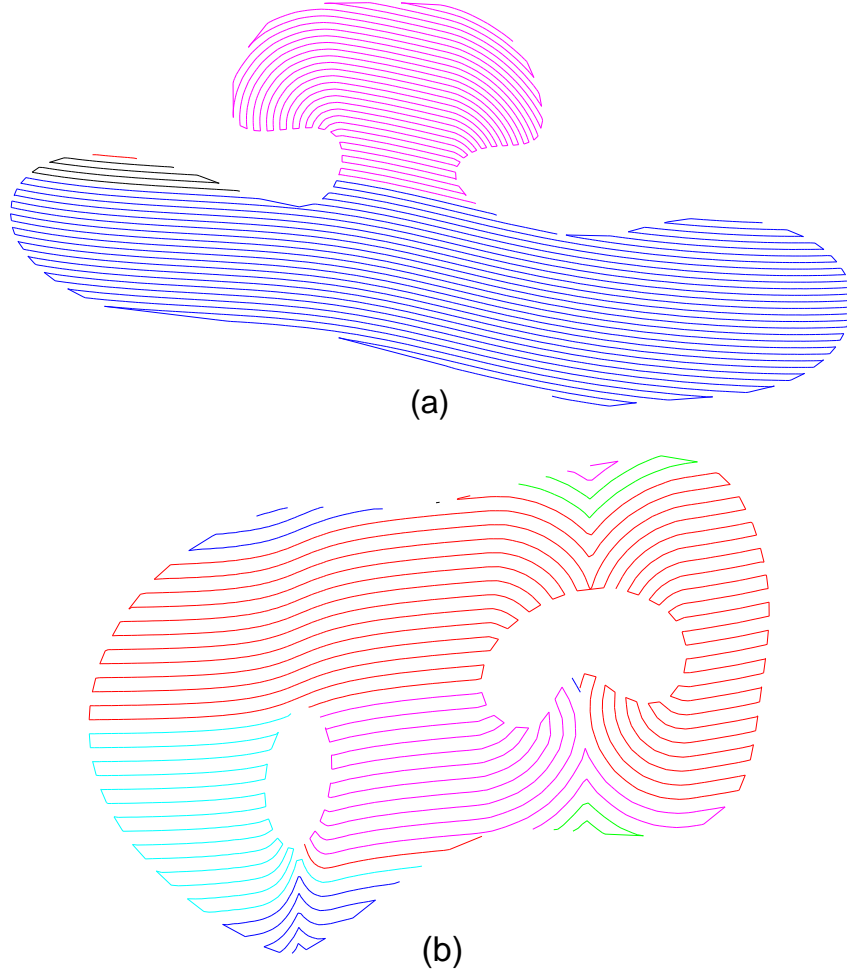
Figure 7.12 Dividing the original scanning path into continuous sub-trajectories for a surface with (a) a concave boundary; (b) a concave boundary and two holes.

$\{r_{k.min}(j) < BL1\}$ for $j = 1, \cdots, m$ and $r_{k.min}(j)$ is the minimum radius of curvature obtained using an osculating circle [25, 26] around vertex v_j considering its one-ring of neighborhood and is defined as:

$$r_{k.min}(j) = \min \left\{ \frac{\|\mathbf{v}_i - \mathbf{v}_j\|^2}{2\mathbf{n}_j^T (\mathbf{v}_i - \mathbf{v}_j)} \right\} \tag{7.6}$$

where $\mathbf{v}_i$ is the position vector of the ith vertex in the one-ring neighborhood and $\mathbf{n}_j$ is the estimated surface normal at jth vertex. With an ideal surface for AWJP process, $I_{curv} = 0$, otherwise it has a value which is to be minimized.

The second index evaluates the smoothness of the generated path and is defined as:

$$I_{path} = \frac{L_{p.q}}{L_{p.t}} \left(\frac{q.BL2}{\sum_{d=1}^{q} r_{path.BL2}(d)} + \frac{\sum_{d=1}^{q} \theta_{path.BL3}(d)}{q.BL3} \right) \tag{7.7}$$

Table 7.2 Indices I_{curv} and I_{path} measured for different surfaces and trajectories.

	Option	I_{curv}	I_{path}
2-D path (Fig. 7.2)	Boundary curve	0	0.3995
Turbine blade (Fig. 7.10)	Furthest vertices	0.0239 to 0.0477	0.0026
Channel (Fig. 7.10)	Boundary curve	0.0116 to 0.2823	0.0042
Fillet (Fig. 7.10)	Boundary curve	0.9147 to 1.8294	0
Surface (a) in Fig. 7.11	Furthest vertices	0	0.0183
Surface (b) in Fig. 7.11	Furthest vertices	0.0293 0.1587 to	0.1892

where $L_{p.t}$ is the total length of the trajectory; $L_{p.q}$ is approximation of the length of trajectory where either r_{path} or θ_{path} exceed the desired limits, respectively $BL2$ and $BL3$ (e.g., $BL2 = 1.5W$ and $BL3 = \pi/6$). Also, $r_{path.BL2}(d) \in \{r_{path}(d) < BL2\}$ for $d = 1, \cdots, q$ and $\theta_{path.BL3}(d) \in \{r_{path}(d) > BL3\}$ for $d = 1, \cdots, q$ which are calculated after projection of the two consecutive lines of the trajectory onto the tangential plane attached to the free-form surface at their intersection to eliminate the effect curvature of surface in this investigation. Again in ideal condition one has $I_{path} = 0$. The points which are located either on the boundary or on the U turn parts of the scanning path are excluded from this evaluation. Indeed, in these locations, the shape of the path depends on the shape of the boundary and sharp turns might mandatorily exist in these areas (e.g. U turns in the left and right sides of the trajectory presented in Fig. 7.2). To solve this problem, either the polishing process can be stopped during the U turns or, if possible, an augmented surface can be used to generate the trajectory for the original surface by extrapolating this surface beyond its current boundaries.

Using I_{curv}, the algorithm evaluates the eligibility of the desired surface to be polished with AWJP technique. Then, using I_{path}, it estimates the performance of the paths generated using several options in AWJP process and finally selects the best one with minimum I_{path}. In Table 7.2 the values of these indices for the surfaces illustrated in Figs. 7.2, 7.10 and 7.11 are presented. As can be seen in this table, with the examples shown in Figs. 7.10 and 7.11, the values of I_{path} are far smaller than the one of the 2-D trajectory presented in Figs. 7.2. However, for Surface (b) in Fig. 7.11, it is larger than the others. This means that the existence of inner holes and concave boundaries can lead to curved paths along the trajectory which may decrease its efficiency in AWJP. On the other hand, with the path generated on the fillet, all the limits are properly preserved and $I_{path} = 0$ but the index I_{curv} is large and thus, a smaller nozzle with shorter W would preferably be used.

7.6   Conclusions

In this paper, a modular method was presented to generate scanning paths for automated abrasive waterjet polishing of free-form surfaces which are modeled by triangular mesh. The method was developed to produce trajectories with a constant offset distance preserved between adjacent curves. For this, the particular requirements of this polishing technique to be preserved by the path generation technique were determined. Then, to generate these paths, through several options, a reference curve was obtained. Afterwards, using geodesic distances in specific directions, the location of the points of the adjacent offset paths were calculated. Finally, the algorithm checked the continuity of the generated trajectory. If it passed beyond the boundaries of the surface, it was then divided into a set of continuous sub-trajectories. Finally, two indices were defined to quantify the effect of the shape of the free-form surface and the generated path on the uniformity of the distribution of the abrasive waterjet on the surface.

Acknowledgments

References

[1] Mao TF, Yang SC, Tsai FC, Hung JC, Yan BH (2010) Experimental investigation of abrasive jet polishing on the free-form machined surfaces of skd61 mold steel using sic particles. Mater Manuf Process 25(9): 965–973

[2] Shafiei N, Getu H, Sadeghian A, Papini M (2009) Computer simulation of developing abrasive jet machined profiles including particle interference. J Mater Process Technol 209(9): 4366–4378

[3] Li Z, Li S, Dai Y, Peng X (2010) Optimization and application of influence function in abrasive jet polishing. Appl Opt 49(15): 2947–2953

[4] Atkar PN, Conner DC, Greenfield A, Choset H, Rizzi AA (2009) Hierarchical segmentation of piecewise pseudoextruded surfaces for uniform coverage. IEEE Trans Autom Sci Eng (USA) 6: 107–120

[5] Feng-yun L, Tian-sheng L (2005) Development of a robot system for complex surfaces polishing based on cl data. Int J Adv Manuf Technol 26(9-10): 1132–1137

[6] Hauth S, Richterich C, Glasmacher L, Linsen L (2011) Constant cusp toolpath generation in configuration space based on offset curves. Int J AdvManuf Technol 53(1-4): 325–338

[7] Nagata F, Watanabe K, Izumi K (2001) Furniture polishing robot using a trajectory generator based on cutter location data. In: Proceedings ICRA. IEEE International Conference on Roboticsand Automation 1: 319–324

[8] Park SC, Chung YC, Choi BK (2003) Contour-parallel offset machining without tool-retractions. Comput Aided Des 35(9): 841–849

[9] Ryuh B, Park SM, Pennock GR (2006) An automatic tool changer and integrated software for a robotic die polishing station. Mech Mach Theory 41(4): 415–432

[10] Sheng W, Chen H, Xi N, Chen Y (2005) Tool path planning for compound surfaces in spray forming processes. IEEE Trans Autom Sci Eng 2(3): 240–249

[11] Yang DCH, Chuang JJ, Han Z, Ding S (2003) Boundary-conformed toolpath generation for trimmed free-form surfaces via coons reparametrization. J Mater Process Technol 138: 138–144

[12] Yuwen S, Dongming G, Zhenyuan J, Haixia W (2006) Iso-parametric tool path generation from triangular meshes for free-form surface machining. Int J Adv Manuf Technol 28(7-8): 721–726

[13] Tam HY (1999) Toward the uniform coverage of surfaces by scanning curves. Comput Aided Des 31(9): 585–596

[14] Tam HY, Lui OCH, Mok ACK (1999) Robotic polishing of free-form surfaces using scanning paths. J Mater Process Technol 95(1-3): 191–200

[15] Tsai MJ, Chang JL, Haung JF (2005) Development of an automatic mold polishing system. IEEE Trans Autom Sci Eng 2(4): 393–397

[16] Surazhsky V, Surazhsky T, Kirsanov D, Gortler SJ, Hoppe H (2005) Fast exact and approximate geodesics on meshes. ACM Trans Graph 24(3): 553–560

[17] Kout A, Muller H (2010) A framework for the generation of distance field based curves on triangular mesh surfaces for nc manufacturing. Tech rep, Department of Computer Science, Technische Universitt Dortmund

[18] Bommes D, Kobbelt L (2007) Accurate computation of geodesic distance fields for polygonal curves on triangle meshes. VMV: 151–160

[19] Yuen P, Mokhtarian F, Khalili N, Illingworth J (2000) Curvature and torsion feature extraction from free-form 3-d meshes at multiple scales. IEE Proc Vis Image Signal Process 147(5): 454–462

[20] Xin SQ, Ying X, He Y (2012) Constant-time all-pairs geodesic distance query on triangle meshes. In: Proc. - I3D: ACM SIGGRAPH Symp. Interact. 3D Graph. Games, Costa Mesa, CA, USA: 31–38

[21] Patrikalakis N, Bardis L (1989) Offsets of curves on rational b-spline surfaces. Engineering with Computers 5: 39–46

[22] Patrikalakis NM, Maekawa T (2002) Shape Inter-rogation for Computer Aided Design and Manufacturing. Springer

[23] Mitchell JSB, Mount DM, Papadimitriou CH (1987) The discrete geodesic problem. SIAM J Comput 16(4): 647–668

[24] Galceran E, Carreras M (2013) A survey on coverage path planning for robotics. Rob Autom Syst 61(12): 1258–1276

[25] Dong C, Wang G (2005) Curvatures estimation on triangular mesh. JZUS: 128–136

[26] Szilvasi-Nagy M (2006) About curvatures on triangle meshes. KoG 10: 13–18

CHAPTER 8

EXPERIMENTAL INVESTIGATION ON ABRASIVE WATERJET POLISHING

8.1 Introduction

In Chapter 2, jet machining techniques (i.e., air-jet and waterjet) and different aspects of their properties were described. Then, the abrasive waterjet machining methods and their capabilities in cutting and polishing processes were investigated. Using this technique for polishing is relatively new and all aspects of its characteristics are not uncovered yet. In most of the works on this topic, this method was used to polish a specific material and the process parameters were optimized for a particular task.

Since the main objective of this study is to develop a robotic system for abrasive waterjet polishing, it is required to design and built a "test rig" to generate actual abrasive waterjet and investigate the performance of this process on surfaces with the same properties as hydraulic turbine blades and determine the effect of different parameters on both the quality of the final surface and the productivity of this technique. This test bench can be used later to test a prototype which will be built as a result of this research (remaining as future work) and evaluate its performance in practice. Therefore, a part of this study is dedicated to design and manufacture of a test rig and perform preliminary tests with the AWJP process. The results can be used in the future tests to implement more complete experiments and obtain the optimal values of the AWJP parameters to polish hydraulic turbine blades and determine the productivity of the process.

8.2 Designing and dimensioning the test rig

The test rig should be designed in such a way that all ranges of the parameters which are considered in the experiments are properly covered. These parameters can be categorized as polishing parameters and design parameters. The polishing parameters which are included in the design considerations are: waterjet speed (pressure of water in upstream of the nozzle), water flow rate, abrasive feeding rate, nozzle diameter/angle/stand-off-distance, and traversing speed of the nozzle. The values of these parameters are adjusted according to the design of the experiments (DOE) methodology. The design parameters are the dimensions of the workpiece and the required volume inside the polishing zone in which the workpiece, polishing nozzle, and the robotic arm are located. In the first step of the design, based on other experimental studies reported in the literature, the required range of the main parameters are selected as listed in Table 8.1. However, the values

Table 8.1 Parameters and their ranges considered in the design of the test rig.

Parameters	Required range	units
Water pressure	10 - 150	bar
Water flow rate	0.5 - 40	l/min
Abrasive feeding rate	50 - 1500	gr/min
Nozzle diameter	0.5 - 2.5	mm
Nozzle angle	15 - 90	deg
Nozzle SOD	0 - 100	mm
Traversing speed	0 - 5	mm/s
Workpiece dimensions (L×W max)	250×250	mm
Polishing zone dimensions (L×W×H)	$1000 \times 800 \times 900$	mm

of some parameters may be found in the literature beyond these ranges, but considering stainless steel as the material of the workpiece (case study) the presented range is enough to test AWJP on samples of turbine blades.

Afterwards, the abrasive waterjet production cycle was designed. Several methods were developed to produce abrasive jet and can be mainly categorized in two types. In the first, the water and abrasives are mixed in a tank and then the mixture is pumped toward the nozzle. The diagram of the cycle of this system is illustrated in Fig. 8.1. During the process, a mixer is continuously mixing the water and abrasive to have a homogenized slurry. A pump sucks the mixture from the mixing tank and discharges the pressurized fluid to the nozzle. In the nozzle head, the mixture passes through an orifice and turns into abrasive jet which is pointed toward the workpiece. In this system, due to the existence of abrasive particles in the fluid a diaphragm pump is needed. A frequency converter is used to adjust the flow rate of the mixture by controlling the speed of the pump. In addition, a pressure valve is used to manually adjust the desired pressure (and so the speed of the waterjet). This valve returns the surplus fluid back to the mixing tank. This system is developed by Waterjet Technologies AG [111, 112] to be used for cleaning, sand blasting, deburring, polishing, decoating, etc.

In the second type, pure water is pumped toward a nozzle head where the abrasives are added to the water either before or after the orifice (similar to the abrasive waterjet cutting method). For this, two mixing methods can be used. If the abrasives are added to the water before the orifice, then a venturi (which works based on the venturi effect) is used to suck the mixture of water and abrasive which was prepared in a separate tank. If dry abrasive particles are mixed with waterjet after the orifice, then an ejector is used (which works again based on the venturi effect). In both cases, the pressurized pure water with the desired pressure and flow rate is produced using a similar cycle as the one illustrated in Fig. 8.1 and then fed to the nozzle head. The schematic of the two
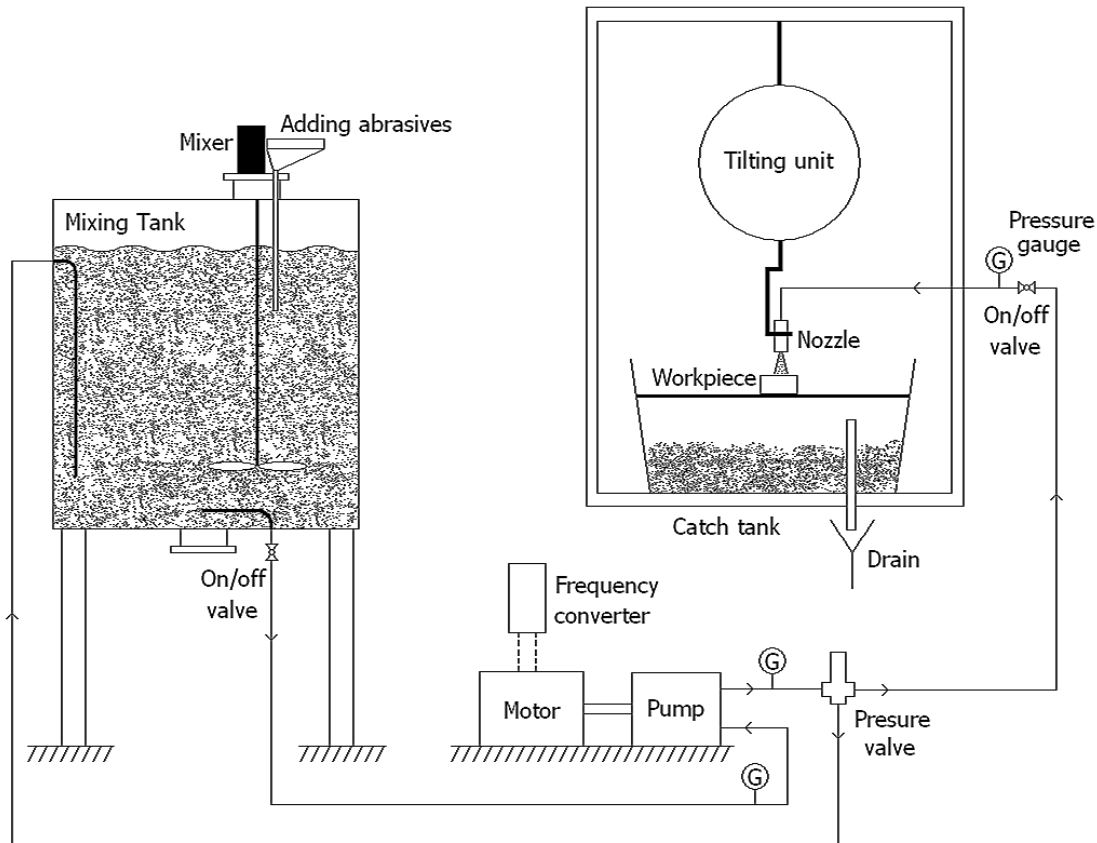
Figure 8.1 Diagram of the waterjet production cycle in which the water and abrasive are mixed before the pump.

mixing methods on the nozzle head are shown in Fig. 8.2.

Considering the three options shown in Figs. 8.1 & 8.2 and after consulting with Waterjet Technologies AG, their methodology was selected as the waterjet production cycle to be used in the test rig. Next, as advised by this company, the main components are chosen as listed in Table 8.2. The catalog of these components are provided in Appendix . As presented in Table 8.2, this system can provide a pressure up to 170 bar and a flow rate (based on Bernoulli's principle, it depends on the inner diameter of the nozzle (orifice) and the water pressure) up to 50 l/min.

In the next step, considering this design and the required characteristics (e.g., duration of the process, area to be polished, etc.), all other components of the test rig are designed. This test rig is mainly composed of three units:

1. **Mixing unit**: made of the mixing tank, mixer, and chassis. In this unit, the abrasive materials are manually added to the water to obtain the desired abrasive/water ratio and the mixer continuously mixes the suspension to have a homogenized mixture. The chassis is used to
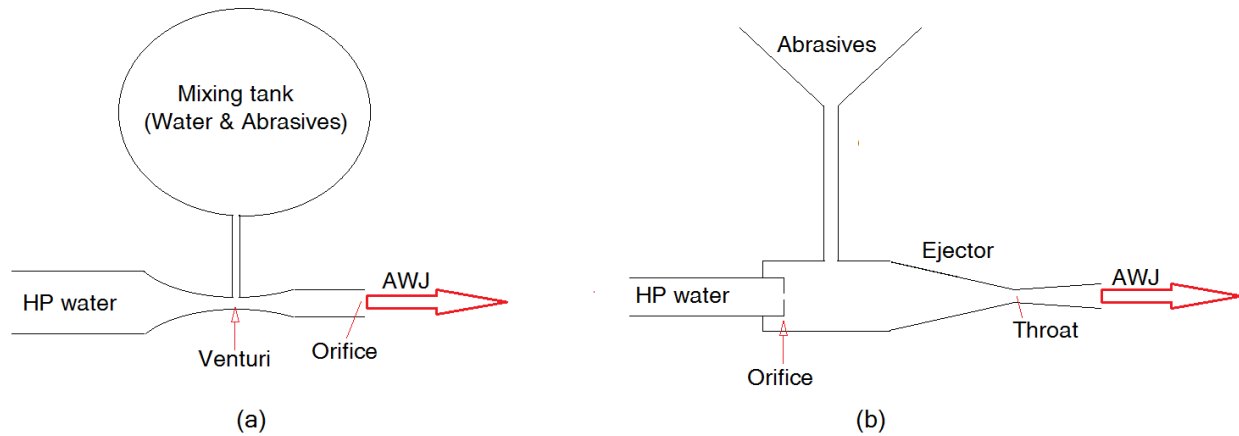
Figure 8.2 Schematic of mixing water and abrasives using (a) a venturi before the orifice and (b) an ejector after the orifice.

Table 8.2 Main components used in the design of the abrasive waterjet production system after consultation with Waterjet Technologies AG.

Component	Model	Properties
Diaphragm pump	Hydra-Cell D15	$P_{max} = 170$ bar, $Q_{max} = 50$ l/min
Electric motor	WEG	20 HP, 1750 RPM, 3-Phase, 550V
Pressure valve	Hydra-Cell C62	Pressure range 35 - 172 bar
Frequency converter	WEG CFW09	20 HP, 500 - 600V
Mixer	Lightnin EV5P25	1/4 HP, 350 RPM
Hosing	Parker	3000 PSI
Nozzle	MVT Type 929	Material: Sapphire, Size: 0.5 - 2.5 mm

place the tank in the proper elevation to maintain the NPSH$_r$ (required Net Positive Suction Head);

2. **Pump unit**: comprised of the pump, electric motor, frequency converter, pressure valve, safety valve, and gauges. This unit provides the desired pressure and flow rate for the tests;

3. **Polishing unit**: includes the polishing unit chassis, catcher tank, bench, tilting unit, nozzle head, septic tank, and transparent shields. In this unit, using the tilting unit the nozzle head is placed in a particular location and orientation (which are identified as polishing parameters) with respect to a workpiece (which is fixed to the bench inside the catcher tank) to perform the polishing process.

The 3-D model of the test rig including these three units and their components to be manufac-
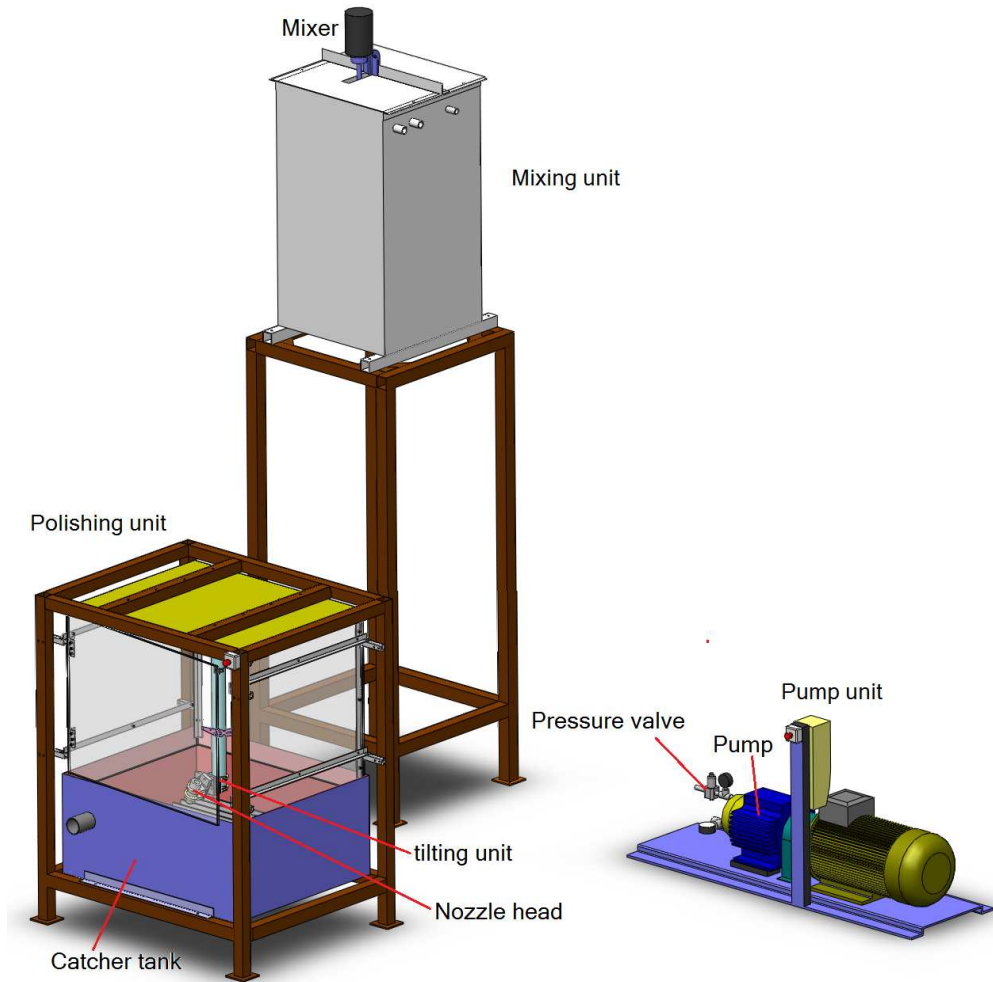
Figure 8.3 3-D model of the test rig including the these three units and their components to be manufactured.

tured (e.g., chasses, mixing tank, catcher tank, bench, tilting unit, etc.) is presented in Fig. 8.3. In this study, since the test rig is used to perform basic investigation on the AWJP process, no auto-mated or robotic system is used to manipulate the nozzle head. Instead, a tilting unit is used to move the nozzle with a fixed orientation with respect to the surface of a flat workpiece. This tilting unit is made of a cross axes X-Y table which is installed upside down on the ceiling of the polishing unit. The nozzle is then connected to this table through a rigid pipe.

8.3 Manufacturing the test rig and challenges

After designing all the structural components and selecting all the required equipment to be installed on the test rig, there were provided and then assembled in the site. The final installation
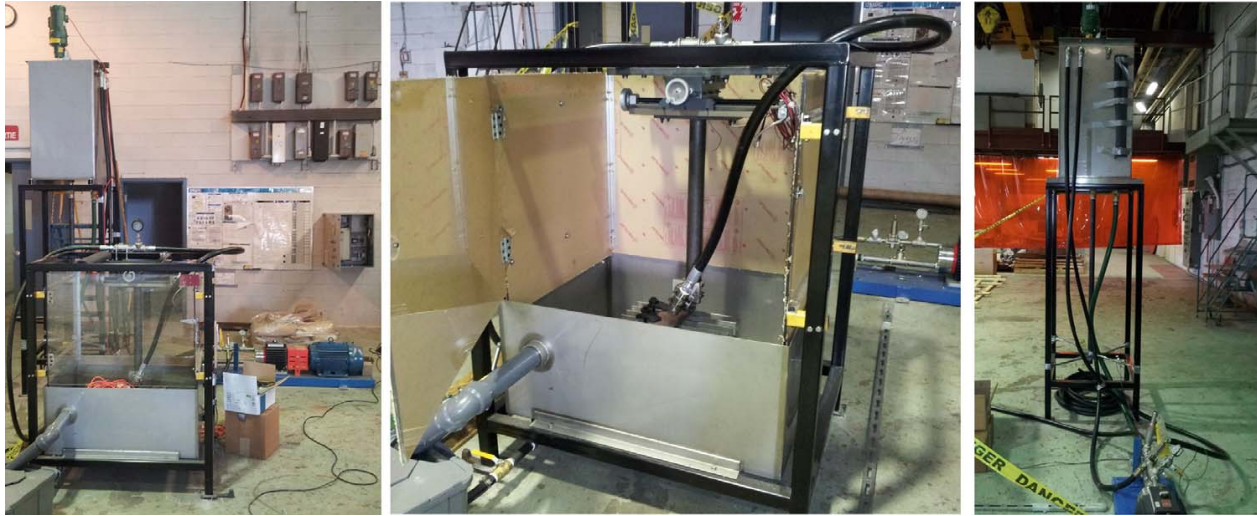
Figure 8.4 Final installation of the test rig (left) all three units; (center) the polishing unit with the nozzle fixed on the tilting device; (right) connection of the hoses to the mixing tank and the pump.

of the test rig designed based on consultation with Waterjet Technologies AG is shown in Fig. 8.4. The units are connected together through flexible medium pressure hoses. Two additional hoses are used to return the surplus fluid from the pressure and safety valves back to the mixing tank. The tilting unit is presented Fig. 8.5. One of the two axes of the X-Y table used for the planar movement of the nozzle head is actuated using a non-back-drivable worm gear DC motor and the other axis is operated manually. The nozzle head is attached to the vertical pipe though a particular tool designed to place this nozzle in the desired position and orientation so that the SOD and nozzle angle can be adjusted.

In the next step, the performance of the rig was tested with pure water. It successfully produces waterjet and all components operated according to the test plan. But, when the abrasives were added to the system, it failed to deliver them to the nozzle head. Thus, the test rig was comprehensively inspected for the possible problems. Then, the reasons for this failure were found as:

– accumulation of the abrasives at the bottom of the tank;
– resistance of the strainer installed on the entrance of the suction line against the flow of abrasives;
– accumulation of the abrasives inside the hoses of both suction and discharge (in particular after the pressure valve) lines.

Then, for troubleshooting of the test rig the following solutions were considered:

– installing the propeller at the bottom of the mixing tank;
– mounting the strainer in the vertical direction to maximize the entrance of abrasive in to the
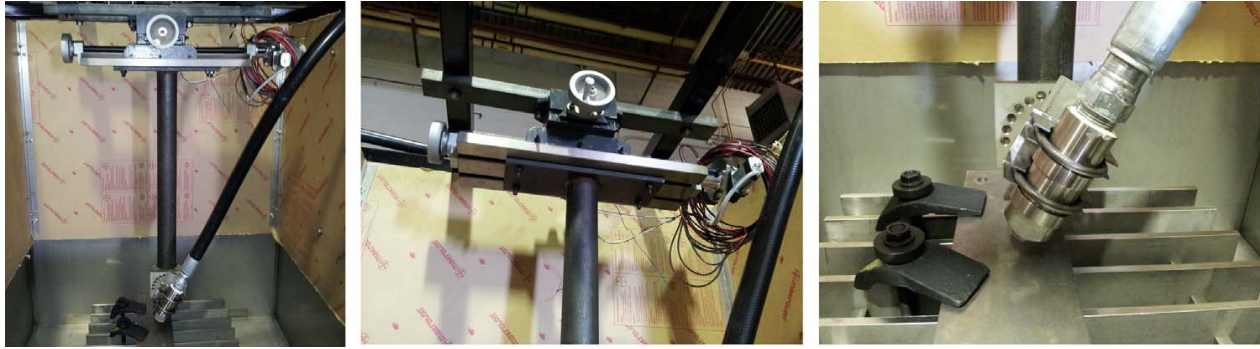
Figure 8.5 (left) final assembly of the tilting unit; (center) cross axes X-Y table actuated in one direction; (right) nozzle head attached to the tip of the tilting unit through parts with adjustable direction and position.

Figure 8.6 Comparing the worn plunger of the pressure valve (right) with the new one (left).

suction line;
– eliminating all low points of the hoses to prevent the accumulation of abrasives inside them;
– reducing the total length and the size of the hoses in the discharge line to increase the speed of the flow and decease the possibility of accumulation of abrasives.

After all these modifications, the abrasives successfully delivered to the nozzle and the abrasive waterjet was generated. But, the pressure valve could not resist the abrasive flow for a long time and its plunger and seat quickly worn out. In Fig. 8.6 the worn plunger is compared to the new one. At the end, considering all the problems with this method of waterjet production and also the possibility of damaging the pump with the abrasives, this technique seemed costly and thus, it was replaced with the third method shown in Fig. 8.2(b). The modified test rig is presented in Fig. 8.7. As shown in this figure, the dry abrasives are added to the pure waterjet inside the ejector.

Figure 8.7 Abrasive feeding system used to add the abrasives to the jet inside the ejector in the modified test rig.

The abrasive hopper was installed on the top of the polishing unit to compensate the problem of weak suction of the ejector at low water pressure. After evaluating the performance of the modified test rig via several tries, it was ready to perform the initial tests on the performance of the AWJP process. This test rig can be used to perform linear and planar polishing experiments, but with the current tilting unit only linear polishing can be done automatically.

8.4 Design of the experiments

The main objective of these experiments are investigating the effect of polishing parameters on the AWJP process (i.e., the final roughness of the polished surface, energy consumption, and the productivity of the process) and also study the shape of the material removal profile. For this, only linear polishing is considered as the initial experiments. In these experiments, based on other investigations reported in the literature, seven polishing parameters are determined as:

1. Nozzle diameter (D)
2. Abrasive type (A)
3. Abrasive feeding rate (W)
4. Nozzle angle (N)
5. Stand-off-distance (S)
6. Water pressure (P)
7. Number of passes (T)

Table 8.3 Definition of the levels of the controlled polishing parameters.

Parameters	units	Levels		
		1	2	3
D	mm	1.5	2	—
A	—	Garnet #120	Glass beads BT10	Corundum F100
W	gr/min	300	800	1200
N	deg	30	60	90
S	mm	20	50	70
P	bar	60	100	140
T	pass	2	4	6
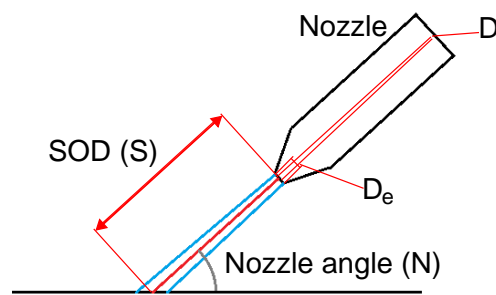
Figure 8.8 Definition of dimensional polishing parameters.

The definition of nozzle angle (N) and stand-off-distance (S) are presented in Fig. 8.8. In these tests, the traversing speed of the nozzle along the polishing line, v_t, is fixed to 1 mm/s. The values of the polishing parameters are selected based on the literature and consultation with Waterjet Technologies AG. To investigate the relationship between the polishing parameters and the outputs (to see if it can be described by a linear function or not), for each parameter, three values (here called as levels) are chosen except for the nozzle (orifice) diameter (D) where only two sizes were available. All the parameters and their levels to be used in the design of experiments (DOE) are listed in Table 8.3. As can be seen in this table, three types of abrasives are considered for the preliminary experiments. The size of abrasive particles are around 100 - 150 μm. Garnet and Corundum abrasives have blocky & sharp shapes but Glass beads have a round shape.

Since the final objective of this experiment is to generalize the relationship between the polishing parameters and the resultant quality of the surfaces of the turbines in large scale, the parameters of the Table 8.3 are redefined as listed in Table 8.4. In this table, $D_e = 4.5$ *mm* is the diameter of the throat of the ejector; W$'$ is the abrasive consumption per square millimeter of the surface; W$''$ is the abrasive/water ratio; Q (m^3/min) is the flow rate of water; ρ is the density of water; η is the

Table 8.4 Redefinition of the controlled input parameters.

Controlled parameters	Physical modeling of the parameters
D (mm)	D/D_e (-)
A (-)	A (-)
W (gr/min)	W' (gr/mm^2) & $W" = \frac{W}{1000\rho Q} \times 100$ (%)
N (deg)	N (deg)
S (mm)	S/D_e (-)
P (bar)	Power$= \frac{1}{\eta}QP = \frac{1}{2\eta}\rho a_o v_w^3$ (watt) & $v_w = C_j\sqrt{\frac{2P}{\rho}}$ (m/s) [113]
T (-)	$t = TL/v_t$ (sec)
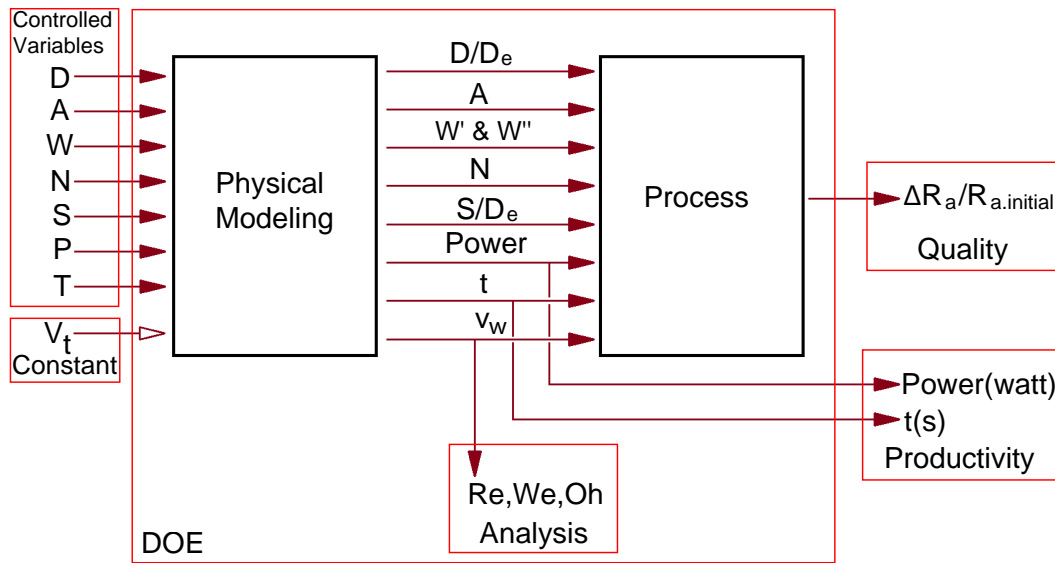
Figure 8.9 Diagram of the design of experiment with controlled input variables, constant input and outputs.

efficiency of the process which is used to calculate the required power to produce the jet; a_o is the area of the cross-section of the orifice; v_w is the speed of the water after the orifice (calculated using Bernoulli principle); C_j is the loss coefficient of the orifice; and L is length of the polishing line.

The diagram of the design of the experiments including the controlled input variables, input constant, redefined physical parameters, and desired outputs is illustrated in Fig. 8.9. In this figure, *Re* is the Reynolds number, *We* is the Weber number, and *Oh* is the Ohnesorge number. These dimensionless numbers will be used in future investigations to characterize the properties of the waterjet [114, 115]. With seven parameters and their associated levels presented in Table 8.3, if all possible combinations as full-factorial experiments (FFE) are chosen then, in total, $2 \times 3^6 = 1458$

Table 8.5 L_{18} orthogonal array of experiments (OAE) presented in Taguchi method

| Experiment | Parameter (level) | | | | | | | $\Delta R_a / R_{a.initial}$ | | | $R_{a.initial}$ | S/N | Mean |
no.	D	A	W	N	S	P	T	Trail 1	Trail 2	Trail 3	(μm)	Ratio	
1	1	1	1	1	1	1	1	***	***	***	***	***	***
2	1	1	2	2	2	2	2	***	***	***	***	***	***
3	1	1	3	3	3	3	3	***	***	***	***	***	***
4	1	2	1	1	2	2	3	***	***	***	***	***	***
5	1	2	2	2	3	3	1	***	***	***	***	***	***
6	1	2	3	3	1	1	2	***	***	***	***	***	***
7	1	3	1	2	1	3	3	***	***	***	***	***	***
8	1	3	2	3	2	1	1	***	***	***	***	***	***
9	1	3	3	1	3	2	2	***	***	***	***	***	***
10	2	1	1	3	3	2	1	***	***	***	***	***	***
11	2	1	2	1	1	3	2	***	***	***	***	***	***
12	2	1	3	2	2	1	3	***	***	***	***	***	***
13	2	2	1	2	3	1	2	***	***	***	***	***	***
14	2	2	2	3	1	2	3	***	***	***	***	***	***
15	2	2	3	1	2	3	1	***	***	***	***	***	***
16	2	3	1	3	2	3	2	***	***	***	***	***	***
17	2	3	2	1	3	1	3	***	***	***	***	***	***
18	2	3	3	2	1	2	1	***	***	***	***	***	***

tests have to be done. Obviously, performing this number of experiments is impractical. Therefore, to decrease the number of these preliminary tests to a reasonable value, the L_{18} orthogonal array of experiments (OAE) presented in the Taguchi method is used [116]. Consequently, the number of the experiments is reduced to 18. However, these tests are not enough to reveal the effect of each parameter on the results. Instead, Taguchi method shows the significance of the parameters on the results. Therefore, this method is suitable for preliminary tests to determine the key parameters. Then, the number of the parameters to be examined in further experiments can be reduced and consequently a more comprehensive DOE such as FFE can be used. The L_{18} orthogonal array for seven parameters with two/ three levels (presented in Table 8.3) is obtained as shown in Table 8.5 [116].

In this table, S/N is the signal to noise ratio which is used to measure and rank of the importance of the parameters with respect to each other. The objective of an engineering design can be classified as smaller-is-better, nominal-is-better, and larger-is-better [116]. In these experiments, the final objective is to maximize the ratio of the difference between the initial and final roughnesses over the initial roughness as $\Delta R_a / R_{a.initial}$. Consequently, the S/N ratios for larger-is-better conditions
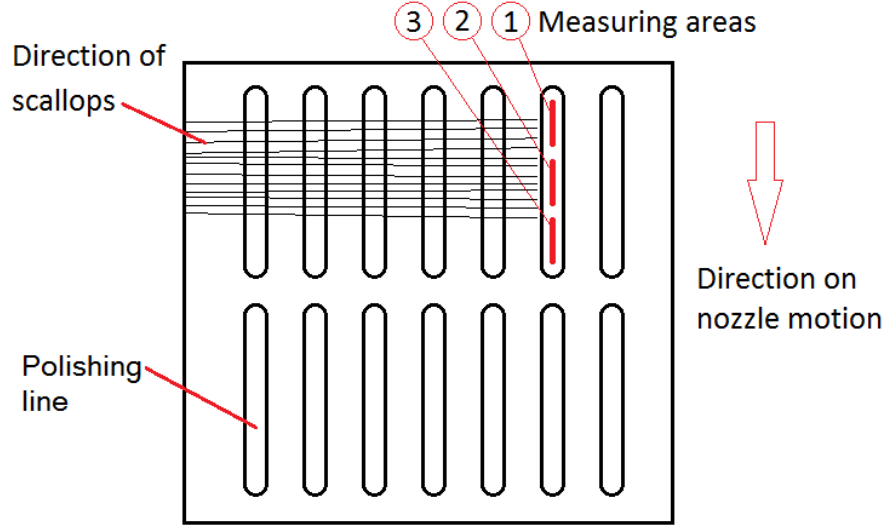
Figure 8.10 Direction of the polishing lines with respect to the scallops on the workpiece and the locations of the measurements of the roughness before and after the process.

are obtained as [116]:

$$S/N_{LB.j} = -10\log\left(\frac{1}{n}\sum_{i=1}^{n}\frac{1}{y_{ij}^2}\right) \tag{8.1}$$

where y_{ij} is the measurment of the abovementioned ratio at the ith trail of the jth experiment. Also, n is the total number of trails for each experiment (with these experiments, one has $n = 3$).

8.5 Experimental tests and preliminary results

As mentioned earlier, in these experiments linear polishing with several passes over a single line is considered. The properties of the workpieces used in this experiment are provided in Table 8.6. As illustrated in Fig. 8.10, the polishing lines are perpendicular to the direction of the scallops on the surface in which the roughness of the surface is maximum. The minimum length of each line to be polished is considered to be 40 mm. As depicted in Fig. 8.10, the roughness of the surface is measured in three locations along each line before and after the tests. Also, errors in the measurements of the roughness is estimated to be less than ± 15 μm (with 95% of confidence level). In the experiments, the roughness of the surface is measured by R_a (i.e. the arithmetic average roughness value). R_a only gives the average value of the distances of the hills/valleys from the mean profile of the surface. However, this parameter does not give any information about the texture of the surface and thus, as illustrated in Fig. 8.11 surfaces with different textures can have the same R_a. With this experiment, the texture of the surface is mainly constituted by of parallel

Table 8.6 Properties of the workpieces used in experiments.

Property	Description
Material [117]	ASTM A743 CA6NM
Chemical composition−% (Max) [117]	$C_{0.06}Mn_1Si_1P_{0.04}S_{0.03}Cr_{14}Ni_{4.5}Mo_1Fe_{85}$
Yield strengh [117]	100 ksi
Surface hardness [117]	Brinell hardness (HBW) 268
Dimension	5" × 5"
Surface machining method	Sawing (with trace of parallel scallops on the surface)
Surface roughness	Measured in the range of 3.3 - 5.3 μm
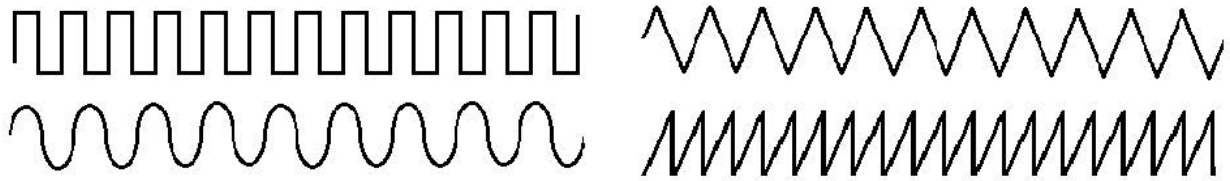
Figure 8.11 Different profiles with almost the same value of R_a.

scallops.

Next, all these experiments are implements according to the Taguchi orthogonal array. Examples of the polished surfaces are provided in Fig. 8.12. Then, the mean values for both initial and final roughnesses in each experiment are calculated and presented in Fig. 8.13. As illustrated in this figure, the final desired roughness $R_{a.dis}$ for the surface of turbine blades is expected to be around 0.3 μm where the best efficiency is expected in hydraulic turbine industry. As shown in Fig. 8.13, in some tests, the roughness of the surface is improved (shown by downward green arrows), in some others the roughness is increased (shown by upward red arrows), and in the rest it is not changed (shown by hollow red circles). However, as mentioned in Table 8.6, the initial surface was not uniform. This problem undesirably affected the result of these tests. Therefore, to be able to interpret the results of these preliminary experiments, as presented in Fig. 8.14, instead of the $R_{a.final}$, the ratio $\Delta R_a/R_{a.initial}$ is calculated which presents the amount of the improvement of the roughness of the surface for its given initial value.

Taking into account the ratios of Fig. 8.14, among all 18 experiments, in test no. 8 the best improvement was obtained. Additionally, with the polishing parameters used in tests no. 6, 7, and 8, the lowest roughnesses were achieved respectively around 2.30, 2.26, and 2.13 μm (with 95% of confidence level). The areas polished in these three tests are presented in Fig. 8.15. As can be noticed from this figure, the other important aspect which should be considered in the AWJP

Figure 8.12 Polished lines on the workpieces obtained as the preliminary results of experiments on the AWJP process

process is the depth of penetration into the workpiece. In polishing process, it is very important to minimize the amount of material removal from the surface and only improve its quality. Thus, obtaining a good quality at the cost of high penetration is not desirable. To evaluate the depth of penetration in these three experiments, the corresponding workpiece was scanned with a CCM machine and by measuring several cross-sections along each of the polished lines, the average shapes of the profiles are obtained and shown in Fig. 8.16. As shown in this figure, in test no. 7, $\Delta Z \approx 540~\mu m$ and in test no.8, $\Delta Z \approx 105~\mu m$ which are not desirable and the surface is almost machined, while in test no.6, $\Delta Z \approx 24~\mu m$. Thus, in test no. 6 the best roughness with minimal penetration was obtained.

In Chapter 7, with the ejector throat used in these experiments, the appropriate pitch distance was estimated to be 4 mm. Knowing this distance, traversing speed of the nozzle, and the number of passes, the area of the polished surface per minute is calculated. Then, it is used to estimate the amount of consumption of the abrasives and energy (and so power) per square millimeter and the
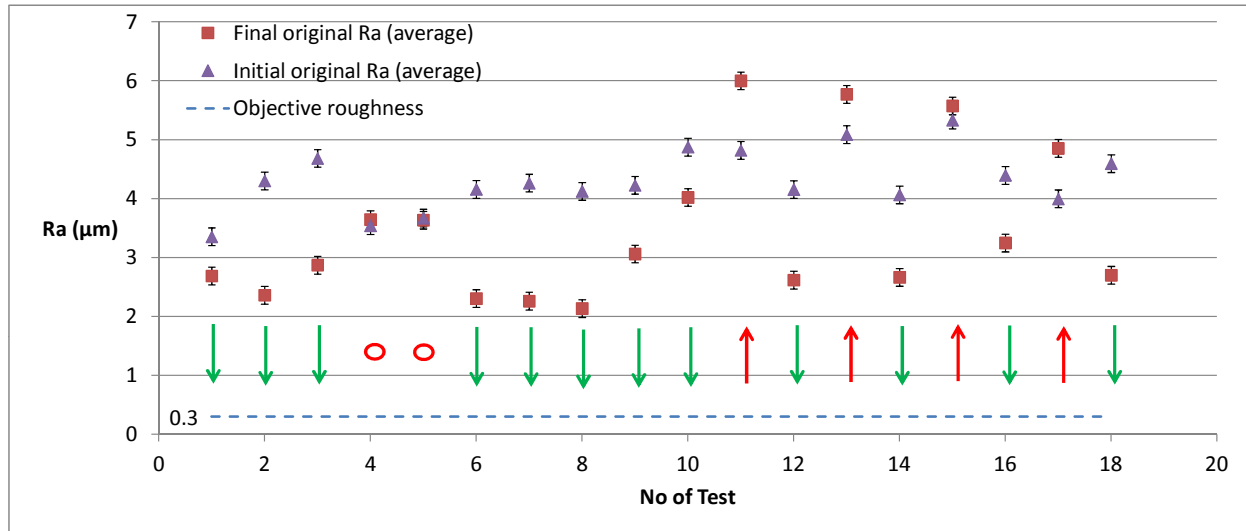
Figure 8.13 Average values of the initial and final roughness obtained in the experiments as well as the final objective roughness.
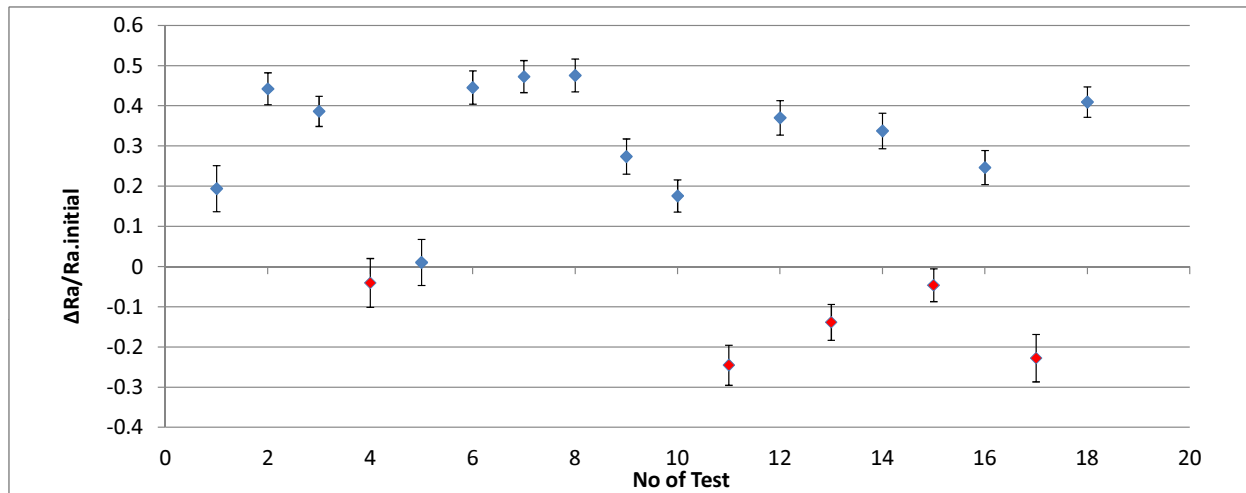
Figure 8.14 Average values of the ratio of the difference between the initial and final roughnesses over the initial roughness obtained for each test.

results are provided in Table 8.7. Afterwards, the relationship between the energy consumption per square millimeter and the improvement in the quality of the polished surface is investigated. This evaluation is done for each abrasive type independently (because there is no correlation between the abrasives) and the results are provided in Fig. 8.17. In this figure, to better understand the effect of the used energy on the improvement of the roughness, this relationship is presented separately for each nozzle diameter. Considering, the two diagrams presented in this figure, possibly, there

Figure 8.15 Examples of polished line in (left) test no. 6; (center) test no. 7; (right) test no. 8.
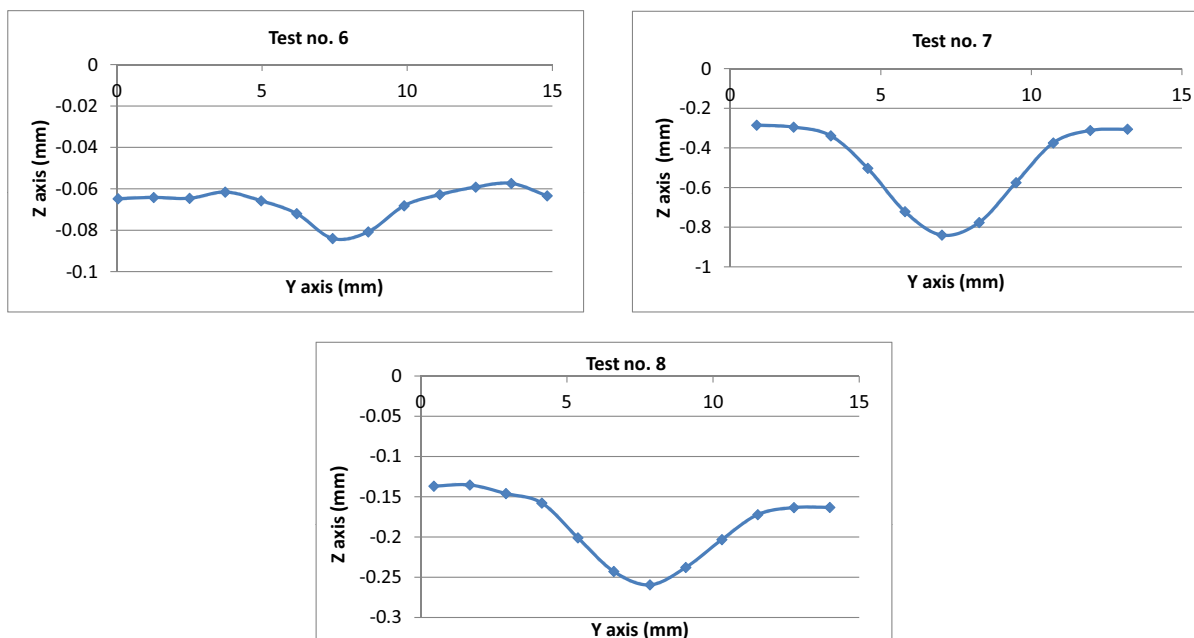
Figure 8.16 Profile of the material removal from the surface and the depth of penetration in test no. 6: $\Delta Z \approx 24 \ \mu m$; test no. 7: $\Delta Z \approx 540 \ \mu m$; test no. 8: $\Delta Z \approx 105 \ \mu m$.

is an optimal value for the energy consumption per square millimeter to give the highest quality of the surface, but there is no correlation between the diagrams to find this value. This shows that with seven input parameters, the number of tests implemented in Taguchi method is not enough to describe this relationship. Therefore, these graphs are only presented to give a clue for further tests where a full-factorial investigation will be done on the process and these relationships can be better observed.

Additionally, the relationship between the abrasive/water ratio (W'') and the improvement of the roughness of the surface is illustrated in Fig. 8.18. As shown in this figure, with garnet and glass beads, by increasing the W'', there are some improvements in the roughness of the surface. But, with corundum no particular correlation can be concluded. Thus, similarly to the evaluation of the effect of the energy, it seems that this relationship cannot be properly determined with only

Table 8.7 Evaluation of the productivity of the process with the preliminary experiments .

Test no	Polished area (mm^2/min)	Abrasive feeding rate (gr/mm^2)	Power (watt)	Energy/area (J/mm^2)	$\Delta R_a/R_{a.initial}$ (Mean)
1	120	2.5	1161.5	580.7	0.194
2	60	13.3	2499.1	2499.1	0.442
3	40	30	4139.8	6209.7	0.386
4	40	7.5	2499.1	3748.7	-0.040
5	120	6.7	4139.8	2069.9	0.010
6	60	20	1161.5	1161.5	0.446
7	40	7.5	4139.8	6209.7	0.473
8	120	6.7	1161.5	580.7	0.476
9	60	20	2499.1	2499.1	0.273
10	120	2.5	4442.9	2221.4	0.176
11	60	13.3	7359.6	7359.6	-0.245
12	40	30	2064.9	3097.3	0.370
13	60	5	2064.9	2064.9	-0.138
14	40	20	4442.9	6664.3	0.338
15	120	10	7359.6	3679.8	-0.046
16	60	5	7359.6	7359.6	0.247
17	40	20	2064.9	3097.3	-0.228
18	120	10	4442.9	2221.4	0.409

18 experiments and a full-factorial test should be considered in the next step of the DOE.

Table 8.8 Response table for S/N Ratios obtained for $(\Delta R_a + c)/R_{a.initial}$.

Level	D	A	W	N	S	P	T
1	-4.243	-7.849	-7.881	-18.019	-7.014	-12.818	-6.269
2	-14.271	-9.574	-14.923	-6.186	-6.083	-4.975	-10.072
3	—	-10.348	-4.967	-3.566	-14.674	-9.978	-11.43
Delta	10.027	2.499	9.955	14.453	8.591	7.844	5.161
Rank	2	7	3	1	4	5	6

8.6 Analysis of variance (ANOVA)

After designing the experiments and performing the tests, the analysis of variance on the results is done. In Eq. (8.1), only the magnitude of $\Delta R_a/R_{a.initial}$ is considered to calculate the S/N value while in the results, there are also changes in the signs of these ratios. Therefore, by adding the constant $c > |\Delta R_{a.min}|$ to ΔR_a, as $(\Delta R_a + c)/R_{a.initial}$, all these ratios will have positive values.
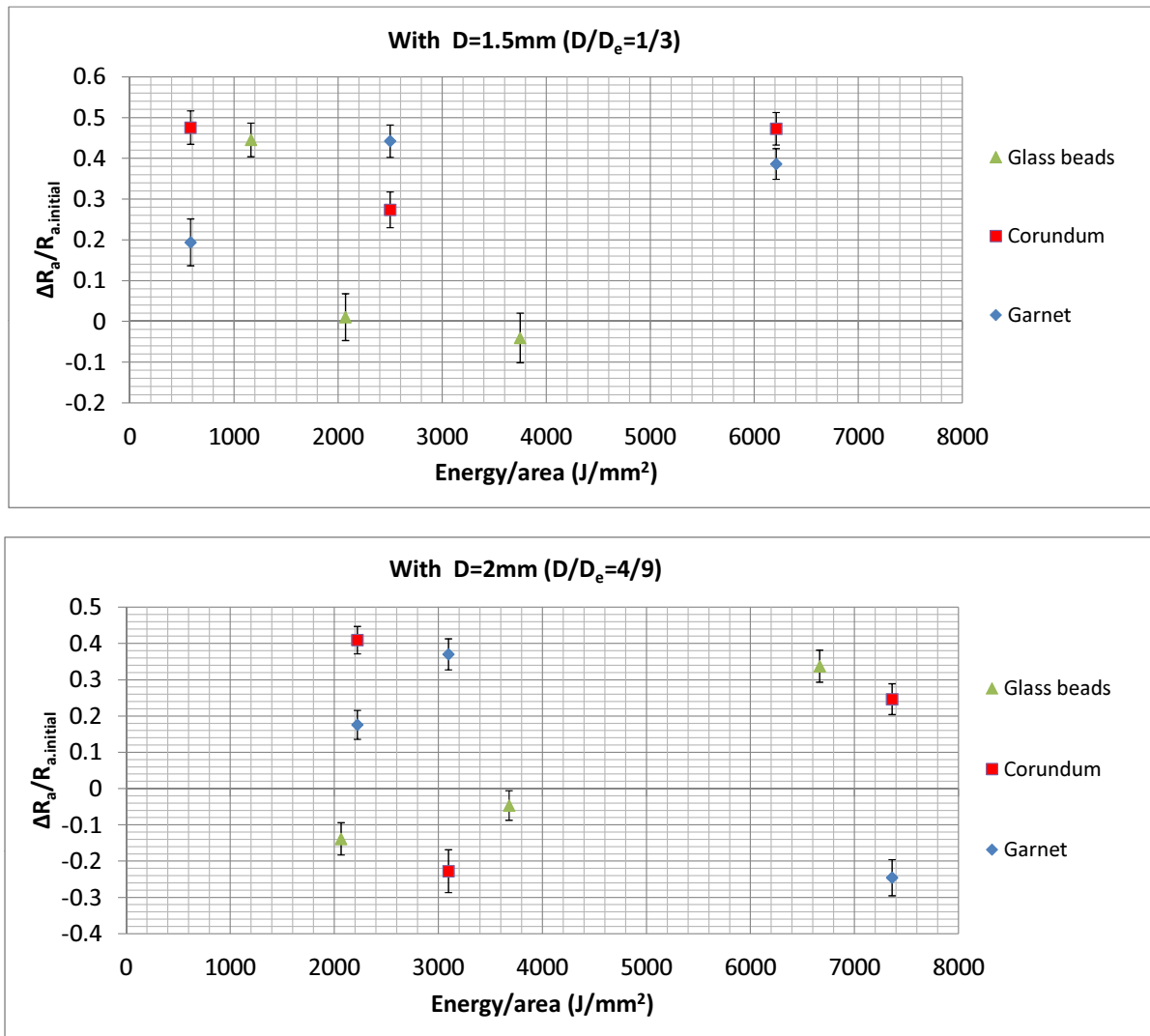
Figure 8.17 Relationship between the used power and improvement in the roughness of the surface $\Delta R_a/R_{a.initial}$, (up) with D=1.5 and (down) with D=2 mm.

Then, the S/N_{LB} ratio is used to determine the importance of polishing parameters on the results of the experiments. As presented in Table 8.8, these ratios are used to rank the parameters from the most to the least important ones. The plot of S/N_{SB} ratios are presented in Fig. 8.19. The difference between the highest and lowest values of the S/N ratios calculated for each parameter shows the effect of that parameter on the results (i.e., higher the difference, higher the importance of that parameter). Consequently, Table 8.8 reveals that nozzle angle (N) and the nozzle diameter (D) have the highest impact on the results, while the number of passes (T) and the type of the abrasive (A) have the lowest effect. However, as mentioned earlier, the Taguchi method does not reveal the optimal values of the parameters.

Next, the ANOVA of the S/N ratio is done and the results are provided in Table 8.9. The F-value
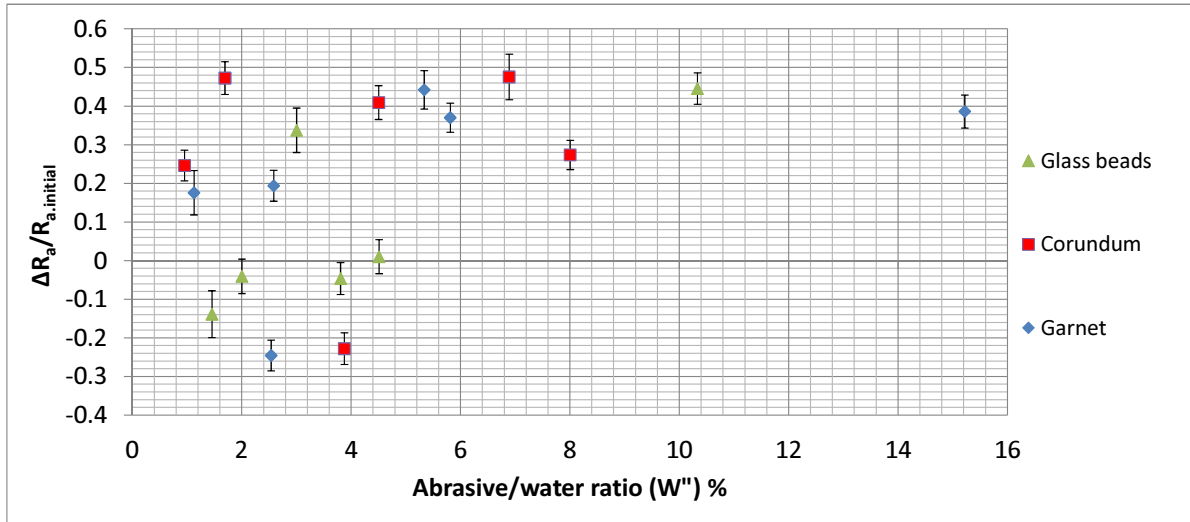
Figure 8.18 Relationship between the abrasive/ water ratio (W'') and improvement in the roughness of the surface $\Delta R_a/R_{a.initial}$.
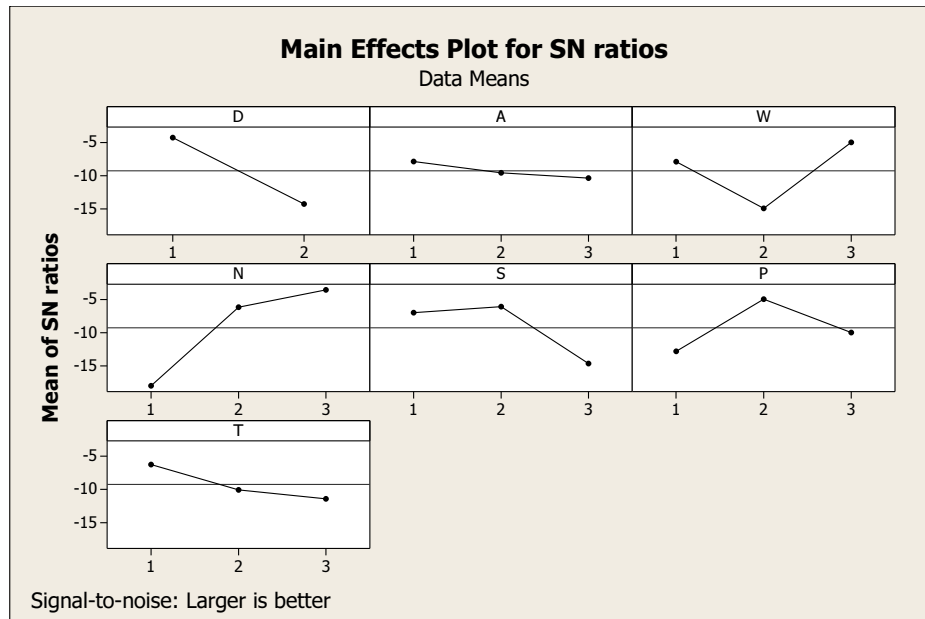
Figure 8.19 Main effects plot for S/N ratios obtained for $(\Delta R_a + c)/R_{a.initial}$.

is then calculated and compared to the $F_{0.1,\{1,2\},4}$ (i.e., 90% confidence level). This comparison shows that these experiments can reveal the effect of the parameters D and N on the results with 90% of confidence. But, for other parameters, the errors in describing their importance are beyond this confidence. With some parameters such as P, T, and A, as shown by P-value, these errors are

Table 8.9 Analysis of variance for S/N ratios obtained for $(\Delta R_a + c)/R_{a.initial}$.

Source	DF	Seq SS	MS	F-value	$F_{0.1,\{1,2\},4}$	P-value
D	1	452.45	452.447	6.55	4.54	0.063
A	2	19.63	9.816	0.14	4.32	0.872
W	2	314.38	157.191	2.27	4.32	0.219
N	2	711.52	355.758	5.15	4.32	0.078
S	2	266.67	133.336	1.93	4.32	0.259
P	2	189.25	94.624	1.37	4.32	0.352
T	2	85.88	42.94	0.62	4.32	0.582
Residual Error	4	276.38	69.095			
Total	17	2316.16				

respectively 35.2%, 58.2 and 87.2%. This issue does not mean that the model in wrong, on the other hand, it only cannot properly describe the effect of these parameters on the results. However, the pearson correlation coefficient shows 88.1% of confidence of the DOE.

8.7 Discussion and future works

Although the DOE used to obtain the relationship between the inputs and outputs of the preliminary experiments faced some errors in determining the importance of polishing parameters, its results can be used as a basis to design a more precise DOE in which the optimal values of each parameter can be estimated. Considering the maximum amounts of S/N ratios presented in Table 8.8 and Fig. 8.19, it seems that D1 and N3 (parameter+level) can result in better roughness with 90% of confidence level. Therefore, they are considered as the most important parameters to be used in the future DOE with their most preferred levels. Additionally, the results show that W3, S2, and P2 may be the other parameters and levels to be used in the design of future tests (with up to 35% error). But, with this model no meaningful prediction can be made for A and T.

For future experiments, the surface of the workpieces should be grinded so that their initial roughness is uniform. This will decrease the errors in the future investigations. Then, by fixing the polishing parameters around the suggested levels, the effect of each parameter is individually investigated. Afterwards, using only the most important parameters, a full-factorial experiments can be implemented to obtain their optimal values which provide the best quality of the surface while the consumption of energy and abrasives are kept at minimum (better productivity).

CHAPTER 9

GENERAL DISCUSSION

9.1 Selection of the architecture of the polishing robot

In turbine manufacturing, it is required to polish all surfaces of the blades of the turbines which are in direct contact with water to obtain the desired quality. Due to the particular advantages of abrasive waterjet polishing as a novel non-conventional method, it was chosen to be used for this task. In this process, the nozzle should be properly manipulated on the surface of large blades as well as their narrow edges to uniformly polish these areas. For this, AWJP was studied and the main parameters affecting its performance were determined. Then, its special properties and requirement were described in Chapter 2. In the same chapter, the requirements of a robotic system to perform this task were determined.

Next, different types of robotic arms(e.g., serial, parallel, and hybrid) as well as their advantages and drawbacks were investigated. To choose the best option for AWJP, these advantages and drawbacks were compared to the requirements of this application.

Serial robots are the most common robots used in industry for different applications. Despite having many capabilities, these robots suffer from some problems which weaken their applicability in AWJP process. Mainly, these problems are:
– the motors would be close to the humid area;
– the possibility of contamination of joints, moving parts, and electrical components with wet abrasives;
– the existence of errors in the positioning of the end-effector due to the open kinematic chain of the robot. Since the workspace of this robot depends on the length of its linkages, having larger workspace can result in higher errors.

Considering the requirements of the AWJP process, linkage-driven parallel robots have several advantages comparing to their serial counterparts. For example, their motors can be installed on the base and they typically have higher stiffness, rigidity and dexterity. Despite these advantages, they also suffer from some drawbacks such as:
– a small workspace and weak compactness;
– the limited rotational capability due to the physical limits of the joints;
– the possible contamination of mechanical parts by abrasives similarly to serial robots.

Cable-driven parallel robots inherit not only some advantages of linkage-driven parallel mechanism, but also gain additional characteristics which allow them to be a preferred option in an

application such as AWJP of large turbines. They have a simple structure, light and low inertia moving parts, typically low friction, and large workspace. More importantly, since only cables are located inside the polishing environment, contamination and humidity have minimum impact on the performance of these systems. However, the rigidity of these mechanisms and their maximum payload depend on the thickness and the pretension of the cables. In addition, due to the flexibly of the cables, they may vibrate during the process. This can weaken the stiffness of the mechanism. But, if the amplitude of the vibration is small enough its negative effect is negligible. On the other hand, this vibration could be beneficial and protect the cables from being contaminated by the sticky abrasives. It should be noted that in AWJP, the precision is mostly important in following the desired trajectory and the exact positioning of the jet towards a particular point is not required.

Hybrid robots are a type of robotic manipulators with a body made of a combination of different kinematic chains. The structure of these robots can be chosen according to the requirements of the desired task. Thus, for AWJP of hydraulic turbine blades, they can be designed in such a way that the main requirements of this process including large workspace and mounting the motors and mechanical parts far from the polishing environment are properly satisfied. However, these mechanisms may also inherit some drawbacks of the individual architectures used in their body, e.g., installing the actuators close to the nozzle if serial systems are used, small workspace in the case of linkage-based parallel structures, and weak compactness and limits in cable tensions when cables are used.

In summary, all these robotic arms have some advantages but also few disadvantages to be used in AWJP process. Therefore, the selection of the best candidate for the design of a robot is a trade-off between their properties considering the requirements of the task. Finally, it was concluded that cable robots (fully restrained types) suffer from low compactness and limited cable tensions. Serial robots are the weakest choice to work in a humid and contaminated environment. Linkage-driven parallel robots have weak compactness, contamination problem and also small workspace. On the other hand, hybrid robots can be designed by combining the aforementioned mechanisms in such a way that their drawbacks are minimized and the main requirements of the AWJP are optimally satisfied. Consequently in this study, a hybrid structure was suggested as a basis for the design of a robot well-suited for AWJP of hydraulic turbine blades.

Regarding to this discussion, the conceptual design of the 5-DOF hybrid AWJP robot illustrated in Fig. 9.1, is proposed. This robot is a serial-parallel mechanism in which a 3-DOF parallel architecture drives the nozzle to the desired position and a 2-DOF wrist maintains the desired orientation of the nozzle. The parallel part is a cable-driven mechanism in which six cables symmetrically surround an actuated prismatic joint which is attached to the center of the base through a passive universal joint. The prismatic joint is rigidly connected to the MP (assumed to be welded to it) to constrain its orientation with respect to the inertial frame attached to the BP at the center of the
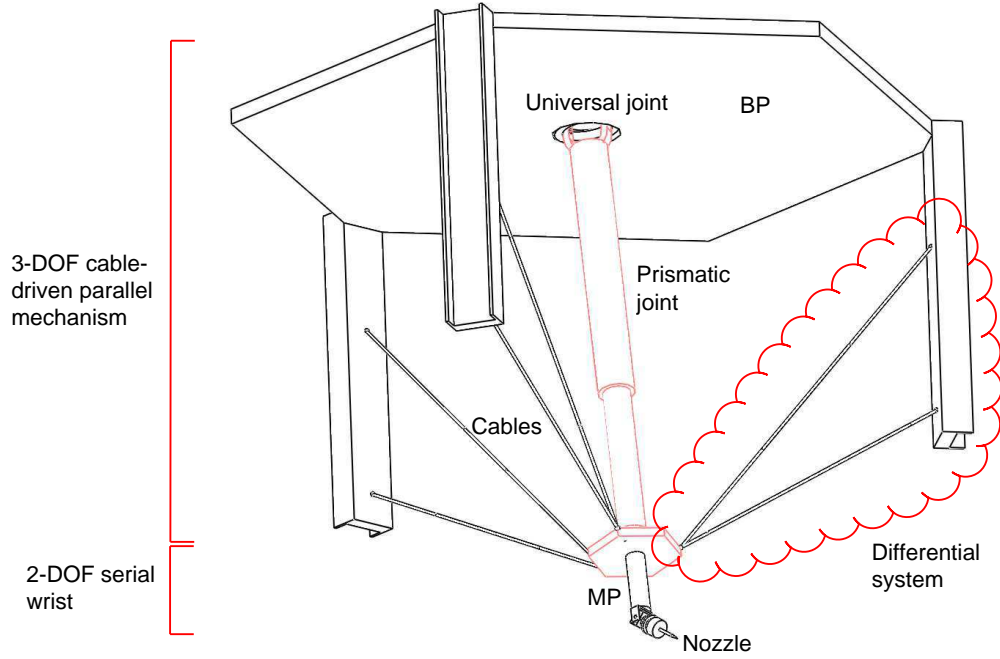
Figure 9.1 Conceptual design of a 5-DOF serial-parallel hybrid robot.

universal joint. This way, the problem of weak compactness of the cable-driven system is solved. In addition, with the help of the central prismatic joint, the stiffness of the mechanism is increased and the negative effects of cable vibrations are reduced. By installing this system from the ceiling a large space can be covered by the mechanism.

On the MP of the cable-driven mechanism, a 2-DOF wrist with serial architecture is installed. To solve the problem of the 2-DOF serial wrist, the two motors can be embedded on the base of the robot (ceiling) and their power can be transmitted to the joints of the wrist using cables. These cables can pass through the body of the prismatic joint and the arrangement illustrated in Fig. 9.2 is used to cancel the effect of change in the length of the prismatic joint on the total length of the driving cables.

This robot should be able to resist the external wrench exerted to its MP by the abrasive waterjet. This wrench is produced due to the weight of the MP and the reaction force of the nozzle. This force is calculated using Newton's second law and fluid dynamics as:

$$\mathbf{f} = -\rho Q \Delta \mathbf{v}, \tag{9.1}$$

where ρ is the density of fluid jet, Q is the flow rate of slurry and $\mathbf{v}$ is the velocity vector of the jet.
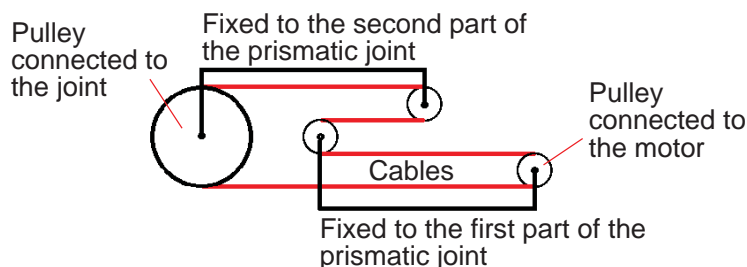
Figure 9.2 Arrangement of the cable and pulley system mounted inside the prismatic joint to transmit the power of a motor installed on the BP to a rotational joint of the wrist.

9.2 Differentially driven cable mechanism

In the next step of this research, the 3-DOF cable-driven part of the proposed 5-DOF hybrid robot is taken into account. Then, in the first two articles (Chapters 5 and 6), improvement of workspaces of cable-driven parallel robots and subsequently, the case study of this research are focused.

Due to unilateral property of cables, redundancy in the number of cables in cable-driven robots is necessary. Furthermore, using more cables can lead to improvement of the workspace and payload of the robot. However, using more cables generally means having more actuators and a complicated control strategy. Thus, in this research, it was proposed to used differentials in the architecture of cable robots to keep the number of actuators at minimum (i.e., $n+1$ in a n-DOF mechanism), while increasing the number of cables. A closely related design to differentials has been proposed in [118, 119] for building cable robots. However, it was not recognized as a part of a much larger family of architectures based on differentials as demonstrated in this research.

When a differential is used to drive the two outputs of a mechanism using a single actuator, an additional degree of freedom is generated and that mechanism is under actuated. Thus, to control all outputs, additional constraints should exist. Also, by combining the differentials (in serial and/or parallel patterns) more outputs can be obtained and therefore, even more constraints are needed. With commonly used differentials, such as the differential of the driving wheels of a car, these constrains are imposed by the environment of the system (e.g., contacts of the wheels with the ground). Since the proposed robot should be statically determined, these constraints have to be created within the body of the mechanism. Therefore, to use differentials in the body of the robot it was needed to know how independently actuated cables can be replaced by differentials and how the MP of the mechanism can be fully constrained.

In the first step of the investigation, the scope of the study was limited to planar robots only actuated with cables (i.e., with no rigid connection between the BP and the MP). Then, through

different types of differentials (e.g., cable and pulley, bevel gear differential, etc.) several cables were actuated using only one motor. It was shown that the tension forces of all cables driven by the same differential are related. In ideal frictionless condition these tensions are assumed to be equal which means better distribution of the force among cables and thus, higher payload of the robot. However, with the same tension in all cables of a differential, it is not possible to generate constraint forces in arbitrary directions. Instead, only one independent force can be generated which is the resultant force of all these cables. So, it was shown that if cable differentials are used in the structure of a cable robot, then their resultant forces should be considered in the kinematic analysis, not the forces of individual cables. Considering these forces, such a mechanism is fully constrained if the force-closure condition is satisfied.

In the next step, the effect of using differentials on the kinematic properties of a cable robot was investigated. It was shown that the resultant force of a cable differential system has a particular property which gives it a significant advantage. Unlike the force vector of a single actuated cable, the direction of the resultant force of a differential is not fixed toward a particular point (i.e. the attachment point of a single cable). Instead, it changes within the plane of the differential (where all cables are coplanar). This property can be used in the design of a cable robot in such a way that its WCW is improved. In addition, since several cables are used in a differential, with the same actuators, larger WFW can be expected. By comparing the wrench-closure and wrench-feasible workspaces of differentially driven planar cable robots with several fully driven types having similar architectural properties and the same number of actuators, improvement of both workspaces was shown. However, the results revealed that the differentials cannot have the same performance as when all their cables are independently actuated.

Analysis of the particular property of the resultant force also unveiled another important aspect. The same property that increases the range of variation in the direction of the resultant force (the positive effect), can decrease its magnitude (the negative effect). Thus, the optimal design of a cable differential is a trade-off between increasing the range of variation of the direction of the resultant force and decreasing its magnitude. This issue should also be taken into account in the selection of the number of cables of a differential and their arrangement. Indeed, unlike fully driven cable robots where using more cables can improve the kinematic properties of the mechanism, with the proposed systems, these properties may be either improved or weakened. In conclusion, in planar cable robots, with a proper design and selection of the arrangement of the cables, using differentials, the kinematic properties of the robot (in particular its WCW and WFW) can be improved.

Afterwards, the arrangement of the cables of a differential was synthesized to generalize the idea of using differentials for planar cable robots. For this, an algorithm was developed and considering the number of connections between the MP and the BP, the total number of possible arrangements of cable differentials with two to ten connections was calculated. Next, considering physical limits

and practical issues, valid arrangements with 2, 3, and 4 connections were obtained. Then, using different mechanisms (namely, bevel gear, planetary gear, cables and pulleys) all valid differentials with 2, 3, and 4 connections were presented. The presented method can also be used for higher number of connection.

In the next step, the application of the proposed differential systems in spatial robots was investigated. In this case, in addition to the planar differential, spatial types can also be used. The latter have the same structure as the planar ones but their cables are distributed in a 3-D space. Clearly, to have such differentials, the cables should connect the MP to the BP in at least three locations. Similarly to the planar case, the same property exists for the direction and the magnitude of the resultant force of a spatial differential. The only difference is that in this case, the direction of the resultant force can change in a 3-D space. This property is helpful in the increase of the workspaces of the spatial robots. However, the same limits should be considered in their design to obtain the optimal arrangement of cables.

After evaluation of their properties, three planar differentials were used in the conceptual design of the proposed robot. In this robot, if all cable differentials are disconnected from the MP, then it gains two rotational DOF. Thus, to fully constrain the MP at least three cable differentials (which are producing three unilateral constraining forces) are needed. Each differential has two cables connecting a point of the MP to two points on the BP (c.f. Fig. 9.1). Consequently, three actuators drive six cables and the fourth one drives the prismatic joint to fully constrain the system. Next, the performance of this cable-driven mechanism was analyzed. For this, first the direct and inverse kinematic as well as the direct and inverse velocity problems were solved. In the analysis of differentially driven mechanisms, conversely to fully driven designs, the total length of all cables of each differential, its speed, and its acceleration should be considered, not these of each individual cable. Afterwards, the relationship between the actuation forces and the external wrench exerted to the MP was obtained. In the Jacobian matrix which defines this relationship, the sum of unit vectors along cables of each differential should be used. Consequently, although there are six cables and one prismatic joint, the Jacobian matrix has a 4×6 structure. It was shown that since the MP is rigidly attached to the prismatic joint, the vectors of the twist (i.e., rotational and linear velocities of the MP) are related. Therefore, this mechanism has 3-DOF and one degree of redundancy (four actuators).

Next, the effect of differentials on the WCW and WFW of the proposed mechanism was investigated. For this, two performance indices, namely I_{WCW} and I_{WFW} were defined to evaluate these two workspaces. These indices are defined in a normalized way so that their range of variations are respectively [1/2, 1] and [1/2, 2]. Also, the limits of the tensions of the cables and the minimum wrench to be resisted on the MP of the mechanism were chosen. Considering these indices, a proper objective function was defined. Finally, genetic algorithm was used to find the best design

parameters which maximize the volume of the two workspaces.

In the calculation of the WFW of the differential cable robots presented in the first two articles (Chapters 5 and 6), since the MP of the mechanisms were fully constrained by the actuators (either using the differentials or the prismatic joint), the WFW is a subset of the WCW. However, in general this proposition may not be true. For example, in cable suspended robots the WCW may not exist while the robot has a WFW. In addition, to find the WFW of the robots, configurations of zonotopes generated by the Minkowski sum of line segments were evaluated. These geometries are created separately by force vectors of the actuators in the tension space and their resultant torque vectors (if they exist) in the torque space. Consequently, in Chapter 5, since a single point MP was used the WFW was only evaluated in the tension space. While in Chapter 6, it was evaluated separately in both tension and torque spaces.

Besides, in this research, it is assumed that the desired wrench set should be exerted by the actuators in all directions in terms of the desired force vector and the desired torque vector (if it exists) respectively in force and torque spaces (which is represented by a circle or sphere contained by respectively a 2-D or a 3-D zonotope defined in each space). However, in general, the wrench set may not be homogenous. For instance, in the case of a planar cable mechanism with four cables and square-shape MP (c.f. Fig. 5.1) the wrench has two force components and one torque component and subsequently, it is non-homogeneous.

Then, similarly to the planar case, the workspaces of the optimized mechanism were compared to two other fully driven cable robots. The results revealed that using differentials, the performance of spatial mechanisms is improved. These results can then be used in the design of the proposed AWJP robot. However, due to the physical limits, it may not be possible to consider all optimal parameters, but they can be used as a guide to have a polishing robot at its best practical performance. The results of this study can also be used as a basis for engineers to design cable robots for different applications with higher performance and larger workspace with low cost.

9.3   Polishing paths generation for AWJP process

The second part of this study was dedicated to the investigation of the requirements of the AWJP in the trajectory generation and production of paths for uniform polishing of the desired surfaces. To do this, first a test rig was developed to perform several experiments and investigate the effects of polishing parameters on the quality of the polished area. After manufacturing this test rig for industrial usage, by preliminary tests on the polishing of straight lines along flat surfaces using AWJ, its performance was investigated. In total, seven polishing parameters were considered in these experiments. Since a full-factorial test considering all combinations of these parameters was not practical, the L_{18} orthogonal array presented in the Taguchi method was used to reduce the

number of experiments to a reasonable value. However, the experiments performed using Taguchi method were not enough to find the optimal values for the polishing parameters. Instead, they gave a clue to realize the significance of the polishing parameters. These results can be used in the future experiments to perform a comprehensive study on the most important parameters. Then, the optimal values of these parameters can be found.

Using these experiments the shape of the profile of the material removal at the polishing spot was estimated. This profile was then used to obtain the properties which should be considered in the generation of polishing paths. The first property was the ratio between the radius of curvature of a free-form surface and the width of the polishing spot. It was shown that to reduce the effect of the radius of curvature of the surface r_k, on the angle between the jet and the surface at the polishing spot, a ratio of $r_{k.min}/W \geq 6$ should be preserved on the entire surface. This way, the maximum variation of this angle is less than 5 degree. Otherwise, it is recommended to use a nozzle with a smaller diameter. The next issue to be checked was the pitch distance p. Based on the exact shape of the profile of the material removal, the pitch distance can be determined. It is a ratio of the width of the polishing spot W. With the profile obtained in the experiments, via trial and error it was shown that with ratio of $p/W \approx 0.4$ the best distribution of the waterjet on the surface (i.e., minimal difference in the depth of the polishing area) was obtained. However, this ratio may vary depending on the shape of this profile.

The last property was the ratio between the radius of curvature of the generated trajectory r_{path} and the width of the polishing area. To obtain the optimum value for this ratio considering the case study, an algorithm was developed to simulate the material removal from a flat surface polished through a scanning path. In this simulation, it was supposed that the previously mentioned $r_{k.min}/W$ ratio is respected and consequently, the effect of the curvature of the surface was excluded from this simulation. The results of this simulation revealed that in the parts of the generated trajectory with high curvature and sharp turns, some areas of the surface were over polished and others under polished. Thus, based on this simulation, two limits were defined for maximum curvature and turns along the polishing paths. It was shown that if $r_{path}/W \geq 1.5$ and $\theta_{path} \leq \pi/6$ (for piecewise paths) then less than 5% of variance in the depth of the polishing area would be expected.

Taking into account these ratios, two indices were defined to evaluate both the curvature of the surface and the configuration of the generated trajectory, for the given W. The first index I_{curv}, evaluates the minimum radii of the curvatures estimated around the vertices of the triangular faces representing the free-form surface. With an ideal surface for AWJP process, one has $I_{curv} = 0$, otherwise, it has a value which is ideally very small. The second index I_{path}, checks the r_{path} and θ_{path} along the path. If the polishing paths are parallel and straight (i.e., no bend or curve exist along the paths), then $I_{path} = 0$, otherwise, similarly to I_{curv}, it has a value which is preferred to be very small.

Thus, with straight parallel lines, the best distribution of waterjet on a surface can be expected. Also, if there are no limits due to the boundaries of a flat surface, then the offsets of the scanning path are naturally straight and parallel. Thus, this path was selected as an appropriate trajectory to be used for AWJP of a free-form surface. Consequently, in the last step, a method was developed to generate scanning paths with constant offset (pitch) distance on free-form surfaces modeled by triangular mesh (which is very common in modeling of such surfaces in computer-aided design). Using this method, the offsets were generated around the reference curve (also known as seed curve) on a free-form surface. Therefore, the reference curve has a crucial impact on the final configuration of the trajectory. Thus, to obtain an optimal path for the AWJP process, this curve should be carefully chosen.

Since the proposed algorithm was developed to generate paths on any arbitrary surfaces (but with a limited curvature) including inner holes and complex boundaries, there was no unique solution to obtain the best reference curve. Therefore, in the proposed method, several options were provided to generate this path. Then, using each option, all points of the reference curve were found. Afterwards, considering the points of current curve (which is initially the reference curve), the positions of all the points of its offset were obtained. For this, geodesic piecewise paths were followed in particular directions with respect to the current path to obtain the next points. This geodesic path was found by unfolding the faces located in the direction toward the next offset point. Using this technique, reconfiguration of the triangular mesh model of the surface was not required.

After calculating the location of all the new points, the latter were modified to obtain the final new offset curves. This procedure was then followed to find all offsets of the scanning path on the entire surface. The end points of each curve were forced to be on the outer boundary of the surface. This way, the U turns of the scanning path were placed on the boundary and consequently their negative effect of the uniformity of polishing process inside the surface was reduced. Then, using other methods such as augmented surface (currently not investigated), these parts of the trajectory could be located beyond the outer boundaries of the desired surface.

The proposed algorithm was also able to detect the discontinuities along the generated trajectories (when the surface has inner holes and/or concave boundaries). In this case, by reconfiguring the initial offsets at the discontinuous areas, the algorithm divided the initial trajectory into several continuous trajectories. In the end, the algorithm checked the performance of the generated path(s) using the index I_{path}. This process was then repeated with other options for the reference curve and finally, the best path was selected. This algorithm was particularly designed to generate polishing paths for AWJP process. However, the proposed methodology can be used to generate trajectories for other applications where a constant offset distance is required.

CHAPTER 10

CONCLUSIONS AND RECOMMENDATIONS

10.1 Conclusions

In this dissertation, the conceptual design of a new cable-driven hybrid robotic system was proposed to polish the free-form surfaces of large hydraulic turbine blades using abrasive water-jet polishing technique. Next, according to the requirements of this technique, a path generation method was presented to produce polishing paths uniformly delivering the abrasive waterjet to the desired surface.

For this, the AWJP process was first investigated and the main parameters affecting its performance were determined. Next, the necessary conditions for manipulation of the jet nozzle over the desired surface were studied and the properties of a robotic arm to appropriately perform this task were determined. Then, the architectures of several robotic systems including serial, linkage-driven parallel, cable-driven parallel, and hybrid robots were taken into account. Knowing the requirements of the AWJP process, the capability of these mechanisms were investigated and the hybrid architecture was suggested as the best candidate for the design of a AWJP robot.

Afterwards, the conceptual design of a 5-DOF hybrid (serial-parallel) robot was proposed. It was made of a 3-DOF cable-driven parallel mechanism and a 2-DOF serial wrist. To improve the workspace, payload and redundancy of the cable-driven mechanism, it was proposed to use differentials to drive cables of this mechanism. Using this technique, the number of required actuators was kept at minimum, i.e., $n+1$ for a n-DOF mechanism. In addition, a prismatic joint was used to improve the compactness and rigidity of the robot.

In the next step, the differentially driven cables were investigated and their differences with independently actuated cables were described. It was shown that in the analysis of a cable differential, the resultant force of all cables of that differential should be considered. Also, with planar robots, the direction of the resultant force is not fixed toward a particular point. Instead, it changes within the plane of that differential. Next, by comparing the WCW and WFW of several planar robots actuated by differentials with their fully driven counterparts, it was shown that using these mechanisms are beneficial and the two types of workspaces are improved with planar robots. Nevertheless, the same resultant property due to the differential increasing the range of variation of the resultant force direction, decreases its magnitude. Thus, the optimal design of a cable differential is a trade-off between these two properties.

Afterwards, a synthesis method was presented to find all possible arrangements of the cables

of a differential to generalize the idea of using these mechanisms in the design of planar cable robots. Finally, valid arrangements with 2, 3, and 4 cable differentials were obtained. However, the presented method is valid for systems with more cables. Next, the application of differentials in spatial robots was investigated. It was shown that, in this case, spatial differentials can also be used and they have similar properties as the planar types.

Then, three planar differentials were used in the conceptual design of the proposed robot where three actuators drive six cables and the fourth one drives the prismatic joint. Thus, this mechanism has 3-DOF and one degree of redundancy. Different aspects of the kinematics of the robot were analyzed. Afterwards, two performance indices, namely I_{WCW} and I_{WFW} were defined to evaluate the WCW and WFW of the proposed mechanism. They were used to find the best design parameters of the mechanism using a genetic algorithm optimization method. The workspaces of the optimized robot was then compared to these of two other fully driven cable robots. It was shown that, similarly to the planar case, the performance of spatial mechanisms are improved using differentials. The results of this study can also be used in the design of other cable-driven robots to improve their kinematic properties at low cost.

As a part of this study, a test rig was built to do preliminary experiments with the AWJP process and investigate the effect of the main parameters on the quality of the polished surface. The results of these initial tests were used to find the relative importance of the polishing parameters. They were also used to estimate the shape of the profile of the material removal at the polishing spot. This profile was then used to obtain the limits which should be respected in the polishing path generation. Taking into account these limits, two performance indices, namely I_{curv} and I_{path} were defined to evaluate both the curvature of the surface and the configuration of the trajectory used to polish that surface.

In second part of this dissertation a method was developed to generate polishing path for AWJP of free-form surfaces modeled by triangular faces. In this method, through different options, a reference curve was obtained which was used as the basis to find the other offset curves. Thus, the reference curve has a crucial impact on the final trajectory. To find the points of the offset curves, geodesic paths were followed in particular directions with respect to the previous curve. After obtaining the initial configuration of the complete path on a free-form surface, the possibility of discontinuities along the generated trajectories was checked. If such occurrences were found, by reconfiguring the initial trajectory in these areas, new continuous trajectories were generated. At the end, using the index I_{path}, the performance of the generated path obtained using each option (which was used to find the reference curve) was evaluated and the best path was selected to be used. This method was particularly designed to generate paths for the AWJP process. However, it can be used to generate trajectories for other applications where a constant offset distance is required.

10.2 Original contributions

✓ Through determining the required properties of a robotic manipulator to be used for abrasive waterjet polishing of large hydraulic turbines, the conceptual design of a new 5-DOF hybrid robot with cable-driven parallel-serial architecture was proposed. This mechanism had particular structural and kinematic properties which allow to properly accomplish this polishing process.

✓ The idea of using cable differentials in the architecture of both planar and spatial cable-driven mechanisms was proposed. Then, the properties of these systems were investigated and the differences in the analysis of the cable robots actuated using these mechanisms and other common cable robots were presented. It was also shown that due to particular characteristics of cable differentials, they can improve the wrench-closure and wrench-feasible workspaces of a cable robot.

✓ A synthesizing method was presented to find all possible arrangements of the cables of a differential mechanism to be used in the architecture of a cable robot. Taking into account physical limits and kinematic properties, the valid arrangements of cable differentials were obtained.

✓ By improving the particular properties of the cable differentials (i.e., increasing the variation of the direction of the resultant force) in a differentially driven cable mechanism, its wrench-closure and wrench-feasible workspaces were optimized.

✓ A path generation method was introduced to produce scanning paths for abrasive waterjet polishing of free-form surfaces. This method is able to generate trajectories with constant offset distance between all adjacent paths on triangular mesh model of a free-form surface. In this method, the reconfiguration of the triangular mesh model of the surface is not required. The proposed method is also able to produce continuous paths on surfaces with inner holes and concave boundaries. Using performance indices, this method is able to evaluate the performance of the generated path in the abrasive waterjet polishing of the desired surface.

10.3 Recommendations

The following subjects are proposed for future investigations:

1. It is needed to practically validate the performance of the proposed cable differentials in the positioning of the MP of a cable robot and evaluate their capability of producing the desired wrench in a particular direction. Therefore, it is suggested to design and build a prototype of a planar cable robot driven by several differentials (e.g., 3 differentials each with two cables) and experimentally test these systems.

2. Next, in is recommended to design and manufacture a small-scale prototype of the proposed spatial hybrid robot. Using this robot, the capability of the cable differentials in the manipulation of the MP and their resistance against external force can be experimentally evaluated. Also, the rigidity and precision of the mechanism in positioning and following a particular trajectory can be examined.

3. Afterward, it is suggested to install the prototype of the proposed mechanism on the existing test rig which was built to perform experimental study on the AWJP process. Then, the polishing nozzle can be attached to the MP of this mechanism. This way, the resistance of the cable differentials against the reaction force of the jet as well as the amount of the vibration of the cables and its effect on the positioning precision of the robot can be tested. Through these experiments, other requirements of the AWJP such as working in humid and contaminated area can also be evaluated.

4. The results of the initial experiments on the abrasive waterjet polishing process was used to reveal the importance of the polishing parameters. In the next step, the polishing parameters with the highest importance can be used to develop a new design of experiment and perform a full-factorial experimental investigation on the polishing process and obtain the optimal values of these parameters. Through these experiments, the relationship between other properties of the process (e.g., required power, consumption of abrasive and water, duration of the process, etc.) and the quality of the polished surface, productivity and other industrial benefits can be achieved.

5. Considering the properties of the AWJP process, it is suggested to investigate the effect of high curvature of the surface (beyond the limits mentioned in this study) on the profile of the material removal. Next, it is proposed to develop a method to generate polishing paths with variable pitch distances which can be found according to the local curvature of the surface. It would then be expected to be able to uniformity polish free-form surfaces with high curvatures. It is also recommended to generate the polishing paths according to the water direction on the surface of turbine blades. By this way, smaller roughness (higher quality) in the direction of water flow may be expected.

REFERENCES

[1] J. Paulo Davim. *Surface Integrity in Machining*. Springer, 2009.

[2] Richard E. Chinn. *Ceramography: Preparation and Analysis of Ceramic Microstructures, chapter4: Grinding and Polishing*. John Wiley & Sons, 2002. 35-44 pp.

[3] R. Balasubramaniam, J. Krishnan, and N. Ramakrishnan. Experimental study on the abrasive jet deburring of cross-drilled holes. *Journal of Materials Processing Technology*, 91(1):178–182, 1999.

[4] H. T. Zhu, C. Z. Huang, J. Wang, Q. L. Li, and C. L. Che. Experimental study on abrasive waterjet polishing for hard-brittle materials. *International Journal of Machine Tools and Manufacture*, 49(7-8):569–578, 2009.

[5] J. M. Fan, C. Y. Wang, and J. Wang. Modelling the erosion rate in micro abrasive air jet machining of glasses. *Wear*, 266(9-10):968–974, 2009.

[6] A. El-Domiaty, H. M. Abd El-Hafez, and M. A. Shaker. Drilling of glass sheets by abrasive jet machining. In *Proceedings of World Academy of Science, Engineering and Technology*, volume 56, pages 61–67, August 2009.

[7] Q. L. Li, J. Wang, and C. Z. Huang. Erosion mechanisms of monocrystalline silicon under a microparticle laden air jet. *Journal of Applied Physics*, 104(3):034903–1–8, 2008.

[8] H. Z. Li, J. Wang, and J. M. Fan. Analysis and modelling of particle velocities in micro-abrasive air jet. *International Journal of Machine Tools & Manufacture*, 49(11):850–858, 2009.

[9] Matthew W. Chastagner and Albert J. Shih. Abrasive jet machining for edge generation. *Transactions of the North American Manufacturing Research Institute of SME*, 35:359–366, 2007.

[10] N. Shafiei, H. Getu, A. Sadeghian, and M. Papini. Computer simulation of developing abrasive jet machined profiles including particle interference. *Journal of Materials Processing Technology*, 209(9):4366–4378, 2009.

[11] Mark J. Jackson and J. Paulo Davim. *Machining with Abrasives*. Springer, 2011.

[12] F. C. Tsai, B. H. Yan, C. Y. Kuan, and F. Y. Huang. A taguchi and experimental investigation into the optimal processing conditions for the abrasive jet polishing of skd61 mold steel. *International Journal of Machine Tools and Manufacture*, 48(7-8):932–945, 2008.

[13] M. Achtsnick, P. F. Geelhoed, A. M. Hoogstrate, and B. Karpuschewski. Modelling and evaluation of the micro abrasive blasting process. *Wear*, 259(1-6):84–94, 2005.

[14] Jianxin Deng and Junlong Sun. Sand erosion performance of b4c based ceramic nozzles. *International Journal of Refractory Metals and Hard Materials*, 26(3):128–134, 2008.

[15] <http://en.wikipedia.org/wiki/File:5-Axis-Waterjet-Cutting-Head.jpg>.

[16] H. T. Liu, E. Schubert, D. McNiel, and K. Soo. Applications of abrasive-fluidjets for precision machining of composites. In *International SAMPE Symposium and Exhibition (Proceedings)*, pages 17–20, Seattle, Washington, May 2010.

[17] Norman C. Franz. High velocity liquid jet, 1970.

[18] Stefan Dreyer. Robot-based 3d waterjet cutting-an environmentally sound technology. Technical report, ABB Review, ABB I-R Robotized Waterjet, Germany, 1997.

[19] H. T. Liu and E. Schubert. Piercing in delicate materials with abrasive-waterjets. *International Journal of Advanced Manufacturing Technology*, 42(3-4):263–279, 2009.

[20] <http://www.waterjets.org>.

[21] M. C. Kong and D. Axinte. Response of titanium aluminide alloy to abrasive waterjet cutting: geometrical accuracy and surface integrity issues versus process parameters. *Proceedings of the Institution of Mechanical Engineers, Part B (Journal of Engineering Manufacture)*, 223 (B1):19–42, 2009.

[22] Vera De Vries, Roland Moser, and Philipp Roth. Automated abrasive water jet pin cutting system. In *International Conference on Applied Robotics for the Power Industry*, pages 1–5, Montreal, Canada, October 2010.

[23] Zhaoze Li, Shengyi Li, Yifan Dai, and Xiaoqiang Peng. Optimization and application of influence function in abrasive jet polishing. *Applied Optics*, 49(15):2947–2953, 2010.

[24] IOP Precision technology: Polishing robot, Shape and polish with abrasive jets, Senter, June, 2003. <http://www.dspe.nl/files/polishong20robot.pdf>.

[25] Y. Ozcelik, R. Ciccu, and G. Costa. Comparison of the water jet and some traditional stone surface treatment methods in different lithotypes. *Construction & Building Materials*, 25(2): 678–687, 2011.

[26] Tsuo-Fei Mao, Shie-Chen Yang, Feng-Che Tsai, Jung-Chou Hung, and Biing-Hwa Yan. Experimental investigation of abrasive jet polishing on the free-form machined surfaces of skd61 mold steel using sic particles. *Materials and Manufacturing Processes*, 25(9):965–973, 2010.

[27] Feng-Che Tsai, Biing-Hwa Yan, Chun-Yu Kuan, Rong-Tzong Hsu, and Jung-Chou Hung. An investigation into superficial embedment in mirror-like machining using abrasive jet polishing. *The International Journal of Advanced Manufacturing Technology*, 43(5-6):500–512, 2009.

[28] Tianxiang Chen and Chengyong Wang. Investigation into roughness of surface polished by abrasive waterjet with taguchi method and dimensional analysis. *Materials Science Forum*, 723:188–95, 2012.

[29] Pham Huu Loc and Fang-Jung Shiou. Abrasive water jet polishing on zr-based bulk metallic glass. *Advanced Materials Research*, 579:211–18, 2012.

[30] Pham Huu Loc, Fang-Jung Shiou, Zong-Ru Yu, and Wei-Yao Hsu. Investigation of optimal air-driving fluid jet polishing parameters for the surface finish of n-bk7 optical glass. *Journal of Manufacturing Science and Engineering, Transactions of the ASME*, 135(1):011015–1–7, 2013.

[31] Yang Zhao, Ji Zhao, Lei Zhang, Lizhe Qi, and Qing Tang. Path planning for automatic robotic blade grinding. In *Proceedings of the 2009 IEEE International Conference on Mechatronics and Automation*, pages 1556–60, Changchun, China, August 2009.

[32] M. C. Lee, S. J. Go, M. H. Lee, C. S. Jun, D. S. Kim, K. D. Cha, and J. H. Ahn. A robust trajectory tracking control of a polishing robot system based on cam data. *Robotics and Computer-Integrated Manufacturing*, 17(1-2):177–183, 2001.

[33] Lin Feng-yun and Lu Tian-sheng. Development of a robot system for complex surfaces polishing based on cl data. *International Journal of Advanced Manufacturing Technology*, 26 (9-10):1132–1137, 2005.

[34] Hon-Yuen Tam, Osmond Chi-Hang Lui, and Alberet C.K. Mok. Robotic polishing of free-form surfaces using scanning paths. *Journal of Materials Processing Technology*, 95(1-3): 191–200, 1999.

[35] Baofu Feng, Quanfang Gai, Quanzhong Zhang, and Guangqi Cai. Development and investigation of a parallel robot with three horizontal sliders for steel snagging. In *International Workshop on Intelligent Systems and Applications ISA*, pages 1–4, Wuhan, China, May 2009.

[36] Cezary Zielinski, Krzysztof Mianowski, Kazimierz Nazarczuk, and Wojciech Szynkiewicz. A prototype robot for polishing and milling large objects. *Industrial Robot: An International Journal*, 30(1):67–76, 2003.

[37] H. Huang, Z. M. Gong, X. Q. Chen, and L. Zhou. Robotic grinding and polishing for turbine-vane overhaul. *Journal of Materials Processing Technology*, 127(2):140–145, 2002.

[38] B. Hazel, J. Cote, P. Mongenot, M. Sabourin, and F. Paquet. Robotic polishing of turbine runners. In *International Conference on Applied Robotics for the Power Industry (CARPI)*, pages 50–51, Zurich, Switzerland, September 2012.

[39] B. Hazel, J. Cote, Y. Laroche, and P. Mongenot. A portable, multi-process, track-based robot for in situ work on hydropower equipment. *Journal of Field Robotics*, 29(1):69–101, 2012.

[40] Ji man Luo, Yan Xing, Dan Wang, and Xing quan Guan. New type parallel robot manipulator of stone machining. In *Proceedings of the IEEE International Conference on Automation and Logistics*, pages 2417–2419, Qingdao, China, September 2008.

[41] Zhongcheng Gui, Qiang Chen, Zhenguo Sun, Wenzeng Zhang, and Kang Liu. Mobile platform for hydraulic turbine blade repair robot. *Frontiers of Mechanical Engineering in China*, 3(2):164–169, 2008.

[42] Daqi Li, Lei Zhang, Ji Zhao, Xu Yang, and Shijun Ji. Research on polishing path planning and simulation of small mobile robot. In *Proceedings of the IEEE International Conference on Mechatronics and Automation*, pages 4941–4945, Changchun, China, August 2009.

[43] Vincent Robin, Laurent Sabourin, Grigore Gogu, and Jean-Michel Fauconnier. Optimisation de trajectoires en usinage et polissage robotises pour pieces de grandes dimensions. In *CPI Programme scientifique realise/Achieve Scientific Program*, pages 1–17, Casablanca, Morocco, 2005.

[44] Luis Basanez and Jan Rosell. Robotic polishing systems: From graphical task specification to automatic programming. *IEEE Robotics and Automation Magazine*, 12(3):35–43, 2005.

[45] Brian Rooks. The softly-softly approach of robotic waterjet cutting. *Industrial Robot: An International Journal*, 28(1):40–44, 2001.

[46] R. G. Hou, C. Z. Huang, H. T. Zhu, H. L. Liu, and B. Zou. Study of the floor typed abrasive water jet spatial machining robot. *Key Engineering Materials*, 487:478–481, 2011.

[47] Fadi Abu Ibrahim. Designing a low cost xy stage for abrasive water jet cutting. Master's thesis, Massachusetts Institute of Technology, June 2004.

[48] Jorge Angeles. *Fundamentals of Robotic Mechanical Systems: Theory, Methods, and Algorithms (Mechanical Engineering Series)*. Springer, 2007.

[49] Mark W. Spong, Seth Hutchinson, and Mathukumalli Vidyasagar. *Robot Modeling and Control*. John Wiley & Sons, 2006.

[50] Robert Norton. *Design of Machinery: An Introduction to the Synthesis and Analysis of Mechanisms and Machines*. McGraw-Hill, 2004.

[51] John J. Craig. *Introduction to Robotics: Mechanics and Control*. Addison-Wesley, 2005.

[52] Samer Yahya, Haider A. F. Mohamed, M. Moghavvemi, and S. S. Yang. A new geometrical inverse kinematics method for planar hyper redundant manipulators. In *Conference on Innovative Technologies in Intelligent Systems and Industrial Applications (CITISIA)*, Monash, Malaysia, July 2009.

[53] Luc Baron. Kinematic inversion of functionally-redundant serial manipulators: Application to deburing tasks. In *The 13th World Multi-Conference on Systemics Cybernetics and Informatics WMSCI: Control Systems, Technologies and Applications*, pages 236–240, Orlando, FL, USA, July 2009.

[54] I. Dinulescu, A. Predescu, G. Boccolato, R. T. Tanasie, and D. Cojocaru. Control of a hyper-redundant robot. In *International Workshop on Robotics in Alpe-Adria-Danube Region, RAAD*, pages 435–440, Hungary, June 2010.

[55] Gregory S. Chirikjian and Joel W. Burdick. Kinematics of hyper-redundant manipulators. In *ASME, Design Engineering Division (Publication) DE, 21st Biennial Mechanism Conference*, pages 391–396, Chicago, IL, USA,, 1990.

[56] Kourosh E. Zanganeh and Jorge Angeles. Inverse kinematics of hyper-redundant manipulators using splines. In *Proceedings of the IEEE International Conference on Robotics and Automation*, pages 2797–2802, Nagoya, Japan, 1995.

[57] Xin Jun Liu and Jinsong Wang. Some new parallel mechanisms containing the planar four-bar parallelogram. *The International Journal of Robotics Research*, 22(9):717–732, 2003.

[58] Frangois G. Pin and Faithlyn A. Tulloch. Resolving kinematic redundancy with constraints using the fsp (full space parameterization) approach. In *Proceedings of the IEEE International Conference on Robotics and Automation*, pages 468–473, Minneapolis, Minnesota , USA, April 1996.

[59] Liu Li. Inverse kinematics analysis of a novel parallel robot with large workspace. In *International Conference on Logistics Systems and Intelligent Management (ICLSIM)*, pages 1259–1262, Piscataway, NJ, USA, January 2010.

[60] Mohammad H. Abedinnasab and G. R. Vossoughi. Analysis of a 6-dof redundantly actuated 4-legged parallel mechanism. *Nonlinear Dynamics*, 58(4):611–622, 2009.

[61] I. A. Bonev, J. Ryu, S. G. Kim, and S. K. Lee. A closed-form solution to the direct kinematics of nearly general parallel manipulators with optimally located three linear extra sensors. *IEEE Transactions on Robotics and Automation*, 17(2):148–156, 2001.

[62] Yangmin Li and Qingsong Xu. Kinematic analysis of 3-prs parallel manipulator. *Robotics and Computer-Integrated Manufacturing*, 23(4):395–408, 2007.

[63] I. A. Bonev, D. Zlatanov, and C. M. Gosselin. Singularity analysis of 3-dof planar parallel mechanisms via screw theory. *Journal of Mechanical Design*, 125(3):573–581, 2003.

[64] Xin Jun Liu, Xiaoqiang Tang, and Jinsong Wang. Hana: A novel spatial parallel manipulator with one rotational and two translational degrees of freedom. *Robotica*, 23:257–270, 2005.

[65] Alessandro Cammarata, Jorge Angeles, and Rosario Sinatra. Kinetostatic and inertial conditioning of the mcgill schonflies-motion generator. *Advances in Mechanical Engineering*, ID 186203:186203 (9 pp.), 2010.

[66] Farhad Tahmasebi. Direct and inverse kinematics of a novel tip-tilt-piston parallel manipulator. NASA/TM-2004-21276, 2004.

[67] Xin Jun Liu, Xiaoqiang Tang, and Jinsong Wang. A novel 2-dof parallel mechanism based design of a new 5-axis hybrid machine tool. In *Proceedings of the IEEE International Conference on Robotics and Automation*, pages 3990–5, Taipei, Taiwan, September 2003.

[68] Samuel Bouchard, Clement Gosselin, and Brian Moore. On the ability of a cable-driven robot to generate a prescribed set of wrenches. *Journal of Mechanical Design, Transactions of the ASME*, 2(1):011010 (10 pp.), 2010.

[69] Simon Perreault and Clement M. Gosselin. Cable-driven parallel mechanisms-application to a locomotion interface. *Journal of Mechanical Design, Transactions of the ASME*, 130(10): 1023011–8, 2008.

[70] Guilin Yang, Wei Lin, Mustafa Shabbir Kurbanhusen, Cong Bang Pham, and Song Huat Yeo. Kinematic design of a 7-dof cable-driven humanoid arm: A solution-in-nature approach. In *Proceedings of the IEEE/ASME International Conference on Advanced Intelligent Mechatronics*, pages 444–449, Monterey, California, USA, July 2005.

[71] Abbas Fattah and Sunil K. Agrawal. On the design of cable-suspended planar parallel robots. *ASME Journal of Mechanical Design*, 127(5):1021–8, 2005.

[72] Guilin Yang, Cong Bang Pham, and Song Huat Yeo. Workspace performance optimization of fully restrained cable-driven parallel manipulators. In *Proceedings of the IEEE/RSJ International Conference on Intelligent Robots and Systems*, pages 85–90, Beijing, China, October 2006.

[73] Jason Pusey, Abbas Fattah, Sunil Agrawal, Elena Messina, and Adam Jacoff. Design and workspace analysis of a 6-6 cable-suspended parallel robot. In *Proceedings of the IEEE/RSJ International Conference on Intelligent Robots and Systems*, pages 2090–5, Las Vegas, Nevada, USA, October 2003.

[74] Wei Jung Shiang, David Cannon, and Jason Gorman. Optimal force distribution applied to a robotic crane with flexible cables. In *Proceedings of the IEEE International Conference on Robotics & Automation*, pages 1948–54, Francisco, CA, USA, April 2000.

[75] Satoshi Tadokoro, Yoshio Murao, Manfred Hiller, Rie Murata, Hideaki Kohkawa, and Toshiyuki Matsushima. A motion base with 6-dof by parallel cable drive architecture. *IEEE/ASME Transactions on Mechatronics*, 7(2):115–123, 2002.

[76] Shabbir Kurbanhusen Mustafa, Guilin Yang, Song Huat Yeo, Win Lin, and I. Ming Chen. Self-calibration of a biologically inspired 7 dof cable-driven robotic arm. *IEEE/ASME Transactions on Mechatronics*, 13(1):66–75, 2008.

[77] S. Kawamura, W. Choe, S. Tanaka, and S. R. Pandian. Development of an ultrahigh speed robot falcon using wire drive system. In *IEEE International Conference on Robotics and Automation*, volume 1, pages 215–20, Nagoya, Japan, May 1995.

[78] Xiaobo Zhou, Seung kook Jun, and Venkat Krovi. Tension distribution shaping via reconfigurable attachment in planar mobile cable robots. *Robotica*, pages 1–12, 2013.

[79] Darwin Lau, Kishor Bhalerao, Denny Oetomo, and Saman K. Halgamuge. On the task specific evaluation and optimisation of cable-driven manipulators. In *Advances in Reconfigurable Mechanisms and Robots I*, pages 707–716, Tianjin, China, July 2012.

[80] Satoshi Tadokoro, Shinsuke Nishioka, Tetsuya Kimura, Motofumi Hattori, Toshi Takamori, and Kiyoshi Maeda. On fundamental design of wire configurations of wire-driven parallel manipulators with redundancy. In *Proceedings of the Japan-USA Symposium on Flexible Automation*, volume 1, pages 151–8, Boston, MA, USA, July 1996.

[81] S. H. Lee, T. A. Lasky, and S. A. Velinsky. Manipulability-based design and analysis of a hybrid manipulator for highway applications. *Mechanics Based Design of Structures and Machines*, 33(1):99–118, 2005.

[82] Haitao Liu, Tian Huang, Jianping Mei, Xueman Zhao, Derek G. Chetwynd, Meng Li, and S. Jack Hu. Kinematic design of a 5-dof hybrid robot with large workspace/limb-stroke ratio. *Journal of Mechanical Design, Transactions of the ASME*, 129(5):530–537, 2007.

[83] Emmanuel Brau and Florian Gosselin. Icare 3d: A new light 3d haptic interface. In *Proceeding of EuroHaptics*, Paris, France, July 2006.

[84] Saeed Behzadipour. Kinematics and dynamics of a self-stressed cartesian cable-driven mechanism. *ASME Journal of Mechanical Design*, 131(6):061005(10 pp.), 2009.

[85] Min Ki Lee, Kun Woo Park, and Byung Oh Choi. Kinematic and dynamic models of hybrid robot manipulator for propeller grinding. *Journal of Robotic Systems*, 16(3):137–50, 1999.

[86] Jin-Ho Kyung, Hyung-Suk Han, Chan-Hoon Park, Young-Ho Ha, and Jeong-Hoon Park. Dynamics of a hybrid serial-parallel robot for multi-tasking machining processes. In *SICE-ICASE International Joint Conference*, pages 3026–3030, Bexco, Busan, Korea, October 2006.

[87] Q. J. Duan, J. L. Du, and X. C. Duan. Kinematic analysis of a hybrid structure. *International Journal of Advanced Robotic Systems*, 9:1–8, 2012.

[88] Doina Pisla, Bogdan Gherman, Calin Vaida, Marius Suciu, and Nicolae Plitea. An active hybrid parallel robot for minimally invasive surgery. *Robotics and Computer-Integrated Manufacturing*, 29(4):203–21, 2013.

[89] Fusaomi Nagata, Yukihiro Kusumoto Yoshihiro Fujimoto, and Keigo Watanabe. Robotic sanding system for new designed furniture with free-formed surface. *Robotics and Computer-Integrated Manufacturing*, 23(4):371–379, 2007.

[90] Michael Rososhansky, Fengfeng Xi, and Yuwen Li. Coverage based tool path planning for automated polishing using contact stress theory. In *IEEE International Conference on Automation Science and Engineering*, pages 592–597, Toronto, Ontario, Canada, August 2010.

[91] <http://en.wikipedia.org/wiki/Lissajous_curve>.

[92] <http://mathforum.org/mathimages/index.php/Lissajous_Curve>.

[93] Daniel C. H. Yang, J. J. Chuang, Z. Han, and S. Ding. Boundary-conformed toolpath generation for trimmed free-form surfaces via coons reparametrization. *Journal of Materials Processing Technology*, 138(1-3):138–144, 2003.

[94] Sun Yuwen, Guo Dongming, Jia zhenyuan, and Wang Haixia. Iso-parametric tool path generation from triangular meshes for free-form surface machining. *International Journal of Advanced Manufacturing Technology*, 28(7-8):721–726, 2006.

[95] Weihua Sheng, Heping Chen, Ning Xi, and Yifan Chen. Tool path planning for compound surfaces in spray forming processes. *IEEE Transactions on Automation Science and Engineering*, 2(3):240–249, 2005.

[96] Qiang Zou and Jibin Zhao. Iso-parametric tool-path planning for point clouds. *Computer-Aided Design*, 45(11):1459–68, 2013.

[97] B. H. Kim and B. K. Choi. Guide surface based tool path generation in 3-axis milling: an extension of the guide plane method. *Computer-Aided Design*, 32(3):191–199, 2000.

[98] Alexander Kout and Heinrich Muller. A framework for the generation of distance field based curves on triangular mesh surfaces for nc manufacturing. Technical report, Department of Computer Science, Technische Universitet Dortmund, 2010.

[99] Hon yuen Tam. Toward the uniform coverage of surfaces by scanning curves. *Computer-Aided Design*, 31(9):585–596, 1999.

[100] Vitaly Surazhsky, Tatiana Surazhsky, Danil Kirsanov, Steven J. Gortler, and Hugues Hoppe. Fast exact and approximate geodesics on meshes. *ACM Transactions on Graphics*, 24(3): 553–560, 2005.

[101] David Bommes and Leif Kobbelt. Accurate computation of geodesic distance fields for polygonal curves on triangle meshes. *VMV*, pages 151–160, 2007.

[102] P. Yuen, F. Mokhtarian, N. Khalili, and J. Illingworth. Curvature and torsion feature extraction from free-form 3-d meshes at multiple scales. *IEE Proceedings: Vision, Image and Signal Processing*, 147(5):454–462, 2000.

[103] Prasad N. Atkar, David C. Conner, Aaron Greenfield, Howie Choset, and Alfred A. Rizzi. Hierarchical segmentation of piecewise pseudoextruded surfaces for uniform coverage. *IEEE Transactions on Automation Science and Engineering*, 6(1):107–120, 2009.

[104] Sang C. Park, Yun C. Chung, and Byoung K. Choi. Contour-parallel offset machining without tool-retractions. *Computer-Aided Design*, 35(9):585–596, 2003.

[105] Steffen Hauth, Claus Richterich, Lothar Glasmacher, and Lars Linsen. Constant cusp tool-path generation in configuration space based on offset curves. *International Journal of Advanced Manufacturing Technology*, 53(1-4):325–338, 2011.

[106] Shi-Qing Xin, Xiang Ying, and Ying He. Constant-time all-pairs geodesic distance query on triangle meshes. In *Proceedings - I3D 2012: ACM SIGGRAPH Symposium on Interactive 3D Graphics and Games*, pages 31–38, Costa Mesa, CA, USA, March 2012.

[107] Joseph S. B. Mitchell, David M. Mount, and Christos H. Papadimitriou. The discrete geodesic problem. *SIAM Journal on Computing*, 16(4):647–668, 1987.

[108] J. A. Sethian and A. Vladimirsky. Fast methods for the eikonal and related hamiltonï£¡ jacobi equations on unstructured meshes. *Proceedings of the National Academy of Sciences of the United States of America*, 97(11):5699–703, 2000.

[109] J. J. Marquez, J. M. Perez, J. Rios, and A. Vizan. Process modeling for robotic polishing. *Journal of Materials Processing Technology*, 159(1):69–82, 2005.

[110] Enric Galceran and Marc Carreras. A survey on coverage path planning for robotics. *Robotics and Autonomous Systems*, 61(12):1258–76, 2013.

[111] <http://www.waterjet-technologies.ch/>.

[112] W. Zesch, S. Honold, Ph. Roth, and V. de Vries. Automated boiler wall cleaning and inspection. In *International Conference on Applied Robotics for the Power Industry*, 2012.

[113] Alain Cornier. *Developpement d'un modele d'enlevement de matiere par granulation utilisant le jet d'eau haute pression: application au demantelement de pneumatiques*. PhD thesis, Ecole Nationale Superieure d'Arts et Metiers Centre de Paris, 2004.

[114] Pierre-Arnaud Beau. *Modelinglisation de l'atomisation d'un jet liquide Application aux sprays Diesel*. PhD thesis, Universite de Rouen, 2006.

[115] Othmane Khatim. *Contribution a la comprehension et a la maitrise du procede d'atomisation de metal liquide*. PhD thesis, Universite de Technologie de Belfort-Montbeliard, 2011.

[116] Phillip J. Ross. *Taguchi Techniques for Quality Engineering*. McGraw Hill Professional, 1996.

[117] Steel Casting Handbook, supplement 8 - High Alloy Data Sheets-Corrosion Series,Steel Founders' Society of America, 2004. <http://www.sfsa.org/sfsa/pubs/hbk/s8.pdf>.

[118] H. Liu and C. Gosselin. A planar closed-loop cable-driven parallel mechanism. *Trans. Can. Soc. Mech. Eng.*, 33(4):587–96, 2009.

[119] H. Liu, C. Gosselin, and T. Laliberte. Conceptual design and static analysis of novel planar spring-loaded cable-loop-driven parallel mechanisms. *J. Mech. Robot.*, 4(2):021001 (1–11), May 2012.

APPENDICES

CATALOGS OF MAIN COMPONENTS USED IN THE TEST RIG

Including :

1. Diaphragm pump

2. Electric Motor

3. Frequency converter

4. Pressure valve

INSTALLATION & SERVICE
D15-991-2400A

Hydra-Cell ®
INDUSTRIAL PUMPS

Models: D-15, G-15

W0083A
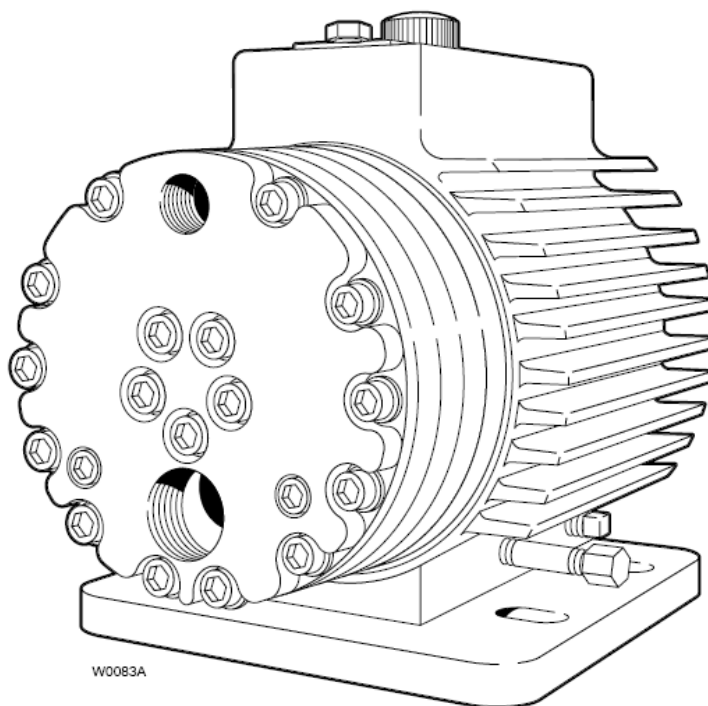
WANNER ENGINEERING, INC.

1204 Chestnut Avenue, Minneapolis, MN 55403
TEL: (612) 332-5681   FAX: (612) 332-6937
TOLL-FREE FAX [US only]: (800) 332-6812

www.hydra-cell.com
email: sales@wannereng.com

D/G-15 Contents

D/G-15 Specifications

Max Pressure

1500 psi (100 bar) @ 1750 rpm
(D/G-15-E Cam only);
2000 psi (140 bar) @ 1450 rpm;
2500 psi (170 bar) @ 1150 rpm

Capacity @ Rated Pressure

	rpm	psi	bar	gpm	l/min
D/G-15-X	1450	500	35	13.4	50
	1450	1500	100	13.0	48
	1450	2000	140	12.7	48
	1150	2500	170	10.3	389
D/G-15-E	1750	500	35	15.1	57
	1750	1500	109	14.1	53
	1450	2000	140	11.5	44
	1150	2500	170	9.4	35

Delivery @ Rated Pressure

	psi	bar	revs/gal	revs/liter
D/G-15-X	500	34.5	109	28.8
	1500	103.5	112	29.6
	2000	138	114	30.2
	2500	172	117	30.9
D/G-15-E	500	34.5	116	20.6
	1500	103.5	124	32.8
	2000	138	126	33.3
	2500	172	128	33.7

Max Inlet Pressure	500 psi (35 bar)
Max Temperature	250°F (121°C) – consult factory for temperatures above 180°F (82°C)
Inlet Port	D-15: 1-1/4 inch NPT G-15: 1-1/4 inch BSPT
Discharge Port	D-15: 3/4 inch NPT G-15: 3/4 inch BSPT
Shaft Diameter	1-1/8 inch (28.58 mm)
Shaft Rotation	Bi-directional
Bearings	Tapered roller bearings
Oil Capacity	2.2 US quarts (2.1 liters)
Weight	145 lbs (66 kg)

Calculating Required Horsepower (kW)*

$$\frac{80 \times rpm}{63,000} + \frac{gpm \times psi}{1,460 - \left(\frac{psi - 500}{20}\right)} = \text{electric motor HP*}$$

$$\frac{80 \times rpm}{84,428} + \frac{gpm \times bar}{511 - \left(\frac{bar - 35}{4}\right)} = \text{electric motor kW*}$$

* rpm equals pump shaft rpm. HP/kW is required application power. Use caution when sizing motors with variable speed drives.

D15-991-2400A

D/G-15 Specifications

Performance

500 PSI (35 bar)
1500 PSI (100 bar)
2000 PSI (140 bar)
2500 PSI (170 bar)

D/G-15-X

D/G-15-E

W0092
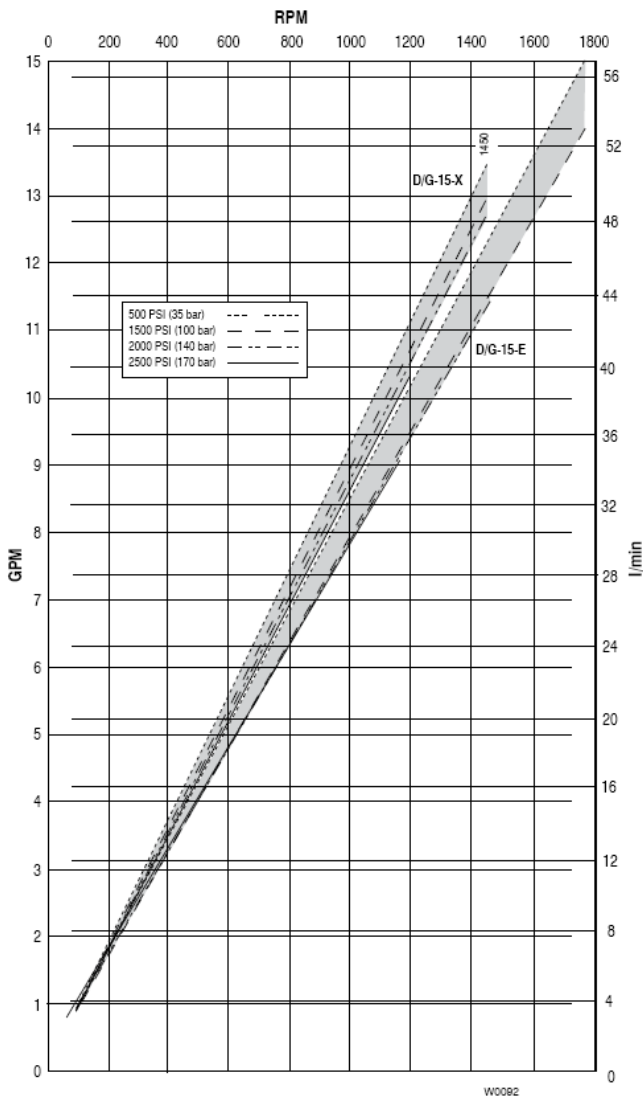
*Pump NPSHr and Lift performance based on randomly selected pumps with water at 70°F (21°C)

Net Positive Suction Head – NPSHr

D/G-15-X

D/G-15-E

W0091

Dry Lift

D/G-15-X

D/G-15-E

W0089
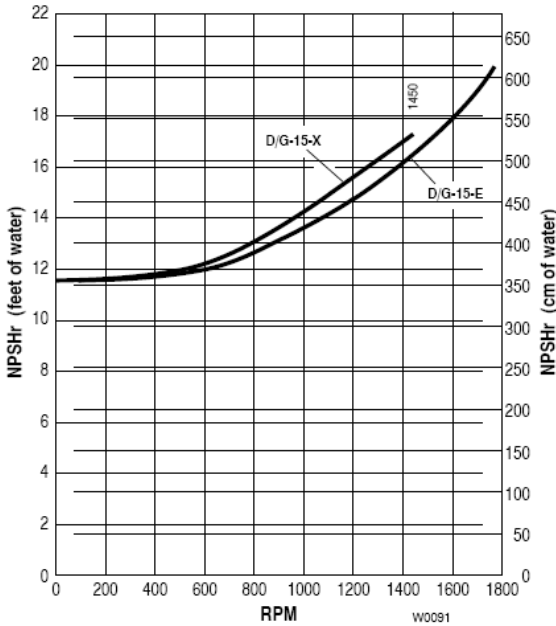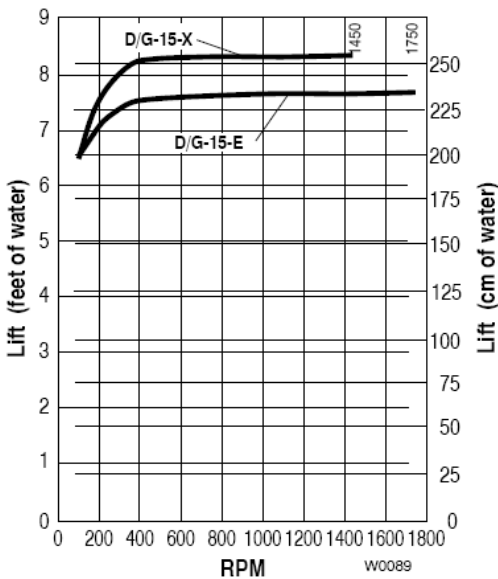
D/G-15 Dimensions

D/G-15 Models <u>without Pump/Motor Adapter</u>

Brass

316 Stainless Steel
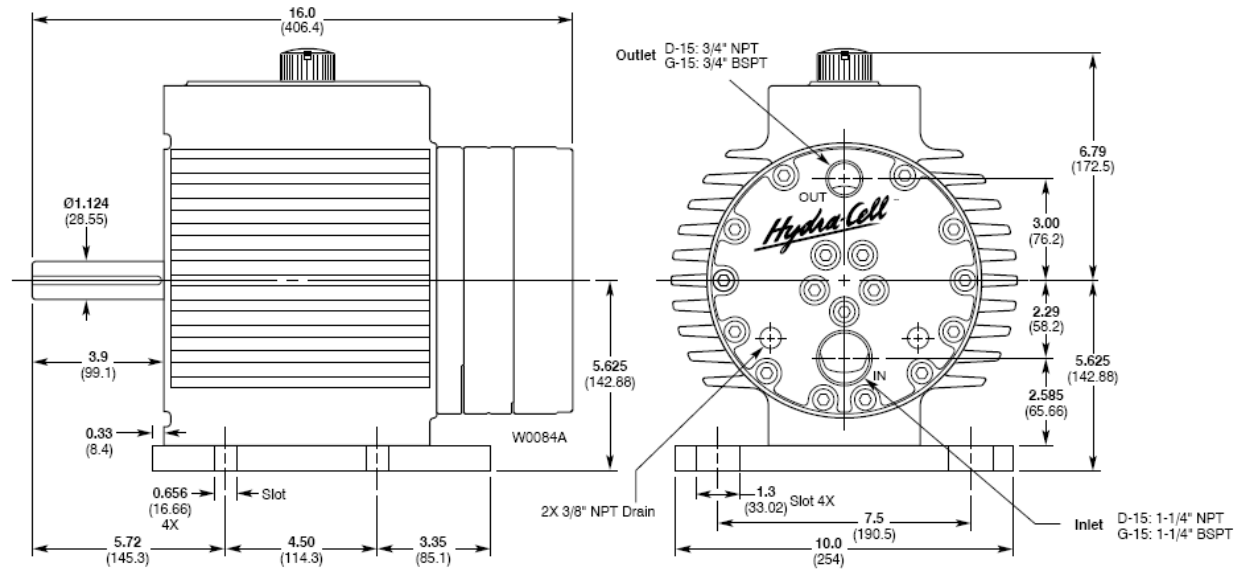
WOLTERS MOTORS & DRIVES, INC.
2885 North Berkley Lake Road - Suite 16
Duluth, Georgia 30096
Phone: (678) 417-5830; **Fax:** (678) 417-5825
Email: info@woltersmotors.com • **Website:** http://www.woltersmotors.com

All Categories > Premium Efficiency AC & DC Motors > WEG NEMA Premium Efficiency Motors > WEG TEFC Three-Phase C-Face NEMA Premium Efficiency Motors (1 - 100HP) > Item # 02018ET3ERS256TC

larger image

Item # 02018ET3ERS256TC, WEG TEFC Three-Phase C-Face NEMA Premium Efficiency Motors (1 - 100HP)

TEFC - THREE PHASE - FOOT MOUNT

WEG'S W21™ NEMA Premium motors meet or exceed all NEMA Premium and CEE requirements for energy efficiency. These TEFC motors are built according to NEMA specifications and designed for operation in moist or dusty atmospheric conditions without affecting their useful life. Premium Efficiency WEG motors are tested according to IEEE 112 std., method 'B' and their efficiency values are certified by UL Labs (CSA C390). Cooling Tower motors will meet Design B torques, maintaining exceedingly high breakdown and locked rotor torque while providing the highest rated efficiency levels.

Applications

- ¿ Chemical plants
- ¿ Compressors
- ¿ Pulp and paper mills
- ¿ Crushers
- ¿ Refineries
- ¿ Pumps
- ¿ Steel mills
- ¿ Fans
- ¿ Cement mills
- ¿ Packaging equipment

Standard Features

- ¿ Most ratings meet Design C Torque
- ¿ Service factor:
    - 1.25 up to 100HP
    - 1.15 from 125HP and up
- ¿ Continuous duty (S1)
- ¿ 104ºF (40ºC) ambient temperature
- ¿ Altitude: 3300 ft (1000m)
- ¿ NPT threaded terminal box
- ¿ F1 mount
- ¿ Stainless steel nameplate AISI 316 with laser etching
- ¿ Color: RAL 6002 (Green)
- ¿ Automatic drain plugs-pressure compensated
- ¿ Regreasable bearings positive pressure lubrication system (frames 254T and up)
- ¿ Gasketed conduit box
- ¿ MGI Part 31 rating for use with VFD - 20:1 constant torque speed range. Speed range can be extended with optional Blower kit.
- ¿ Class 1, Div 2, Groups B, C & D, T3C
- ¿ Three-phase, 2, 4, 6 and 8 pole, 60Hz
- ¿ Voltage: 208-230/460V, 200V, 460V or 575V

- ¿ 50/60Hz rated up to 60HP (Same HP for both frequencies) (For 75HP and up available)
- ¿ Totally Enclosed Fan Cooled - TEFC (IP55) water tight and dust tight enclosure
- ¿ Squirrel cage rotor/Aluminum die cast
- ¿ V-ring slingers on both endshields (586/7 frame equipped with labyrinth taconite seal as standard)
- ¿ Ball bearings are supplied as standard (RB part numbers supplied with roller bearings)
- ¿ 1045 Carbon Steel Shaft for frames up to 365T.
- ¿ 4140 steel shaft for motors 404T and above. (3600 RPM motors supplied with 1045)
- ¿ NEMA dimensions
- ¿ Class 'F' insulation for all frames
- ¿ Class 'H' impregnation resin
- ¿ Temperature rise: Class 'B' (80ºC)
- ¿ NEMA Design 'B'

Optional Features

- ¿ Special voltages
- ¿ Specially designed shaft
- ¿ Space heaters
  (standard on 586/7 frames)
- ¿ Thermistor, Thermostats or RTD's (PT100)
- ¿ Additional terminal box
- ¿ Drip cover (canopy) for shaft down applications
- ¿ Cable glands
- ¿ 'C' and 'D' flanges for all ratings
- ¿ Roller bearings on drive end available for all frames
- ¿ Labyrinth taconite seal available on all ratings

Specifications

HP	20 HP
RPM	1800 RPM
Voltage	208-230 V 460 V
FL Amps[1]	24.4 A
FL Efficiency	93.0 %
Frame	256TC
Motor Type	TEFC
Multi. Symbol	RSP
'C' Dimension	24.925 in
Weight	259 lbs

Variable Frequency Drive

CFW 09

Three Phase 200-240V - 1.5 - 75 HP

Three Phase 380-480V - 1.5 - 500 HP

Three Phase 500-600/690V - 2 - 500 HP

60.0H

Frequencia Motor
P005=   60.0 Hz

CFW 09
VECTRUE INVERTER

DIGITAL INPUT PROGRAMMING
FUNCTIONS
GENERAL ENABLING
ROTATES/STOP (RAMP ENABLING)
ON/OFF
FWD/REV
LOCAL/REMOTE
ROTATION DIRECTION
MULTI-SPEED
JOG
2nd RAMP
RESET
NO EXTERNAL FAULT
• ELECTRONIC POTENTIOMETER
• DISABLES FLYING START
• (PID) AUTOMATIC MANUAL

DeviceNet

LAY OUTPUTS
Version   Plus Version
RL2   RL1

PAMENSKY

WEG

CFW 09 - Variable Frequency Drive

The CFW 09's Vectrue Technology combines V/F, Sensorless Vector and Closed Loop Vector (with encoder) control techniques in one product. Optimal Braking saves the need for the dynamic braking resistor in some applications allowing a more compact and economical solution.

Standard Features

- V/Hz or Sensorless Vector Control via parameter selection
- Self Tuning to motor parameters
- NEMA 1 Enclosure up to 200HP
- IP20 Enclosure from 250 to 500HP
- 200-240V, 380-480V or 500-600/690V input voltage
- Single or Three-phase input voltage up to 3HP/230V
    *Call 1 877 PAMENSKY for higher than 3HP
- 150% current overload capacity
- DC bus connections accessible
- Detachable Smart Keypad with dual display and Copy Function
- 32 bit RISC microprocessor controlled PWM output
- 1.25 / 2.5 / 5 / 10 kHz adjustable switching frequency
- Six isolated programmable digital inputs
- Three programmable relay outputs (250Vac / 1A)
- Two isolated programmable analog inputs
- Two programmable analog outputs (0 - 10 Vdc)
- Protective features: Over current, motor overload, drive over temperature, output phase-to-phase and phase-to-ground short circuit, DC bus over and under voltage, power supply under voltage and phase loss and external fault

Standard Features - cont.

- Control features: Linear and "S" ramp acceleration and deceleration, local/remote control, DC braking, torque boost, motor slip compensation, electronic pot, preset speeds, adjustable V/Hz profile, maximum and minimum adjustable motor speed limits, three skip frequencies, adjustable output current limit, JOG, ride-thru, flying start and PID regulator
- Display readings: Motor speed, frequency, voltage, current and torque, output power (kW), last ten faults, drive status, digital and analog I/O status, hours powered and hours running
- Ambient: 32°F (0°C) to 104°F (40°C), 3300 ft (1000m) altitude, 90% humidity, non-condensing

Optional Features

- Closed loop vector control
- Remote keypad with cable and mounting frame
- RS-232 or RS-485 Serial Interface
- On/Off line PC programming with Superdrive
- Fieldbus Comm: Profibus DP, DeviceNet or Modbus RTU (Requires optional RS-232 or RS-485 Interface), Ethernet TCP/IP
- Encoder buffered output
- Additional digital and analog I/O
- Dynamic Braking capabilities for most models

CFW 09 - Table of Products

380-480V - With Optional Dynamic Braking

Electrical Data							Mechanical Data				Purchasing Data	
Current (A)		Built-In Dynamic Braking	Maximum Applicable Motor				Frame	Weight (lb)	Degree of Protection	Dimensions (in) H x W x D	WEG Part Number	List Price
			Constant Torque		Variable Torque							
CT	VT		HP	KW	HP	KW						
38	45	Yes	25	19	30	22	4	50	NEMA 1	18.70 x 9.84 x 10.79	CFW090038T3848EODBZ	$5,790
45	54	Yes	30	22	30	22	4	50	NEMA 1	18.70 x 9.84 x 10.79	CFW090045T3848EODBZ	7,884
60	70	Yes	40	30	50	37	5	90	NEMA 1	21.65 x 13.19 x 10.79	CFW090060T3848EODBZ	9,984
70	86	Yes	50	37	60	45	5	90	NEMA 1	21.65 x 13.19 x 10.79	CFW090070T3848EODBZ	10,832
86	105	Yes	60	45	75	55	6	121	NEMA 1	26.57 x 13.19 x 11.77	CFW090086T3848EODBZ	13,457
105	130	Yes	75	55	100	55	6	121	NEMA 1	26.57 x 13.19 x 11.77	CFW090105T3848EODBZ	15,678
142	174	Yes	100	75	125	90	7	154	NEMA 1	32.87 x 13.19 x 12.20	CFW090142T3848EODBZ	18,515

500-600V

Electrical Data							Mechanical Data				Purchasing Data	
Current (A)		Built-In Dynamic Braking	Maximum Applicable Motor				Frame	Weight (lb)	Degree of Protection	Dimensions (in) H x W x D	WEG Part Number	List Price
			Constant Torque		Variable Torque							
CT	VT		HP	KW	HP	KW						
2.9	4.2	Yes	2	1.5	2	2.2	2	13	NEMA 1	11.4 x 7.2 x 7.7	CFW090002T5060ESZ	$1,742
4.2	7	Yes	3	2.2	5	4	2	13	NEMA 1	11.4 x 7.2 x 7.7	CFW090004T5060ESZ	1,801
7	10	Yes	5	3.7	7.5	5.5	2	13	NEMA 1	11.4 x 7.2 x 7.7	CFW090007T5060ESZ	2,305
10	12	Yes	7.5	5.5	10	7.5	2	13	NEMA 1	11.4 x 7.2 x 7.7	CFW090010T5060ESZ	2,413
12	14	Yes	10	7.5	15	9.2	2	13	NEMA 1	11.4 x 7.2 x 7.7	CFW090012T5060ESZ	2,935
14	14	Yes	15	9.2	15	9.2	2	13	NEMA 1	11.4 x 7.2 x 7.7	CFW090014T5060ESZ	3,271
22	27	Optional	20	15	25	18.5	4	50	NEMA 1	18.7 x 9.8 x 10.8	CFW090022T5060ESZ	4,194
27	32	Optional	25	18.5	30	22	4	50	NEMA 1	18.7 x 9.8 x 10.8	CFW090027T5060ESZ	4,928
32	32	Optional	30	22	30	22	4	50	NEMA 1	18.7 x 9.8 x 10.8	CFW090032T5060ESZ	6,708
44	53	Optional	40	30	50	37	7	154	NEMA 1	32.9 x 13.2 x 11.8	CFW090044T5060ESZ	8,941
53	63	Optional	50	37	60	45	7	154	NEMA 1	32.9 x 13.2 x 11.8	CFW090053T5060ESZ	10,550
63	79	Optional	60	45	75	55	7	154	NEMA 1	32.9 x 13.2 x 11.8	CFW090063T5060ESZ	12,558
79	99	Optional	75	55	100	75	7	154	NEMA 1	32.9 x 13.2 x 11.8	CFW090079T5060ESZ	14,928
107	147	External DB	100	75	150	110	8E	253	NEMA 1	45.1 x 16.1 x 14.6	CFW090107T5069ESZ	18,119
147	196	External DB	150	110	200	150	8E	253	NEMA 1	45.1 x 16.1 x 14.6	CFW090147T5069ESZ	27,295
211	211	External DB	200	150	200	150	8E	253	NEMA 1	45.1 x 16.1 x 14.6	CFW090211T5069ESZ	36,995
247	315	External DB	250	185	300	220	10E	682	IP20	46.6 x 27.5 x 22.9	CFW090247T5069ESZ	39,018
315	343	External DB	300	220	350	250	10E	682	IP20	46.6 x 27.5 x 22.9	CFW090315T5069ESZ	42,264
343	318	External DB	350	250	400	300	10E	682	IP20	46.6 x 27.5 x 22.9	CFW090343T5069ESZ	56,796
418	472	External DB	400	300	500	370	10E	682	IP20	46.6 x 27.5 x 22.9	CFW090418T5069ESZ	61,225
472	555	External DB	500	370	600	450(370)	10E	682	IP20	46.6 x 27.5 x 22.9	CFW090472T5069ESZ	65,161

500-600V - With Optional Dynamic Braking

Electrical Data							Mechanical Data				Purchasing Data	
Current (A)		Built-In Dynamic Braking	Maximum Applicable Motor				Frame	Weight (lb)	Degree of Protection	Dimensions (in) H x W x D	WEG Part Number	List Price
			Constant Torque		Variable Torque							
CT	VT		HP	KW	HP	KW						
22	27	Yes	20	15	25	18.5	4	50	NEMA 1	18.7 x 9.8 x 10.8	CFW090022T5060EODBZ	$5,526
27	32	Yes	25	18.5	30	22	4	50	NEMA 1	18.7 x 9.8 x 10.8	CFW090027T5060EODBZ	6,516
32	32	Yes	30	22	30	22	4	50	NEMA 1	18.7 x 9.8 x 10.8	CFW090032T5060EODBZ	8,833
44	53	Yes	40	30	50	37	7	154	NEMA 1	32.9 x 13.2 x 11.8	CFW090044T5060EODBZ	11,490
53	63	Yes	50	37	60	45	7	154	NEMA 1	32.9 x 13.2 x 11.8	CFW090053T5060EODBZ	13,454
63	79	Yes	60	45	75	55	7	154	NEMA 1	32.9 x 13.2 x 11.8	CFW090063T5060EODBZ	16,120
79	99	Yes	75	55	100	75	7	154	NEMA 1	32.9 x 13.2 x 11.8	CFW090079T5060EODBZ	18,968

Notes: The maximum motor power ratings listed above are based on WEG 2 and 4 pole motors. For motors with different numbers of poles (ie. 6 and 8 poles), other voltages and/or from other manufacturers, specify the VFD through the motor rated current.

Why the CFW 09?

CFW 09 - Optimal Braking™

For applications requiring short stopping times and/or stops under high inertial loading, the traditional braking devices call for Dynamic Braking, in which the load kinetic energy is regenerated to the inverter DC link and the excess of which is dissipated in the form of heat in a braking resistor which is interlinked to the power circuit. The CFW 09 VSD has a
built-in "Optimal Braking ®" function, for the vector mode, enabling an optimal braking which can cater for many applications that could previously only be solved by dynamic braking. This technological innovation enables high dynamic performance activation/starts to be obtained with braking torques about 5 times the DC braking torque besides the great advantage of eliminating the need for a braking resistor.
The graph shows the advantage of this new braking system " Optimal Braking ®", thereby ensuring an ideal solution for braking applications at low cost.

CFW 09 - Other Advantages

- High performance RISC 32 bit microprocessor
- Vector and Scaler Control with selection by parameter
- Detachable SMART keypad with dual display (LCD and LED)
- Wide power range: 1.1.. 1,100 kW
- Variable and Constant Torque ratings
- Degree of Protection NEMA 1 / IP 20 standard up to 200HP, IP20 from 250HP and NEMA 4X / IP56 in stainless steel enclosure up to 10HP
- Compact design
- Simplified installation and programming
- Oriented start-up
- Through surface mounting option
- On/Off-line PC programming with SuperDrive software (Optional)
- DC bus connections available
- Fieldbus network communication: Profibus DP, DeviceNet, or Ethernet TCP/IP (optional). Modbus RTU (built-in) also available
- International certifications including UL and cUL, CE, C-Tick and IRAM

Typical Braking Torque x Speed curve for motors driven by the CFW 09
— Dynamic Braking Torque Curve
— Optimal Braking™ Torque Curve
— DC Braking Torque Curve

CFW 09 - Technical Data

Power Supply	Voltage	Three-phase:	220-230 V: 220 230 V (+10% -15%)
			380 - 480 V: 380 / 400 / 415 / 440 / 460 / 480 V (+10%, - 15%)
			500 - 600 V; 500 - 690 V; 660 - 690 V; 660/690 (+ 10%. -15%)
	Frequency		50 / 60 Hz +/- 2 Hz (48 ... 62 Hz)
	Phase Unbalance		Up to 3%
	Cos (Displacement Power Factor)		Greater lhan 0.98 at full load
Enclosure	Degree of Protection		NEMA 1/IP 20 (sizes 1...8 and 8E), IP20 (sizes 9,10 and 10E)
			NEMA 4X I IP 56 (modules up to 10HP)
	Finishing Color		Plastic Cover - Light Gray PANTONE 413 C (sizes 1 and 2)
			Metallic Cover and Sides - Light Gray RAL 7032 (sizes 3 to 10)
			Base - Dark Gray RAL 7022 (sizes 3 to 10)
Control	Power Supply		Switched Mode Power Supply Fed from the DC Link
	Microprocessor		32 bit RISC Technology
	PWM Technique		SVM Sine wave PWM (Space Vector Modulation)
			Software Implemented Current flux and Speed Regulators (Full Digital)
	Control Modes		V / F
			Sensorless Vector (without encoder)
			Vector with Encoder
	Switching Frequency		1.25 / 2.5 / 5.0 / 10 kHz
	Frequency Range		0...1020 Hz for V / Hz Control
			0...408 Hz for Vector Control
	Overload Capacity		150% for 60 seconds every 10 minutes
			180% for 1 second every 10 minutes
	Efficiency		Greater than 97% at full load
Performance	Speed Control	V / F Mode	Regulation (wilh Slip Compensation) : 1% 01 Motor Rated Speed
			Resolution: 1 rpm (Keypad Reference)
			Speed Regulation Range: 1: 20
		Sensorless Vector Mode	Regulation: 0.5% of Motor Rated Speed
			Resolution: 1 rpm (Keypad Reference)
			Speed Regulation Range: 1:100
		Encoder Vector Mode	Regulation with:
			10 bit Analogy Reference: +1- 0.1% 01 Motor Rated Speed
			14 bit Analogy Reference: +- 0.01% 01 Motor Rated Speed
			Digital Reference (Ex: Keypad): + / - 0.01 % of Motor Rated Speed
			Speed Regulation Range: Down to 0 rpm
	Torque Control	Vector Modes	Regulation: + - 10% of Motor Rated Torque
			Range: O ... 150% 01 Motor Rated Torque
Control Inputs	Analog		2 Programmable Differential Input (10 bit) : 0...10 V 0...20 mA or 4...20 mA
			1 Programmable Bipolar Input (14 bit): -10 ... + 10 V 0...20 mA or 4...20 mA <D
			1 Programmable Isolated Input (10 bit) : O ... 10 V 0...20 mA or 4...20 mA <D
	Digital		6 Programmable Isolated Input: 24 Vdc
			1 Programmable Isolated Input: 24 Vdc
			1 Programmable Isolated Input: 24 Vdc (for Motor PTC Thermistor)
	Encorder		1 Isolated Differential Encoder Signals Output: 5 ...15 Vdc External Power Supply
Communication	Serial		RS-232 wilh KCS-GFW09 Kn <D - RS-485 Isolated with EBA or EBB Board <D
			Protocolo Johnson Contols-N2 (optional)
	Fieldbus		Modbus RTU Standard, Profibus DP, DeviceNet, EtherNet / IP, DeviceNet Drive Profile with KFB kits.
Safety	Protections	D C Link Under Voltage	Output Short Circuit
		D C Link Over Voltage	Output Ground Fault
		Drive Over Temperature	External Fault
		Motor Over Temperature	Self -diagnosis Fault
		Output Over Current	Programming Error
		Motor Overload (i x t)	Serial Communication Fault
		Dynamic Braking Resistor Overload	Motor or Encoder Connection Fault
		CPU / EPROM Error (watchdog)	Power Supply Ohase Fault (30 A and above models)
		Encoder Fault	Keypad Connection Fault
Ambient	Temperature		0°C (32°F)...40°C (104°F), up to 50°C (122°F) with 2% / °C (1,1% / °F) output current derating
	Humidity		5...90% Non Condensing
	Altitude		0...1000m (3300ft), up to 4000m (13100ft) with 10% / 1000m (3% / 1000ft) output current derating
Conformities	EMC Directive 89 / 336 / EEC - EM 61800-3		Elec tromagnetie Compatibil -Industrial Environment - EMC - Emission and Immunitv
	LVD 73 / 23 / EEC		low Voltage Directive
	IEC 146		Semiconductor drive
	UL 508C		Power Conversion Enuinment
	EN 50178		Electronic Equipment for Use in Power Installations
	EN 61010		Safety Requirements for Electrical Equipament for Measurement Control and laboratory Use
Certifications	UL (USA) and cUL (CANADA)		Underwriters laboratories Ine. USA
	CE (EUROPE)		Phoenix Test-Lab GmbH – Germany (Competent Body)
	IRAM (ARGENTINA)		Instituto Argentino de Normalización
	C-Tiek (AUSTRALIA) 2250/1132383		Australian Communications Aulhority

CFW 09 - Technical Data

Keypad	Programming	General Drive Functions Programming			
	Controls	Start/Stop , Increase/Decrease Speed, JOG, FWD/REV and Local/Remote			
	Monitoring	Speed Reference (rpm)		Oulput Current (A)	
		Motor Speed (rpm)		Oulput Voltage (Vac)	
		Speed Proportional Value (Ex: ft/min)		Drive Status	
		Output Frequency (Hz)		Digital Inputs Status	
		DC Link Voltage (Vdc)		Transistor Outputs Status	
		Motor Torque (%)		Relay Outputs Status	
		Outout Power (kW)		Analog Inputs Value	
		Hours Powered Up (h)		Four Last Faults	
		Hours Enabled (h)		Fault Messages	

Control Features and Options	**Standard**	Keypad wilh LCD + LED displays (HMI-CFW09-LCD)			
		Password to protect drive programming			
		LCD display language selection: English, Spanish and Portuguese			
		Control mode selection (via parameter): V / F, Sensorless Vector or Vector with Encoder			
		Fault auto-diagnosis and auto-reset			
		Parameters reset to factory or user default			
		Drive Self-tuning to motor and load (Vector Modes)			
		Specific unit indication (Ex: l/s, t/h, %, etc.)			
		Motor slip compensation (V / F Mode)			
		Manual and automatic Torque Boost (V / F Mode)			
		Adjustable V / F Curve (V / F Mode)			
		Minimum and maximum speed limits			
		Output current limit			
		Adjustable motor overload protection			
		Digital gain and offset adjustments for the analog inputs			
		Digital gain adjustment for the analog outputs			
		JOG function			
		JOG + I JOG - Function (momentary speed increase/decrease)			
		COPY Function (Drive ® Keypad or Keypad ® Drive)			
		Comparison functions for lhe digital outputs: N* > Nx; N > Nx; N < Nx; N = O; N = N*; Is > Ix ; Is < Ix; T > Tx and T < Tx			
		Where: N = Motor speed; N* = Speed reference; Is = Output Current and T = Motor torque			
		Linear and S independent acceleration and deceleration ramps, two sets of ramps			
		DC Braking			
		Optimal Braking (Vector Modes)			
		Built-in dynamic braking transistor – Models up to 45A/220-230V and up to 30A/380-480V and up to 14A/500-600V			
		Multi-speed function (up to 8 preset speeds)			
		Speed Profiling function			
		Hour meter and Wattmeter			
		Overlapping PID Regulator (for automatic control of level, pressure, flow, etc.)			
		FWD I REV selection			
		Local I Remote operation selection			
		Flying Start function (restart with the motor spinning)			
		Skip Speed (critical speed rejection)			
		Ride-Through (operation during momentary power loss)			
		Built-in dynamic braking transistor:			
		Models: 6 ... 45 A / 220 - 230 V and 36 ... 30 A / 380 - 480 V			
		FieldBus communication: Modbus RTU built-in			
	Options	Simplified keypad (with LED display only)		HMI-CFW09-LED	
		IP 55 Remote keypad (LED display only)		HMI-CFW09-LED-N4	
		IP 55 Remote keypad (LCD + LED displays)		HMI-CFW09-LCD-N4	
		Remote Keypad cable (3.3, 6.6,10.16.25 and 35 ft)		CAB - HMI 09-X	
		Blank Keypad for local Installation		TCL - CFW09	
		Blank Keypad for remote installation		TCR - CFW09	
		Remote Keypad frame kit		KMR - CFW09	
		I/O Expansion Boards		EBA . OX - CFW09	
				EBB .OX.- CFW09	
				EBC1 .OX- CFW10	
				EBE1. OX - CFW09	
		FieldBus Communications kits (Mounted inside drive)	Profibus DP	KFB - PD	
			DeviceNet	KFB - DN	
			DeviceNet Drive Profile	KFB - DD	
			ElherNet I IP	KFB - EN	
		VSD I PC Communication kit	Software SUPERDRIVE	KSD - CFW09	
			Conectores e Cabos		
			KCS - CFW09		
		Intertace Serial Module RS-232		KCS - CFW09	
		Built-in dynamic braking transistor Models: 54...130 A / 220-230 V and 38...142 A / 380-480 V		"DB" Models	
		External dynamic braking module	Models 180...600A/220-230V e 380-480V	DBW - 01	
			Models 107...472A/500-690V	DBW - 02	
			Models 100...428A/660-690V		
		Easy mounting kit wilh flange (for sizes 3...8)		KMF - CFW09	
		Removable mounting kit (for sizes 9...10)		KME - CFW09	
		Inductor kit for DC link (for sizes 2...8)		KIL - CFW09	
		EMC filter with high attenuation capacity		RF	